Region-of-Interest Imaging with C-arm Computed Tomography

Bildgebung kleiner Volumen in der C-Bogen Computertomographie

Der Technischen Fakultät
der Friedrich-Alexander-Universität
Erlangen-Nürnberg

zur

Erlangung des Doktorgrades Dr.-Ing.

vorgelegt von

Yan Xia

aus

Yanan, Shaanxi, China

Als Dissertation genehmigt
von der Technischen Fakultät
der Friedrich-Alexander-Universität Erlangen-Nürnberg

Tag der mündlichen Prüfung:	17. März 2016
Vorsitzender des Promotionsorgans:	Prof. Dr. Peter Greil
Gutachter:	Prof. Dr.-Ing. Andreas Maier Prof. Frederic Noo, Ph.D

Abstract

C-arm based flat-detector computed tomography (FDCT) is a promising approach for neurovascular diagnosis and intervention since it facilitates proper analysis of surgical implants and intra-procedural guidance. In the majority of endovascular treatments, intra-procedural updates of the imaged object often are restricted to a small diagnostic region of interest (ROI). Such targeted ROI is often the region of intervention that contains device/vessel specific information such as stent expansion or arterial wall apposition. Following the principle of *as low as reasonably achievable* (ALARA), it is highly desirable to reduce unnecessary peripheral doses outside an ROI by using physical X-ray collimation, leading to substantial reduction of patient dose. However, such a technique gives rise to severely truncated projections from which conventional reconstruction algorithms generally yield images with strong truncation artifacts.

The primary research goal of this thesis, therefore, lies on the algorithmic development of various truncation artifact reduction techniques that are dedicated for different imaging scenarios. First, a new data completion method is proposed that utilizes sinogram consistency conditions to estimate the missing sinogram. Although it is only extended to a 2D fan-beam geometry, preliminary results suggest the method is promising regarding truncation artifact reduction and attenuation coefficient recovery. Thereafter, three algorithms are presented, which either follow the analytic filtered backprojection (FBP) frame or are by construction in an iterative manner. They are capable of generating a 3D image from transaxially truncated data and thus appear to be closer to clinical applications. The first approach is the refinement of an existing truncation robust algorithm – ATRACT, which is implicitly effective with respect to severely truncated data. In this thesis, ATRACT is modified to more practically-useful reconstruction methods by expressing its expensive non-local filter as an efficient 1D/2D analytic convolution. The second approach is targeted to particular imaging applications that require an ROI with high image quality for diagnosis, and also a surrounding region with the relatively low resolution for orientation. To accomplish this task, an interleaved acquisition strategy that acquires both a sparse set of global non-truncated data and a dense set of truncated data is presented, along with three associated algorithms. The third approach is an attempt to exploit low-dose patient-specific prior knowledge for the extrapolation of truncated projections. The comparative evaluation clearly depicts the algorithmic performance of all investigated 3D methods under a uniform evaluation framework. In general, ATRACT appears to be more robust than the explicit water cylinder extrapolation in severe truncation case. Contrary to the heuristic methods, the techniques that come with either a sparse set of global data or prior knowledge achieve the ROI reconstructions in a more accurate and robust manner. The decision on which method should be selected relies on multiple factors, but the presented results could be used as the first indicator for the ease of such selection.

Kurzfassung

C-Bogen-basierte Flachdetektor-Computertomographie ist ein vielversprechendes Instrument für die chirurgische Behandlung sowie zur Diagnose neurovaskulärer Krankheiten. Hierbei erlaubt das Verfahren die Analyse chirurgischer Implantate, sowie die Führung von Operationswerkzeugen noch während des Eingriffs. In der Mehrheit der endovaskulären Behandlungen sind nur kleine Bereiche der Anatomie von Interesse, sodass das Blickfeld, engl. Volume-of-Interest (VOI), in der Regel beschränkt ist. Das VOI wird hierbei oft so gewählt, dass nur Objekt- und Gefäßspezifische Informationen wie z.B. die Ausdehnung eines Stents oder die arterielle Wandapposition beinhaltet sind. Um dem Prinzip von "so niedrig wie angemessen erreichbar" zu folgen, ist es nötig, Röntgendosis außerhalb des VOI mittels Kollimation abzuschirmen, was zu einer deutlichen Reduzierung der Patientendosis führt. Jedoch sind die daraus resultierenden Projektionsbilder eingeschränkt, was bei Verwendung gewöhnlicher Rekonstruktionsalgorithmen typischerweise zu Trunkierungsartefakten führt.

Das hauptsächliche Ziel der Dissertation liegt in der algorithmischen Entwicklung verschiedener Korrekturmethoden von Trunkierungsartefakten, die für gängige Aufnahmeverfahren geeignet sind. Zuerst wird eine neuartige Extrapolationsmethode untersucht, die Konsistenzbedingungen des Sinograms benutzt um fehlende Daten wiederherzustellen. Obwohl die Methode derzeit auf die 2D Fächerstrahlgeometrie begrenzt ist, zeigen die Ergebnisse eine deutliche Reduzierung der Trunkierungsartefakte. Außerdem werden drei Algorithmen vorgestellt, die entweder mit einer analytischen, gefiltereten Rückprojektion oder einer iterativen Rekonstruktion arbeiten. Diese ermöglichen eine 3D Rekonstruktion von lateral trunkierten Projektionsdaten, und sind deshalb vor allem für die klinische Anwendung geeignet. Die erste Methode ist eine Weiterentwicklung des ATRACT Algorithmus, welche vor allem bei stark trunkierten Daten effektiv ist. Die rechenaufwendige, globale Filterung von ATRACT wurde durch eine effiziente 1D bzw. 2D Faltung zu einem praktisch nutzbaren Algorithmus erweitert. Die zweite Methode ist auf Bildgebungapplikationen ausgerichtet, bei denen das VOI eine hohe Bildqualität aufweisen muss, z.B. für diagnostische Zwecke. Gleichzeitig soll auch die Umgebung des VOI mit geringer Auflösung dargestellt werden um die Orientierung zu vereinfachen. Hierzu wird ein neuartiges Akquisitionsprotokoll vorgestellt sowie drei dedizierte Rekonstruktionsalgorithmen welche für die daraus resultierenden Projektionsdaten erstellt wurden. Die dritte Methode zielt darauf ab, patienten spezifische Vorkenntnisse für die Expolation der trunkierten Projektionen zu nutzen. In der Auswertung wird das algorithmische Verhalten der untersuchten 3D Methoden in einem einheitlichen Evaluierungsrahmen dargestellt. Im allgemeinen ist ATRACT robuster als die explizite Extrapolation, besonders bei schwerer Trunkierung. Im Gegensatz zu heuristischen Methoden, führen Ansätze, welche einen gewissen Anteil nicht-trunkierter Daten oder aber Vorkenntnisse über den Patient zur Verfügung haben, zu einem genaueren und stabileren Ergebnis. Die dargestellten Ergebnisse liefern einen Vergleich von verschiedenen trunkierungskorrigierten Rekonstruktionsverfahren und helfen somit die Auswahl für einen individuell passenden Ansatz zu erleichtern.

Acknowledgment

During the last three and a half years, I have had the great fortune to work as a Ph.D. candidate at the University of Erlangen-Nuremberg on an exciting research project in collaboration with Siemens Healthcare. I would like to use this opportunity to thank everyone who was involved in this project for the support and for valuable discussions over the years.

In particular, I would like to express my sincere gratitude to my supervisor Prof. Dr.-Ing. Andreas Maier for first introducing me to the exciting world of image reconstruction, for his continuous support of my Ph.D. study, and also for his encouragement, patience, and immense knowledge. His constant guidance helped me in all the time of research and writing of this thesis.

Besides my supervisor, I would like to thank another member of my thesis committee, Prof. Dr. Frederic Noo, for reviewing my thesis, for his insightful feedback and encouragement, and for the questions which incented me to widen my research from various perspectives.

My sincere thanks also go to Dr.-Ing. Sebastian Bauer, who has been my industrial supervisor at Siemens and who provided me constant support regarding all kinds of questions. I am very grateful to his aspiring guidance, invaluably constructive criticism, and friendly advice regarding my work.

Moreover, I am thankful to the collaborating experts from Siemens Healthcare: Dr.-Ing. Frank Dennerlein, Dipl.-Inf. Yu Deuerling-Zheng and Dr. Günter Lauritsch. I want to thank them for many valuable discussions and feedback on my work, and for enabling an excellent research environment at Siemens.

Furthermore, I would like to thank my current and former colleagues at the Pattern Recognition Lab, for establishing the pleasant and friendly working atmosphere at the lab. In particular, I would like to say thank you to Martin Berger, for the inspiring discussions, for the time we were working together on the consistency conditions that motivated the whole work in Chapter 3, and for all the fun we have had during the last years. Also, many thanks to Dr.-Ing. Kerstin Müller, Dr.-Ing. Michael Manhart and Chris Schwemmer, for their constant support and guidance at the beginning of my Ph.D. phase. There are many other people at the lab I would like to thank. For example, Dr.-Ing. Christian Riess, Shiyang Hu, Yanye Lu, Bastian Bier, and Peter Fischer for providing help or inspiring discussions. Furthermore, I would like to thank my student Thomas Kästner and Yixing Huang, for their excellent work and the technical assistance on the research conducted in Chapter 5.

I gratefully acknowledge the financial support of Siemens Healthcare and the Erlangen Graduate School in Advanced Optical Technologies (SAOT).

Last but not least, I would like to thank my family and my girlfriend for supporting me spiritually throughout writing this thesis.

Erlangen, March 22nd 2016 Yan Xia

Contents

I Clinical Background and General ROI Reconstruction Methods 1

Chapter 1 Introduction 3
1.1 Motivation . . . 3
1.1.1 Radiation and Radiation Dose Reduction . . . 3
1.1.2 ROI Imaging with X-ray Collimation . . . 6
1.1.3 Primary Application: Neurointervention with C-arm CT . . . 8
1.1.4 Challenges . . . 10
1.2 Original Contributions . . . 10
1.3 Organization of the Thesis . . . 12

Chapter 2 Region-of-Interest (ROI) Imaging: State of the Art 17
2.1 Geometry and Notations . . . 17
2.2 FDK Algorithm and Truncation Artifacts . . . 18
2.2.1 FDK Reconstruction Algorithm . . . 18
2.2.2 Truncation Artifact . . . 20
2.3 Heuristic Truncation Artifact Reduction Methods . . . 21
2.3.1 Heuristic Extrapolation Schemes . . . 21
2.3.2 Sinogram Recovery using Sinusoidal Trace . . . 24
2.3.3 Data Completion using Prior Scan . . . 26
2.4 Exact Reconstruction Algorithm from Truncated Data . . . 26
2.4.1 DBP Reconstruction Algorithm . . . 27
2.4.2 Data Sufficiency Condition . . . 28
2.4.3 DBP with Prior Knowledge . . . 31
2.5 ROI Imaging-Specific Adaption Strategies . . . 31
2.5.1 Filtered ROI Imaging . . . 31
2.5.2 Offset Detector Acquisition . . . 32
2.6 Other Truncation Artifact Reduction Techniques . . . 32
2.6.1 Wavelet-based ROI Reconstruction . . . 32
2.6.2 Lambda Tomography . . . 33
2.7 Discussion and Summary . . . 34

Chapter 3 Accurate Data Extrapolation using Data Consistency Conditions 37
3.1 Introduction and Motivation . . . 37
3.2 Consistency Conditions . . . 38
3.2.1 Helgason-Ludwig (HL) Consistency Conditions . . . 39
3.2.2 Chebyshev-Fourier Representation . . . 39
3.2.3 2D Fourier-based HL Consistency Conditions . . . 41

3.2.4 HLCC in Fan-beam Geometry 42
3.3 Data Extrapolation Using HLCC 43
3.4 Experiment and Results 45
3.5 Discussion and Conclusions 48
3.5.1 Discussion 48
3.5.2 Conclusions 50

II Towards Clinical Application of ROI Reconstruction Algorithms using C-arm CT 51

Chapter 4 Approximate Truncation Robust Computed Tomography – ATRACT 53

4.1 Introduction and Motivation 53
4.2 2D Radon-based ATRACT Algorithm 54
4.3 Analytic Convolution Formulation 57
4.3.1 2D Convolution-based ATRACT 57
4.3.2 ATRACT with 1D Row-wise Filtering 59
4.4 Empirical Residual Artifact Reduction Methods 61
4.4.1 Bias/Offset Correction 61
4.4.2 Gradient Artifact Reduction for Off-Centered ROI 62
4.5 Summary 63

Chapter 5 Region-of-Interest Reconstruction Algorithms for Shutter Scan Acquisition 65

5.1 Introduction and Motivation 65
5.2 Interleaved Data Acquisition Scheme – Shutter Scan 67
5.3 Shutter Scan Reconstruction Algorithms 68
5.3.1 Joint Weighted FDK/ATRACT Reconstruction 69
5.3.2 Parallel Reconstruction with Volumetric Combination 70
5.3.3 Prior Image Driven Projection Detruncation 73
5.4 Summary 76

Chapter 6 Patient Bounded Extrapolation Method using Low-Dose Priors 79

6.1 Introduction and Motivation 79
6.2 Patient Boundary Estimation with Priors 80
6.2.1 Patient Shape Model Estimation using Slice-wise Ellipse 82
6.2.2 Patient Boundary Estimation for Arbitrary Projections 84
6.3 Adaptive Extrapolation Schemes 84
6.3.1 Patient Bounded Water Cylinder Extrapolation 84
6.3.2 Patient Bounded Square Root Extrapolation 85
6.3.3 Cosine-based Transition Smoothing 86
6.4 Summary 86

Chapter 7 Evaluation and Results 87

7.1 Experimental Setup 87
7.1.1 Clinical Dataset and Scan Configuration 87

7.1.2 Truncation Simulation 89
7.1.3 Image Quality Metrics 91
7.1.4 Standard FDK Reconstruction 91
7.2 ATRACT Specific Evaluation and Parametrization 92
7.2.1 Implementation Details 92
7.2.2 Computational Performance 93
7.2.3 Image Quality Assessment 93
7.3 SSR Specific Evaluation and Parametrization 101
7.3.1 Implementation Details 101
7.3.2 Image Quality Assessment 103
7.4 PBE Specific Evaluation and Parametrization 108
7.4.1 Implementation Details 108
7.4.2 Image Quality Assessment 109
7.5 Comparative Evaluation among ATRACT, SSR and PBE 113
7.5.1 Image Quality Assessment 116
7.5.2 Radiation Dose vs. Image Quality 121
7.6 Summary and Discussion 126

Chapter 8 Outlook **129**

Chapter 9 Summary **131**

Appendix **135**

List of Symbols and Abbreviations **137**

List of Figures **141**

List of Tables **143**

Bibliography **145**

PART I

Clinical Background and General ROI Reconstruction Methods

CHAPTER 1

Introduction

1.1 Motivation 3
1.2 Original Contributions 10
1.3 Organization of the Thesis 12

An essential issue in radiology today is how to reduce patient dose without compromising image quality. In many clinical applications and workflows, such as follow-up examination of deployed stents/flow-diverters, cochlear implants and needle biopsies, only a small portion of the patient may be of diagnostic interest. This enables the idea of region of interest (ROI) imaging, utilizing an X-ray beam collimator to transaxially and axially shield unnecessary radiation during image acquisition. In this manner, only the diagnostic ROI is being irradiated by X-rays, resulting in a substantial reduction in patient dose. However, the resulting transaxially truncated projections pose a challenge to conventional reconstruction algorithms and could yield a dramatic degradation of image quality if no effective counter-measures are performed to rectify truncation artifacts. Therefore, the primary focus of this thesis lies on the algorithmic development of various truncation artifact reduction techniques that are suitable for different ROI imaging applications.

This chapter first presents the general motivation and remaining challenges of ROI imaging in Section 1.1. Then, a summary of the major scientific contributions of this thesis to the progress of research and an overview of the thesis chapters are described in Sections 1.2 and 1.3, respectively.

1.1 Motivation

1.1.1 Radiation and Radiation Dose Reduction

Nowadays, even though the most frequent X-ray examinations are still conducted by using two-dimensional (2D) fluoroscopy, the utilization of three-dimensional (3D) cone-beam imaging systems, such as diagnostic Computed Tomography (CT) or angiographic C-arm Computed Tomography (C-arm CT), has increased immensely over the years. 3D imaging has advantages of offering more precise anatomical information and higher low-contrast resolution and is thus preferred by many clinicians for complex imaging tasks [Miss 00, Hoch 02, Suga 02].

However, X-ray examinations through 3D imaging involve substantial radiation dose and have already become the biggest medical contributor of annual collective

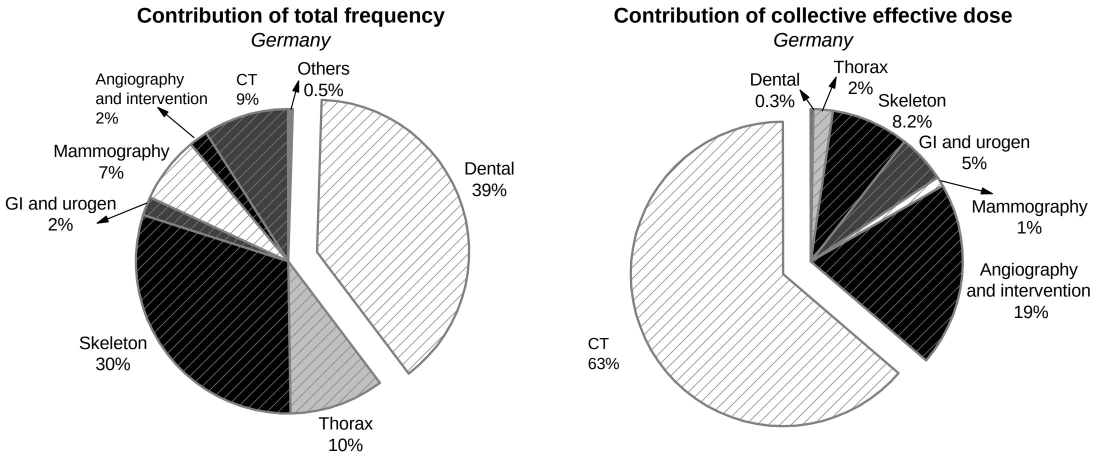

Figure 1.1: Contribution of various X-ray imaging procedures to total frequency (left) and to collective effective dose (right) in Germany, 2012. Statistics are taken from *Umweltradioaktivität und Strahlenbelastung im Jahr 2013* [BMUB 13].

Type of examination	Effective dose E [mSv]
Radiographic examinations	
Teeth	≤ 0.01
Extremities	$\leq 0.01 - 0.1$
Skull	$0.03 - 0.1$
Cervical spine (2 projections)	$0.1 - 0.3$
Thorax (1 projection)	$0.02 - 0.08$
Mammography (2 projections)	$0.2 - 0.6$
Thoracic spine (2 projections)	$0.5 - 0.8$
Lumbar spine	$0.8 - 1.8$
Pelvis	$0.5 - 1.0$
Abdomen	$0.6 - 1.2$
Examinations with radiography/fluoroscopy	
Stomach	$6 - 12$
Intestine (small intestine or colon)	$10 - 18$
Gall bladder	$1 - 8$
Urinary tract	$2 - 5$
Phlebography	$0.5 - 2$
Arteriography and intervention	$10 - 30$
CT examinations	
Skull	$2 - 4$
Spine	$2 - 11$
Thorax	$6 - 10$
Abdomen	$10 - 25$

Table 1.1: Mean value of the effective dose E of X-ray relevant examinations on standard patients with a body weight of 70 ± 5 kg. Statistics are taken from [BMUB 13].

dose to the population [BMUB 13]. As shown in Fig. 1.1, both interventional and diagnostic CT cause large radiation doses compared with other traditional 2D X-ray imaging procedures. It can also be argued that CT examinations and angiographic interventions occupy only 9% and 2% of total examinations, but made contributions of as high as 63% and 19% to the collective effective dose, respectively.

Effective dose E, that is calculated from the measured dose weighted by the organic tissue sensitivity, can be used as a measurement for potential radiation risk. Table 1.1 presents standard values of E for various X-ray examinations published by German Federal Ministry for the Environment, Nature Conservation, and Nuclear Safety ([BMUB 13]). We can see that the radiation dose levels from most of the CT or fluoroscopy examinations are already higher than the annual natural background radiation (e.g., caused by radon gas or cosmic radiation) of about 3.1 millisievert (mSv) (according to Sources and Effects of Ionizing Radiation, UNSCEAR 2008 Report [UNSC 10]).

Base on these statistics, radiological examinations have been increasingly received attention regarding radiation protection and reduction. Two general guiding principles of radiation protection of patients are developed by the International Commission on Radiological Protection (ICRP)[ICRP 07a, ICRP 07b]:

1. Justification: *The imaging procedure should be judged to do more good (e.g., diagnostic efficacy of the images) than harm (e.g., detriment associated with radiation induced cancer or tissue effects) to the individual patient. Therefore, all examinations using ionizing radiation should be performed only when necessary to answer a medical question, treat a disease, or guide a procedure. The clinical indication and patient medical history should be carefully considered before referring a patient for any X-ray examination.*

2. Optimization: *X-ray examinations should use techniques that are adjusted to administer the lowest radiation dose that yields an image quality adequate for diagnosis or intervention (i.e., radiation doses should be As Low as Reasonably Achievable (ALARA)). The technique factors used should be chosen based on the clinical indication, patient size, and anatomical area scanned; and the equipment should be properly maintained and tested.*

The optimization principle suggests that the X-ray imaging process must be optimized towards dose reduction and the examination is performed using radiation doses that must be kept following ALARA, consistent with the interventional/diagnostic tasks. These guidelines have driven radiologists, physicists, technologists and researchers over the years to develop new methods of radiation dose reduction without compromising the image quality.

So far, various strategies and technologies have been developed to reduce the radiation dose. The first choice for modern scanners is to adjust the X-ray tube current according to patient size and shape, to minimize the radiation dose (i.e., automatic exposure control (AEC)). Using this method, a dose reduction of 20-40% can be achieved, depending on the body region and the size of the patient [Gies 99, Mulk 05]. Further dose reduction strategies involve adjusting kilovoltage (kV) based on the patient size [McCo 09], noise control strategies in reconstruction or data processing

[Wang 06, Bai 09], improving detector efficiency [Hsie 09] and adoption of iterative reconstruction algorithms [Elba 02, Lasi 07].

Alternatively, an examination-specific dose reduction strategy is to employ X-ray beam collimation so that only a diagnostic region of interest (ROI) is exposed to X-rays and thus avoid unnecessary radiation doses in the peripheral region. This method yields a dose reduction of up to 90%, depending on the size of the imaged volume to be irradiated [Maie 13]. Since it is the foundation of this research, ROI imaging will be elaborated in detail in the following.

1.1.2 ROI Imaging with X-ray Collimation

For both diagnostic CT and interventional C-arm CT, the dimensions of the imaged field of view (FOV) primarily depends on the detector size, if no collimation is taken. For instance, standard angiographic C-arm systems are typically equipped with a flat detector in the size of $30 \times 40\,\mathrm{cm}^2$ with a resolution of 2480×1920 pixels. Such a detector allows the reconstruction of a non-collimated volume of 22 cm (in-plane) and 16 cm (in the z-axis), with a spatial resolution of up to $0.1 \times 0.1 \times 0.1\,\mathrm{mm}^3$. Although the FOV is large, the surgeon/physician's focus can be relatively small, such as the region of the intervention, the cochlea in the inner ear, an implanted stent or a coiled aneurysm in a vessel. Figure 1.2 shows four different clinical applications representing needle biopsy procedure (top-left), tumor therapy (top-right), endovascular treatment of an intracranial aneurysm (bottom-left) and cochlear implant (bottom-right), respectively. In each of the patient cases, a potentially optimal FOV is selected and indicated by a white rectangle or circle. The suspected disease presentation or the diagnostic ROI is recognized as the Kirschner wire (K-wire)($\sim$ 4 cm length), the targeted residual tumor ($\sim$ 8 cm diameter), the deployed stent ($\sim$ 3 cm length) and the right inner ear ($\sim$ 3.5 cm depth), respectively. It can be seen that in these clinical examples, the actual ROIs that the physician would target only cover a small fraction of the total scan volume, thus imaging of the complete FOV may not be necessary.

Following the ALARA principle, it is highly desirable to reduce these unnecessary peripheral doses by using ROI imaging strategies. That means, X-ray beams need to be collimated in both horizontal and vertical directions to image only the suspected disease area or the diagnostic ROI and shield the radiation exposure outside the ROI. Nowadays, a collimator is equipped on most of CT/C-arm CT scanners. It is a highly attenuating metallic barrier (typically made of lead or tungsten) positioned between the X-ray source and patient (prepatient collimation), with an aperture in the middle to define the beam coverage. The collimator provides a mean to save patient dose by limiting the irradiated field to fit the ROI. Figure 1.3 depicts a non-truncated projection of the clinical data (left) and the corresponding medium truncated ROI projection via a real collimation (right).

The reduction of the FOV in a 3D volume is approximately proportional to the reduction of radiation dose. It has been demonstrated in [Maie 13] that the effective dose E can be reduced dramatically using C-arm based ROI imaging. With non-truncated data, i.e., an FOV of $30 \times 40\,\mathrm{cm}^2$, the resulting effective dose E is up to 2.7 mSv in a standard head scan. When only a subregion of $5 \times 4\,\mathrm{cm}^2$ is irradiated, the

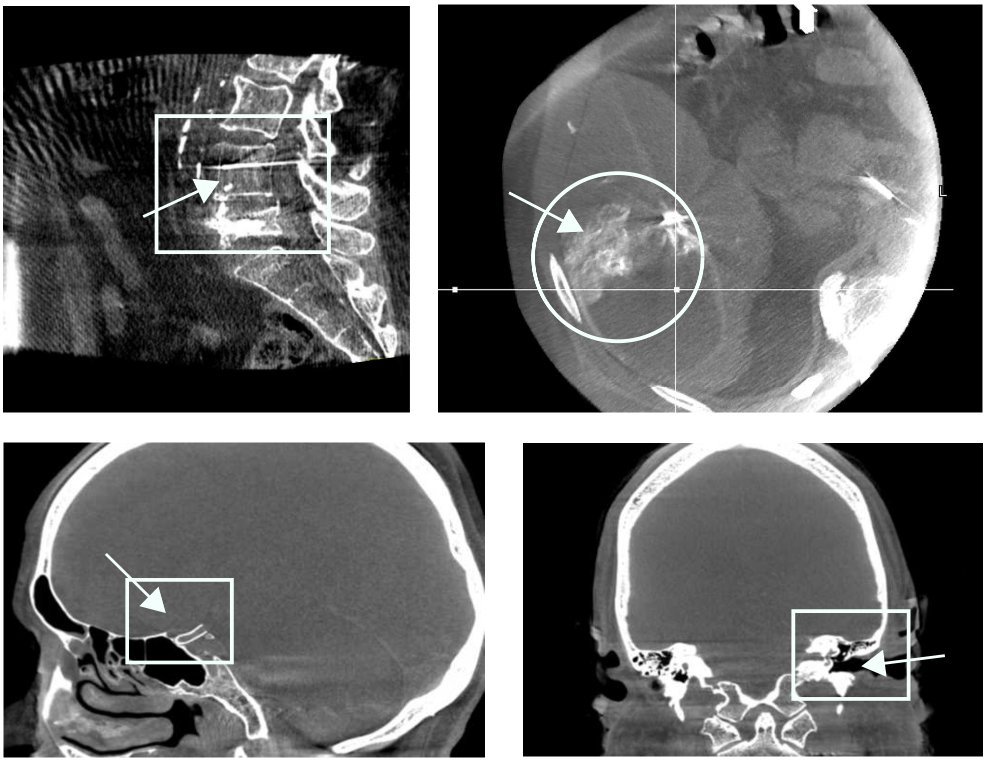

Figure 1.2: Four different clinical examples representing needle biopsy procedure (top-left), tumor therapy (top-right), endovascular treatment of an intracranial aneurysm (bottom-left) and cochlear implant (bottom-right), respectively. The white rectangle or circle indicates the potentially optimal FOV and the arrow indicates the ROI in each case. Images courtesy of Siemens Healthcare GmbH, © Siemens Healthcare.

effective dose is dramatically reduced to 0.1 mSv, by a factor of 27. Note that even this reduced FOV still covers the region of intervention, such as for cochlear implants or stent/flow-diverters deployment etc., at a considerably low X-ray dose.

Although it is beyond the scope of this thesis, using collimation is also found to improve image quality within the ROI, for instance, the reduction of X-ray scatter on the detector. This is because the X-ray collimator limits the field of the patient being exposed to radiation, and this will reduce the overall number of scattered photons (more specifically, the ratio of scattered to primary photons is reduced). It has been shown that scattered radiation is roughly proportional to the scan FOV [Dobb 00]. That means, if the area of the irradiated field is reduced by half, scattered radiation is likewise reduced by 50%. Relevant research and investigation on using collimation to reduce X-ray scatter in cone-beam breast CT can be found in [Chen 08b]. Furthermore, Cho *et al.* [Cho 07] showed that ROI imaging can be used not only for reducing imaging radiation exposure to the patient and scatter to the detector but also for potentially increasing the spatial resolution of reconstructed images in microCT.

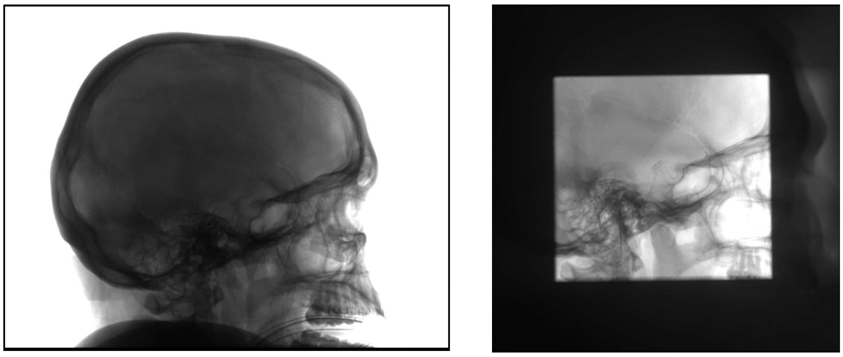

Figure 1.3: Illustration of a projection image acquired from (left) full FOV scan and (right) ROI scan. Images courtesy of CHI St. Luke's Health - Baylor St. Luke's Medical Center, Houston, TX, USA.

1.1.3 Primary Application: Neurointervention with C-arm CT

Every year about 30,000 people in the United States suffer an intracranial aneurysm rupture and the annual rate of aneurysm rupture is approximately 10 per 100,000 persons. Intracranial aneurysms are usually treated by endovascular embolization. It is a surgical procedure primarily involving apposition of micro devices (e.g., coils or stent) in the parent artery or aneurysm, to prevent blood flow into the aneurysm sac over time. The utilization of intracranial stents has immensely increased after self-expandable stents were developed specifically for the endovascular treatment. It has been shown that full stent deployment and good apposition of the stent margins to the arterial wall are of major importance for a successful embolization [Benn 05]. Thus, clear visualization of both the stent struts and their adaptions to arterial walls and aneurysmal lumen presents a great need for imaging systems.

Angiographic C-arm Computed Tomography (C-arm CT) was initially targeted at neuroendovascular imaging of contrast-enhanced vascular structures. Figure 1.4 shows two typical C-arm angiography scanners for different applications. Such scanners are able to provide projection radiography, fluoroscopy, and digital subtraction angiography (DSA) in a single setup, within the interventional radiological suite. Moreover, C-arm systems can also generate CT-like 3D volumetric images that offer both high low-contrast resolution and 3D spatial orientation of anatomical structures. This is particularly valuable for endovascular treatment since 3D images could facilitate proper analysis of a surgical implant and intra-procedural guidance [Akpe 05, Doel 08]. Technically, these imaging tasks may also be assigned to 2D fluoroscopy on angiographic C-arm systems. However, some surgical devices, such as stents or flow-diverters, often possess desirable material characteristics such as low-profile and high flexibility, and thus are difficult to be visible in 2D fluoroscopic images. Figure 1.5 gives an example to illustrate the superiority of 3D imaging over conventional 2D fluoroscopy when localizing a low-profile stent with respect to the treatment region.

Although 3D imaging facilitates the neurovascular diagnosis and intervention such as endovascular embolization, it involves large cumulative radiation dose to the patient when repeated scans or follow-ups are performed over the same anatomical

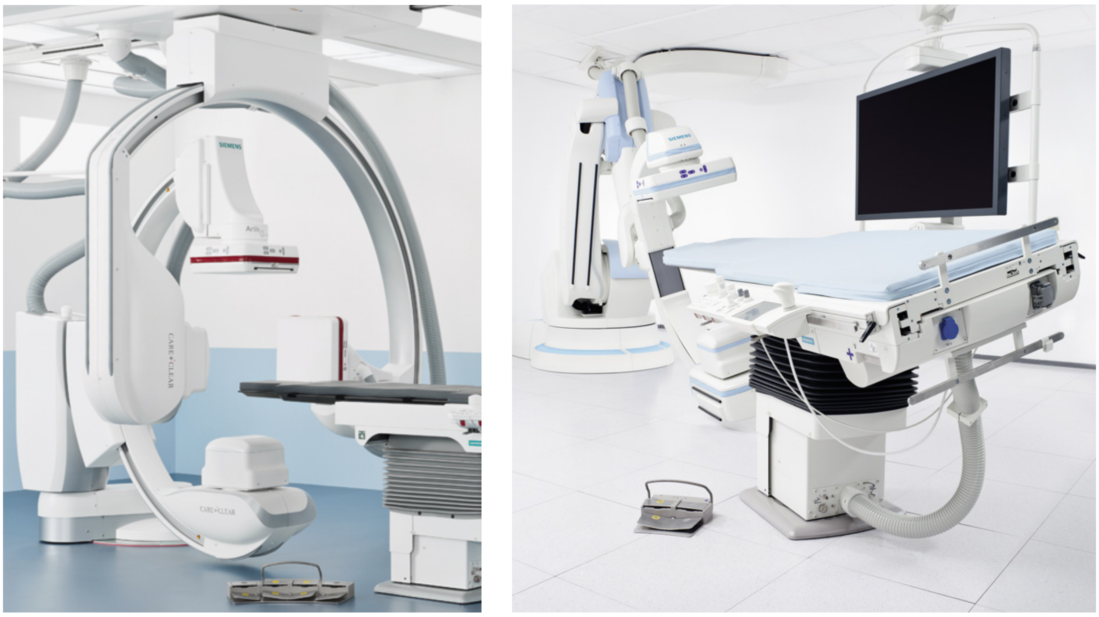

Figure 1.4: C-arm angiography systems (Siemens Healthcare GmbH, Forchheim, Germany): (left) biplane system typically used in neurointervention and (right) robotic monoplane system that is typically used in a surgical environment. Images courtesy of Siemens Healthcare GmbH, © Siemens Healthcare.

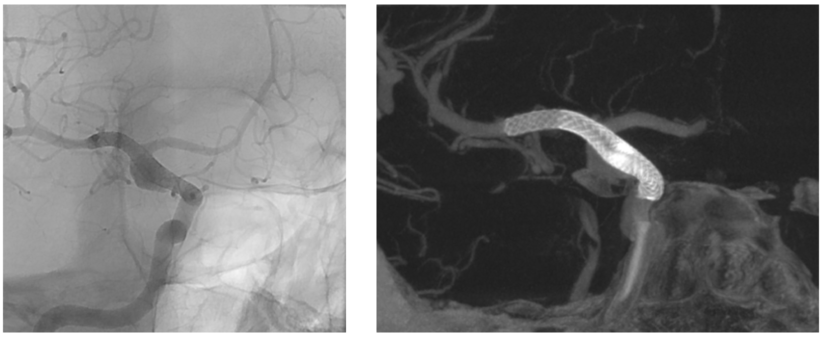

Figure 1.5: Visualization of a deployed neurological stent with respect to the treatment region in (left) view-aligned 2D fluoroscopic image, and (right) rendered volume from 3D imaging. Images courtesy of CHI St. Luke's Health - Baylor St. Luke's Medical Center, Houston, TX, USA.

region. In the majority of endovascular treatments, intra-procedural updates of the imaged object often are restricted to a small targeted ROI. Such an ROI is often the region of intervention that contains device specific information such as stent expansion, margin apposition, and aneurysm neck coverage, etc. Under such circumstances, the X-ray beam can be collimated closely to the ROI only (e.g., stents, coils, or flow-diverters) within the patient, reducing unnecessary radiation doses outside the ROI. By doing so, a considerable reduction of radiation doses to the patient and higher contrast due to reduced scatter can be achieved.

1.1.4 Challenges

In most angiographic C-arm systems, 3D volumetric images are obtained using analytical filtered-backprojection (FBP) reconstruction algorithms, such as the Feldkamp-Davis-Kress (FDK) method [Feld 84]. The FDK algorithm is both efficient and robust, yielding superior reconstructions in practice. However, due to the non-local property of the ramp filter within FDK, reconstruction of any point of an object requires the knowledge of the projections even far away from the point at the same transaxial position. This requirement, however, is not satisfied anymore if projections are transaxially collimated during 3D ROI imaging. Therefore, the direct application of FDK on truncated data leads to severe truncation artifacts. These artifacts manifest as a bright ring/cupping at the edge of the 3D ROI images and noticeably contaminate the reconstruction results.

As a counter-measure, heuristic extrapolation schemes, e.g., the water cylinder extrapolation [Hsie 04], are usually applied, as a pre-processing step, to reduce truncation artifacts. However, such methods primarily rely on techniques that complete the truncated data by means of a continuity assumption at the truncation edge and thus appear to be *ad-hoc*. It is of practical significance to develop an algorithm for C-arm based ROI imaging that is of comparable accuracy to FDK reconstructions from non-truncated projection data.

Furthermore, there also arises some imaging applications that require spatially varying image quality, e.g., a high resolution inside an ROI for diagnosis and relative low image quality outside the ROI for orientation. For these applications, information outside the ROI yields rather adequate image quality but allows an overview orientation such as locating other organs, catheters or surrounding landmarks. Both the acquisition and reconstruction of such data also pose challenges to conventional reconstruction algorithms.

1.2 Original Contributions

The scientific focus of this work lies on the algorithmic development of various truncation artifact reduction techniques that fulfill different imaging application scenarios. This section provides an overview of the original contributions of this thesis along with the corresponding scientific publications.

ROI Imaging without Prior Knowledge

Reconstruction algorithms that require no prior knowledge are potentially suitable for any clinical workflows. These algorithms pose little constraints on the availability of prior image data such as preoperative scans and involve no additional dose to the patient. The following research has been conducted in this category:

- An algorithm that uses neither prior knowledge nor explicit extrapolation is developed. It follows the analytic FDK framework, but is by construction more robust with respect to truncated data. Two variants are suggested to further improve computational efficiency and image accuracy. Furthermore, several steps that need to be undertaken to make the algorithm suitable for clinical application are presented.

- A sinogram completion method based on data consistency conditions is proposed. The consistency conditions are theoretically derived from the Helgason-Ludwig conditions and can be efficiently evaluated via 2D FFT. The method aims to reduce both high-frequency cupping artifacts as well as low-frequency bias, in the reconstructed volume.

These original algorithmic developments were presented at three international conferences [Xia 12, Xia 13a, Xia 13b]. Parts of the work have also been published in two journal articles [Xia 14b, Xia 14c] and submitted to a journal [Xia 15a] (under review).

ROI Imaging with Prior Knowledge

In C-arm CT, some specific applications indeed provide prior information, e.g., fluoroscopic images during an isocenter procedure. It is found that image quality can be considerably improved with such information. In this thesis the following achievements have been made in this category:

- A concept of a new interleaved acquisition scheme is proposed, which would allow acquiring both a high number of truncated data and a low number of non-truncated data within one C-arm sweep. Moreover, three reconstruction pipelines that are particularly dedicated to such data are developed. All methods are able to generate a 3D image with spatially varying image quality.

- A refined extrapolation scheme, based on the estimation of a 3D patient outline model, is suggested. The method brings about a major improvement in image quality for C-arm based ROI 3D imaging, with essentially low-dose, prior fluoroscopic images.

These original algorithmic contributions were presented at two international conferences [Kaes 15, Xia 14a]. Parts of the work have also been published in a journal article [Xia 15b].

Image Quality Assessment

Reducing radiation exposure while retaining the high quality of images is the main goal of this research. To this end, the following image quality assessments were conducted:

- An ROI algorithm that requires no prior knowledge has been evaluated towards clinical application in endovascular treatment.
- All proposed 3D algorithms have been comparatively evaluated in a uniform framework. To validate the robustness of these methods for realistic problems, we used 16 clinical datasets from different patients that were acquired in an interventional suite.

Both points underline the practical relevance and impact of the current research. Parts of the work were presented at two medical conferences [Chin 12, Ahme 14] and have been submitted to a clinical journal [Chin 15].

In summary, the results of the thesis were presented at seven international conferences [Chin 12, Xia 12, Xia 13a, Xia 13b, Kaes 15, Ahme 14, Xia 14a] and three journal publications [Xia 14b, Xia 14c, Xia 15b].

1.3 Organization of the Thesis

This section presents an organization of the thesis with a brief description of each chapter that provides a reading guide to this thesis. Furthermore, a graphical overview of the thesis structure is also presented in Fig. 1.6.

Chapter 2 - Region-of-Interest Imaging: State of the Art

This chapter first introduces the traditional FDK reconstruction algorithm and explains why it fails at obtaining an accurate image from transaxially truncated data. Then, a literature overview of previous related work is provided, including empirical, approximated reconstruction methods, data completion methods using prior knowledge, exact reconstruction schemes as well as ROI imaging-specific adaption strategies.

Chapter 3 - Accurate Data Extrapolation using Data Consistency Conditions

This chapter suggests a new direction for data extrapolation scheme. The aim is to take advantage of data consistency conditions to achieve superior image quality within an ROI. To this purpose, firstly the existing data consistency conditions (Helgason-Ludwig) along with their variants are reviewed. Motivated by the previous observations, a set of the consistency conditions in the Fourier space is theoretically derived. Then, we propose a method that extrapolates the truncated sinogram with data from a uniform ellipse of which the parameters are determined by optimizing these consistency conditions. Finally, preliminary experimental results from a simulated phantom are presented.

Chapter 4 - Approximate Truncation Robust Computed Tomography - ATRACT

In this chapter, the original truncation robust algorithm, namely ATRACT, is first derived in the Fourier domain. Although it is robust to data truncation, the method involves performing 2D Radon transform and its inversion for each projection and thus is computationally very expensive. For practical use, two variants of the original ATRACT are proposed. One is based on expressing the 2D Radon-based filter as an efficient 2D convolution with an analytically derived kernel. The second variant is to adapt ATRACT in 1D to further reduce computational complexity. Both variants lead to a noticeable computational speed-up and thus make ROI imaging applicable to interventional workflows. Finally, several steps are presented that need to be undertaken to make the algorithm suitable for clinical application.

Chapter 5 - Region-of-Interest Reconstruction Algorithms for Shutter Scan Acquisition

This chapter presents a proof-of-concept study of a new interleaved acquisition, namely shutter scan. That is, within one scan, to generate a high number of truncated projections and a low number of full/non-truncated FOV projections simultaneously. This technique would allow obtaining a 3D image with a particularly high-resolution ROI while capturing the external anatomical structures by reconstructing a sparse set of non-truncated projections. Even though that would involve the acquisition of a sparse group of non-truncated projections, the overall applied dose still remains considerably below the amount of a conventional scan. However, strong streaking and cupping artifacts will arise in the reconstruction of shutter scan data. Therefore, three reconstruction strategies are suggested that are capable of reconstructing and combining such data and lead to a hybrid volume with spatially varying image quality.

Chapter 6 - Patient Bounded Extrapolation Method using Patient-Specific Low-Dose Priors

This chapter addresses a prior image-based extrapolation method that brings about major improvements in the accuracy of 3D ROI imaging, even in the presence of severely truncated data. The method utilizes two non-collimated fluoroscopic images that are usually generated during the isocentering procedure before a 3D acquisition. It does not require any additional hardware and can be readily integrated into the existing interventional workflow. First, a rough 3D patient shape is estimated from two fluoroscopic projections, using per-slice ellipse fitting. Forward projecting this 3D model for any projection angle acquired during the actual ROI scan gives the patient bounded information for the corresponding projection. Then, improved detruncated/extrapolated projection data could be obtained by adapting the extrapolated profile to fit the known profile boundary points.

Chapter 7 - Evaluation and Results

The reconstruction algorithms presented in Chapter 4 to Chapter 6 come with a different trade-off between image quality and radiation dose and may thus be suitable for different application scenarios. This motivates us to conduct a detailed comparative evaluation of the proposed algorithms using a uniform framework in Chapter 7. At the beginning of the chapter, the experimental setup is described that includes studied clinical datasets, truncation simulation as well as image quality metrics. Then, each of proposed methods is evaluated individually/internally with its several variants/parameters. After this parametrization, the best candidate of each group of the algorithms is picked for the following comparative evaluation. Finally, evaluation results are discussed and conclusions are drawn.

Chapter 8 - Outlook

In this chapter, future research work and directions to address the remaining issues of C-arm based 3D ROI imaging are discussed.

Chapter 9 - Summary

The final chapter gives an overview of the conducted research and the progress achieved by the scientific work presented in this thesis.

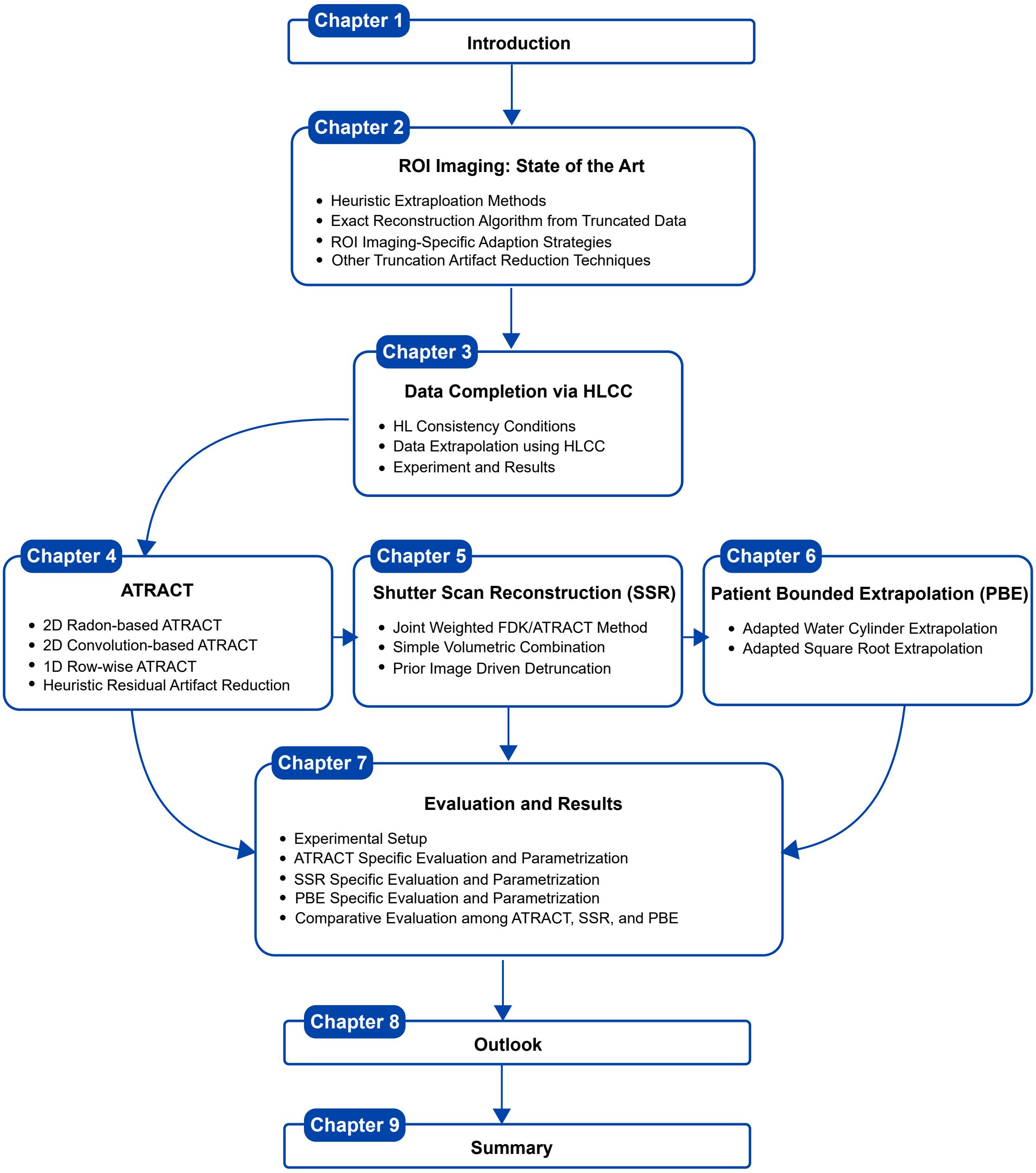
Chapter 1
Introduction
Chapter 2
ROI Imaging: State of the Art
Heuristic Extraploation Methods
Exact Reconstruction Algorithm from Truncated Data
ROI Imaging-Specific Adaption Strategies
Other Truncation Artifact Reduction Techniques
Chapter 3
Data Completion via HLCC
HL Consistency Conditions
Data Extrapolation using HLCC
Experiment and Results
Chapter 4
ATRACT
2D Radon-based ATRACT
2D Convolution-based ATRACT
1D Row-wise ATRACT
Heuristic Residual Artifact Reduction
Chapter 5
Shutter Scan Reconstruction (SSR)
Joint Weighted FDK/ATRACT Method
Simple Volumetric Combination
Prior Image Driven Detruncation
Chapter 6
Patient Bounded Extrapolation (PBE)
Adapted Water Cylinder Extrapolation
Adapted Square Root Extrapolation
Chapter 7
Evaluation and Results
Experimental Setup
ATRACT Specific Evaluation and Parametrization
SSR Specific Evaluation and Parametrization
PBE Specific Evaluation and Parametrization
Comparative Evaluation among ATRACT, SSR, and PBE
Chapter 8
Outlook
Chapter 9
Summary

Figure 1.6: A graphical overview of the thesis structure.

CHAPTER 2

Region-of-Interest (ROI) Imaging: State of the Art

2.1 Geometry and Notations 17
2.2 FDK Algorithm and Truncation Artifacts 18
2.3 Heuristic Truncation Artifact Reduction Methods 21
2.4 Exact Reconstruction Algorithm from Truncated Data 26
2.5 ROI Imaging-Specific Adaption Strategies 31
2.6 Other Truncation Artifact Reduction Techniques 32
2.7 Discussion and Summary 34

Tomographic ROI reconstruction from transaxially truncated projection data is always challenging and can result in strong truncation artifacts. Such artifacts typically manifest as a high-frequency cupping effect and a low-frequency bias in the 3D volumetric image. This chapter provides a thorough literature overview of previously published work concerning the reduction of these truncation artifacts. Section 2.1 introduces the 3D imaging geometry and associated notations that are used in this thesis. Section 2.2 provides a few examples to illustrate why the analytical FDK algorithm cannot tolerate any data truncation. Thereafter, Section 2.3 reviews several existing heuristic extrapolation methods as well as various data completion strategies. Section 2.4 shows how the truncation problem can be partially solved using an alternative Radon inversion – the differentiated backprojection method (DBP) and presents its several variants and the associated sufficiency conditions. In Section 2.5, two ROI imaging-specific modifications, namely filtered ROI imaging and offset detector acquisition, are described. Furthermore, two alternative ROI reconstruction techniques, wavelet based localization and lambda tomography, are introduced in Section 2.6. Finally, Section 2.7 discusses the pros and cons of these state-of-the-art methods and summarizes the chapter.

2.1 Geometry and Notations

This section introduces the imaging geometry and associated notations, which are needed throughout this thesis. Let us denote the object density function $f(\mathbf{x})$ with $\mathbf{x} = (x, y, z)$. Focusing on the 3D cone-beam (CB) imaging geometry with a flat-

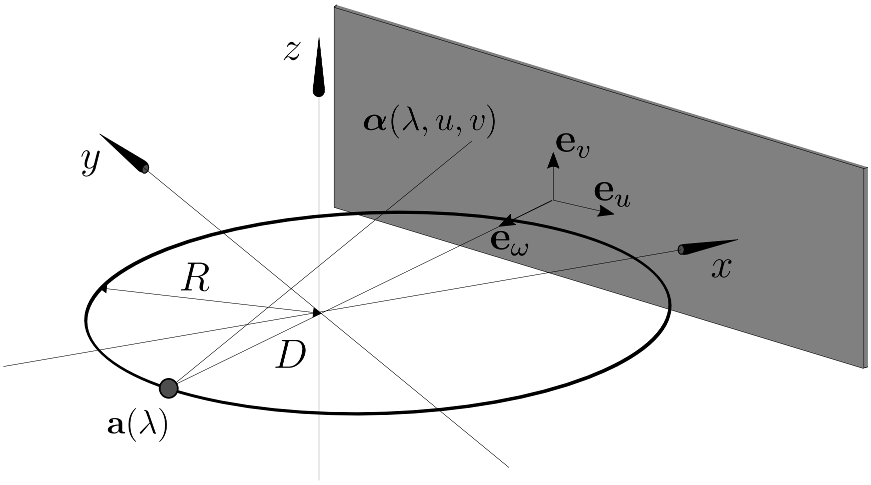

Figure 2.1: Illustration of the circular cone-beam geometry with a flat-panel detector. Notations: $\mathbf{a}(\lambda) = (R\cos\lambda, R\sin\lambda, 0)$ describes the trajectory of the X-ray source, with the patient-detector distance R and the rotation angle λ. $\mathbf{e_w}(\lambda)$ is the unit vector orthogonal to the flat-panel detector, and $\mathbf{e_u}(\lambda)$ and $\mathbf{e_v}(\lambda)$ are the orthogonal unit vectors at distance D from the source.

panel detector shown in Fig. 2.1, we assume that the X-ray source moves along a circular trajectory $\mathbf{a}(\lambda) = (R\cos\lambda, R\sin\lambda, 0)$ during the scan with R indicating the source-isocenter distance. The vector pair (u, v) denotes the detector coordinate and the point $(0, 0)$ is set to the orthogonal projection of $\mathbf{a}(\lambda)$ onto detector plane. Then, the 2D projection $g(\lambda, u, v)$ at the rotation angle λ obtained for all possible unit vectors $\boldsymbol{\alpha}(\lambda, u, v)$ can be written as

$$g(\lambda, u, v) = \int_0^\infty f(\mathbf{a}(\lambda) + t\boldsymbol{\alpha}(\lambda, u, v))\, dt, \tag{2.1}$$

with

$$\boldsymbol{\alpha}(\lambda, u, v) = \frac{1}{\sqrt{u^2 + v^2 + D^2}} \left(u\mathbf{e}_u(\lambda) + v\mathbf{e}_v(\lambda) - D\mathbf{e}_\omega(\lambda)\right), \tag{2.2}$$

where D is the source-detector distance, $\mathbf{e}_\omega(\lambda) = (\cos\lambda, \sin\lambda, 0)$ is the unit vector orthogonal to the detector plane and pointing toward the source, and $\mathbf{e}_u = (-\sin\lambda, \cos\lambda, 0)$ and $\mathbf{e}_v = (0, 0, 1)$ are orthogonal unit vectors in the direction along which u and v are measured.

2.2 FDK Algorithm and Truncation Artifacts

2.2.1 FDK Reconstruction Algorithm

The reconstruction problem is to restore $f(\mathbf{x})$ from CB data $g(\lambda, u, v)$ collected over a suitable angular range, e.g., of π plus fan-beam angle in a short-scan acquisition. The Feldkamp–Davis–Kress algorithm (FDK) [Feld 84], which is an effective extension of the 2D fan-beam filtered backprojection (FBP), is commonly used for the circular cone-beam reconstruction due to its simplicity and efficiency. It approximately computes an estimate $f^{(\mathrm{FDK})}$ of the real object function f by backprojecting the filtered projection data $g_F^{(\mathrm{FDK})}$. For a moderate cone-angle, the differences between $f^{(\mathrm{FDK})}$ and f are small and often acceptable. More specifically, the standard FDK algorithm consists of the following three steps:

- *Step 1:* Cosine- and Parker-like weighting of projection data to obtain pre-scaled projection data $g_1(\lambda, u, v)$:

  $$g_1(\lambda, u, v) = \frac{Dm(\lambda, u)}{\sqrt{D^2 + u^2 + v^2}} g(\lambda, u, v), \tag{2.3}$$

  where $m(\lambda, u)$ denotes a weight which is constantly 0.5 for a full circular scan but has to be determined to approximate the data redundancy for a short scan [Park 82].

- *Step 2*: 1D row-wise ramp filtering to obtain filtered projection data $g_F(\lambda, u, v)$:

  $$g_F^{(\mathrm{FDK})}(\lambda, u, v) = \int_{-\infty}^{\infty} h_R(u - u')\, g_1(\lambda, u', v)\, du', \tag{2.4}$$

  where $h_R(u)$ is the ramp filter kernel in the spatial domain that is defined as follows

  $$h_R(u) = \int_{-1/2}^{1/2} |\omega_u| \exp(j2\pi\omega_u u)\, d\omega_u = \frac{1}{2}\frac{\sin(\pi u)}{\pi u} - \frac{1}{4}\left(\frac{\sin\left(\frac{\pi u}{2}\right)}{\frac{\pi u}{2}}\right)^2 \tag{2.5}$$

  with the Fourier representation of the ramp kernel $|\omega_u|$.

- *Step 3:* 3D cone-beam backprojection with a weighting function of the source-detector distance to get the estimated object function $f^{(FDK)}(\mathbf{x})$:

  $$f^{(\mathrm{FDK})}(\mathbf{x}) = \int_{\lambda_1}^{\lambda_2} \frac{RD}{[R - \mathbf{x}\cdot\mathbf{e}_w(\lambda)]^2} g_F(\lambda, u, v) d\lambda, \tag{2.6}$$

  where $\mathbf{x} = (x, y, z)$ and $[\lambda_1,\ \lambda_2]$ is the short scan angular range.

Apart from its simplicity and efficiency, another important advantage is that FDK, compared with the exact methods proposed in [Kats 03, Zou 04], nicely handles data truncation in the axial direction benefiting from its row-wise filtering. However, due to the non-local property of the ramp kernel, FDK is unable to accurately reconstruct transaxially truncated data and gives rise to severe truncation artifacts in reconstructed images. A detailed explanation will be provided in the following section.

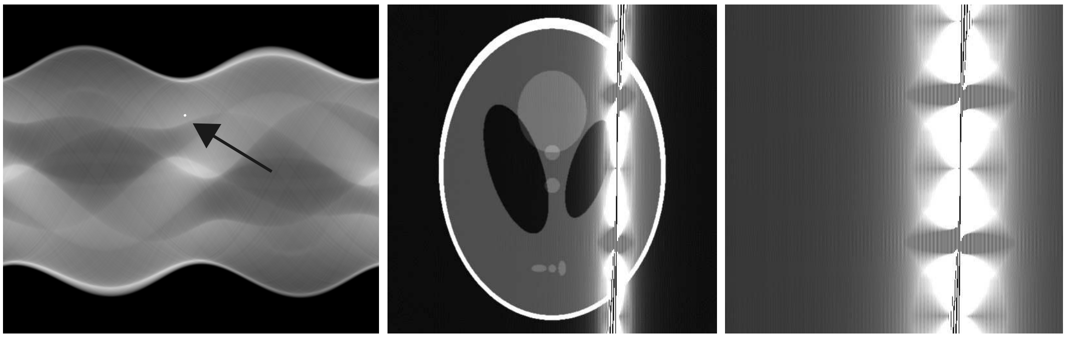

Figure 2.2: Illustration of the non-local property of the FDK algorithm: (left) sinogram of the object with a single distorted pixel (pointed by the arrow), (middle) reconstruction from the contaminated sinogram and (right) difference image with respect to the reference.

2.2.2 Truncation Artifact

The data truncation is caused either by the limitation of the detector size or by specifically obstructing the X-ray beams using a physical collimation primarily for the reduction of the patient dose, as described in Section 1.1.2. This thesis focuses on the latter case although both cases pose a challenge for the straightforward application of the FDK algorithm.

For a long period of time, it is believed that accurate reconstruction of an object of interest is impossible if projection data are truncated, since only an incomplete set of the line integrals of the entire object is available in such scenarios. This belief partly results from the non-uniqueness solution for the interior problem[1], and partly from the non-local property of analytic FBP/FDK algorithms.

Let us recall the filtering and backprojection steps in the FDK algorithm [Eqs. (2.4) and (2.6)], which implicitly imply the non-local property of the algorithm: g_F is computed by an integral over the range $[-\infty, \infty]$ with respect to u. Since the ramp filter kernel $h_R(\cdot)$ has an infinite support, each point in this interval is required. Even a single point contamination or missing will degrade the complete projection after filtering. In the following backprojection step, each filtered projection g_F makes a contribution of each single point in the reconstructed image [see Eq. (2.6)]. Therefore, even a single pixel distortion in projection data will prevent FDK algorithm to accurately reconstruct the original object. Figure 2.2 illustrates this case, where the Shepp-Logan phantom was reconstructed from a complete sinogram with one pixel being set to a singularity value (indicated by the black arrow). The difference image shows that the errors from this single distorted pixel are distributed over the entire image domain.

Thus, due to its non-local characteristic, the FDK algorithm cannot accurately reconstruct the object from the truncated projection data, in which the unmeasured data are replaced by 0. Specifically, the FDK ramp filtering of each truncated projection has a sudden change at the boundaries of the scan FOV, between the measured data and zeros (caused by truncation), introducing artificial frequencies and resulting in noticeably bright rim artifacts at the border of the ROI. Such artifacts are often referred to as high-frequency cupping artifacts in literature. Figure 2.3 shows an example of a typical truncation-induced cupping artifact in cone-beam truncated data. This patient dataset was acquired on a C-arm CT system (Artis-Zee, Siemens Healthcare, Forchheim, Germany) in a clinical environment. Note that although the artifacts reduce towards the center of the ROI, a low-frequency bias/offset appears everywhere in the reconstructed volume and the relative contrast is also modified.

---

[1] Later on, Noo *et al.* [Noo 04], Defrise *et al.* [Defr 06], Ye *et al.* [Ye 07] and Kudo *et al.* [Kudo 08] proved that it is also possible to get the uniqueness of solution to ROI problem if some data sufficiency conditions are satisfied. We describe these methods in more detail in Section 2.4.

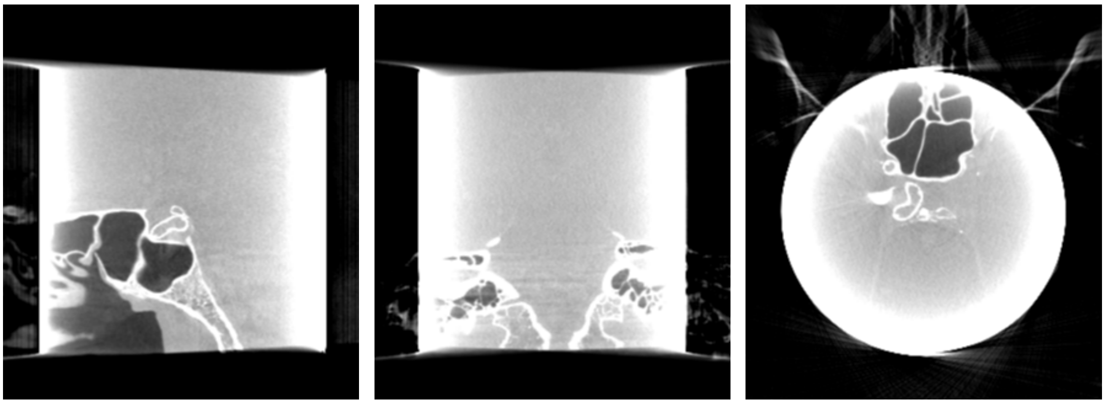

Figure 2.3: Illustration of truncation artifacts in the FDK reconstruction of truncated data: (left) sagittal slice, (middle) coronal slice and (right) transversal slice. Images courtesy of CHI St. Luke's Health - Baylor St. Luke's Medical Center, Houston, TX, USA.

2.3 Heuristic Truncation Artifact Reduction Methods

This section provides an overview of several commonly-used heuristic extrapolation methods and data completion schemes for ROI reconstruction.

2.3.1 Heuristic Extrapolation Schemes

It is intuitively expected that the artifacts caused by truncation of the projection data can be dramatically reduced if the unmeasured part of these projections is approximately estimated by an appropriate mathematical extrapolation function. This extrapolation function typically provides a smooth continuation at the truncation transition region such that analytic FBP/FDK-type algorithms can be applied with less artificial high-frequency artifacts (i.e., cupping artifacts). In general, such a smooth continuation is applied row-wise by using 1D segments of a selected mathematical function that are fitted to the projection line, leading to a combined projection that consists of the originally measured truncated part and the extrapolated part. Moreover, the extrapolation function also incorporates any available prior information/estimation from the measured projection data, such as the assumption of the object shape or texture, so that quantitative accuracy of reconstruction images can be further restored.

Suppose $g_{\lambda,v}(u)$ is a truncated 1D projection line at the given detector row v and rotation angle λ, measured in an interval $[u_{\min}, u_{\max}]$. Then, the complete projection line yields

$$g_{\lambda,v}^{(\text{extrap})}(u) = \begin{cases} g_{\lambda,v}(u) & u_{\min} \leq u \leq u_{\max} \\ e(u) & \text{else} \end{cases} \tag{2.7}$$

with a selected extrapolation function $e(u)$.

So far, various extrapolation functions have been used in the literature, such as symmetric mirroring of projection images (Ohnesorge *et al.* [Ohne 00]), water cylinder/ellipse extrapolation (Hsieh *et al.* [Hsie 04], Maltz *et al.* [Malt 07]), smooth function estimation (Van Gompel *et al.* [Van 04]), square root function extrapolation (Sourbelle *et al.* [Sour 05]), optimization-based extrapolation (Maier *et al.* [Maie 12]) and hybrid extrapolation scheme (Zellerhoff *et al.* [Zell 05]). Below we shortly describe three popular extrapolation schemes, along with the schematic illustration of each principle shown in Fig. 2.4. For convenience, all extrapolation functions are described only for the right portion of the truncated projection; the left portion is extrapolated analogously.

The extrapolation scheme of Ohnesorge *et al.* [Ohne 00] uses a symmetric mirroring of the measured data with a cosine weighting, to approximate the unknown part of projection data:

$$e_{\text{mirror}}(u) = \left(2g_{\lambda,v}(u_{\max}) - g_{\lambda,v}(u_{\max} - u)\right)\cos\left(\frac{u - u_{\max}}{u_{\text{ext}} - u_{\max}}\right), \tag{2.8}$$

where the interval $[u_{\max}, u_{\text{ext}}]$ defines the extrapolated region. In the method of Hsieh *et al.* [Hsie 04], the missing data are estimated by integrals along parallel rays through a 2D water cylinder as follows:

$$e_{\text{water}}(u) = 2\mu\sqrt{r^2 - (u - u_c)^2}, \tag{2.9}$$

where μ denotes the water attenuation coefficient, u_c denotes the location of the fitted cylinder with respect to the detector row and r denotes the radius. As described in Hsieh's work [Hsie 04], the parameters u_c and r can be determined by

$$u_c = \frac{g_{\lambda,v}(u_{\max})\, g'_{\lambda,v}(u_{\max})}{4\mu^2}, \quad r = \sqrt{\frac{g_{\lambda,v}(u_{\max})}{4\mu^2} + u_w^2}, \tag{2.10}$$

where $g'_{\lambda,v}(u_{\max})$ denote the slope of the truncation projection boundary calculated over several samples. Moreover, based on the observation that the cross-section boundary of the patient can be locally approximated as an ellipse, Sourbelle *et al.* suggested [Sour 05] the square root function can be a good extrapolation function for estimating patient body:

$$e_{\text{square}}(u) = \sqrt{a \cdot u^2 + b \cdot u + c}. \tag{2.11}$$

To determine the parameters a, b, and c, the following continuity equations are used:

$$g_{\lambda,v}(u_{\max}) = \sqrt{a \cdot u_{\max}^2 + b \cdot u_{\max} + c}, \tag{2.12}$$

$$g'_{\lambda,v}(u_{\max}) = \frac{b + 2a \cdot u_{\max}}{2g_{\lambda,v}(u_{\max})}, \tag{2.13}$$

$$g_{\lambda,v}(u_{\text{bound}}) = \sqrt{a \cdot u_{\text{bound}}^2 + b \cdot u_{\text{bound}} + c} = 0, \tag{2.14}$$

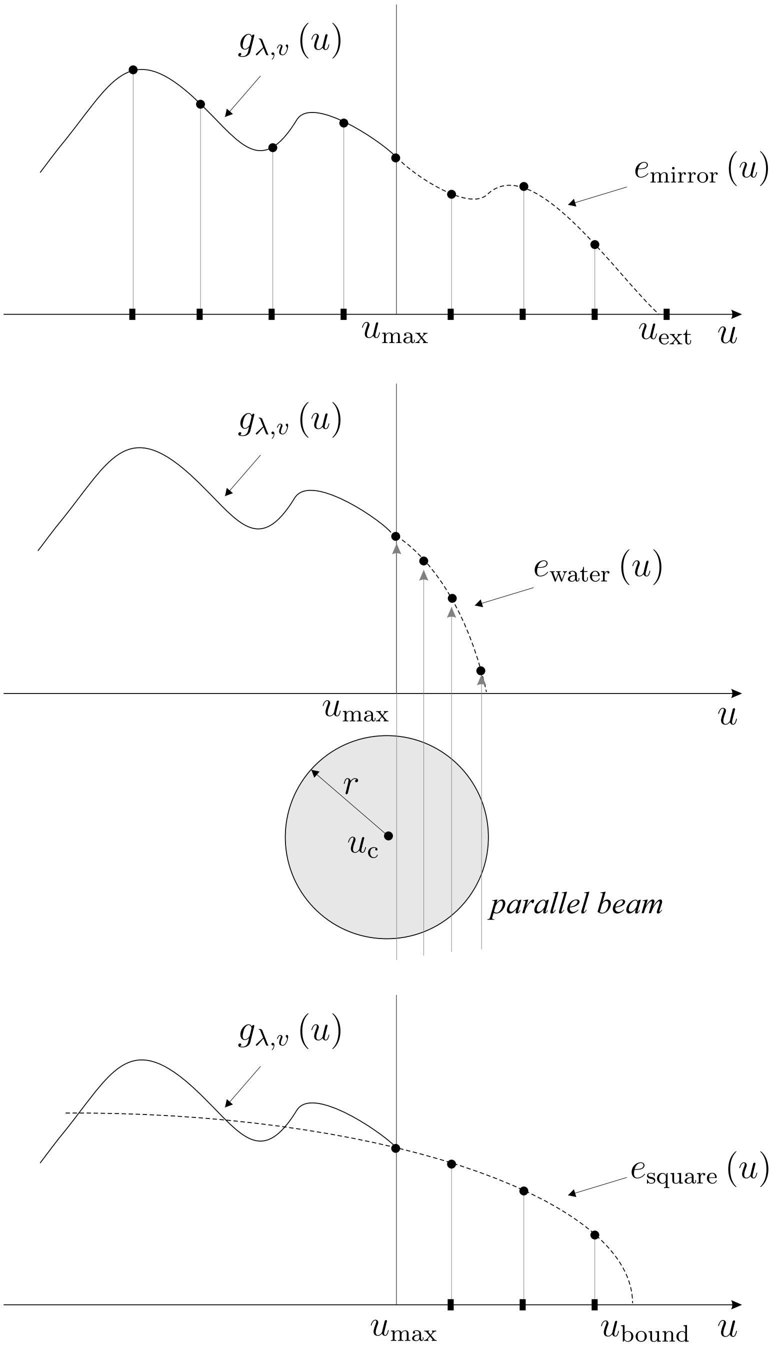
$g_{\lambda,v}(u)$
$e_{\mathrm{mirror}}(u)$
u_{max}
u_{ext}
u
$g_{\lambda,v}(u)$
$e_{\mathrm{water}}(u)$
u_{max}
u
r
u_{c}
parallel beam
$g_{\lambda,v}(u)$
$e_{\mathrm{square}}(u)$
u_{max}
u_{bound}
u

Figure 2.4: Schematic illustration of the principle of three commonly used heuristic extrapolation schemes: (top) symmetric mirroring extrapolation $e_{\mathrm{mirror}}(u)$, (middle) water cylinder extrapolation $e_{\mathrm{water}}(u)$ and (bottom) square root function extrapolation $e_{\mathrm{square}}(u)$. For convenience, all extrapolation functions are described for the right portion of the truncated projection; the left portion is extrapolated analogously.

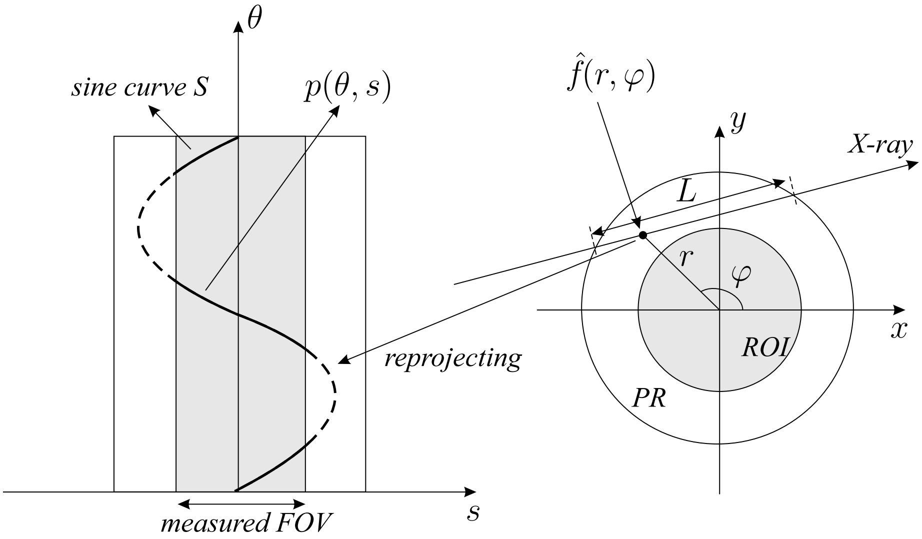

Figure 2.5: Schematic illustration of the principle of data completion method using a sine curve S. The basic assumption is that the data are consistent and continuous along S curves, so that the truncated parts of an S curve (dashed) can be estimated using the measured parts (solid).

where u_{bound} denotes the patient boundary information. This additional information is generally not available but can be roughly estimated either using the zero-order consistency condition (all projections yield the same projection mass [Hsie 04]) or from attenuation values of the orthogonal projection according to a water-equivalent thickness approximation [Malt 07].

The explicit extrapolation methods are usually preferred in ROI reconstruction for three reasons: they can be applied as a pre-processing step before reconstruction and thus are compatible with most existing image reconstruction algorithms; the methods are computationally very efficient; they are capable of estimating the missing data heuristically without the requirement of prior knowledge. However, it may be difficult to apply these heuristic methods to severe truncation cases that are often encountered in ROI scans.

2.3.2 Sinogram Recovery using Sinusoidal Trace

Contrary to a 1D row-wise extrapolation discussed in the previous section, Chityala *et al.* [Chit 05] and Zamyatin *et al.* [Zamy 07] proposed a global data completion scheme that utilizes angular interpolation along the sine curves S that represent the sinusoidal paths traced by the projection of an object point while the X-ray source rotates around the isocenter.

The key assumption is that, if the feature corresponding to the sine curve does not overlay any other feature, it will directly give the attenuation coefficient corresponding to that feature. Thus, every point in the peripheral region (PR), i.e. outside the ROI, corresponds to a sine curve in the projection image and its intensity will be the minimum attenuation value along that sine curve. Consider a 2D imaging geometry and assume $p(\theta, s)$ is the truncated sinogram of a 2D image $f_{2\text{D}}(x, y)$. Let $f(r, \varphi)$

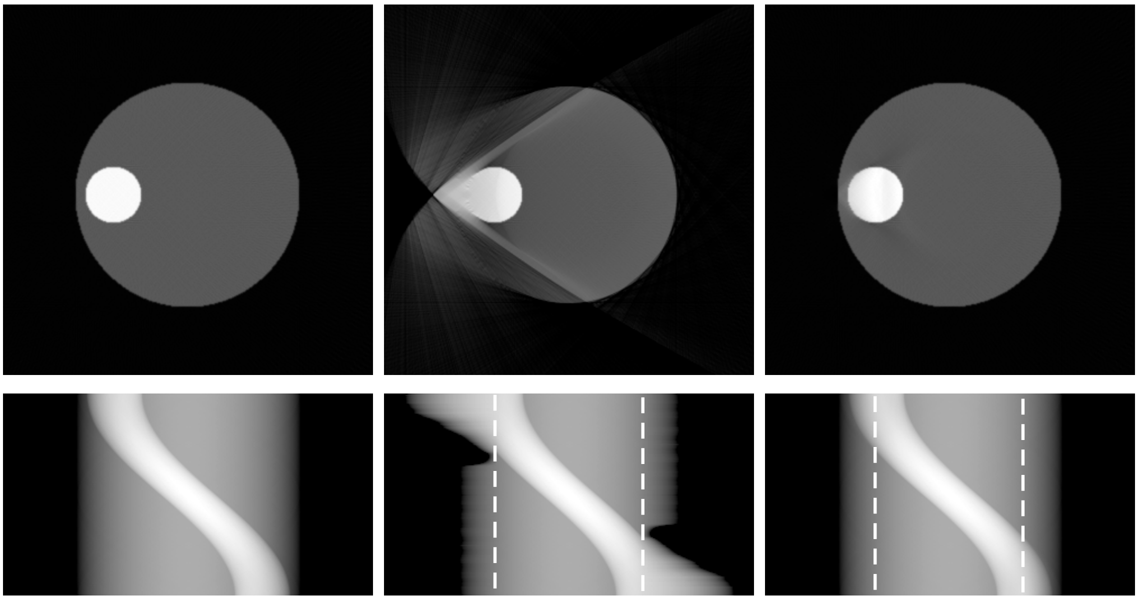

Figure 2.6: Example of the sinogram completion using sine curve traces: (left) full reconstruction from the non-truncated sinogram, (middle) ROI reconstruction from restored sinogram using the water cylinder extrapolation proposed in [Hsie 04], (right) ROI reconstruction from restored sinogram using the method proposed in [Zamy 07]. The region within the two dashed lines is the actually measured FOV.

be the polar representation of the object function outside the ROI, i.e., in the PR. Then, based on Chityala and Zamyatin's assumption $f\left(r,\varphi\right)$ can be estimated by the minimum value along the associated sine curve S as (also see Fig. 2.5 for a graphical illustration):

$$f\left(r,\varphi\right)=\frac{p_{\min}\left(r,\varphi\right)}{L} \tag{2.15}$$

with the minimum value $p_{\min}\left(r,\varphi\right)$ computed as

$$p_{\min}\left(r,\varphi\right)=\min_{(\theta,s)\in S}p\left(\theta,s\right), \tag{2.16}$$

where L denotes the length of X-ray path through the object. Once $f\left(r,\varphi\right)$ was obtained, the extended region of the sinogram could be obtained by reprojecting $f\left(r,\varphi\right)$ back to the corresponding sine curve. However, the intensity outside the ROI may be greater than that of the inside, if there is a superposition of sine curves at some locations in the sinogram. Thus, intensities must be equalized prior to back-projection [Zamy 07]. Figure 2.6 shows an example of the sinogram completion using the sine curve traces, compared with the heuristic water cylinder extrapolation proposed by Hsieh *et al.* [Hsie 04].

Later, Constantino *et al.* [Cons 09] proposed a similar idea in hard-field tomography. The algorithm first uses the Hough transform to identify individual sinusoidal signals in the 2D sinogram and then estimates missing sinogram samples along such traces.

2.3.3 Data Completion using Prior Scan

The data incompleteness caused by truncation in a collimated ROI scan can also be handled in a more accurate manner if previous, non-truncated projections of the complete object are available.

In microCT, it has been shown that increasing the spatial resolution can facilitate improved accuracy in many assessment tasks. One strategy to increase the resolution is the exploitation of the geometric magnification in cone-beam CT. This can be achieved by scanning the object positioned at a small distance from the source so that the area of interest covers a larger part of the detector. However, due to limited detector size, the method results in data truncation for a large geometric magnification. Azevedo *et al.* [Azev 95] proposed a method that acquires a second full scan at lower resolution by placing the object close to the detector such that it is able to fit in the detector size. Then, a forward projection of the low resolution reconstruction is performed, which is later used to estimate the missing data in the high resolution scan.

Similarly, Ruchala *et al.* [Ruch 02], Wiegert *et al.* [Wieg 05] and Kolditz *et al.* [Kold 10] proposed a method for projection data extension based on the exploitation of prior knowledge. To this purpose, a previously acquired 3D reference image covering the whole object (with fewer or no truncations) is combined with truncated ROI data acquired during the intervention. This reference image may either be acquired earlier during the intervention on the same interventional CT system or may be available from a previous low-dose CT scan. Either an image-based registration or a camera-based registration is performed due to the repositioning of the patient between two acquisitions. Furthermore, a linear intensity transformation is applied to the forward-projected data, to compensate the intensity mismatch between two datasets, due to different beam quality and scatter radiation. Later, Kolditz *et al.* [Kold 12] resolved the acquisition and registration problems by moving the interventional C-arm instead of the patient.

Alternatively, Sen Sharma *et al.* [Sen 13] suggested acquiring an additional scan but with only a small number of non-truncated projections. Then, interpolation and extrapolation steps are applied on this sparse set of global projections, followed by a combination with the subsequently acquired truncated ROI projection data in the sinogram domain. However, the image quality of reconstructions highly depends on the number of non-truncated projections. Yu *et al.* [Yu 09a] developed an ROI reconstruction scheme that is able to use two global non-truncated projections to cope with truncation artifacts. The method is based on compressed sensing iterative techniques and thus comes with high computational effort, which may limit its use in clinical applications.

2.4 Exact Reconstruction Algorithm from Truncated Data

Although being sensitive to transaxial data truncation, the FBP-type algorithms, for decades, were the only closed form analytic expression for image reconstruction.

Inspired by the result from PI-line-based exact helical reconstruction [Zou 04], Noo *et al.* proposed a new analytical reconstruction method, namely differentiated backprojection method (DBP), based on the relationship between the backprojection of the derivative of the projection data and the 1D finite Hilbert inversion along specific lines of the object function [Noo 04]. It is proven that an exact reconstruction of the object ROI can be obtained if some data sufficiency conditions are satisfied by the imaging configuration. In the following, the DBP method and its variants are introduced, and then the reason why DBP circumvents the non-locality issue encountered by the FBP-type methods is explained.

2.4.1 DBP Reconstruction Algorithm

In this section, we shortly review the derivation of DBP that was presented in [Noo 04], which consists of the following two steps.

Differentiated Backprojection

Let $b_\phi(\mathbf{r})$ represents a 2D image that is the result of backprojecting the derivative of the 1D projections $p(\theta, s)$ with respect to the variable s, i.e.

$$b_\phi(\mathbf{r}) = \int_0^\pi \operatorname{sgn}(\sin(\theta - \phi)) \frac{\partial p(\theta, s)}{\partial s} d\theta, \tag{2.17}$$

where $\mathbf{r} = (x, y)$, $s = \mathbf{r} \cdot \boldsymbol{\alpha}$, $\boldsymbol{\alpha} = (\cos\theta, \sin\theta)$ and ϕ is a constant angle. Then, substituting the differentiated projection by its Fourier representation yields

$$\begin{aligned} b_\phi(\mathbf{r}) &= 2\pi \int_0^\pi \int_{-\infty}^{\infty} j\xi \operatorname{sgn}(\sin(\theta - \phi)) P(\theta, \xi) \exp(j2\pi\xi(\mathbf{r} \cdot \boldsymbol{\alpha})) d\xi d\theta \\ &= 2\pi \int_0^\pi \int_{-\infty}^{\infty} j \operatorname{sgn}(\sin(\theta - \phi)\xi) P(\theta, \xi) \exp(j2\pi\xi(\mathbf{r} \cdot \boldsymbol{\alpha})) |\xi| d\xi d\theta \end{aligned} \tag{2.18}$$

where $P(\theta, \xi)$ is the 1D Fourier transform of $p(\theta, s)$ with respect to the variable s, i.e.:

$$P(\theta, \xi) = \int_{-\infty}^{\infty} p(\theta, s) \exp(-j2\pi\xi s) ds. \tag{2.19}$$

By using the Fourier slice theorem that links the 1D Fourier transform of the projection, i.e. $P(\theta, \xi)$, to the 2D Fourier transform of the object function, i.e. $F(\xi\boldsymbol{\alpha})$, we obtain

$$b_\phi(\mathbf{r}) = 2\pi \int_0^\pi \int_{-\infty}^{\infty} j \operatorname{sgn}\left(\xi\boldsymbol{\alpha} \cdot \boldsymbol{\beta}^\perp\right) F(\xi\boldsymbol{\alpha}) \exp(j2\pi\xi(\mathbf{r} \cdot \boldsymbol{\alpha})) |\xi| d\xi d\theta, \tag{2.20}$$

where $\boldsymbol{\beta} = (\cos\phi, \sin\phi)$ and $\boldsymbol{\alpha} \cdot \boldsymbol{\beta}^\perp = \sin(\theta - \phi)$. Then, the polar coordinates are converted into the Cartesian coordinates $\boldsymbol{\nu} = (\nu_1, \nu_2) = \xi\boldsymbol{\alpha}$:

$$b_\phi(\mathbf{r}) = 2\pi \int_{-\infty}^{\infty} \int_{-\infty}^{\infty} j \operatorname{sgn}\left(\boldsymbol{\nu} \cdot \boldsymbol{\beta}^\perp\right) F(\boldsymbol{\nu}) \exp(j2\pi(\mathbf{r} \cdot \boldsymbol{\nu})) d\nu_1 d\nu_2. \tag{2.21}$$

For now, it is readily noted that the differentiated backprojection $b_{\phi}\left(\mathbf{r}\right)$ relates to the Hilbert transform of the original object $H_{\phi}f_{2\mathrm{D}}\left(\mathbf{r}\right)$ by

$$b_{\phi}\left(\mathbf{r}\right)=-2\pi H_{\phi}f_{2\mathrm{D}}\left(\mathbf{r}\right) \tag{2.22}$$

with

$$H_{\phi}f_{2\mathrm{D}}\left(\mathbf{r}\right)=\int_{-\infty}^{\infty}\int_{-\infty}^{\infty}-j\operatorname{sgn}\left(\boldsymbol{\nu}\cdot\boldsymbol{\beta}^{\perp}\right)F\left(\boldsymbol{\nu}\right)\exp\left(j2\pi\left(\mathbf{r}\cdot\boldsymbol{\nu}\right)\right)d\nu_{1}d\nu_{2}. \tag{2.23}$$

It should be emphasized that the direction of the Hilbert transform of an image, i.e. with angle ϕ, can be controlled by rearranging the projection $p\left(\theta,s\right)$ using the symmetry property $p\left(\theta,s\right)=p\left(\theta+\pi,-s\right)$. It is desirable to select a direction in which the truncation is not present. In the next section, we will show how this selection subsequently circumvents the problem of non-locality.

Finite Hilbert Inversion

According to Eq. (2.22), it is intuitive that the object function can be recovered from the differentiated backprojection $b_{\phi}\left(\mathbf{r}\right)$ by a 1D Hilbert inversion along parallel lines specified by $\boldsymbol{\beta}$, i.e. $f_{2\mathrm{D}}\left(\mathbf{r}\right)=H_{\phi}^{-1}\left(H_{\phi}f_{2\mathrm{D}}\left(\mathbf{r}\right)\right)$. Here particularly a weighted version of the Hilbert transform, namely finite inverse Hilbert transform [Mikh 57], was applied such that $H_{\phi}f_{2\mathrm{D}}\left(\mathbf{r}\right)$ only needs to be known in an interval that covers the object support in the direction $\boldsymbol{\beta}$. Finally, the 2D object function $f_{2\mathrm{D}}\left(\mathbf{r}\right)$ can be recovered by this finite Hilbert inversion for all s and $t\in\left[L_{s}+\varepsilon,U_{s}+\varepsilon,\right]$:

$$\begin{aligned}f_{2\mathrm{D}}\left(\mathbf{r}\right)=f_{2\mathrm{D}}\left(s\boldsymbol{\beta}^{\perp}+t\boldsymbol{\beta}\right)&=\frac{-1}{\sqrt{\left(t-L_{s}\right)\left(U_{s}-t\right)}}\\&\left(\int_{L_{s}}^{U_{s}}\sqrt{\left(t'-L_{s}\right)\left(U_{s}-t'\right)}\frac{H_{\phi}f_{2\mathrm{D}}\left(s\boldsymbol{\beta}^{\perp}+t\boldsymbol{\beta}\right)}{\pi\left(t-t'\right)}dt'+C_{s}\right),\end{aligned} \tag{2.24}$$

where $s=\mathbf{r}\cdot\boldsymbol{\beta}^{\perp}$, $t=\mathbf{r}\cdot\boldsymbol{\beta}$ and the bounds L_{s}, U_{s}, ε are searched such that $f_{2\mathrm{D}}\left(s\boldsymbol{\beta}^{\perp}+t\boldsymbol{\beta}\right)$ is zero outside $\left[L_{s}+\varepsilon,U_{s}+\varepsilon,\right]$ and $H_{\phi}f_{2\mathrm{D}}\left(s\boldsymbol{\beta}^{\perp}+t\boldsymbol{\beta}\right)$ is known in the interval $\left[L_{s},U_{s}\right]$.

The benefit of considering this two-step DBP algorithm is two-fold: First, the derivative is a pure local operator and can thus be accurately computed even in the presence of data truncation. That means the backprojected image is not influenced by the truncation. Second, although the resulting inverse Hilbert transform is a non-local operator, the object function can still be accurately recovered through the entire line, if certain conditions are satisfied. Figure 2.7 presents some examples of the reconstruction using the DBP method from truncated data. The red circle or ellipse indicates the region where the backprojected image $b_{\phi}\left(\mathbf{r}\right)$ is not affected by data truncation. The subsequent finite Hilbert inversion [Eq. (2.24)] is performed along each vertical line within the white boundaries.

2.4.2 Data Sufficiency Condition

Now we elaborate the data sufficiency conditions that the DBP method depends on. Suppose A and B are two disjoint regions of the object. Region B consists of the

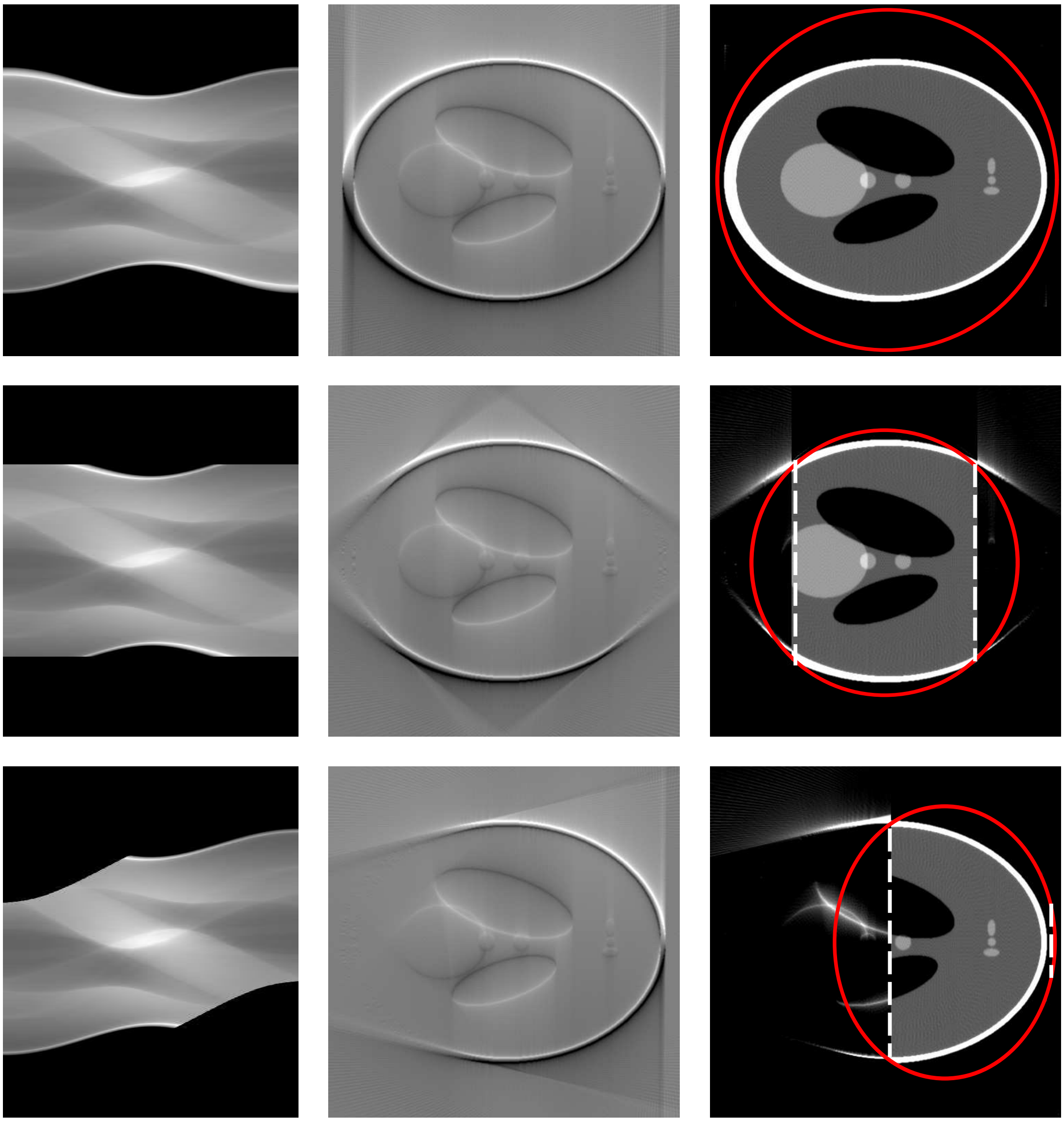

Figure 2.7: Examples of the DBP reconstruction from (top row) the complete data, and (middle and bottom rows) the truncated data. From left column to right column: the sinogram, differentiated backprojection $b_\phi(\mathbf{r})$ and the final reconstruction using the finite Hilbert inversion [Eq. (2.24)]. The red circle or ellipse indicates the ROI. Note that the finite Hilbert inversion is performed along each vertical line within the white boundaries.

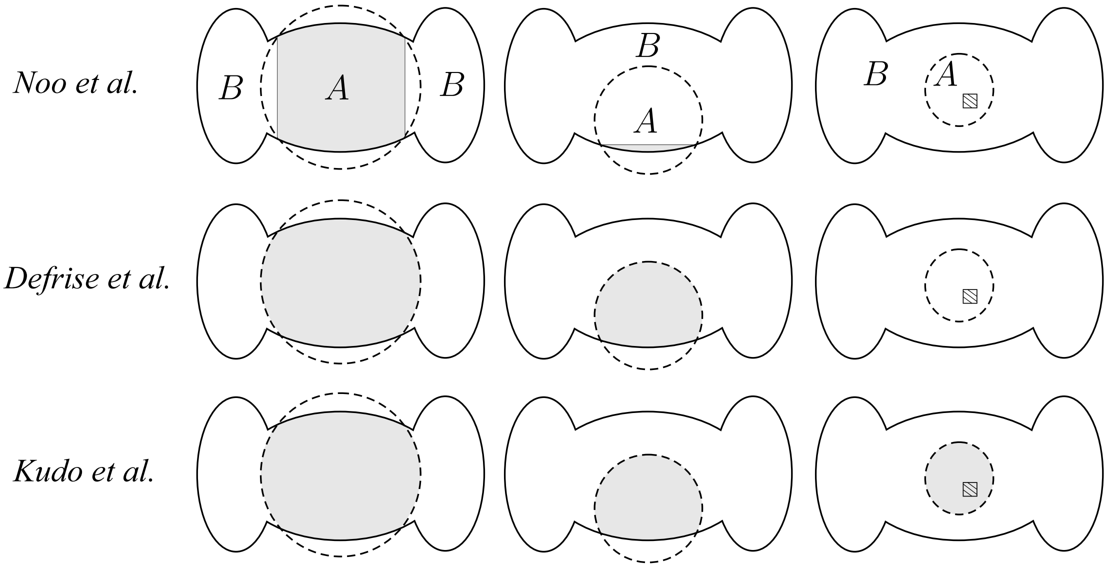

Figure 2.8: Schematic illustration of the data sufficiency conditions of Noo *et al.* [Noo 04] (top row), Defrise *et al.* [Defr 06] (middle row) and Kudo *et al.* [Kudo 08] (bottom row). The gray areas indicate reconstructable regions in each method.

points that are truncated in some projections while Region A is never truncated; see Fig. 2.8 for an illustration. Then, the sufficiency condition can be summarized as: *DBP can be applied to recover an ROI inside Region A, which lies with the union lines that do not contact Region B.* Figure 2.8 (top row) exemplarily shows the reconstructable region (indicated as a gray area) of three different truncation scenarios when using the DBP method proposed by Noo *et al.* [Noo 04].

Based on the results of Noo *et al.* [Noo 04], Defrise *et al.* [Defr 06] enlarged the reconstructable region from a given dataset by investigating the possibility of a truncated Hilbert inversion, i.e., recovering a real variable from its Hilbert transform along a segment that only partially covers the object support but with at least one ending point outside the support. This study leads to a new sufficiency condition: *DBP can be applied to recover an ROI inside Region A, which lies with the union lines that contact Region B mostly at one side* [Defr 06]. Figure 2.8 (middle row) illustrates the enlarged reconstructable region (indicated as a gray area) from the same dataset given in the first row.

It is noted that neither of these methods can reconstruct an ROI that is entirely embedded in the object support, as shown in the third column of Fig. 2.8. This problem is often referred to as *interior problem* and is proven to be solvable if prior knowledge regarding the reconstructed ROI is available. Two types of prior information that are commonly used in practice, namely a known subregion in an ROI and a sparsity model of an ROI, are introduced below.

2.4.3 DBP with Prior Knowledge

Known Subregion

The first prior knowledge can be used to solve interior problem is a known subregion in an ROI, which could be obtained in advance in some scenarios, such as air in airways or images from prior scans. Inspired by the results of Noo and Defrise, Ye *et al.* [Ye 07], Kudo *et al.* [Kudo 08] and Courdurier *et al.* [Cour 08] used a similar DBP approach and investigated the truncated Hilbert inversion based on a known subregion. They demonstrated that the interior problem can be exactly and stably solved if a tiny subregion in the ROI is known. That means, the remaining problem in the previous sufficiency conditions, as shown in the third column of Fig. 2.8, can be completely solved using their approach.

Due to the absence of corresponding analytic inversion formula for these extended uniqueness theorems, iterative algorithms, such as the projection onto convex sets (POCS) method [Defr 06, Kudo 08], or maximum likelihood expectation maximization (ML-EM) [Zhan 07], were used to reconstruct interior images from fully truncated data. Although these algorithms are computationally expensive, they have the advantage to be applicable to various types of truncation problems.

Piece-wise Constant Assumption

Using a known subregion as prior knowledge has its limitations since there are a lot of situations where no precise information is available on any subregion. Therefore, the second kind of prior knowledge was proposed based on the heuristic assumption that an ROI is piecewise constant or piecewise polynomial [Yu 09b, Yu 09c, Yang 10]. Similarly, no closed form analytic formula is available in this case. Thus, the compressed sensing (CS)-based iterative algorithms, such as the total variation (TV) minimization or high order total variation (HOT) minimization were suggested, coupled with the data discrepancy minimization, to stably solve the interior problem [Kats 12].

2.5 ROI Imaging-Specific Adaption Strategies

This section discusses two ROI imaging-specific modifications in the acquisition strategy, which involve either deploying additional hardware, i.e., a non-uniform X-ray beam filter or adapting of current acquisition settings, i.e, shifting the detector during acquisitions.

2.5.1 Filtered ROI Imaging

Rather than fully truncating CT data, several techniques have been suggested to use a physical X-ray filter to shield significantly (but not completely) the portion of the X-ray beam that does not intersect the ROI. By doing so, a substantial reduction of the total dose can be achieved, while the patient information outside the ROI is still roughly captured. In this manner, the truncation problem is circumvented and the standard FDK algorithms can be applied again. These techniques are often referred to as filtered ROI imaging in literature.

The idea was first proposed in 2D fluoroscopy imaging by Rudin *et al.* [Rudi 92]. The purpose was to use an X-ray attenuating filter to reduce the patient dose during interventional endovascular procedures. Later, Chityala *et al.* [Chit 04] extended the filtered ROI concept to 3D tomographic imaging. The results were acceptable but artifacts and considerable intensity differences arose in the reconstruction. Chen *et al.* [Chen 08a] applied the filtered ROI imaging in cone-beam breast CT and demonstrated that by using filter mask not only dose levels were noticeably reduced both inside and outside the ROI, but also the contrast-to-noise ratio within the ROI was improved due to less scatter radiation. However, due to low energy in mammography, structural information outside the ROI was barely visible. Schafer *et al.* [Scha 10] proposed the corresponding filtered ROI imaging technique in a rotational angiographic system and addressed two technical issues: significant spatial movements of the ROI during gantry rotation and large intensity differences in the transition region. Similarly, Bier *et al.* [Bier 13a, Bier 13b] suggested a truncation artifact reduction method based on the observation that weak scattered radiation still reaches the detector and is detected outside the measured FOV, even if axial or transaxial collimation is employed. They demonstrated that such information can be used to estimate the truncated part of the object.

2.5.2 Offset Detector Acquisition

The standard angiographic C-arm system is equipped with a flat-panel detector, in which the size of the FOV yields 220 mm in diameter for regular circular scans. This size is smaller than the typical patient body diameters of $300 - 500$ mm. Also, in microCT, placing the object close to the X-ray source yields high geometric magnification, leading to a higher spatial resolution but a smaller FOV. In these cases, the object appears larger than the FOV, unavoidably resulting in data truncation. In order to increase the FOV to circumvent the truncation problem, several authors [Cho 96, Wang 02, Greg 03, Scha 11, Herb 15] proposed to offset the detector in the direction tangential to the acquisition trajectory. This offset detector acquisition, also termed as displaced detector acquisition, provides an asymmetric coverage of the object at different projection angles, so that the transaxial extent of the object can be fully covered. However, the resulting asymmetric acquisition gives rise to severe shading artifacts or high deviation of pixel values, which need to be accounted for during reconstruction.

2.6 Other Truncation Artifact Reduction Techniques

2.6.1 Wavelet-based ROI Reconstruction

The non-local property of the ramp filtering stems from the Hilbert transform, which is discontinued in the derivative of the Fourier transform of an object function at the origin. Berenstein *et al.* [Bere 93] and Olson *et al.* [Olso 94] showed that these non-local filtering procedures will not increase the essential support of a function, if the Fourier transform of this function vanishes to high order at the origin (or, equivalently, the function itself has many vanishing moments). It was also noted that wavelets that are in general constructed with a large number of zero moments are the good candidate for these functions.

The wavelet-based ROI reconstruction was first introduced by Olson *et al.* [Olso 94]. This algorithm follows the FBP framework and reconstructs an ROI image directly from the 1D wavelet transform of the sinogram at each angle. However, their approach is only essentially local, because a sparse set of non-truncation projections is needed. Later, Delaney *et al.* [Dela 95] and Rashid-Farrokhi *et al.* [Rash 97] proposed a multiresolution tomographic reconstruction algorithm that only requires truncated data. In this method, instead of reconstructing the original object function from its projections, the decomposition of the object function on a 2D wavelet basis is first recovered. The standard ramp filter is replaced by two pairs of scaling and wavelet ramp filters, and the filtering step is conducted in the Fourier domain. Finally, the original function is recovered through a conventional multiresolution reconstruction filterbank from the filtered coefficients. Rashid-Farrokhi *et al.* [Rash 97] demonstrated that by particularly designing wavelets that have both compact support and a large number of vanishing moments, rapid decay after ramp filtering is observed in both scaling and wavelet functions. This suggests that the discrete wavelet and scaling coefficients of an object function can be computed locally using its truncated projections. Based on these previous studies, Zhao *et al.* [Zhao 00] formulated the FDK cone-beam reconstruction from the wavelet perspective and derived a formula for 3D ROI reconstruction. The authors observed that both severe cupping artifacts and significant constant bias could be reduced in experimental results.

2.6.2 Lambda Tomography

In contrast to standard ROI reconstruction algorithms, lambda tomography focuses on boundary information only. Consider a 2D geometry, let $f(\mathbf{r})$ be a 2D object function with $\mathbf{r} = (x, y)$. Then, an approximate function Λf is reconstructed from its local projections as

$$\widehat{\Lambda f\left(\boldsymbol{\xi}\right)} = \|\boldsymbol{\xi}\|\, \hat{f}\left(\boldsymbol{\xi}\right) \tag{2.25}$$

with $\boldsymbol{\xi} = (\xi, \eta)$ and $\hat{f}(\boldsymbol{\xi})$ being the 2D Fourier transform of the function $f(\mathbf{r})$ defined as

$$\hat{f}\left(\boldsymbol{\xi}\right) = \int_{\mathbb{R}^2} f\left(\mathbf{r}\right) \cdot e^{-j\boldsymbol{\xi}\mathbf{r}} d\mathbf{r}, \tag{2.26}$$

where Λ is the Calderon operator that corresponds to the square root of the negative Laplacian $-\triangle :\ \Lambda = (-\triangle)^{1/2}$. Lambda tomography is to reconstruct a gradient-like function $\Lambda f(\mathbf{r})$ only from truncated projection data. However, $\Lambda f(\mathbf{r})$ is cupped in regions where f is constant. Faridani *et al.* [Fari 92] studied the properties of the Calderon operator and its adjoint, stated that a linear combination could considerably neutralize such cupping artifacts. Due to its pure local characteristic, several authors further developed the lambda tomography, such as computing it from a generalized Radon transform, an extension for limited angle and cone-beam geometry, etc.; see, among others [Kats 97, Kats 06, Yu 06b, Yu 06c].

In general, although it is unable to provide quantitative assessment, lambda tomography is mathematically important. Typically, the method is commonly used for visualization of the object due to enhanced boundary information.

2.7 Discussion and Summary

This chapter reviewed the current state of the art in ROI imaging from truncated data. We firstly provided an overview of commonly-used heuristic extrapolation schemes that typically target to reduce high-frequency artifacts by providing a smooth continuation at the truncation transition region. These methods include symmetric mirroring of projection images (Ohnesorge *et al.* [Ohne 00]), water cylinder/ellipse extrapolation (Hsieh *et al.* [Hsie 04], Maltz *et al.* [Malt 07]), smooth function estimation (Van Gompel *et al.* [Van 04]), square root function extrapolation (Sourbelle *et al.* [Sour 05]), optimization-based extrapolation (Maier *et al.* [Maie 12]) and hybrid extrapolation scheme (Zellerhoff *et al.* [Zell 05]). Although these methods can be carried out without prior information, they rely on heuristics. The degree of accuracy of these extrapolations highly depends on the level of truncation. They may be difficult to correct for the severe truncations that are often encountered in ROI scans because the large missing portion of projection data is almost unpredictable and hard to be empirically extrapolated in an accurate manner.

The sinogram recovery method by tracing sinusoidal sinogram curves proposed by Chityala *et al.* [Chit 05], Zamyatin *et al.* [Zamy 07] and Constantino *et al.* [Cons 09] could outperform the 1D row-wise “blind” extrapolation schemes. However, they may also fail in severe truncation cases since less reliable measured data is available for angular interpolation along the sine curves. Besides, the basic assumption of these methods, i.e., assuming the feature corresponding to a sine curve does not overlay any other feature, may also be invalid when restoring an object with complex structures.

The data completion using a prior scan proposed by Ruchala *et al.* [Ruch 02], Wiegert *et al.* [Wieg 05], Kolditz *et al.* [Kold 10] and Sen Sharma *et al.* [Sen 13] can extend the collimated regions in an accurate manner. These methods, however, require a certain clinical workflow, on which we cannot always rely. Also, the additional scans may interrupt the interventional workflow and increase additional radiation exposure to the patient.

The DBP method developed by Noo *et al.* [Noo 04], Defrise *et al.* [Defr 06], Kudo *et al.* [Kudo 08] and Ye *et al.* [Ye 07] can achieve a stable and exact ROI reconstruction from laterally truncated data. However, such reconstruction schemes, either depend on the certain data sufficiency conditions or come with rather high computational demand, may also prohibit their practical use in interventional clinical routines.

Chityala *et al.* [Chit 04], Chen *et al.* [Chen 08a] and Schafer *et al.* [Scha 10] deployed an X-ray attenuating filter between the X-ray source and the patient such that the truncation problem can be circumvented. However, the method may complicate data acquisition due to the deployment of additional hardware and also is at a cost of reducing the impact of dose reduction. The difference in dose reduction compared with a pure ROI scan can be even considerable in the field of neurointervention, when only a micro device, e.g. an implanted stent, is required to be examined multiple times.

In summary, the review of current state of the art in ROI imaging reveals the open problems that remain to be investigated. Therefore, this thesis focuses on the technical development of various improved truncation artifact reduction techniques, particularly for an interventional clinical setting. The contribution towards high quality images from laterally truncated data is several-fold, which is reflected in the following chapters of the thesis. In the next chapter, a new sinogram extrapolation method is firstly proposed that uses sinogram consistency conditions to estimate the missing sinogram data in a more robust manner.

CHAPTER 3

Accurate Data Extrapolation using Data Consistency Conditions

3.1 Introduction and Motivation 37
3.2 Consistency Conditions 38
3.3 Data Extrapolation Using HLCC 43
3.4 Experiment and Results 45
3.5 Discussion and Conclusions 48

The main goal of ROI imaging is to reduce dose without compromising image quality. Each of the truncation artifact reduction methods addressed in the previous chapter has its advantages and disadvantages to these two aspects. This chapter presents a novel sinogram completion method that improves image quality without exposing additional dose to the patient. To estimate the missing data more precisely, the approach makes use of the Fourier-based Helgason-Ludwig (HL) consistency conditions, which mathematically express the overlap of information between the projection images. The organization of this chapter is as follows. In Section 3.1, we introduce the HL consistency conditions and describe how these consistency conditions have been exploited so far. Section 3.2 first reviews the HL consistency conditions in their original formulation as well as the modified Chebyshev-Fourier representation, followed by a theoretical derivation of the 2D Fourier-based conditions and an extension to the fan-beam geometry. In Section 3.3, we design a cost-function that incorporates the newly derived consistency conditions into an extrapolation framework. In Section 3.4, experiments using the Shepp-Logan phantom are conducted, and results are presented. Eventually, we discuss relevant issues and draw conclusions in Section 3.5.

3.1 Introduction and Motivation

It has been demonstrated that any physically consistent sinogram has a strong restriction in its functional form [Loui 83]. This restriction is expressed by Helgason-Ludwig (HL) consistency conditions [Helg 65, Ludw 65], which are mathematical expressions to describe precisely the overlap of information between different projections [Clac 13]. The HL consistency conditions play an important role in image reconstruction from imperfect projection data (e.g., due to noise, motion or truncation) since these projections no longer satisfy the HL conditions. Related works involve using the HL conditions to estimate motion parameters directly from a sinogram [Yu 06a, Yu 07, Berg 14] or solving the problem of limited angle tomography using a variational formulation that incorporates the HL conditions [Prin 90]. In positron emission tomography (PET), the HL consistency conditions were also used for attenuation correction if no transmission data is available [Welc 97].

This chapter addresses a consistency-based sinogram completion method, which also has been exploited in the literature. The methods proposed in [Hsie 04] and [Sour 05] implicitly used the zeroth-order HL consistency condition, i.e., the direct current (DC) term is the same for all projections, as a constraint for data extrapolation. The first-order condition, which corresponds to the first moment of the projections and describes the so-called "center of mass", was also used to facilitate the extrapolation procedure [Star 05]. Later, the elliptical extrapolation suggested in [Gomp 06] explicitly used a small subset of the consistency conditions in the original HL formulation (projection moment theorem) so that large numerical instability can be avoided when computing the moment terms. The approach in [Kudo 91] modified this original formulation by expanding the Radon transform in terms of its basis functions and incorporated not only one or two HL consistency conditions, but theoretically an infinite number of such constraints. However, the HL consistency conditions proposed in [Kudo 91] were represented in the Chebyshev-Fourier domain, which increased computational complexity for practical applications. To simplify the computation, the method in [Xu 10] refined the Chebyshev-Fourier representation of HL conditions using an FFT with an additional cosine transform along the detector channel. Furthermore, a fan-beam to parallel-beam rebinning is required since the consistency conditions were only derived for a parallel-beam geometry.

In this chapter, we first derive the HL consistency conditions in the 2D Fourier domain from their original formulation. The Fourier representation shows that there is a zero energy region appearing in the Fourier transform of the sinogram (symmetry for a parallel-beam and asymmetry for a fan-beam geometry). This property was also demonstrated in [Edho 86, Mazi 10], which is referred to as the Fourier property of the sinogram and which was approximately arrived at using the parallel-/fan-beam sinogram of a delta point object. Several applications using this Fourier property can be found in [Karp 88, Xia 95, Bai 13, Berg 14, Pohl 14]. In this chapter, we theoretically prove the equivalence between the HL consistency conditions and the Fourier property of the sinogram. Then, we show the advantages of applying these Fourier-based consistency conditions: first, an infinite number of conditions are considered; and second, 2D Fourier transform via FFT is computationally more efficient than the Chebyshev-Fourier transform [Kudo 91] or Lagrange-Fourier transform [Prin 90]. These features allow us to develop an efficient data extrapolation method by optimization of a cost-function based on the Fourier-based HL conditions.

3.2 Consistency Conditions

This section first reviews the HL consistency conditions in the original formulation as well as the modified Chebyshev-Fourier representation, followed by a theoretical derivation of the 2D Fourier-based consistency conditions and an extension to the fan-beam geometry.

3.2.1 Helgason-Ludwig (HL) Consistency Conditions

The original formulation of HL consistency conditions we review in this section is also referred to as the projection moment theorem in the literature [Kudo 91]. Suppose the object is supported on the unit disk centered at the origin. Let $a_n(\theta)$ be the n-th moment of the sinogram $p(\theta, s)$ with respect to the detector bin s, which is defined as

$$a_n(\theta) = \int_{-1}^{1} s^n p(\theta, s)\, ds. \tag{3.1}$$

Then, the function $a_n(\theta)$ does not change arbitrarily when the rotation angle θ varies. The Fourier series expansion of $a_n(\theta)$ can be written as follows

$$a_n(\theta) = \sum_{k=0}^{\infty} a_{nk} \exp(jk\theta), \tag{3.2}$$

with Fourier coefficients a_{nk} given by

$$a_{nk} = \frac{1}{2\pi} \int_{0}^{2\pi} a_n(\theta) \exp(-jk\theta)\, d\theta. \tag{3.3}$$

Then, it is readily proven [Natt 01] that all a_{nk} necessarily satisfy

$$a_{nk} = 0, \quad \text{for } |k| > n. \tag{3.4}$$

3.2.2 Chebyshev-Fourier Representation

The derivation of the Chebyshev-Fourier version of HLCC is similar to the one in [Kudo 91]. But the difference is that we use the Chebyshev polynomial of the *first kind* to replace the monomial term s^n, instead of the Chebyshev polynomial of the *second kind* as shown in [Kudo 91].

Inserting (3.1) into (3.3) yields:

$$a_{nk} = \frac{1}{2\pi} \int_{0}^{2\pi} \int_{-1}^{1} p(\theta, s)\, s^n \exp(-jk\theta)\, ds d\theta. \tag{3.5}$$

Note that the functions $s^n \exp(-jk\theta)$ do not form a set of orthogonal basis functions on $L_2(Z, (1-s^2)^{-1/2})$[1], where $-1 \leq s < 1$. In the following we show that the monomial s^n can be replaced by a nth-order orthogonal polynomial, such that the HL consistency conditions are tractable to use in reconstruction. The sinogram $p(\theta, s)$ can be expanded in a series as:

---

[1] The Radon transform maps the Hilbert space $L_2(\Omega^2)$ consisting of finite norm objects $f(x, y)$ to the Hilbert space $L_2(Z, (1-s^2)^{-1/2})$ consisting of finite norm sinograms $p(\theta, s)$.

$$p\left(\theta,s\right)=\frac{1}{\pi}\sum_{n=-\infty}^{\infty}\sum_{k=0}^{\infty}b_{nk}\left(1-s^{2}\right)^{-1/2}T_{n}\left(s\right)\exp\left(jk\theta\right), \tag{3.6}$$

where b_{nk} denote the expansion coefficients and $T_n\left(\cdot\right)$ denotes the nth-order Chebyshev polynomial of the *first kind*, which is defined by

$$T_{n}\left(s\right)=\frac{n}{2}\sum_{i=0}^{[n/2]}c_{i}\left(2s\right)^{n-2i}=\cos\left(n\arccos\left(s\right)\right) \tag{3.7}$$

with

$$c_{i}=\frac{\left(-1\right)^{i}\left(n-i-1\right)!}{i!\left(n-2i\right)!}. \tag{3.8}$$

Let p_1, p_2 $\in L_2(Z,\left(1-s^2\right)^{-1/2})$, we define the inner product of p_1 and p_2 as follows:

$$\langle p_{1},p_{2}\rangle=\int_{0}^{2\pi}\int_{-1}^{1}p_{1}\left(\theta,s\right)p_{2}\left(\theta,s\right)\sqrt{(1-s^{2})}dsd\theta. \tag{3.9}$$

From Appendix A.1 we show that $T_n\left(s\right)\left(1-s^2\right)^{-1/2}\exp\left(jk\theta\right)$ form an orthogonal basis of $L_2(Z,\left(1-s^2\right)^{-1/2})$. Then, we can obtain an expression of the expansion coefficients b_{nk} as a scalar product

$$\begin{aligned}b_{nk}&=\left\langle p,\,\frac{1}{\pi}T_{n}\left(s\right)\left(1-s^{2}\right)^{-1/2}\exp\left(-jk\theta\right)\right\rangle\\&=\frac{1}{\pi}\int_{0}^{2\pi}\int_{-1}^{1}p\left(\theta,s\right)T_{n}\left(s\right)\exp\left(-jk\theta\right)dsd\theta\end{aligned} \tag{3.10}$$

By comparing Eq. (3.5) with (3.10), it is noted that the coefficients b_{nk} are related with a_{nk} by the following combination

$$b_{nk}=\frac{n}{2}\sum_{i=0}^{[n/2]}c_{i}2^{n-2i}a_{n-2i,k}. \tag{3.11}$$

Then, we obtain Chebyshev-Fourier representation of the HL conditions as

$$\begin{aligned}&|k|>n\\\Longrightarrow\ &|k|>n-2i &&(i=0,1,..,n/2)\\\Longrightarrow\ &a_{n-2i,k}=0 &&(\text{see Eq.}(3.4))\\\Longrightarrow\ &b_{nk}=0.\end{aligned} \tag{3.12}$$

In sum,

$$b_{nk}=0\,,\text{for }|k|>n. \tag{3.13}$$

3.2.3 2D Fourier-based HL Consistency Conditions

We perform the 2D Fourier transform to both sides of Eq. (3.6)

$$P\left(\eta,\xi\right)=\frac{1}{\pi}\int_0^{2\pi}\int_{-1}^{1}\sum_{n=-\infty}^{\infty}\sum_{k=0}^{\infty}b_{nk}\left(1-s^2\right)^{-1/2}T_n\left(s\right) \times\exp\left(jk\theta\right)\exp\left(-j\left(\eta\theta+\xi s\right)\right)dsd\theta. \quad (3.14)$$

Because the term

$$\sum_{n=-\infty}^{\infty}\sum_{k=0}^{\infty}b_{nk}T_n\left(s\right)\exp\left(jk\theta\right)\exp\left(-j\left(\eta\theta+\xi s\right)\right)$$

is uniformly convergent, the order of the integral operators and the sum operators can be changed:

$$\begin{aligned}P\left(\eta,\xi\right)&=\frac{1}{\pi}\sum_{n=-\infty}^{\infty}\sum_{k=0}^{\infty}b_{nk}\int_0^{2\pi}\int_{-1}^{1}\left(1-s^2\right)^{-1/2}T_n\left(s\right)\\&\times\exp\left(jk\theta\right)\exp\left(-j\left(\eta\theta+\xi s\right)\right)dsd\theta\\&=\frac{1}{\pi}\sum_{n=-\infty}^{\infty}\sum_{k=0}^{\infty}b_{nk}\int_{-1}^{1}\left(1-s^2\right)^{-1/2}T_n\left(s\right)\exp\left(-j\xi s\right)ds\\&\times\int_0^{2\pi}\exp\left(-j\left(\eta-k\right)\theta\right)d\theta\end{aligned} \quad (3.15)$$

Because the orthogonality of complex exponential, we know

$$\int_0^{2\pi}\exp\left(-j\left(\eta-k\right)\theta\right)d\theta=\begin{cases}0, & \eta\neq k\\ 2\pi, & \eta=k\end{cases} \quad (3.16)$$

Then, we obtain

$$\begin{aligned}P\left(\eta,\xi\right)&=2\sum_{n=-\infty}^{\infty}b_{n\eta}\int_{-1}^{1}\left(1-s^2\right)^{-1/2}T_n\left(s\right)\exp\left(-j\xi s\right)ds\\&=2\sum_{n=-\infty}^{\infty}b_{n\eta}\frac{J_n\left(-\xi\right)}{2\left(-j\right)^n}\quad\text{(see Appendix A.2)}\end{aligned} \quad (3.17)$$

where J_n is the *first kind* Bessel function of order n. According to Debye's relation, we know that $J_n\left(\xi\right)$ decays exponentially for $|n|>|\xi|$. From Eq. (3.13) we also know that $b_{n\eta}=0$ for $|\eta|>n$. Thus, we get 2D Fourier representation of the HL conditions as follows:

$$P\left(\eta,\xi\right)\approx 0\,,\text{for}\,|\eta|>\xi. \quad (3.18)$$

So far, we only assume that the object is supported on the unit disk. If the object is supported by a disk with a radius r, then we replace s by $s'=s/r$ (where$|s'|\leq 1$) in Eqs. (3.14) and (3.17) such that we finally obtain the following conditions

$$P\left(\eta,\xi\right)\approx 0\,,\text{for}\,|\eta|>r\xi, \quad (3.19)$$

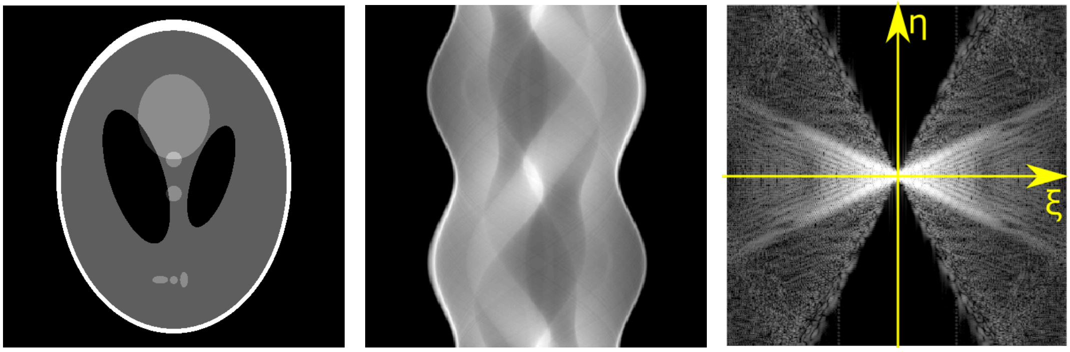

Figure 3.1: Illustration of zero coefficients in the 2D Fourier transform of a sinogram: (left) Shepp-Logan phantom, (middle) the corresponding sinogram and (right) the 2D Fourier transform of the sinogram.

where r is the largest object support. Note that this property was also found in [Edho 86] by investigating the parallel-beam sinogram of a point object. Figure 3.1 illustrates a double wedge region of zero coefficients in the 2D Fourier transform of a sinogram, for $|\eta| > r\xi$.

3.2.4 HLCC in Fan-beam Geometry

With variable substitution, i.e., $\theta = \beta + \alpha$, $s = R\sin\alpha$ (β is the rotation angle in the fan-beam geometry, α is the opening fan angle and R is the source-to-isocenter distance), the projection moment theorem (i.e. Eq. (3.5)) in fan-beam notation can be expressed as

$$a_{nk} = \frac{1}{2\pi}\int_0^{2\pi}\int_{-\pi/2}^{\pi/2} p_{\text{Fan}}(\beta,\alpha)(R\sin\alpha)^n \exp(jk(\beta+\alpha))\, d\beta d(R\sin\alpha) \tag{3.20}$$

where

$$a_{nk} = 0, \quad \text{for } |k| > n. \tag{3.21}$$

Similar to the parallel-beam case, we consider the object support is r and expand $p_{\text{Fan}}(\beta,\alpha)$ in the Chebyshev-Fourier space as:

$$p_{\text{Fan}}(\beta,\alpha) = \frac{1}{\pi}\sum_{n=-\infty}^{\infty}\sum_{k=0}^{\infty} b_{nk}\frac{T_n(R\sin\alpha/r)}{\sqrt{1-(R\sin\alpha/r)^2}}\exp(jk(\beta+\alpha)). \tag{3.22}$$

Also, we readily obtain the relation $b_{nk} = 0$, for $|k| > n$. Then, 2D Fourier transform of both sides of Eq. (3.22), along with the simplification according to Eq. (3.16) yields

$$\begin{aligned} P_{\text{Fan}}(\eta,m) &= \frac{1}{\pi}\int_0^{2\pi}\int_{-\pi/2}^{\pi/2}\sum_{n=-\infty}^{\infty}\sum_{k=0}^{\infty} b_{n\eta}\frac{T_n(R\sin\alpha/r)}{\sqrt{1-(R\sin\alpha/r)^2}} \\ &\quad \times \exp(jk(\beta+\alpha))\exp(-j(\eta\beta+m\alpha))\, d\alpha d\beta \\ &= \frac{1}{\pi}\sum_{n=-\infty}^{\infty} b_{n\eta}\int_{-\pi/2}^{\pi/2}\frac{T_n(R\sin\alpha/r)}{\sqrt{1-(R\sin\alpha/r)^2}} \\ &\quad \times \exp(j(\eta-m)\alpha)\, d\alpha. \end{aligned} \tag{3.23}$$

According to Eq. (9.3) in Appendix A.2, the innermost integral with respect to α becomes

$$\begin{aligned}
&\int_{-\pi/2}^{\pi/2} \frac{T_n\left(R\sin\alpha/r\right)}{\sqrt{1-\left(R\sin\alpha/r\right)^2}} \exp\left(j\left(\eta-m\right)\alpha\right) d\alpha \\
&= \frac{1}{2\left(-j\right)^n} \int_{-\pi/2}^{\pi/2} \left[\int_{R^1} \exp\left(-j\xi R\sin\alpha\right) J_n\left(r\xi\right) d\left(r\xi\right)\right] \exp\left(j\left(\eta-m\right)\alpha\right) d\alpha \\
&= \frac{r}{2\left(-j\right)^n} \int_{R^1} J_n\left(r\xi\right) \int_{-\pi/2}^{\pi/2} \exp\left(-j\xi R\sin\alpha + j\left(\eta-m\right)\alpha\right) d\alpha d\xi \\
&= \frac{r}{2\left(-j\right)^n} \int_{R^1} J_n\left(r\xi\right) J_{\eta-m}\left(R\xi\right) d\xi. \qquad (3.24)
\end{aligned}$$

It is known that the Weber-Schafheitlin's integral $J_n\left(r\xi\right) J_{\eta-m}\left(R\xi\right)$ decays very fast for $R\left|n\right| > r\left|\eta-m\right|$ [Natt 01]. Together with the relation $b_{n\eta} = 0$, for $|\eta| > n$, we finally arrive at

$$P_{\text{Fan}}\left(\eta, m\right) \approx 0 \text{ , for } R|\eta| > r\left|\eta-m\right|. \qquad (3.25)$$

For an equally-spaced fan-beam geometry, we apply the 2D Fourier transform to Eq. (3.22) with respect to β and u:

$$P_{\text{Fan}}\left(\eta, l\right) = \frac{1}{\pi} \int_0^{2\pi} \int_{-1}^{1} \sum_{n=-\infty}^{\infty} \sum_{k=0}^{\infty} b_{nk} \frac{T_n\left(R\sin\alpha/r\right)}{\sqrt{1-\left(R\sin\alpha/r\right)^2}} e^{jk(\beta+\alpha)} e^{-j(\eta\beta+lu)} du d\beta \qquad (3.26)$$

where $u = D\tan\alpha$ and D denotes the source-detector distance. Since D is large compared to u (for a small fan angle), we can make an approximation $u \approx D\alpha$. Then, we follow a similar derivation as for Eq. (3.24):

$$\begin{aligned}
&\int_{-1}^{1} \frac{T_n\left(R\sin\alpha/r\right)}{\sqrt{1-\left(R\sin\alpha/r\right)^2}} \exp\left(j\left(\eta-lD\right)\alpha\right) d\left(D\alpha\right) \\
&= \frac{rD}{2\left(-j\right)^n} \int_{R^1} J_n\left(r\xi\right) J_{\eta-lD}\left(R\xi\right) d\xi. \qquad (3.27)
\end{aligned}$$

Finally, we obtain the HL conditions for an equally-spaced fan-beam geometry:

$$P_{\text{Fan}}\left(\eta, l\right) \approx 0 \text{ , for } R|\eta| > r\left|\eta-lD\right|. \qquad (3.28)$$

Note that both Eqs. (3.25) and (3.28) were approximately arrived at in [Mazi 10] when investigating the fan-beam sinogram of a delta function point.

3.3 Data Extrapolation Using HLCC

The HL consistency conditions play an important role in image reconstruction as they can be used as a measure to restore consistency of imperfect projection data (e.g., due to noise, motion or truncation). In this work, we take advantage of the theory derived before for data extrapolation with truncated projection data. A flowchart of our proposed projection completion algorithm can be described as follows (also see Fig. 3.2 for an illustration):

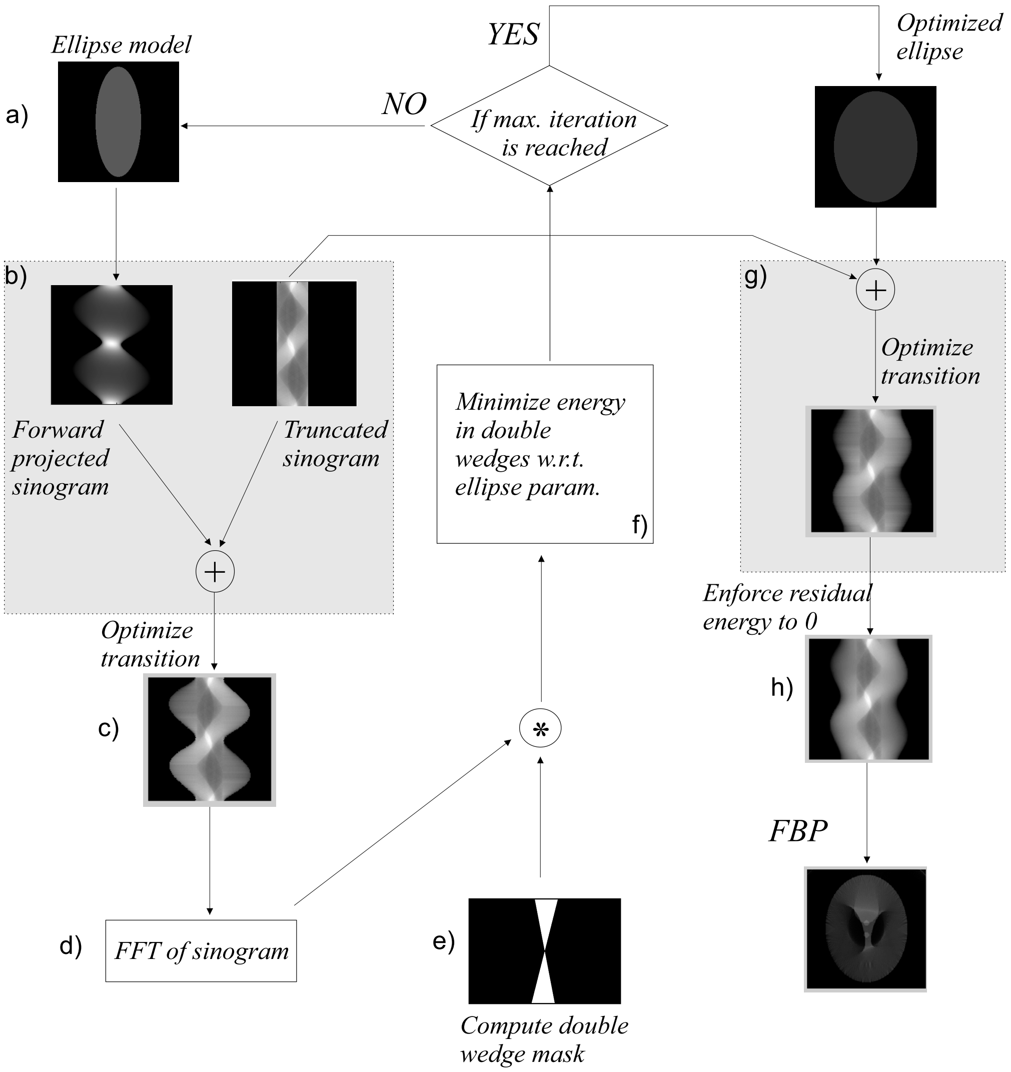
Ellipse model
a)
YES
NO
If max. iteration is reached
Optimized ellipse
b)
Forward projected sinogram
Truncated sinogram
Optimize transition
c)
d)
FFT of sinogram
e)
Compute double wedge mask
Minimize energy in double wedges w.r.t. ellipse param.
f)
g)
Optimize transition
Enforce residual energy to 0
h)
FBP

Figure 3.2: Flowchart of the proposed sinogram completion scheme: Set up an ellipse model for sinogram completion and optimize model parameters (here the two ellipse radii) by enforcing the Fourier constraints.

Step 1: Detect the double-wedge region from the 2D Fourier transformed truncated sinogram and calculate the object support (i.e., solve for r in Eq. (3.28)).

Step 2: Set up a shape model for sinogram completion (de-truncation) and fit the model to the measured (truncated) data with a de-truncation optimization algorithm that enforces the constraint that the values within the double-wedge region of the Fourier transformed sinogram are zero.

a) Set up a uniform ellipse model with the initialized two radii. For reasons of simplicity, we assume a uniform density of the measured object. The density can be determined by two ways: 1) heuristic preset, e.g., water density; 2) extrapolate the sinogram up to the object support, reconstruct using an FBP framework and use the mean of the reconstructed object as the density value.

b) Complete the truncated sinogram using forward projections of the ellipse model. Here, the forward projections only need to be computed for the regions outside the scan FOV.

c) Optimize (adapt/smooth) the transition region of the completed sinogram by adding/subtracting an offset to each row of the forward projected sinogram. The offset values are computed by comparing two neighboring pixels from the forward projected and the measured sinogram. Note that this re-scaling / intensity adjustment of the forward projected sinogram also weakens the impact of the ellipse density such that it is not mandatory to set the density as an additional optimization parameter.

d) Perform 2D Fast Fourier transform (FFT) of the combined sinogram.

e) Generate a double-wedge mask.

f) Minimize the energy in the double-wedge region by optimizing the ellipse parameters.

g) Based on the estimated ellipse parameters, perform the sinogram completion and apply transition smoothing, as already described in c).

h) Perform 2D FFT, set the residual energy in the double-wedge region to zero (hard constraint) and perform an inverse 2D FFT. To improve the reconstruction result, this step can be performed in an iterative manner.

Step 3: The resulting completed (detruncated) sinogram (being optimized in the Fourier domain) is reconstructed using any reconstruction algorithm that can be applied on the non-truncated projection data, e.g. the standard FBP framework.

3.4 Experiment and Results

The proposed method was validated and evaluated on the Shepp-Logan phantom. The dataset was virtually collimated (by setting the area outside of the scan FOV to

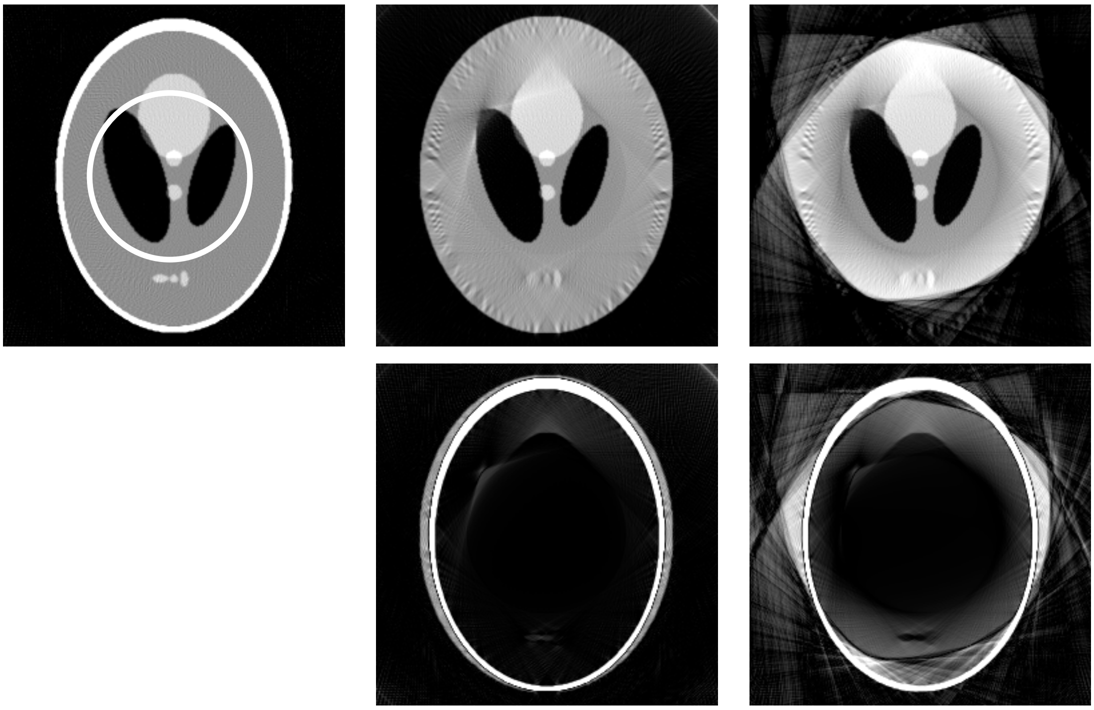

Figure 3.3: Reconstruction results of the Shepp-Logan phantom (radius of the ROI: 60 pixels, display window [0, 0.35]). From left to right: reference from non-truncated data, proposed correction method, and water cylinder extrapolation (cf. Hsieh *et al.* [Hsie 04]). The difference images with respect to the reference image are presented in the bottom row. The white circle in the reference indicates the ROI.

zero) to a medium ROI and a small ROI. The sinogram of the Shepp-Logan phantom consists of 720 channels and 360 views over 360° rotation angle (full scan). Then, the phantom was reconstructed in a 256×256 matrix. The radius of the medium ROI is 60 pixels and the radius of the small ROI is 30 pixels. We also investigate the performance of the state-of-the-art water cylinder extrapolation method [Hsie 04] and compare it with our proposed method.

The detection of the wedge region in Step 1 can be performed using model-based segmentation techniques with known properties such as line-symmetry for a parallel-beam sinogram and point-symmetry for a fan-beam case. For proof of concept, in current work we assume that the object support r is known and thus the wedge region can be directly computed using Eq. (3.28). Then, in e) we set up a binary double wedge mask with zero entries outside the double-wedge region and one within the double-wedge region. After applying the mask (element-wise multiplication) on the Fourier transformed completed sinogram from d) we sum up the energy in the double-wedge region.

For the task of minimization in f), we use a Differential Evolution (DE) optimization [Stor 97] to search large spaces of candidate solutions and avoid local minima. It

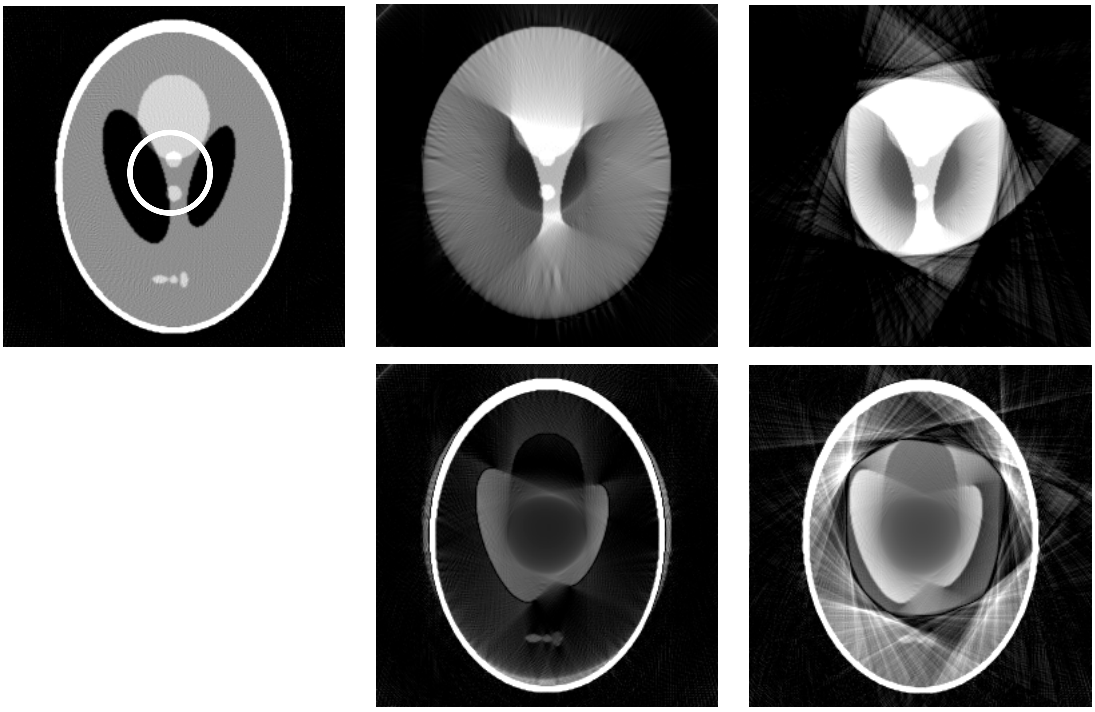

Figure 3.4: Reconstruction results of the Shepp-Logan phantom (radius of the ROI: 30 pixels, display window [0, 0.35]). From left to right: reference from non-truncated data, proposed correction method, and water cylinder extrapolation (cf. Hsieh *et al.* [Hsie 04]). The difference images with respect to the reference image are presented in the bottom row. The white circle in the reference indicates the ROI.

is a stochastic, population-based global optimization method that appears fairly fast and robust for non-differentiable and nonlinear objective functions. It uses a fixed number N of parameter vectors as a population for each iteration (also referred to as a generation). Firstly, the trial parameter vectors are initialized on an interval which defines upper and lower bounds of parameters. At each iteration/generation, new parameter vectors are generated by adding a weighted difference vector (with a weighting factor F) between two population members to a third member. These newly generated vectors are mixed with a predetermined target vector with probability CR, generating the new trial vector. Finally, the new trial vector is admitted for the next iteration/generation if and only if it yields a lower value of the objective function. These aforementioned steps continue until some stopping criterion is reached. In this work, we choose Scheme DE 1 proposed in [Stor 97] with parametrization: $N = 20$, $F = 0.8$ and $CR = 0.7$. We stop the optimization procedure if a preset maximum iteration number is reached.

Shown in Figs. 3.3 and 3.4 are the reconstruction results from the Shepp-Logan phantom with different degrees of truncation (medium/small FOV). Difference images with respect to the reference FBP reconstruction from the original non-truncated data are also presented. As expected, in the medium truncation case, both methods are able to effectively reduce truncation-induced cupping artifacts and yield the visually comparable results to that of non-truncated FBP. Only fairly small errors within the ROI of the difference images confirm this observation. We also found that for

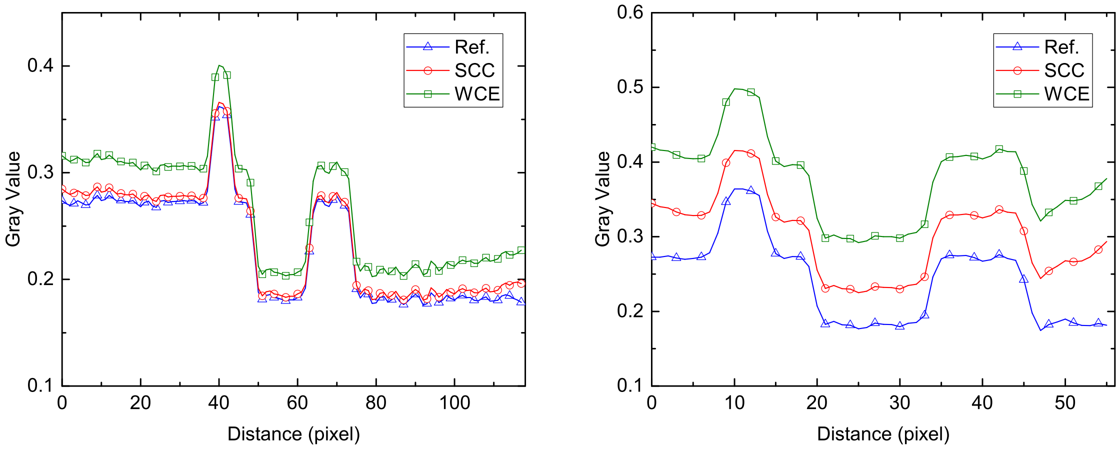

Figure 3.5: Plots of the line profile through the central vertical line for each algorithm in the medium truncation case (left) and in the severe truncation case (right). Here, SCC denotes the proposed sinogram-based consistency condition method and WCE denotes the conventional water cylinder extrapolation method.

the Shepp-Logan phantom with a simple structure, the proposed method is able to accurately estimate the outline of the object. In contrast, the water cylinder extrapolation scheme only yields inferior shape estimation due to 1D “blind” row-wise extrapolation that aims to fulfill the continuity assumptions. Figure 3.4 shows the case of severe truncation, where in general the reconstruction bias becomes larger as fewer data can be used for extrapolation. This case is thus more challenging for truncation correction algorithms. In this case, the reconstruction from the proposed method clearly outperforms the water cylinder extrapolation in terms of reduction of both the high frequency cupping and low frequency bias. Line profiles depicted in Fig. 3.5 basically confirm the visual observation above. Moreover, it is found that the proposed method still yields a relatively accurate shape estimation in such severe truncation.

Figure 3.6 shows values of the cost function with respect to two ellipse radii during the optimization procedure for the medium truncation and severe truncation cases. After five iterations, the best evaluation values are obtained from the coordinates $(94, 120)$ for the medium truncation case and at $(91, 111)$ for the severe truncation case, compared with the original object size $(87, 117)$.

3.5 Discussion and Conclusions

3.5.1 Discussion

The Fourier-based Helgason-Ludwig consistency conditions are derived for both the parallel-beam and fan-beam geometry, as described in Eqs. (3.19), (3.25) and (3.28). The derivation outcomes indicate the Fourier property of the physically consistent

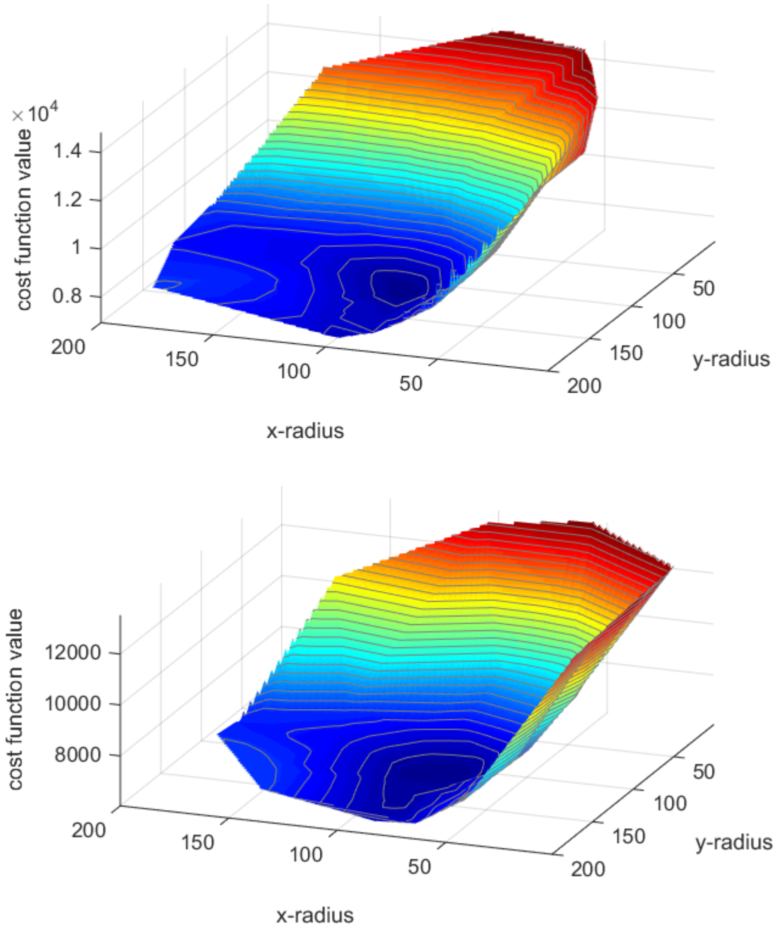

Figure 3.6: The values of the cost function with respect to two ellipse radii during the optimization procedure for (top) the medium truncation case and (bottom) the severe truncation case. After 5 iterations, the best evaluation values are obtained at the coordinates $(94, 120)$ for the medium truncation case and at $(91, 111)$ for the severe truncation case, compared with the original object size $(87, 117)$.

sinogram: there are zero coefficients forming a double wedge region (symmetry for parallel-beam and point-symmetry for fan-beam geometry) in its 2D Fourier transform. The same property was also observed previously in the literature by investigating the parallel-/fan-beam sinogram of a delta point object [Edho 86, Mazi 10]. In [Mazi 10], the authors clarify that the approximation to a Bessel function (see Eq. (8) in [Mazi 10]) was arrived at intuitively and is validated empirically.

Motivated by these previous practical observations, we present the theoretical derivation in this chapter. Our derivation stems directly from the original formulation of the HL consistency conditions and is theoretically exact for the parallel-beam geometry and the equal-angle fan-beam geometry. In the case of the equally-spaced fan-beam geometry, such a derivation is not straightforward. To derive a similar property, we made an approximation that $u \approx D\alpha$ under an assumption that the opening fan-angle is small. Therefore, there could potentially be a misestimation of the zero-energy region for large fan angles, as also observed in [Mazi 10].

The benefits of the Fourier-based consistency conditions are: First, rather than using a small subset of the consistency conditions as proposed in [Hsie 04, Sour 05, Star 05, Gomp 06], an infinite number of conditions are implicitly considered in the Fourier representation. And second, the 2D Fourier transform via FFT is computationally more efficient than other transforms, such as the Chebyshev-Fourier transform [Kudo 91] or Lagrange-Fourier transform [Prin 90]). This allows us to develop more efficient sinogram recovery schemes, as demonstrated in this chapter.

The sinogram-based extrapolation scheme we proposed in this work estimates the truncated sinogram with data from a uniform ellipse of which the parameters are determined by optimizing the HL consistency conditions. Experiments on the Shepp-Logan phantom yielded promising results. There are some limitations to this Fourier constrained extrapolation method applied to ROI reconstruction. First, the current derivation only involves the sinogram of a centered object. It is not clear how the zero energy region will change for off-centered cases. Second, for evaluation we used a full scan fan-beam geometry. We observed that for a short scan acquisition, in which projection data is acquired only over a range of π plus the fan angle, some non-zero values also appear in zero-energy region, which may affect the optimization procedure. Thus, corresponding consistency conditions that also account for off-centered objects and short scan acquisitions would be interesting for future work.

3.5.2 Conclusions

In this chapter, we theoretically derived the 2D Fourier-based HL consistency conditions that can be evaluated very efficiently via FFT. Then, we proposed a method that extrapolates the truncated sinogram with data from a uniform ellipse of which the parameters are determined by optimizing these consistency conditions. The forward projection of the optimized ellipse can be used to complete the truncation data. The reconstruction results indicate that the proposed approach substantially outperforms the conventional water cylinder extrapolation approach [Hsie 04], particularly for severe truncation, regarding both image quality and residual artifacts.

PART II

Towards Clinical Application of ROI Reconstruction Algorithms using C-arm CT

CHAPTER 4

Approximate Truncation Robust Computed Tomography – ATRACT

4.1 Introduction and Motivation 53
4.2 2D Radon-based ATRACT Algorithm 54
4.3 Analytic Convolution Formulation 57
4.4 Empirical Residual Artifact Reduction Methods 61
4.5 Summary 63

As described in Chapter 2, heuristic extrapolation methods typically rely on techniques that complete the truncated data using a continuity assumption and thus are *ad-hoc* in the presence of severe truncation. In this chapter, we present a new truncation artifact reduction method, namely Approximated Truncation Robust Algorithm for Computed Tomography (ATRACT), for 3D ROI imaging that is implicitly more robust with respect to severely truncated data. It follows the analytic FDK framework, but achieves the non-local filtering in an alternative, more robust manner with respect to data truncation. This chapter starts with a general introduction of several variants of ATRACT in Section 4.1. In Section 4.2, we present the derivation of 2D Radon-based ATRACT that is mathematically important but appears computationally expensive. For practical use, we present two variants of the original ATRACT. One is based on expressing the non-local filter as an efficient 2D convolution with an analytically derived kernel. The second variant is to apply ATRACT in 1D to further reduce computational complexity. These two variants are presented in Section 4.3. Section 4.4 discusses two empirical correction techniques to compensate remaining artifacts from the ATRACT results. Eventually, we summarize the content of this chapter in Section 4.5.

Parts of this work have already been published in Dennerlein *et al.* [Denn 11, Denn 13], and Xia *et al.* [Xia 12, Xia 13a, Xia 14b, Xia 14c].

4.1 Introduction and Motivation

It is known that a reduction of the field of view (FOV) in 3D X-ray imaging is approximately proportional to a reduction of the radiation dose. The resulting truncation, however, poses a challenge to conventional reconstruction algorithms. Explicit heuristic extrapolation methods described in Section 2.3 are usually preferably applied to tackle the truncation problem because they are compatible with most conventional reconstruction algorithms, computationally efficient and capable of estimating the missing data heuristically without the requirement of prior knowledge. However, these explicit extrapolation methods may be difficult to apply in severe truncation cases that are often encountered in ROI scans (e.g., imaging surgical stents or coils during endovascular treatment), due to less reliable measured data. Thus, it is of practical significance to develop an algorithm for severe truncation tasks that is of comparable accuracy to reconstructions from non-truncated data. In addition to high image quality, we are also interested in an algorithm that is suitable for any clinical workflow. The algorithm should pose as little constraints as possible on the availability of prior image data such as preoperative scans and prior image information collected during the intervention. Any such constraint would immediately imply a restriction of the applicability of the algorithm to a workflow that provides exactly the required data. Furthermore, no additional low-dose scan should be required, as the delay caused by patient repositioning and the acquisition itself introduces another burden on the interventional operator and impairs the ease of use of the method.

In this chapter, we present a new truncation artifact reduction method (ATRACT) for 3D ROI imaging that is implicitly more robust with respect to severely truncated data than those of explicit extrapolation schemes. The proposed method follows the analytic FBP framework and can be carried out without explicit extrapolation or prior knowledge. The method was originally derived in [Denn 11] using solely spatial domain reformulation of an alternative 2D Radon inversion. The intuitive idea was to reformulate the standard FDK algorithm into a reconstruction scheme that is by construction less sensitive to lateral data truncation. To this end, the non-local ramp filtering was decomposed into a 2D Laplace filtering and a 2D Radon-based residual filtering step. We thus refer to this method as 2D Radon-based ATRACT throughout this thesis. This algorithm, however, involves performing the 2D Radon transform and its inversion on each 2D projection image and thus appears computationally expensive. Also, as demonstrated in [Denn 13], ATRACT yields a global scaling/offset issue in the reconstructed ROI volume, compared with the reference FDK reconstruction from non-truncated data. Furthermore, we found that a linear gradient-like artifact arises in the ATRACT results when reconstructing an off-centered ROI from asymmetrically collimated data.

Therefore, it is our goal to refine the original Radon-based ATRACT method to a more practically-useful reconstruction algorithm, in terms of both computational efficiency and image quality.

4.2 2D Radon-based ATRACT Algorithm

In this section, the Radon-based ATRACT algorithm is analytically derived using the Fourier slice theorem. Note that this derivation is intuitively conducted in the Fourier domain and the reformulation steps, therefore, differ from the original derivation in [Denn 11] that uses solely spatial domain reformulation of an alternative 2D Radon inversion. However, both derivations arrive at an identical two-step filtering algo-

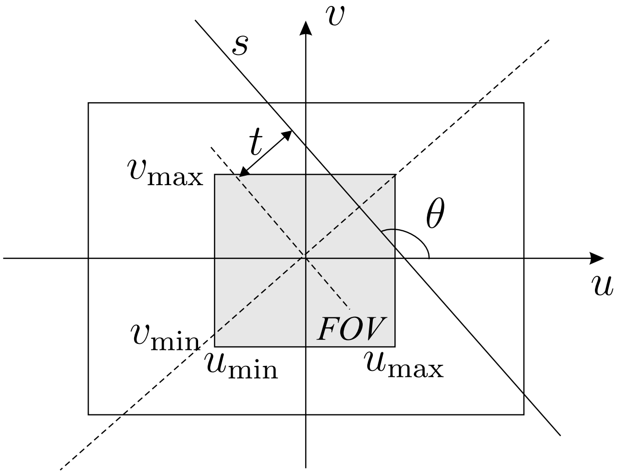

Figure 4.1: Geometry and associated notations: u and v denote the projection coordinates; s and θ denote the Radon domain coordinates. Suppose the projection is truncated to the FOV of $\Omega_\lambda = [u_{\min}, u_{\max}] \times [v_{\min}, v_{\max}]$.

rithm, as will be shown below. For further interest of the spatial domain derivation, we refer to [Denn 11, Denn 13].

Specifically, the main idea is to find an equivalent of the 1D ramp filter within FDK so that the filtering procedure is intrinsically less sensitive to data truncation. Consider the circular cone-beam geometry shown in Fig. 2.1, along with the detector coordinates defined in Fig. 4.1, the standard ramp filtering [see Eq. (2.4)] can be expressed in the 2D Fourier domain as

$$g_F(\lambda, \mathbf{u}) = \iint\limits_{-\infty}^{\infty} G(\lambda, \boldsymbol{\omega}) \left|\omega_u\right| \exp\left(j2\pi \mathbf{u} \cdot \boldsymbol{\omega}\right) d\boldsymbol{\omega}, \tag{4.1}$$

where G represents the 2D Fourier transform of the pre-weighted projection g_1 and $\boldsymbol{\omega} = (\omega_u, \omega_v)$ are the corresponding Fourier coefficients with respect to $\mathbf{u} = (u, v)$. Converting the Cartesian coordinates (ω_u, ω_v) to the associated polar coordinates (ω, θ) yields

$$g_F(\lambda, \mathbf{u}) = \int\limits_{0}^{2\pi} \int\limits_{-\infty}^{\infty} G(\lambda, \omega\boldsymbol{\theta}) \left|\omega \cos\theta\right| \exp\left(j2\pi\omega \mathbf{u} \cdot \boldsymbol{\theta}\right) \omega d\omega d\theta, \tag{4.2}$$

where $\boldsymbol{\theta} = (\cos\theta, \sin\theta)$. Further using trigonometric function identities (i.e. $\cos\theta = -\cos(\theta + \pi)$ and $\sin\theta = -\sin(\theta + \pi)$) to Eq. (4.2) gives

$$g_F(\lambda, \mathbf{u}) = \int\limits_{0}^{\pi} \int\limits_{-\infty}^{\infty} G(\lambda, \omega\boldsymbol{\theta}) \left|\omega \cos\theta\right| \exp\left(j2\pi\omega \mathbf{u} \cdot \boldsymbol{\theta}\right) \left|\omega\right| d\omega d\theta. \tag{4.3}$$

An important step of the derivation is to decompose the ramp filter kernel $|\omega \cos\theta|$ as follows

$$g_F(\lambda,\mathbf{u}) = \int_0^{\pi}\int_{-\infty}^{\infty} \frac{-1}{4\pi^2|\omega|}|\cos\theta|\left[(j2\pi\omega)^2 G(\lambda,\omega\boldsymbol{\theta})\right]\exp(j2\pi\omega\mathbf{u}\cdot\boldsymbol{\theta})|\omega|\,d\omega d\theta. \quad (4.4)$$

With rearrangement of some integrands and the use of the Fourier slice theorem that relates the 2D Fourier transform of the projection image $G(\lambda,\omega\boldsymbol{\theta})$ to its Radon transform in the 1D Fourier domain, we obtain

$$g_F(\lambda,\mathbf{u}) = \frac{-1}{4\pi^2}\int_0^{\pi}|\cos\theta|\int_{-\infty}^{\infty}(j2\pi\omega)^2 P(\lambda,\theta,\omega)\exp(j2\pi\omega s^*)\,d\omega d\theta, \quad (4.5)$$

where $s^* = \mathbf{u}\cdot\boldsymbol{\theta}$ and $P(\lambda,\theta,\omega)$ represents the 1D Fourier representation of the Radon transform of g_1 with respect to s, i.e.,

$$P(\lambda,\theta,\omega) = \int_{-\infty}^{\infty}\iint_{-\infty}^{\infty} g_1(\lambda,\mathbf{u})\,\delta(\mathbf{u}\cdot\boldsymbol{\theta}-s)\exp(-j2\pi\omega s)\,d\mathbf{u}ds. \quad (4.6)$$

For now, it is noted that by inserting Eq. (4.6) into (4.5), the Fourier transform of g_1 cancels out its subsequent inversion and the only remained term is the inverse Fourier transform of $(j2\pi\omega)^2$, which corresponds to the Laplace operator in the spatial domain, i.e., the second-order derivative with respect to s. Since the Radon transform and its dual are intertwining operators for the Laplace operation, we can exchange the Laplace operation and Radon transform as follows

$$\begin{aligned}\frac{\partial^2}{\partial s^2}\mathcal{R}(g_1)(\lambda,\theta,s)\,|_{s=s^*} &= \iint_{-\infty}^{\infty}\frac{\partial^2}{\partial s^2}g_1(\lambda,\mathbf{u})\,\delta(\mathbf{u}\cdot\boldsymbol{\theta}-s)\,d\mathbf{u}\\ &= \iint_{-\infty}^{\infty}\left(\frac{\partial^2}{\partial u^2}+\frac{\partial^2}{\partial v^2}\right)g_1(\lambda,\mathbf{u})\,\delta(\mathbf{u}\cdot\boldsymbol{\theta}-s)\,d\mathbf{u} \quad (4.7)\end{aligned}$$

where $\mathcal{R}(g_1)$ denotes the Radon transform of g_1. Finally, by combining Eqs. (4.5) and (4.7), along with Eqs. (2.3) and (2.6) in the FDK algorithm, we arrive at the 2D Radon-based ATRACT algorithm that comes with a two-stage filtering:

- *Step 1:* Cosine- and Parker-like weighting of projection data to obtain pre-scaled projection data g_1:

$$g_1(\lambda,u,v) = \frac{Dm(\lambda,u)}{\sqrt{D^2+u^2+v^2}}g(\lambda,u,v) \quad (4.8)$$

- *Step 2*: 2D Laplace filtering to obtain projection data g_2:

$$g_2(\lambda,\mathbf{u}) = \left(\frac{\partial^2}{\partial u^2}+\frac{\partial^2}{\partial v^2}\right)g_1(\lambda,u,v) \quad (4.9)$$

- *Step 3:* 2D Radon-based filtering to get filtered projection data $g_F^{(\mathrm{ATRACT})}$:

$$g_3(\lambda, \theta, s) = \iint\limits_{-\infty}^{\infty} g_2(\lambda, \mathbf{u})\, \delta(\mathbf{u} \cdot \boldsymbol{\theta} - s)\, d\mathbf{u}\,, \tag{4.10}$$

$$g_F^{(\mathrm{A2D})}(\lambda, u, v) = \frac{-1}{4\pi^2} \int\limits_0^{\pi} |\cos\theta| g_3(\lambda, \theta, s^*)\, d\theta \tag{4.11}$$

- *Step 4:* 3D cone-beam backprojection to get the estimated object function $f^{(\mathrm{ATRACT})}$:

$$f^{(\mathrm{A2D})}(\mathbf{x}) = \int\limits_{\lambda_1}^{\lambda_2} \frac{RD}{[R - \mathbf{x} \cdot \mathbf{e}_w(\lambda)]^2} g_F(\lambda, u, v) d\lambda\,. \tag{4.12}$$

The advantages of this two-step filtering can be summarized as follows: 1) The local 2D Laplace operation only introduces errors at the boundaries of the FOV, where outer neighboring values are unknown due to truncation, but nowhere else inside the FOV. In the numerical implementation, we remove any incorrect values at the FOV boundaries by setting them to zeros after Laplace filtering. With the FDK method, such a removal is not straightforward, due to the non-local character of the ramp filter; 2) Implicit extrapolation with zeros beyond the FOV boundaries in the second-order derivative domain yields a better approximation for the missing data than an explicit extrapolation on g or g_1, i.e. before differentiation; 3) Although the 2D Radon-based filtering is a non-local operation, it is less sensitive to data inconsistencies than the 1D ramp filtering (we explain this point in Section 4.3.1); 4) Furthermore, as the 2D filtering is performed for all detector elements simultaneously, this reduces outliers that may be caused by individual 1D processing of detector lines. Consequently, even though no explicit extrapolation is used during the filtering steps in ATRACT, the filtered result g_F will not contain a noticeable artificial structure at the edge of transaxial truncation compared with that of the FDK method.

4.3 Analytic Convolution Formulation

This section discusses two variants of the original Radon-based ATRACT. One is based on expressing the residual filter as an efficient 2D convolution with an analytically derived kernel. The second variant is to apply ATRACT in 1D to further reduce computational complexity. Both lead to a noticeable computational speed-up and thus make ATRACT-based ROI imaging applicable to interventional routines.

4.3.1 2D Convolution-based ATRACT

A numerical implementation of ATRACT that directly adopts Eqs. (4.10) and (4.11) for the non-local residual filtering is computationally very expensive, because the 2D Radon transform and Radon inversion have to be executed once for each projection image. Moreover, Eqs. (4.10) and (4.11) require frequent interpolations, so a loss of the spatial resolution in the reconstruction is unavoidable. For practical use of ATRACT, an implementation of the non-local filtering operation using a 2D convolution with respect to u and v is suggested to increase computational efficiency. Now we analytically derive the convolution formula that replaces the 2D Radon-based filter in the original ATRACT algorithm. Note that this analytical formula has the potential to increase the spatial resolution in the ATRACT reconstructions and significantly increases computational performance (due to FFT-based computations) compared with a direct implementation using Eq. (4.10) and (4.11). We refer to the new method as 2D ATRACT in the following. With a small modification, Eq. (4.10) can be rewritten as follows:

$$g_3\left(\lambda, \theta, s\right) = \int\limits_{-\infty}^{\infty} g_2\left(\lambda, s\boldsymbol{\theta} + t\boldsymbol{\theta}^{\perp}\right) dt, \tag{4.13}$$

where $\boldsymbol{\theta} = (\cos\theta, \sin\theta)$ and $\boldsymbol{\theta}^{\perp} = (-\sin\theta, \cos\theta)$. Inserting (4.13) into (4.11) yields

$$g_F^{(\mathrm{A2D})}\left(\lambda, u, v\right) = C_1 \int\limits_{0}^{\pi} |\cos\theta| \int\limits_{-\infty}^{\infty} g_2\left(\lambda, s^{*}\boldsymbol{\theta} + t\boldsymbol{\theta}^{\perp}\right) dt d\theta, \tag{4.14}$$

with $C_1 = -1/\left(4\pi^2\right)$. The inner line integral can be further modified as follows

$$\begin{aligned} g_F^{(\mathrm{A2D})}\left(\lambda, u, v\right) &= C_1 \int\limits_{0}^{\pi} |\cos\theta| \int\limits_{-\infty}^{\infty} g_2\left(\lambda, \left(\mathbf{u}\cdot\boldsymbol{\theta}\right)\boldsymbol{\theta} - \hat{t}\boldsymbol{\theta}^{\perp}\right) d\hat{t} d\theta, \\ &= C_1 \int\limits_{0}^{\pi} |\cos\theta| \int\limits_{-\infty}^{\infty} g_2\left(\lambda, \mathbf{u} - \hat{t}\boldsymbol{\theta}^{\perp}\right) d\hat{t} d\theta. \end{aligned} \tag{4.15}$$

Let $\mathbf{u}' = (u', v') = \hat{t}\boldsymbol{\theta}^{\perp}$ with $u' = -\hat{t}\sin\theta$ and $v' = \hat{t}\cos\theta$. Then, the area element $d\hat{t}d\theta$ can be replaced by $|\mathbf{J}|du'dv'$, where $|\mathbf{J}|$ is the determinant of the Jacobian, i.e.,

$$|\mathbf{J}| = \frac{1}{|\mathbf{J}|^{-1}} = 1/\det\left(\frac{\partial\left(\hat{t}, \theta\right)}{\partial\left(u', v'\right)}\right) = 1/\begin{vmatrix} \frac{\partial\hat{t}}{\partial u'} & \frac{\partial\theta}{\partial u'} \\ \frac{\partial\hat{t}}{\partial v'} & \frac{\partial\theta}{\partial v'} \end{vmatrix} = 1/\begin{vmatrix} -\sin\theta & \cos\theta \\ \hat{t}\cos\theta & -\hat{t}\sin \end{vmatrix} = 1/|\hat{t}|. \tag{4.16}$$

Also, it is easy to obtain the following equalities

$$|\hat{t}| = \sqrt{u'^2 + v'^2} \quad \text{and} \quad \cos\theta = \frac{v'}{\sqrt{u'^2 + v'^2}}. \tag{4.17}$$

Now, inserting $\mathbf{u}' = \hat{t}\boldsymbol{\theta}^{\perp}$, $d\hat{t}d\theta = |\mathbf{J}|\, du'dv'$, Eqs. (4.16) and (4.17) into (4.15), we finally obtain the 2D convolution formula:

$$g_F^{(\mathrm{A2D})}\left(\lambda, u, v\right) = \int\limits_{u_1}^{u_2}\int\limits_{v_1}^{v_2} g_2\left(\lambda, u - u', v - v'\right) h_{2D}\left(u', v'\right) du'dv', \tag{4.18}$$

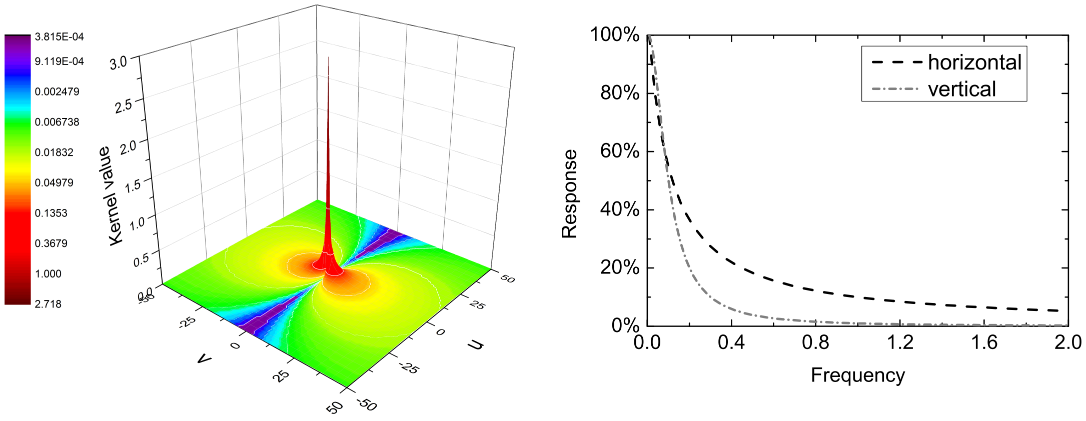

Figure 4.2: Illustration of the 2D convolution kernel in (left) spatial domain and (right) Fourier domain. Note that the frequency response implies that the 2D kernel possesses a low-pass character, which is able to provide a regularizing effect to suppress inconsistencies introduced in truncated data.

where the analytical 2D kernel $h_{2D}\left(u',v'\right)$ is determined as follows:

$$h_{2D}\left(u',v'\right) = C_1|\cos\theta||\mathbf{J}| = C_1\frac{|v'|}{u'^2+v'^2}. \tag{4.19}$$

The plot of the 2D analytical kernel is given in Fig. 4.2. A similar kernel has been also found in the field of phase contrast CT [Bron 06]. The frequency representation of the analytical 2D kernel is given as

$$H_{2D}\left(\omega_u,\omega_v\right) = C_1\frac{|\omega_u|}{\omega_u^2+\omega_v^2}, \tag{4.20}$$

where $H_{2D}\left(\omega_u,\omega_v\right)$ denotes the 2D Fourier transform of $h_{2D}\left(u,v\right)$.

The newly derived analytic kernel allows us to explain why the non-local ATRACT residual filtering is less sensitive to data inconsistencies. As shown in Fig. 4.2 (right), the residual filter is a low-pass filter. This is beneficial since the data function g_2 contains inconsistencies due to implicit constant extrapolation to 0 outside the FOV, the filtering provides a regularizing effect that is able to suppress these introduced inconsistencies in the projection image. Figure 4.3 exemplarily shows the impact of a truncated projection image on the 1D ramp filtering and 2D ATRACT filtering. As can be seen, the two-step ATRACT filtering can produce more robust results than that of the ramp filtering in terms of cupping artifact reduction. However, from the error image we found that 2D ATRACT filtering suffers an offset or bias-like artifact. This problem will be further addressed in Section 4.4.

4.3.2 ATRACT with 1D Row-wise Filtering

For further improvements in filtering speed, we will derive and investigate a 1D version of ATRACT. It is known that the computational complexity of a 2D FFT for a $N\times N$ image is proportional to $N^2\log_2 N^2$, i.e. $2\cdot N^2\log_2 N$. Applying a 1D FFT to each row of the same image yields a complexity of $N\cdot N\log_2 N$, which implies a reduction of a factor of 2. Moreover, additional padding in the axial direction, as

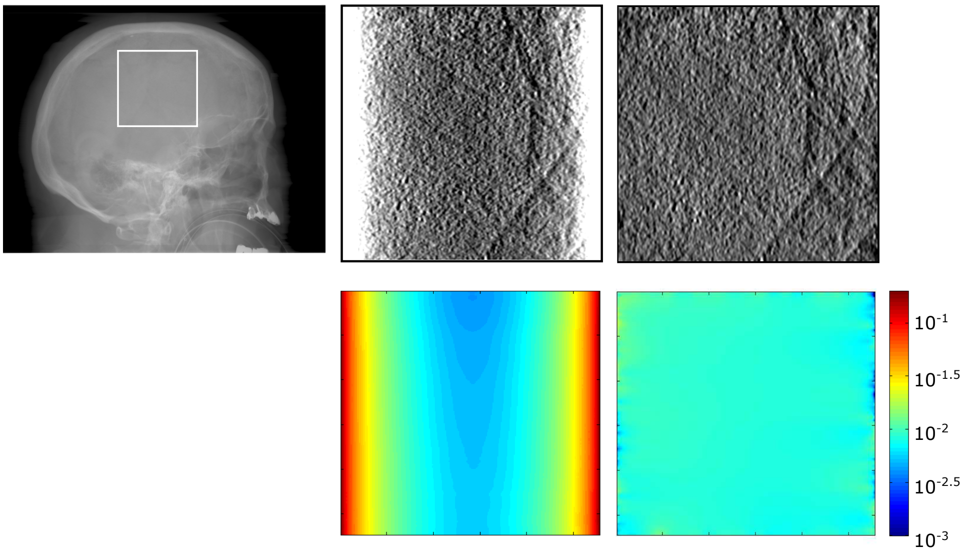

Figure 4.3: Illustration of different impacts of truncation on ramp filtering and 2D ATRACT filtering. Top row from left to right: A projection of a clinical head scan (Images courtesy of CHI St. Luke's Health - Baylor St. Luke's Medical Center, Houston, TX, USA) with the actually measured homogeneous region indicated by the white rectangle, ramp filtering of the measured region, 2D ATRACT filtering of the measured region. Bottom row: Visualization of filtering errors (logarithmic scale) in corresponding filtered projections with respect to a reference filtering of the non-truncated projection. Note that the errors in 2D ATRACT are almost evenly distributed while a cupping-like error distribution appears in the 1D ramp filtering.

would be required for the 2D FFT-based filtering, is avoided. This contributes to further reduction of computation time when using 1D row-wise filtering.

We will derive the 1D ATRACT method starting with an alternative decomposition of the ramp filter as follows

$$g_F^{(\mathrm{A1D})}(\lambda, u, v) = \frac{\partial g_1(\lambda, u, v)}{\partial u} * \frac{1}{2\pi^2 u}, \tag{4.21}$$

where the symbol * denotes the 1D convolution operation. To derive the 1D ATRACT algorithm, Eq. (4.21) can be modified as

$$g_F^{(\mathrm{A1D})}(\lambda, u, v) = \int_{-\infty}^{u} \frac{\partial^2 g_1(\lambda, u', v)}{\partial u'^2} du' * \frac{1}{2\pi^2 u}. \tag{4.22}$$

Using the property of convolution, we can move the anti-derivative operator to the Hilbert kernel

$$g_F^{(\mathrm{A1D})}(\lambda, u, v) = \frac{\partial^2 g_1(\lambda, u, v)}{\partial u^2} * \int_{-\infty}^{u} \frac{1}{2\pi^2 u'} du'. \tag{4.23}$$

The first part of (4.23) is the 1D Laplace operation, i.e. the second-order derivative with respect to u (detector row) and the second operation can be computed as a 1D convolution with the kernel $\ln|u|/2\pi^2$. The expression of the 1D analytical kernel in the Fourier domain can be obtained by using Fourier transform of $\ln|u|$, which yields

$$H_{1D}\left(\omega_u\right) = \int_{-\infty}^{-\infty} \frac{1}{2\pi^2} \ln|u| \exp\left(-j2\pi u\omega_u\right) du = -\frac{1}{4\pi^2}\frac{|\omega_u|}{\omega_u^2}. \tag{4.24}$$

It can be observed that analogous to the 2D kernel, the 1D residual kernel possesses a low-pass property and its plot in the Fourier domain is consistent to the horizontal line profile in Fig. 4.2. Fundamentally, the 1D version of ATRACT fulfills the three reasons that ATRACT is robust to data truncation: 1) 1D Laplace is a local operation and can thus be computed accurately on the truncated data ; 2) All values after Laplace are closer distributed around 0, which enables implicit zero extrapolation be a good approximation; 3) Also importantly, the 1D residual kernel shown in Eq. (**??**) or (4.24) possesses a low-pass property and thus is less sensitive to data truncation. However, compared with the 2D version, 1D ATRACT coming with a single row-wise processing may lose the consistency along the axial direction. This somewhat degrades the image quality as we will see in the evaluation section.

4.4 Empirical Residual Artifact Reduction Methods

In general, ATRACT provides reconstructions of high quality even in the presence of severe data truncation. However, several remaining artifacts can still be observed in the reconstructed volume. In this section, we suggest two empirical correction techniques to respectively compensate for these artifacts.

4.4.1 Bias/Offset Correction

As mentioned before, the 2D and 1D ATRACT filtering suffer from an offset or bias-like artifact in the projection domain, compared with ramp filtering of non-truncated data. This is because after the filtering process the mean value of the truncated projection data is removed. Thus, subsequent backprojection will be only correct up to an offset. Depending on the calibration information available, one of two procedures is used to deal with this problem.

Offset Correction

If two non-truncated projections are available in the related acquisition scenario or the parameters were initially calculated, then we can more effectively compensate the offset problem by calibrating the projection-related parameters in the projection domain. The correction scheme is simply accomplished by adding a rotation angle-related constant $\epsilon\left(\lambda\right)$ to after ATRACT filtering and ϵ is estimated through the following model:

$$\epsilon\left(\lambda\right) = a_1 \cdot \sum_{u_{\min}}^{u_{\max}} \sum_{v_{\min}}^{v_{\max}} g\left(\lambda, u, v\right) + a_2 + a_3 \cdot \left(u_{\max} - u_{\min}\right) \cdot \left(v_{\max} - v_{\min}\right), \tag{4.25}$$

where a_1, a_2 and a_3 represent the model coefficients that need to be calibrated. As mentioned above, the offset problem can be considered as the mean value loss in the projection image by ATRACT filtering. We empirically found that such information is related to the attenuation summation and truncation size. It is an interesting observation because we can approximately recover this information, i.e. $\epsilon(\lambda)$, by setting the attenuation-related linear parameters a_1 and a_2 and truncation size-related parameter a_3. All these parameters are calibrated by measuring the differences (offsets) between homogeneous subregions inside two ATRACT filtered ROI projections $g_F^{(\mathrm{ATRACT})}$ and the associated reference projections $g_F^{(\mathrm{FDK})}$(non-truncated).

Min-Max Scaling

If neither non-truncated projections nor the calibration parameters in offset correction [Eq. (4.25)] are provided in the given scenario, then a simple min-max scaling method is applied in the volume domain, to roughly align the total intensity values to a reasonable range ($-1024 \sim 3072$ HU). This approach is used to avoid clamping the over-saturated values caused by an incorrect offset in the last stage of the imaging pipeline and should only be used when offset correction cannot be applied.

$$f(\mathbf{x})^{\mathrm{aligned}} = \frac{f(\mathbf{x}) - \min(f(\mathbf{x}))}{\max(f(\mathbf{x})) - \min(f(\mathbf{x}))} \cdot 4096 - 1024. \tag{4.26}$$

Normally, the min-max scaling can only enable a linear relationship, rather than an exact HU value match, between the FDK reconstruction from a full data and ATRACT-based ROI reconstruction inside the ROI. The offset correction, on the other hand, is able to provide a more accurate match to that of FDK from non-truncated data.

4.4.2 Gradient Artifact Reduction for Off-Centered ROI

The artificial high frequencies can be effectively eliminated by removing the high spikes at the borders of the scan FOV, after Laplace filtering. However, when the magnitudes of the spikes at both sides differ a lot, which typically occurs when acquiring an off-centered ROI, there is a gradient appearing in the ATRACT filtered projections. After backprojection, such a gradient artifact also propagates into the volume domain.

To compensate this gradient, the magnitude difference between two sides of spikes (after Laplace filtering) is first extracted before removing them. Then, we incorporate such information into ATRACT filtered projections, to compensate for the resulting gradient. More specifically, for each projection, the following steps are performed.

Firstly, heights of the spike from the left and right borders (denoted as h_1 and h_2) are extracted from projections after Laplace filtering. Note that for a 2D projection image, the average values along the boundary column (where the spike arises) are computed as:

$$h_1(\lambda) = \sum_{v_{\min}}^{v_{\max}} g_2(\lambda, u_{\min}, v), \quad \text{and} \quad h_2(\lambda) = \sum_{v_{\min}}^{v_{\max}} g_2(\lambda, u_{\max}, v). \tag{4.27}$$

Secondly, the increment slope n of the two spikes can be computed as:

$$n = \frac{h_1(\lambda) - h_2(\lambda)}{u_{\max} - u_{\min}}. \tag{4.28}$$

Finally, we estimate a linear line from the increment slope and add/subtract (depend on the sign of the slope) it over original filtered 2D projection images as:

$$\breve{g}_F^{(\mathrm{ATRACT})}(\lambda, u, v) = g_F^{(\mathrm{ATRACT})}(\lambda, u, v) + \tau n \cdot u \tag{4.29}$$

where τ is the coefficient of this linear model and can be empirically estimated by comparing $\breve{g}_F^{(\mathrm{ATRACT})}(\lambda, u, v)$ to the ramp-filtered non-truncated data $g_F^{(\mathrm{FDK})}$.

4.5 Summary

In this chapter, we investigated a new truncation artifact reduction method, namely ATRACT, that is intrinsically more robust with respect to severely truncated data. It follows the analytic FDK framework but replaces the ramp filter with the Laplacian and a non-local residual filter. We presented two variants of ATRACT, which are more practically-useful, particularly in terms of computational efficiency. The first one, 2D ATRACT, aims to express the non-local filter as an efficient 2D convolution with an analytically derived kernel. The second variant is an attempt to apply ATRACT in 1D to further reduce computational complexity. As will be shown in Chapter 7, both variants lead to a noticeable computational speed-up compared with the original ATRACT method, while still retain reconstructions of high quality. Furthermore, we suggested two empirical correction techniques to compensate remained artifacts from the ATRACT results, which bring ATRACT-based ROI imaging closer to clinical application.

CHAPTER 5

Region-of-Interest Reconstruction Algorithms for Shutter Scan Acquisition

5.1 Introduction and Motivation 65

5.2 Interleaved Data Acquisition Scheme – Shutter Scan 67

5.3 Shutter Scan Reconstruction Algorithms 68

5.4 Summary 76

In some clinical applications, such as cancer or tumor treatments, reconstructing an image inside the ROI alone may be sub-optimal, since the outer region, i.e., the peripheral region (PR), may also contain useful information, such as surrounding landmarks or so-called organs-at-risk. This chapter presents a novel interleaved acquisition strategy that would utilize a fast collimator to acquire both truncated and non-truncated projection data within a single sweep. Using this technique, it is possible to image a particular ROI with relatively high image quality while simultaneously capturing the external anatomical structures, i.e., the PR information, by reconstructing a sparse set of full projections. Even though this would involve the acquisition of a sparse set of non-truncated projections, the overall applied dose still remains considerably below the amount of a conventional scan. This chapter is organized as follows. In Section 5.1, we explain why the shutter scan is practically useful in clinical applications and discuss the related work, followed by introducing the concept and possible realization of shutter scan in Section 5.2. Since the data acquired from shutter scan are not compatible with conventional reconstruction methods, in Section 5.3, we suggest three reconstruction algorithms that are capable of dealing with shutter scan data. These algorithms are either in an analytic formulation or in an iterative manner, or in a hybrid form. At last, Section 5.4 summarizes the content of this chapter.

Parts of this work have already been published in Kaestner *et al.* [Kaes 15].

5.1 Introduction and Motivation

Three-dimensional (3D) region-of-interest (ROI) imaging has been shown to be a valuable tool in cone-beam CT by providing 3D anatomical information at a predefined target region at a considerably low dose. Since the physical collimation is narrowed in both transaxial and axial direction such that only a diagnostic ROI is exposed to the X-ray beam, little information is available outside the ROI. However, in some clinical applications reconstructing an image inside the ROI alone may be sub-optimal, since the outer region, also referred to as the peripheral region (PR), may also be advantageous in image-guided therapy and interventional procedures. One of such potential applications involves applying 3D ROI imaging in cancer or tumor treatments. Although the tumor region can be visualized in an ROI image, the so-called organs-at-risk may not, which also need to be identified in the treatment region to prevent further damage. Also, surrounding landmarks that are usually required to assist patient positioning are desired to be visualized for facilitating treatment setup. Another example is to employ C-arm based ROI imaging to detect interventional micro devices, such as stents, coils or cochlea implants. In these cases, the PR may contain relevant information that is helpful for orientation in order to reach the desired location of a stenosis where the stent is deployed. In general, these clinical applications do not require a highly reliable or high resolution PR but rather adequate image quality that allows an overview orientation such as locating other organs or a catheter. Conventionally, to obtain an image with spatially varying image quality, two consecutive scans were usually acquired and combined. At first, a low-dose overview scan of the whole patient was acquired, followed by a high-dose ROI acquisition at a target ROI using an X-ray physical collimator [Kold 10]. This method, however, may require an additional registration step to align projections from both scans due to the repositioning of the patient.

In this chapter, a proof-of-concept study of a new acquisition scheme, namely the shutter scan, is conducted. That is, within one scan, to generate a high number of truncated projections to image only the ROI and a low number of full FOV projections covering the PR. Using this technique, we would be able to image a particular ROI with relatively high resolution while simultaneously capturing the external anatomical structures, i.e., the PR information, by reconstructing a predetermined sparse set of full projections. Even though that would involve the acquisition of a sparse group of non-truncated projections, the overall applied dose still remains considerably below the amount of a conventional scan. However, various artifacts will arise in the reconstruction of shutter scan data. First, the acquired subset of truncated projections is not compatible with conventional reconstruction algorithms. As a consequence, the reconstructed volume will be impaired by severe truncation artifacts. Furthermore, a sparse set of full projections also gives rise to the reconstruction of strong streaking artifacts that may distract the observer from relevant structures. Therefore, it is of practical importance to develop such an algorithm that copes with acquired shutter scan data. In this work, we propose three algorithms that are capable of reconstructing and combining such data and lead to a hybrid volume with spatially varying image quality.

So far, only a small number of research groups investigated in this direction. Lu *et al.* [Lu 14] proposed a method using a similar scan protocol that acquires two groups of X-ray projections with different mAs levels and collimation, depending on projection angles. Although their objective is also to reconstruct an image that has a high quality inside the ROI and a relatively low quality in the PR, the two groups of data were acquired in an independent manner. Firstly, a dense set of low-dose non-truncated projections was acquired to yield an additional estimation outside the ROI, followed by a sparse group of high-dose truncated projections. These sparsely acquired truncated projections were detruncated using forward projections of the first group and then reconstructed using a tight-frame (TF)-based iterative algorithm to achieve a high-quality ROI image. Alternatively, a nested ROI imaging acquisition was suggested by Leary *et al.* [Lear 14], which is similar to the proposed shutter scan method. By deploying a dynamic multileaf collimator (MLC), data acquisition aims to image two nested ROIs (instead of an ROI and a PR in our case), namely inner ROI and outer ROI, simultaneously. The dose and contrast noise ratio (CNR) to an outer ROI relative to an inner ROI can be controlled by defining several different MLC sequence ratios with a preset number of inner to outer collimator apertures. Furthermore, during acquisition the authors selected to keep at least two consecutive MLC shapes from the inner or outer ROI sequences. The reconstruction was carried out using the FDK algorithm and by performing a data extrapolation scheme proposed in [Kadr 95, Roba 12]. However, this approach cannot preserve HU values compared with the FDK reconstruction from non-truncated data.

5.2 Interleaved Data Acquisition Scheme – Shutter Scan

In this section, we elaborate the principle of the shutter scan data acquisition that is dedicated to enriching ROI imaging. The concept of the shutter scan is schematically illustrated in Fig. 5.1. The acquisition is interleaved as a function of rotation angle to generate two groups of different projections at a single sweep. The first group of projections is acquired at sparsely located projection angles (e.g., every tenth of the angulation) without collimating the X-ray beam. The benefit of acquiring a low number of non-truncated projections is two-fold: First, we can obtain a reconstructed image that has an adequate image quality in the PR such that a relatively reasonable estimation of regions outside the ROI is allowed. Second, these non-truncated projections, which yield a large FOV, could potentially improve the accuracy of the ROI reconstruction. The second group consists a large number of truncated projections and is acquired at a densely located projection angles (all except non-truncated projection angles). These projections are sufficient to reconstruct an ROI image of high quality, if an efficacious truncation correction step is applied.

In order to acquire both the non-truncated projections and truncated projections within a single scan, the shutter scan would need a fast dynamic collimator to transaxially and axially block radiation to the patient body during the gantry rotation. The collimator should be capable of changing its position and size dynamically over the entire possible range, while the C-arm is rotating from one angular position to another. For a detailed investigation of the translation speed of the collimator leaves during the gantry rotation, we refer to the work in [Heus 11]. While the X-ray beams are collimated to the ROI for most projection angles, at every n-th frame the collimator opens completely to acquire a full FOV non-truncated projection. We hereby introduce the term “sparsity” indicating the frequency of acquired full projections.

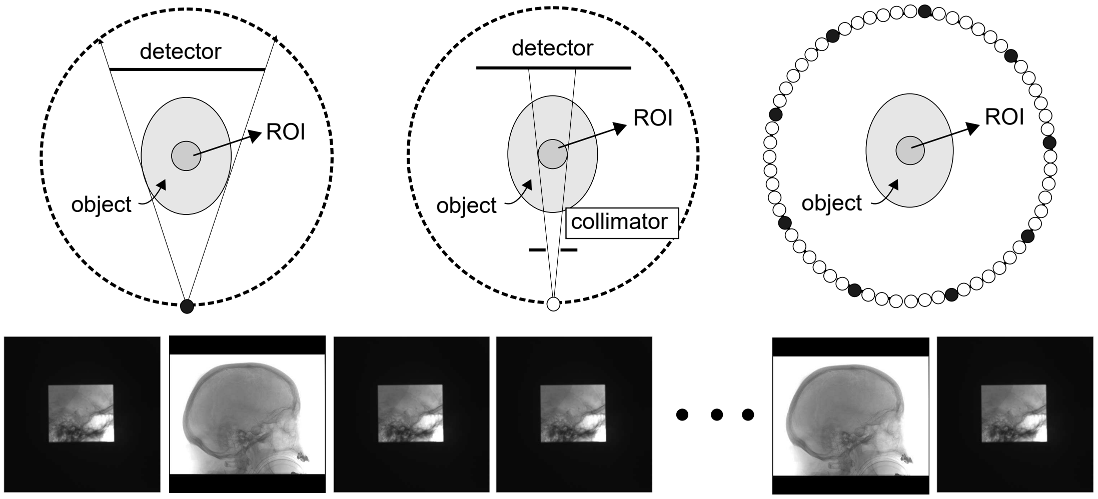

Figure 5.1: Schematic illustration of the concept of the shutter scan. The acquisition is interleaved as a function of rotation angle to generate two groups of different projections (truncated and non-truncated projections) during a single sweep.

For instance, a sparsity of $k = 10$ corresponds to an acquisition protocol where every 10-th projection is a non-truncated full projection. It is expected that the different sparsity levels in a shutter scan are meant to maintain a constant dose and image quality within the ROI, while relatively altering both aspects in the PR.

It should be emphasized that even though the shutter scan involves the acquisition of a sparse set of non-truncated projections, the overall applied dose would remain considerably below the amount of a conventional scan. Assume that a full FOV scan corresponds to 100% radiation dose, then an ROI scan where, for example, 70% of the FOV is collimated, will result in only about 30% of the radiation dose to the patient. In comparison to that, a shutter scan acquisition where, e.g., 50 non-truncated and 446 truncated projections are acquired (496 in total), leads to an additional radiation dose of roughly 7%. In this manner, information of both, the ROI and PR, can be incorporated into a single volume.

5.3 Shutter Scan Reconstruction Algorithms

As discussed in the previous chapter, the shutter scan simultaneously produces a sparse set of non-truncated projections and a dense set of truncated projections. However, neither of these projection data is directly compatible with the standard FDK algorithm. In this section, we suggest three reconstruction algorithms that are capable of dealing with shutter scan data. These shutter scan algorithms, which combine two sets of acquired data either in the projection domain or in the volume domain, in general show a similar performance within the ROI but yield noticeably distinct image quality/characteristics in the PR. In the following, we start with a straightforward approach, namely joint weighted FDK/ATRACT method, that processes the two groups of projection data in the projection domain.

5.3.1 Joint Weighted FDK/ATRACT Reconstruction

This subsection addresses a straightforward approach, as shown in Fig. 5.2, that separately pre-processes the two groups of data in the projection domain. That is, the sparse acquired non-truncated projections are filtered via the conventional FDK ramp filtering, while the dense set of truncated projections are filtered via the ATRACT algorithm to reduce truncation artifacts. Finally, both groups of projections are backprojected into a single volume by using a standard 3D voxel-driven cone-beam backprojection. However, two scale/offset-related issues still need to be addressed before we obtain the combined reconstructed volume.

Scaling and Offset Correction

Since the non-truncated projections are only sparsely acquired at a low number of rotation angles, the resulting image intensity in the PR region may be relatively lower compared with the intensity within the ROI that is reconstructed from a dense set of data. To counteract the scale/offset issue, we introduce a weighting factor that is applied to the ramp-filtered full projections. The region that relates to the PR (outside scan FOV) is weighted by a sparsity-related factor k, whereas the region inside the scan FOV is weighted by a constant 1.

Also, filtering of a truncated projection with the ATRACT algorithm yields a different scaling and offset issue on projection intensity values compared with the standard ramp filtering of a non-truncated projection. Therefore, we propose a fully automated correction scheme in this work. This correction model is based on a patient-specific regression model, which is applied to the filtered truncated projections. More specifically, firstly, the linear regression parameters (i.e., the mean $\mu^{(\mathrm{FDK})}$ and standard deviation $\sigma^{(\mathrm{FDK})}$) are computed from a homogeneous subregion in the reference FDK projections, i.e. the ramp filtered non-truncated projections. Then, all following ATRACT filtered truncated projections $g_{\mathrm{ATRACT}}\left(\lambda, u, v\right)$ are aligned to a same intensity/noise level, based on this pre-computed linear regression model, as follows

$$\breve{g}^{(\mathrm{ATRACT})}\left(\lambda, u, v\right) = \frac{g^{(\mathrm{ATRACT})}\left(\lambda, u, v\right) - \mu^{(\mathrm{ATRACT})}}{\sigma^{(\mathrm{ATRACT})}} \sigma^{(\mathrm{FDK})} + \mu^{(\mathrm{FDK})}, \qquad (5.1)$$

where $\breve{g}^{(\mathrm{ATRACT})}$ denotes the corrected ATRACT projection, μ_{ATRACT} and σ_{FDK} denote the mean and the standard deviation from a homogeneous subregion of g_{ATRACT}.

We repeat the correction process until the next non-truncated projection is reached and then the linear regression parameters will be updated according to the first step. As a consequence, a continuous update of these correction parameters is performed and the scaling and offset artifacts in ATRACT filtered projections are corrected by a reference nearby.

Discussion

The joint weighted FDK/ATRACT method has advantages of being easy to implement and computationally very efficient. Its computational complexity is comparable to that of FDK, if 1D ATRACT is adopted. However, severe streaking artifacts will

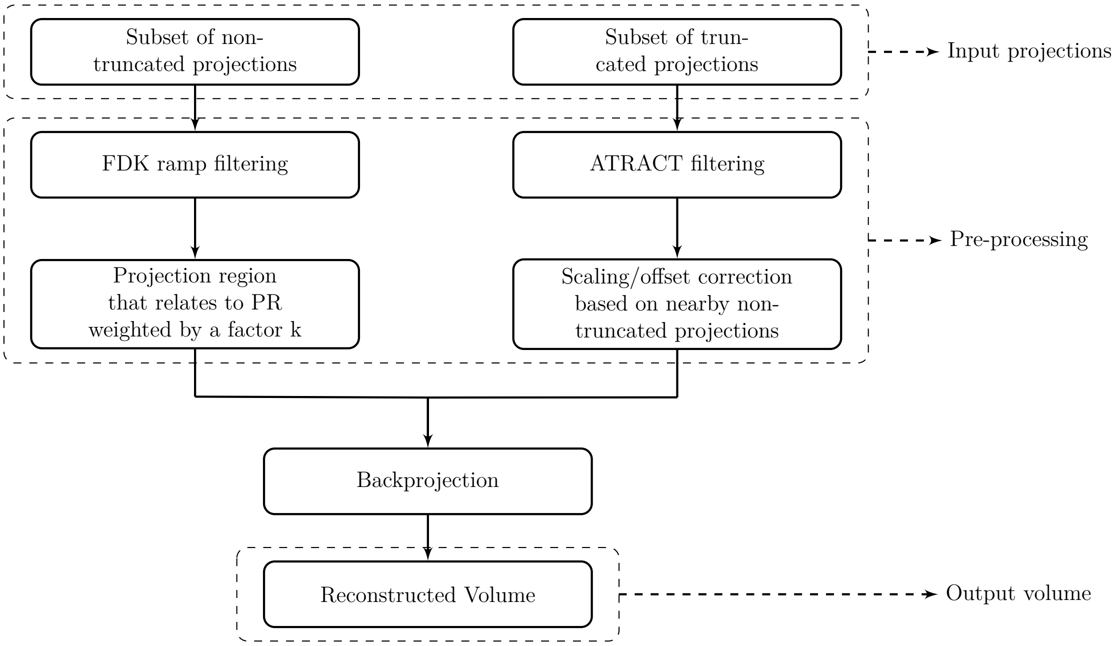
Subset of non-truncated projections
Subset of truncated projections
Input projections
FDK ramp filtering
ATRACT filtering
Pre-processing
Projection region that relates to PR weighted by a factor k
Scaling/offset correction based on nearby non-truncated projections
Backprojection
Reconstructed Volume
Output volume

Figure 5.2: Flowchart of the first approach: Non-truncated projections are filtered with the ramp filter and are locally weighted by a sparsity-related factor k outside the ROI. The truncated projections are filtered using ATRACT and an offset/scaling correction is applied after the filtering. Both sets of filtered projection data are then backprojected into a single volume to obtain the final result.

appear in the PR due to the direct implementation of FDK on sparse projection data. Particularly in a high sparsity level, these streaks may be too strong to identify the relevant anatomical structures of the patient.

5.3.2 Parallel Reconstruction with Volumetric Combination

The second approach involves a volumetric combination of two initial reconstruction images obtained by backprojecting two parallel processed projection data. The combined volume is a hybrid one, containing both the relatively low-resolution PR reconstructed from the sparse set of non-truncated data and the high-resolution ROI from the dense set of truncation data. The flowchart of this algorithm is depicted in Fig. 5.3. Further details are elaborated in the following.

The group of truncated projections is independently filtered and backprojected using ATRACT so that we obtain a high quality ROI image. For the sparse set of full FOV projections, to reduce streaking artifacts, we use an iterative reweighted TV minimization method that consists of a SART (simultaneous algebraic reconstruction technique) data fidelity term and a weighted TV regularization.

Reweighted TV Minimization

In the following we elaborate this iterative algorithm in detail. As frequently addressed in the literature [Yu 09b, Yu 09c, Yang 10], the general process of an iterative

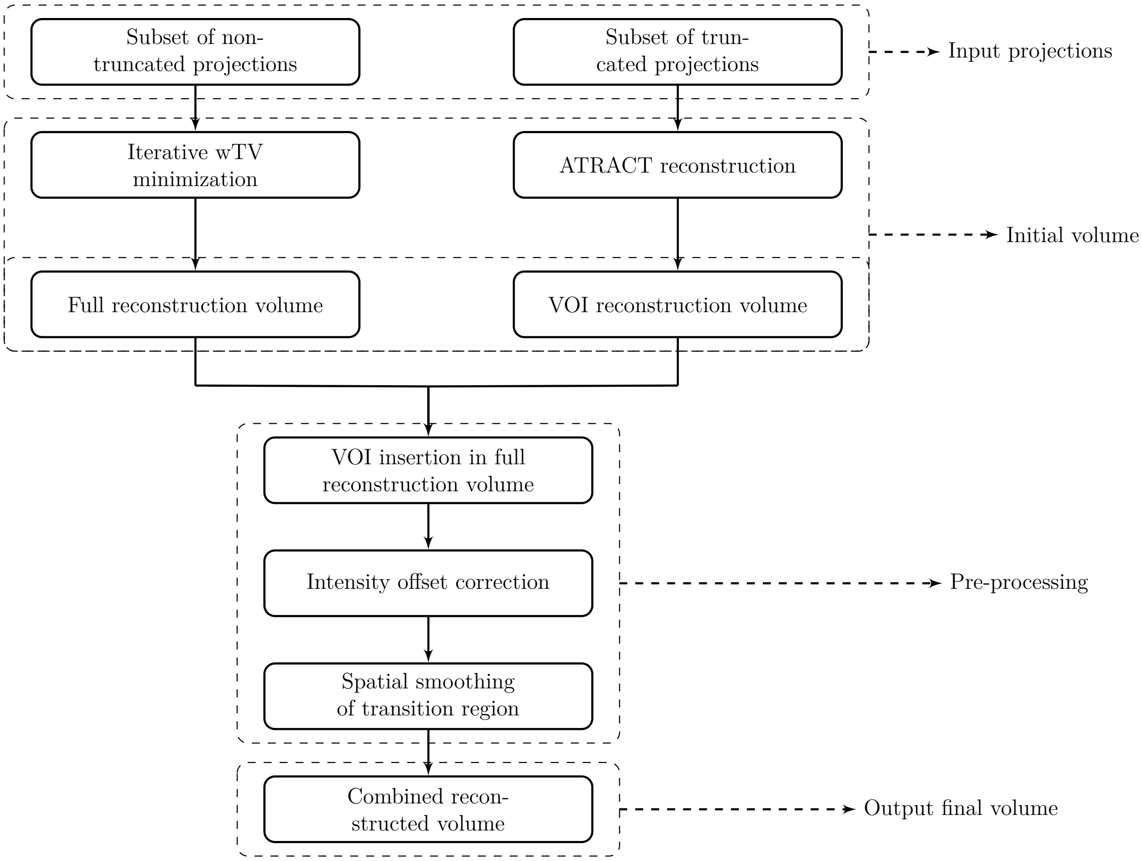
Subset of non-truncated projections
Subset of truncated projections
Input projections
Iterative wTV minimization
ATRACT reconstruction
Initial volume
Full reconstruction volume
VOI reconstruction volume
VOI insertion in full reconstruction volume
Intensity offset correction
Pre-processing
Spatial smoothing of transition region
Combined reconstructed volume
Output final volume

Figure 5.3: Flowchart of the second approach: The set of non-truncated projections is reconstructed using the wTV minimization algorithm to obtain an overview volume. The set of truncated projections is processed with the ATRACT algorithm to obtain an ROI reconstructed volume. An offset correction of the ROI is performed before both volumes are combined. This is followed by a cosine smoothing of the transition region to create the final reconstructed volume.

image reconstruction from incomplete data involves the following constrained optimization problem:

$$\min_{f} \|f\|_{\mathrm{TV}} \quad \text{subject to} \quad \|\mathbf{R}f\left(\mathbf{x}\right) - g\|_2^2 \leq \kappa, \tag{5.2}$$

where $\mathbf{R}$ describes the X-ray transform, $f\left(\mathbf{x}\right)$ denotes the reconstructed image with $\mathbf{x} = (x, y, z)$, g denotes the measured projection data and κ characterizes the raw data consistency. The data fidelity term is minimized using the standard SART. To ensure a minimization of the TV term $\|\cdot\|_{\mathrm{TV}}$, we used in this thesis an iterative reweighted total variation (wTV) minimization algorithm proposed in [Cand 08], which is formulated as follows:

$$\min_{f} \sum_{x,y,z=1}^{N_x,N_y,N_z} \omega_{x,y,z} \left\|\nabla f_{x,y,z}\right\|, \quad \text{and} \quad \omega_{x,y,z} = \frac{1}{\left\|\nabla f_{x,y,z}\right\| + \epsilon}, \tag{5.3}$$

where $f_{x,y,z}$ denotes the value in f assigned to the voxel with index (x, y, z) in a volume of size $N_x \times N_y \times N_z$, $\nabla f_{x,y,z}$ denotes the gradient of the image, $\omega_{x,y,z}$ denotes the

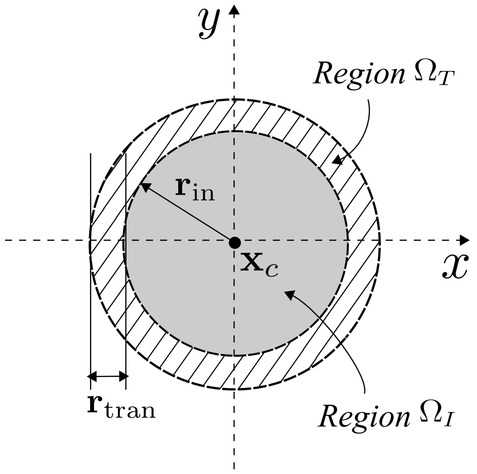

Figure 5.4: Illustration of the transition region Ω_T and inner ROI region Ω_I that are used to define the cosine smoothing function $\omega_{\cos}(\mathbf{x})$.

weighting matrix, and ϵ is a parameter that influences the image quality. Note that the weights are chosen to be inversely proportional to the image gradient magnitude, so that $\omega_{x,y,z} \|\nabla f_{x,y,z}\|$ is approximately equal to 0, if the image gradient $\|\nabla f_{x,y,z}\|$ is 0 or close to 1, if the image gradient $\|\nabla f_{x,y,z}\|$ is nonzero. In other words, the whole optimization term minimizes the number of nonzero image gradient values that is actually the L_0-Norm. This method is able to efficaciously enhance the data sparsity and was proven to be able to restore the Shepp-Logan phantom with only 10 pseudo-radial lines [Cand 08]. A detail implementation of the wTV minimization algorithm will be provided in Section 7.3.1 in the evaluation part.

Transition Smoothing

When simply combining both reconstructed volumes, i.e. the full volume and the ROI volume, an abrupt transition region will be clearly visible. Therefore, it is desirable to realize a smooth transition region without a noticeable boundary between the ROI and the full volume. This can be done by performing a cosine smoothing of the intensity values at the boundary of the ROI. Suppose the ROI volume center is located at $\mathbf{x}_c = (x_c, y_c, z_c)$. The inner ROI region Ω_I and the transition region Ω_T surrounding the inner boundary at slice $z = z_c$ are defined as (also see Fig. 5.4 for a graphical illustration):

$$\Omega_I = \left\{ \mathbf{x} \mid \sqrt{(x - x_c)^2 + (y - y_c)^2} \in [0, r_{\text{in}}] \right\} \tag{5.4}$$

$$\Omega_T = \left\{ \mathbf{x} \mid \sqrt{(x - x_c)^2 + (y - y_c)^2} \in [r_{\text{in}}, r_{\text{in}} + r_{\text{tran}}] \right\} \tag{5.5}$$

where r_{in} denotes the radius of inner boundary circle and r_{tran} denotes the transition length in the radial direction. Then, the cosine smoothing weights $\omega_{\cos}(\mathbf{x})$ can be applied slice-wise in a radial manner as follows:

$$\omega_{\cos}(\mathbf{x}) = \begin{cases} \frac{1}{2} + \frac{1}{2}\cos\left(\pi \frac{\|\mathbf{x}-\mathbf{x}_c\|_2 - r_{\text{tran}}}{r_{\text{tran}}}\right) & \mathbf{x} \in \Omega_T \\ 1 & \mathbf{x} \in \Omega_I \\ 0 & \text{else} \end{cases} \tag{5.6}$$

To obtain the final reconstruction volume $f(\mathbf{x})$, the weighted ROI volume $f_{\text{ROI}}(\mathbf{x})$ is combined with the wTV volume $f_{\text{wTV}}(\mathbf{x})$ as follows:

$$f(\mathbf{x}) = \omega_{\cos}(\mathbf{x})\, f_{\text{ROI}}(\mathbf{x}) + (1 - \omega_{\cos}(\mathbf{x}))\, f_{\text{wTV}}(\mathbf{x}). \tag{5.7}$$

Discussion

Although wTV reconstruction yields noticeably less streaking artifacts than that of FDK, independently processing of two groups of projection data is also problematic. Firstly, two volumetric images, before a combination, may also yield different intensity levels. That means, additional image processing for equalization of relative image intensity between the ROI volume and the overview volume is required. Secondly, truncated projections also contain some information outside ROI, which may help to improve image quality in the PR. This information, however, was discharged during the combination procedure.

5.3.3 Prior Image Driven Projection Detruncation

This section presents an approach that utilizes an iteratively reconstructed initial volume as prior image served for a subsequent detruncation/extrapolation process. Inspired by the work of Ritschl *et al.* [Rits 13], the approach in total involves three steps. First, an initial volume is reconstructed from the measured sparse set of non-truncated projections. To avoid strong streaking artifacts, here again we use the iterative wTV minimization algorithm as described in the previous section. Then, we forward-project the initially reconstructed volume to complete the group of truncated projections that was also acquired in the shutter scan. This step is also referred to as detruncation. By doing so, we obtain a complete set of hybrid projection data that consists of originally measured projection data and artificially forward projected data inside and outside the measured FOV, respectively. The last step in this pipeline involves the standard FDK reconstruction that will lead to a final output volume with spatially varying image quality. The flowchart of the method is shown in Fig. 5.5. Further details are elaborated in the following sections.

Forward Projection

To perform the second reconstruction with improved image quality, it is necessary to complete the measured truncated projections outside the ROI with the information from the initial wTV volume. To this end, we need to forward-project the initial volume to the original imaging geometry with the same detector size. The forward

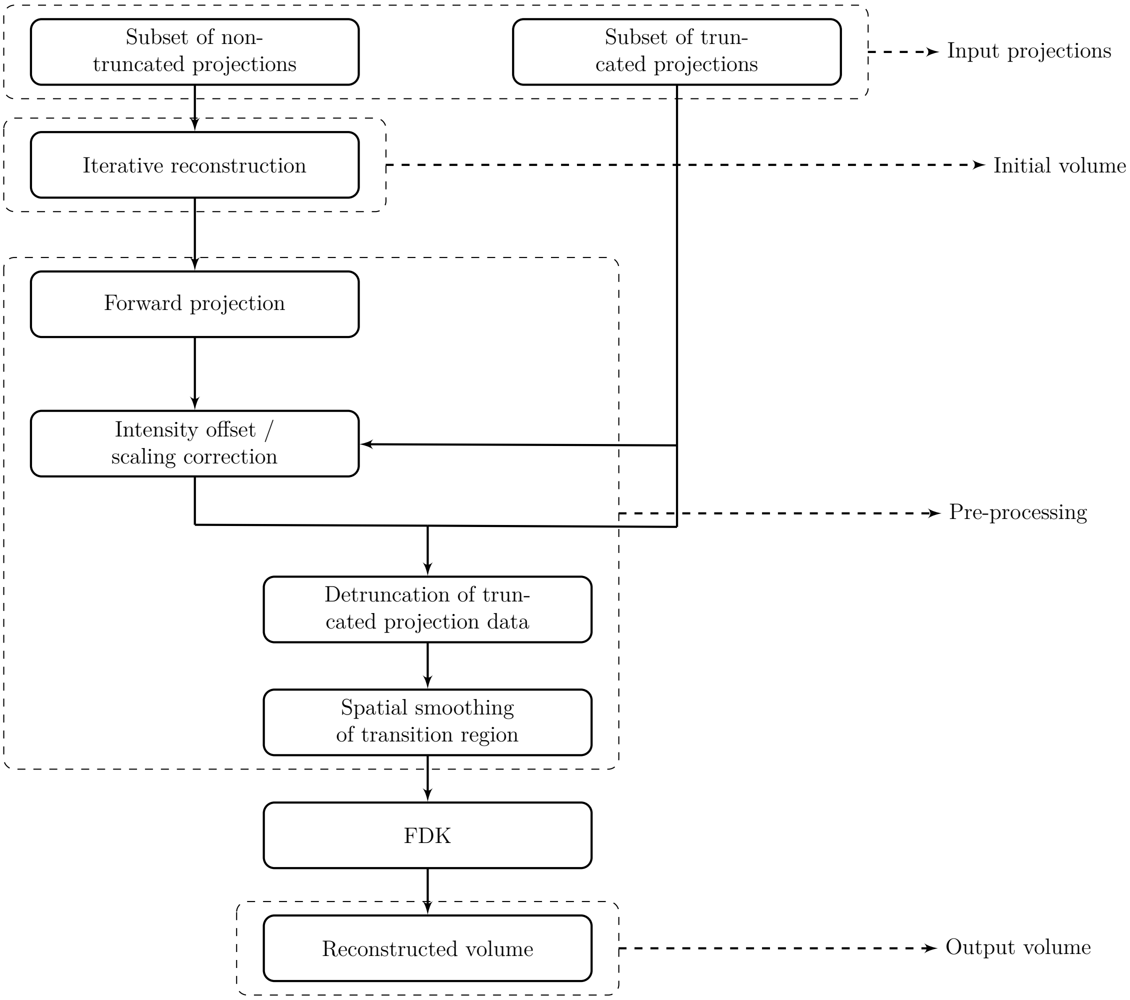
Subset of non-truncated projections
Subset of truncated projections
Input projections
Iterative reconstruction
Initial volume
Forward projection
Intensity offset / scaling correction
Pre-processing
Detruncation of truncated projection data
Spatial smoothing of transition region
FDK
Reconstructed volume
Output volume

Figure 5.5: Flowchart of the third approach: An initial reconstruction is obtained by using an iterative wTV algorithm on the sparse set of non-truncated projections. Then, the initial reconstruction is forward projected to complete the measured truncated projections from the shutter scan. An offset/scaling correction is applied on these forward projections before the actual detruncation step of the truncated projections is taken. A smoothing of the transition region is further performed and all projections are reconstructed into the final volume via FDK.

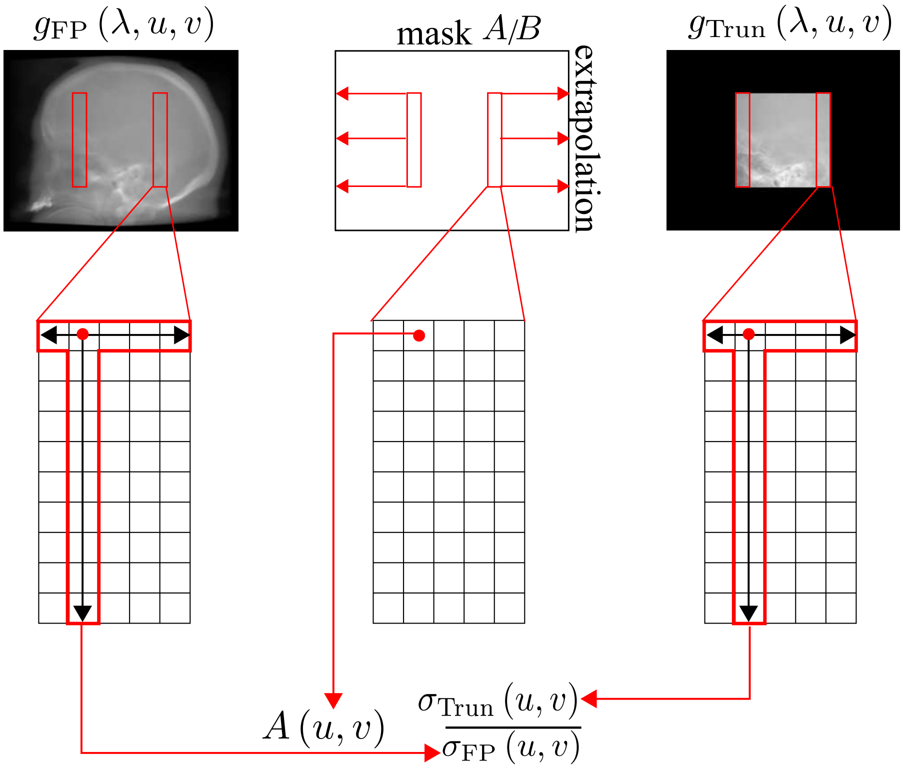
$g_{\mathrm{FP}}(\lambda, u, v)$
mask A/B
extrapolation
$g_{\mathrm{Trun}}(\lambda, u, v)$
$A(u, v)$
$\sigma_{\mathrm{Trun}}(u, v)$
$\sigma_{\mathrm{FP}}(u, v)$

Figure 5.6: Illustration of how to compute two parameter masks $A(u, v)$ and $B(u, v)$ for each projection that contain all transformation parameters for a single pixel (u, v). To obtain $A(u, v)$ for instance, we calculate the standard deviations over the whole column in u-direction and over the row in v-direction in the transition regions for both the forward projections $g_{\mathrm{FP}}(\lambda, u, v)$ and the truncated projections $g_{\mathrm{Trun}}(\lambda, u, v)$.

projection step was performed by a ray-driven algorithm. This algorithm calculates each ray, described by the source position and a detector pixel position, through the wTV reconstructed volume while accumulating the line integral values. In practice, the forward projection is only necessary to be performed on the angulations that correspond to truncated projections and also outside the measured FOV.

Projection Adjustment and Smoothing

The original collimated data and the forward projected data are combined in the projection domain. Here, some adjustments are needed to handle incorrect forward projection values, especially in the transition region. These adjustments are very crucial for the subsequent pre-processing steps. Our correction strategy follows the method proposed in [Wieg 05, Kold 10]. That is, additional overlapping regions on both sides of the measured projection (truncated) are also forward-projected. Values are compared with the corresponding overlapping regions of measured data such that the transformation parameters can be obtained. More specifically, we define two transformation parameters A and B indicating the scale and offset as follows

$$A = \frac{\sigma_{\mathrm{Trun}}}{\sigma_{\mathrm{FP}}}, \quad \text{and} \quad B = \mu_{\mathrm{Trun}} - A \cdot \mu_{\mathrm{FP}}, \tag{5.8}$$

where σ_{Trun}, σ_{FP} correspond to the standard deviations and μ_{Trun}, μ_{FP} correspond to the mean values of the transition region for the truncated projections $g_{\mathrm{Trun}}\left(\lambda, u, v\right)$ and the forward projections $g_{\mathrm{FP}}\left(\lambda, u, v\right)$, respectively.

In the following, for each projection we compute two parameter masks $A\left(u, v\right)$ and $B\left(u, v\right)$ that contain all transformation parameters for a single pixel (u, v); also see Fig. 5.6 for a graphical illustration. To do so, we first calculate the mean values and the standard deviations over the whole column in u-direction and over the row in v-direction in the transition regions for both the forward projections and the measured projections (truncated). Then, the individual transformation parameters are calculated based on these values [Eq. (5.8)] and then filled in the parameter masks $A\left(u, v\right)$ and $B\left(u, v\right)$ at the corresponding rows and columns. In order to obtain values of the masks outside the transition region, the outermost values of the parameter masks are constantly extrapolated to the borders of the detector in both directions. Finally, the actual transformation of each pixel of the forward projection is achieved according to:

$$g_{\breve{\mathrm{FP}}}\left(\lambda, u, v\right) = A\left(u, v\right) \cdot g_{\mathrm{FP}}\left(\lambda, u, v\right) + B\left(u, v\right) \tag{5.9}$$

where $g_{\breve{\mathrm{FP}}}\left(\lambda, u, v\right)$ represents the adjusted forward projection at rotation angle λ.

With an additional cosine weighting, we ensure a smooth transition region in the combined projection data, such that abrupt changes of the values at the boundary of the ROI can be avoided. The cosine smoothing weights are calculated following the principle of Eq. (5.6) but rather row-wise along the detector line (u-direction).

Discussion

The prior image based detruncation we proposed in this section fully utilizes two groups of projection data from a shutter scan and thus appears more promising than those of separately processing strategies under investigation. However, using iterative reconstruction scheme requires frequent forward- and back-projection procedures, which seems computationally not very efficient. As an alternative, a non-linear edge preserve filters, such as bilateral filter, could be potentially applied to generate a compromised result.

5.4 Summary

In this part of the thesis a novel concept of data acquisition, namely shutter scan, was introduced. It would acquire both a high number of truncated projections and a low number of full FOV projections within one C-arm sweep. This data acquisition is advantageous in various clinical applications that require imaging a particular ROI with relatively high image quality while simultaneously capturing the external anatomical structures, i.e., the PR information, with a relatively low image quality. Along with acquired shutter scan data, we suggested three reconstruction algorithms that are capable of dealing with such data. These newly proposed algorithms involve either pre-processing projection data in a separate manner and backprojecting them in a single volume, or a straightforward volumetric combination of two individually reconstructed images or even a projection merge via forward projection of an initial iteratively reconstructed volume. Although all methods lead to a hybrid volume with spatially varying resolution, the resulting image quality and characteristics, particularly in the PR, will noticeably differ from one to another. The corresponding evaluations of different algorithmic performances of the shutter scan are presented in Chapter 7.

CHAPTER 6

Patient Bounded Extrapolation Method using Low-Dose Priors

6.1 Introduction and Motivation 79
6.2 Patient Boundary Estimation with Priors 80
6.3 Adaptive Extrapolation Schemes 84
6.4 Summary 86

Three-dimensional (3D) C-arm based ROI imaging is a valuable tool in interventional radiology for therapy planning and guidance. A necessary initial step prior to a 3D acquisition is to isocenter the patient with respect to the target to be scanned. To this end, low-dose fluoroscopic X-ray acquisitions are usually applied from anterior-posterior (AP) and medio-lateral (ML) views. Based on this, the patient is isocentered by repositioning the table. In this chapter, we propose a robust extrapolation method that makes use of these non-collimated fluoroscopic images to improve image quality in 3D ROI reconstruction. Section 6.1 explains the practical importance of the proposed method. Sections 6.2 and 6.3 present the investigated two-step extrapolation pipeline. The first step, as described in Section 6.2, involves the estimation of a rough 3D patient shape based on two orthogonal prior images and then re-projecting the 3D model in any given C-arm rotation angle to obtain patient boundary information in the associated projection. Section 6.3 discusses the second step that incorporates the estimated patient boundary information into existing extrapolation schemes. Finally, the last section summarizes the whole chapter.

Parts of this work have already been published in Xia *et al.* [Xia 14a, Xia 15b].

6.1 Introduction and Motivation

Three-dimensional ROI imaging with C-arm systems provides anatomical information in a predefined 3D target region at a considerably low X-ray dose. As described in Chapter 1, in neurointervention some applications only require a small ROI to be imaged, e.g., examination of a deployed stent or coil, resulting in severe truncation of the projection data. However, conventional reconstruction algorithms generally yield images with heavy truncation artifacts from these laterally severely truncated projections [Herm 81].

Although various previous approaches concerning the truncation artifact reduction were proposed, as discussed in Chapter 2, only few meet our requirement. Popular heuristic extrapolation techniques [Ohne 00, Hsie 04, Van 04, Sour 05] aim to estimate the missing data using a smooth continuation assumption at the truncation edges. Although these methods can be carried out without prior information, they rely on heuristics and thus may be difficult to correct for the severe truncations that are often encountered in ROI scans. The sinogram recovery by tracing sinusoidal sinogram curve (Chityala *et al.* [Chit 05] and Zamyatin *et al.* [Zamy 07]) may also fail since less measured data is available for angular interpolation along the sine curves. Maltz *et al.* [Malt 07] estimated the thickness of the patient by calculating water-equivalent thicknesses from the measured attenuation profiles, so that the unknown patient boundary can be approximated. However, in practice, the presence of any non-water tissue (air, bond or metal implants) might result in a substantial over/under-estimation of the actual object thickness. The differentiated backprojection method (DBP) investigated by Noo *et al.* [Noo 04], Defrise *et al.* [Defr 06], Kudo *et al.* [Kudo 08] and Ye *et al.* [Ye 07] could potentially achieve a stably and exact ROI reconstruction. However, such reconstruction schemes, either need certain data sufficiency conditions or come with rather high computational demand, may prohibit their use in interventional clinical routines. The data completion using prior scan proposed by Ruchala *et al.* [Ruch 02], Wiegert *et al.* [Wieg 05], Kolditz *et al.* [Kold 10] and Sen Sharma *et al.* [Sen 13] can extend the collimated regions in an accurate manner. These additional scans, however, may interrupt the interventional workflow and cost extra radiation dose to the patient.

In this chapter, we present a patient-bounded extrapolation method that leads to significant improvements in the accuracy of 3D ROI imaging, even in the presence of severely truncated data. The method does not require any additional hardware and can be readily integrated into the existing interventional workflow. Moreover, the proposed method only involves small vector/matrix multiplications on boundary points and thus are computationally comparable to heuristic extrapolation schemes. It is based on the fact that prior to a 3D scan, two fluoroscopic X-ray acquisitions are generally performed from anterior-posterior (AP) and medio-lateral (ML) views, to isocenter the patient with respect to the target to be scanned; see Fig. 6.1. These fluoroscopic acquisitions require considerably low X-ray dose. The fundamental idea of the proposed method is to estimate a 3D shape model of the patient from these low-dose non-truncated fluoroscopic images and then exploit this patient-specific *a priori* shape knowledge for the extrapolation of truncated projections.

6.2 Patient Boundary Estimation with Priors

This section starts with an overview of the proposed patient-bounded extrapolation method, which consists of the following steps. First, we estimate the rough 3D patient shape based on two fluoroscopic projections, using per-slice ellipse model fitting. Forward-projecting this 3D model for any projection angle acquired during the actual ROI scan gives the patient bounded information for the corresponding

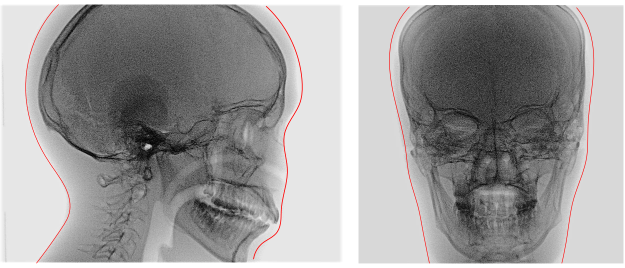

Figure 6.1: Illustration of fluoroscopic X-ray projections from medio-lateral view and anterior-posterior view from an anthropomorphic head phantom. They require considerably low X-ray dose and are usually acquired prior to a 3D scan, to examine if the diagnostic VOI is optimally centered. The red outlines indicate the extracted boundary information.

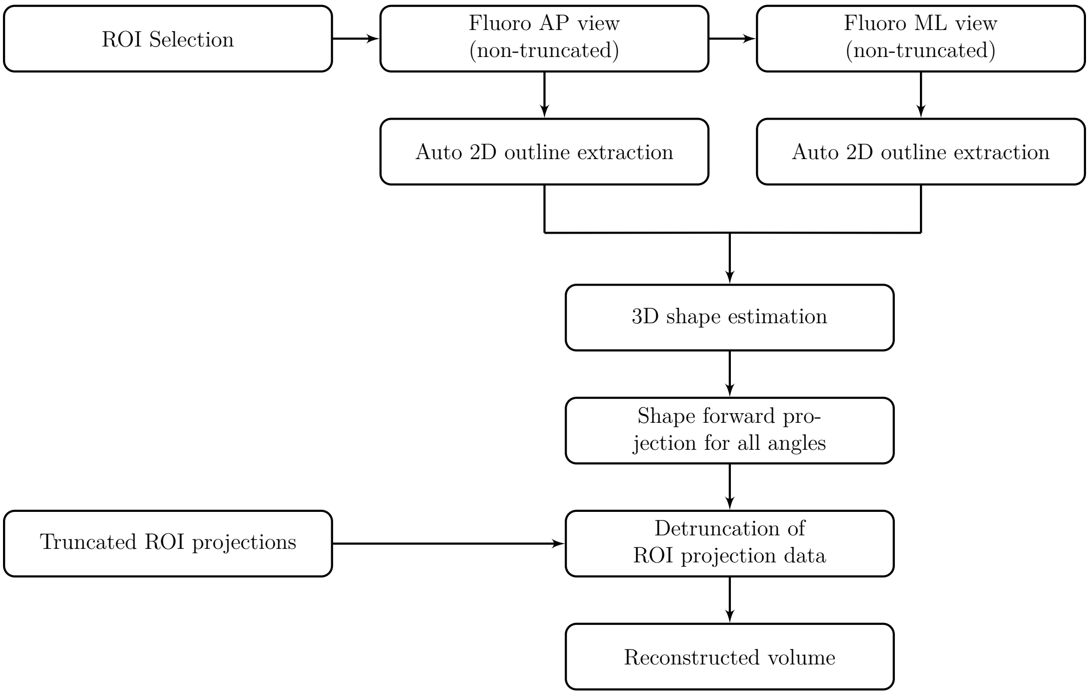
ROI Selection
Fluoro AP view (non-truncated)
Fluoro ML view (non-truncated)
Auto 2D outline extraction
Auto 2D outline extraction
3D shape estimation
Shape forward projection for all angles
Truncated ROI projections
Detruncation of ROI projection data
Reconstructed volume

Figure 6.2: Flowchart of the proposed patient boundary extrapolation procedure.

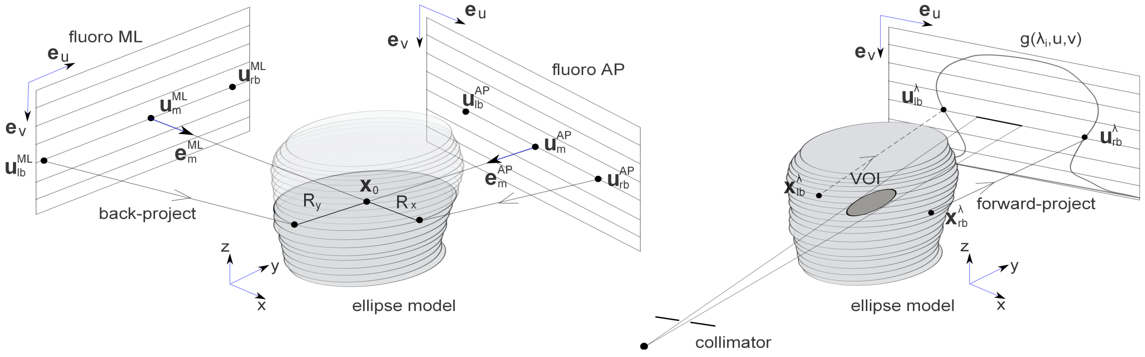

Figure 6.3: Illustration of the patient-bounded extrapolation scheme. (Left) Contour-bounded slice-wise ellipse fitting. (Right) Forward-projection of the boundaries of the previously estimated patient shape model at a given C-arm rotation view provides the patient boundary in the projection domain.

projection. Then, detruncated projection data could be obtained by adapting the extrapolated profile to fit the known profile boundary points. The flowchart of the algorithm is illustrated in Fig. 6.2. The details are elaborated in the following sections; also see Fig. 6.3 for notations.

6.2.1 Patient Shape Model Estimation using Slice-wise Ellipse

The first step is to extract the boundaries from fluoroscopic images shown as the red outlines in Fig. 6.1. Here we can readily detect the edges by using an empirically pre-set air/tissue threshold. Suppose $\mathbf{u}_{lb}^{AP} = \left(u_{lb}^{AP}, v_i, 1\right)$, $\mathbf{u}_{rb}^{AP}$, $\mathbf{u}_{lb}^{ML}$, and $\mathbf{u}_{rb}^{ML}$ are the homogeneous coordinates of the segmented left and right boundary points at detector row v_i of the 2D fluoroscopic images from AP and ML view. Let $\mathbf{P}^{\lambda} \in \mathbb{R}^{3\times 4}$ be the projection matrix at the C-arm rotation angle λ that maps position $\mathbf{x} = [x, y, z]$ in the C-arm coordinate frame to a position $\mathbf{u} = [\omega u, \omega v, \omega]$ in the 2D projection plane:

$$\mathbf{u} = \mathbf{P}^{\lambda} \begin{bmatrix} \mathbf{x} \\ 1 \end{bmatrix}. \tag{6.1}$$

The matrix $\mathbf{P}^{\lambda}$ can be decomposed as follows:

$$\mathbf{P}^{\lambda} = \left[\mathbf{P}_{13}^{\lambda} \mid \mathbf{p}_{4}^{\lambda}\right] = [\mathbf{AR} \mid \mathbf{At}], \tag{6.2}$$

where $\mathbf{R} \in \mathbb{R}^{3\times 3}$ denotes the rotation matrix, $\mathbf{t} \in \mathbb{R}^{3}$ denotes the translation vector, and $\mathbf{A} \in \mathbb{R}^{3\times 3}$ the intrinsic parameter matrix. Then, we can compute the direction unit vector $\mathbf{e}_m^{AP}$, $\mathbf{e}_m^{ML}$ of the ray that connects the source to the middle point of the two boundaries, i.e., $\mathbf{u}_m^{AP} = \left(\mathbf{u}_{lb}^{AP} + \mathbf{u}_{rb}^{AP}\right)/2$ and $\mathbf{u}_m^{ML} = \left(\mathbf{u}_{lb}^{ML} + \mathbf{u}_{rb}^{ML}\right)/2$, as:

$$\mathbf{e}_m^{AP} = \frac{(\mathbf{P}_{13}^{AP})^{-1}\mathbf{u}_m^{AP}}{\|(\mathbf{P}_{13}^{AP})^{-1}\mathbf{u}_m^{AP}\|_2}, \quad \mathbf{e}_m^{ML} = \frac{(\mathbf{P}_{13}^{ML})^{-1}\mathbf{u}_m^{ML}}{\|(\mathbf{P}_{13}^{ML})^{-1}\mathbf{u}_m^{ML}\|_2}, \tag{6.3}$$

where $\mathbf{P}^{-1}$ denotes the pseudo-inverse of the matrix $\mathbf{P}$. Now the ray equations can be expressed as

$$\mathbf{l}_m^{AP}(t) = \mathbf{s}^{AP} + t\mathbf{e}_m^{AP}, \text{ and } \mathbf{l}_m^{ML}(l) = \mathbf{s}^{ML} + l\mathbf{e}_m^{ML}, \tag{6.4}$$

where $\mathbf{s}^{AP}$ and $\mathbf{s}^{ML}$ denote the X-ray source positions at AP and ML views, which can be computed using $\mathbf{s} = -\mathbf{P}_{13}^{-1}\mathbf{p}_4$, and $t, l \in \mathbb{R}$.

Then, the center of the fitted ellipse $\mathbf{x}_0$ is estimated by computing the intersection of the two rays $\mathbf{l}_m^{AP}$ and $\mathbf{l}_m^{ML}$. Here, we confine to breaking the problem down to a 2D line intersection by setting the third component of the 3D lines to zero, i.e., $\mathbf{s}^{AP}\mathbf{I}_z = \mathbf{s}^{ML}\mathbf{I}_z = 0$ and $\mathbf{e}_m^{AP}\mathbf{I}_z = \mathbf{e}_m^{ML}\mathbf{I}_z = 0$, where $\mathbf{I}_z = \begin{bmatrix} 0 & 0 & 1 \end{bmatrix}^T$. The reason to make such an approximation is that we only need to compute the $u-$axis coordinates of the object boundary in the forward projection procedure. The $v-$axis coordinates are already given as the detector row indexes where we extracted the outline information, i.e., v_i. Then, the problem is to solve the intersection of the following 2D line equations:

$$\begin{cases} y = ax + b \\ y = cx + d \end{cases} \tag{6.5}$$

with

$$\begin{aligned} a &= \frac{\mathbf{e}_m^{ML}\mathbf{I}_y}{\mathbf{e}_m^{ML}\mathbf{I}_x}, \quad b = \mathbf{s}^{ML}\mathbf{I}_y - a\mathbf{s}^{ML}\mathbf{I}_x \\ c &= \frac{\mathbf{e}_m^{AP}\mathbf{I}_y}{\mathbf{e}_m^{AP}\mathbf{I}_x}, \quad d = \mathbf{s}^{AP}\mathbf{I}_y - a\mathbf{s}^{AP}\mathbf{I}_x \end{aligned} \tag{6.6}$$

where $\mathbf{I}_x = \begin{bmatrix} 1 & 0 & 0 \end{bmatrix}^T$ and $\mathbf{I}_y = \begin{bmatrix} 0 & 1 & 0 \end{bmatrix}^T$. So far, we computed the first two components of the intersection point $\mathbf{x}_0$. To establish a 3D model in the volume domain, the third component of $\mathbf{x}_0$ can be approximated by the third component of the closest point between the two 3D lines $\mathbf{l}_m^{AP}$ and $\mathbf{l}_m^{ML}$, which is given by

$$\mathbf{x}_0\mathbf{I}_z := \mathbf{x}_{\text{clo}}\mathbf{I}_z \tag{6.7}$$

with the closest point determined by:

$$\mathbf{x}_{\text{clo}} = \mathbf{s}^{AP} + \frac{\left(\left(\mathbf{s}^{ML} - \mathbf{s}^{AP}\right) \times \mathbf{e}_m^{ML}\right) \cdot \left(\mathbf{e}_m^{AP} \times \mathbf{e}_m^{ML}\right)}{\|\mathbf{e}_m^{AP} \times \mathbf{e}_m^{ML}\|^2}\mathbf{e}_m^{AP}. \tag{6.8}$$

Now we need to determine the radii R_x, R_y of the ellipse. The line equation of the rays from AP view that connects the patient boundary and source can also be expressed as (e.g. right boundary) $\mathbf{l}_r^{AP}(h) = \mathbf{s}^{AP} + h\mathbf{e}_r^{AP}$, where $\mathbf{e}_r^{AP}$ is computed using $\mathbf{u}_{rb}^{AP}$ similar to Eq. (6.3). Suppose $\mathbf{x}_r$ is the point located on the line $\mathbf{l}_r^{AP}$ that satisfies $\mathbf{x}_r\mathbf{I}_y = \mathbf{x}_0\mathbf{I}_y$, i.e., with the same y-axis coordinate as $\mathbf{x}_0$; also see Fig. 6.4 for illustration. Then, the radius along the x-axis R_x can be approximated as follows:

$$R_x = (\mathbf{x}_r - \mathbf{x}_0)\,\mathbf{I}_x. \tag{6.9}$$

In analogy, we can use the boundary from ML view to determine the radius of the ellipse along the y-axis R_y.

So far, for each detector row v_i we computed an associated ellipse that is used to approximate a slice of the patient outline in the volume domain. This ellipse is parametrized by the center $\mathbf{x}_0$ and two radii R_x and R_y.

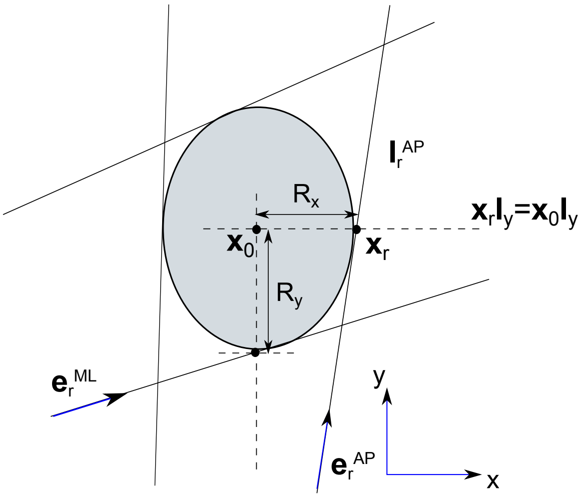

Figure 6.4: Illustration of how to approximate the ellipse radii R_x and R_y. To estimate R_x for instance, we need to compute the x-axis distance between $\mathbf{x}_0$ and $\mathbf{x}_r$ (a point located on the line $\mathbf{l}_r^{AP}$ that has the same y -axis coordinate as $\mathbf{x}_0$). Such an approximation is valid due to the small fan angle in C-arm system.

6.2.2 Patient Boundary Estimation for Arbitrary Projections

With the estimated ellipse in the volumetric image domain, we can compute the left and right patient boundaries of that ellipse for any given C-arm rotation angle λ as follows:

$$\mathbf{x}_{lb}^{\lambda} = \mathbf{x}_0 - r\mathbf{e}_u, \tag{6.10}$$

$$\mathbf{x}_{rb}^{\lambda} = \mathbf{x}_0 + r\mathbf{e}_u, \tag{6.11}$$

where $r = \sqrt{(R_y \cos\lambda)^2 + (R_x \sin\lambda)^2}$ and $\mathbf{e}_u$ denotes the unit vector in detector row direction. Then, we forward-project these voxel positions onto the 2D projection plane using Eq. (6.1), also cf. Fig. 6.3:

$$\mathbf{u}_{lb}^{\lambda} = \mathbf{P}^{\lambda}\begin{bmatrix}\mathbf{x}_{lb}^{\lambda}\\ 1\end{bmatrix}, \quad \text{and } \mathbf{u}_{rb}^{\lambda} = \mathbf{P}^{\lambda}\begin{bmatrix}\mathbf{x}_{rb}^{\lambda}\\ 1\end{bmatrix}. \tag{6.12}$$

The estimated patient left and right boundaries at the detector row v_i and rotation angle λ, i.e., $\left(u_{lb}^{\lambda}, v_i\right)$ and $\left(u_{rb}^{\lambda}, v_i\right)$, can be obtained with $u_{lb}^{\lambda} = \mathbf{u}_{lb}^{\lambda}\mathbf{I}_x/\mathbf{u}_{lb}^{\lambda}\mathbf{I}_z$ and $u_{rb}^{\lambda} = \mathbf{u}_{rb}^{\lambda}\mathbf{I}_x/\mathbf{u}_{rb}^{\lambda}\mathbf{I}_z$.

6.3 Adaptive Extrapolation Schemes

6.3.1 Patient Bounded Water Cylinder Extrapolation

Based on the estimated patient boundaries in the VOI scan projection data, we are in the position to apply any extrapolation technique and adapting it according to the restriction that the extrapolated profile must end at the known patient boundaries.

In this paper, we adapt the water cylinder approach of Hsieh *et al.* [Hsie 04] by expanding or compressing the initial extrapolated lines to fulfill this restriction. Let $g_{\lambda,v}(u)$ be the projection data at the given detector row v and rotation angle λ. Then, extrapolation is carried out row-wise as

$$\widetilde{e}_{\text{water}}(u) = 2\mu\sqrt{r^2 - \kappa^2 (u - u_c)^2} \tag{6.13}$$

where μ denotes the water attenuation coefficient, u_c denotes the location of the fitted cylinder with respect to the detector row and r denotes the radius. As described in Hsieh's work [Hsie 04], the parameters u_c and r can be determined by

$$u_c = \frac{g_{\lambda,v}(u_t)\, g'_{\lambda,v}(u_t)}{4\mu^2}, \; r = \sqrt{\frac{g_{\lambda,v}(u_t)}{4\mu^2} + u_c^2} \tag{6.14}$$

where u_t and $g'_{\lambda,v}(u_t)$ denote the truncation boundary position and slope of the truncation projection boundary samples, respectively. In contrast to the formulation by Hsieh *et al.*, in Eq. (6.13) we introduce κ that serves as a scaling factor to stretch or shrink the extrapolated profiles. The values of κ can be computed by using the boundary index u_b (here we do not distinguish the left or right boundary. Both are denoted as u_b) that we obtained in the previous section:

$$\kappa^2 = \frac{r}{u_b - u_c}. \tag{6.15}$$

6.3.2 Patient Bounded Square Root Extrapolation

As an alternative, we also investigate the square root function extrapolation that was proposed by Sourbelle *et al.* [Sour 05]. For a given detector row v and rotation angle λ, the extrapolation function is provided as

$$\widetilde{e}_{\text{square}}(u) = \sqrt{a \cdot u^2 + b \cdot u + c}. \tag{6.16}$$

To determine the parameters a, b, and c, the following continuity equations are used:

$$g_{\lambda,v}(u_t) = \sqrt{a \cdot u_t^2 + b \cdot u_t + c}, \tag{6.17}$$

$$g'_{\lambda,v}(u_t) = \frac{b + 2a \cdot u_t}{2g_{\lambda,v}(u_t)}, \tag{6.18}$$

where u_t and $g'_{\lambda,v}(u_t)$ denote the position and slope of the truncation edge, respectively. We integrate the patient boundary information into (6.16) such that the extrapolated profile ends at u_b:

$$g_{\lambda,v}(u_b) = \sqrt{a \cdot u_b^2 + b \cdot u_b + c} = 0. \tag{6.19}$$

Thus, the three parameters a, b, and c can be determined using these three equations.

6.3.3 Cosine-based Transition Smoothing

To enforce the smoothness of the transition region, the measured data $g_{\lambda,v}(u)$ and the extrapolation data $\widetilde{e}(u)$ are combined by a cosine-like smooth weighting function in a predefined transition interval. The range of the transition interval is empirically determined by using 1/30 of number of the pixels at the measured detector row. For the right side of truncated image for instance, the transition interval is $[u_{\text{trans}}, u_t]$ and the extrapolated values in this transition interval can be computed as follows

$$g_{\lambda,v}^{\text{trans}}(u) = g_{\lambda,v}(u) \cdot (1 - \omega(u)) + \widetilde{e}(u) \cdot \omega(u), \tag{6.20}$$

with the weight function $\omega(u)$ given by

$$\omega(u) = \frac{1}{2} + \frac{1}{2}\cos\left(\pi \frac{u - u_t}{u_t - u_{\text{trans}}}\right) \tag{6.21}$$

where $\widetilde{e}(u)$ indicates the extrapolated data by using either method proposed above.

6.4 Summary

In this chapter, we investigated a patient-bounded extrapolation method that potentially leads to significant improvements in the accuracy of 3D ROI imaging, even in the presence of severely truncated data. The method does not require any additional hardware and can be readily integrated into the existing interventional workflow. It is based on the fact that prior to a 3D scan, two fluoroscopic X-ray acquisitions are generally performed from two orthogonal views, to isocenter the patient. These fluoroscopic acquisitions require considerably low X-ray dose and have to be acquired anyway during an isocentering procedure. The fundamental idea of the proposed method is to estimate a 3D shape model of the patient from these low-dose non-truncated fluoroscopic images and then exploit this patient-specific *a priori* shape knowledge for the extrapolation of truncated projections. The proposed method is well-suited for neurointerventions since: 1) The ellipse is a good model for the head; 2) the low-dose fluoroscopic images are usually non-collimated and cover the entire object of interest. This also implies the limitation of this method. That is, the imaged object should be fully covered in the fluoroscopic images from both views. Note that this requirement may not be fulfilled for a body scan due to limited size of the flat detector in a C-arm system. In this chapter, we only incorporated the exploited patient boundary information into the water cylinder extrapolation [Hsie 04] and the square root function extrapolation [Sour 05]. But, theoretically, this information can also be applied to other extrapolation schemes such as proposed in [Ohne 00, Zell 05, Malt 07].

CHAPTER 7

Evaluation and Results

7.1 Experimental Setup 87
7.2 ATRACT Specific Evaluation and Parametrization 92
7.3 SSR Specific Evaluation and Parametrization 101
7.4 PBE Specific Evaluation and Parametrization 108
7.5 Comparative Evaluation among ATRACT, SSR and PBE 113
7.6 Summary and Discussion 126

The reconstruction algorithms presented in Chapter 4 to Chapter 6 come with a different trade-off between image quality and radiation dose and may thus be dedicated for various application scenarios. In this chapter, a detailed comparative evaluation of all proposed algorithms for 3D ROI reconstruction is presented. This chapter is organized as follows. In Section 7.1, we describe the experimental setup including the studied clinical datasets, truncation simulation as well as image quality metrics. Section 7.2 to Section 7.4 present the algorithm-specific evaluation and parametrization for each of three proposed methods, individually. After this internal comparison and parametrization, the best candidate of each group is picked out for the comparative evaluation of different categories. This is presented in Section 7.5. Finally, we discuss the evaluation results and draw the conclusions in Section 7.6.

7.1 Experimental Setup

In this section, the clinical datasets used for assessing the quality of the developed algorithms are presented, followed by the definition of eight ROIs differing from each other either by the size or position. Thereafter, we introduce the assessment metrics for qualifying the reconstruction quality of the clinical data, which will later on be used for the evaluation.

7.1.1 Clinical Dataset and Scan Configuration

To validate the robustness for realistic applications, the proposed methods were retrospectively evaluated on 16 clinical datasets from different patients (data courtesy of CHI St. Luke's Health - Baylor St. Luke's Medical Center, Houston, TX, USA). All datasets were acquired in an interventional suite equipped with a biplane flat-panel detector angiographic C-arm (Axiom Artis Zee, Siemens Healthcare GmbH,

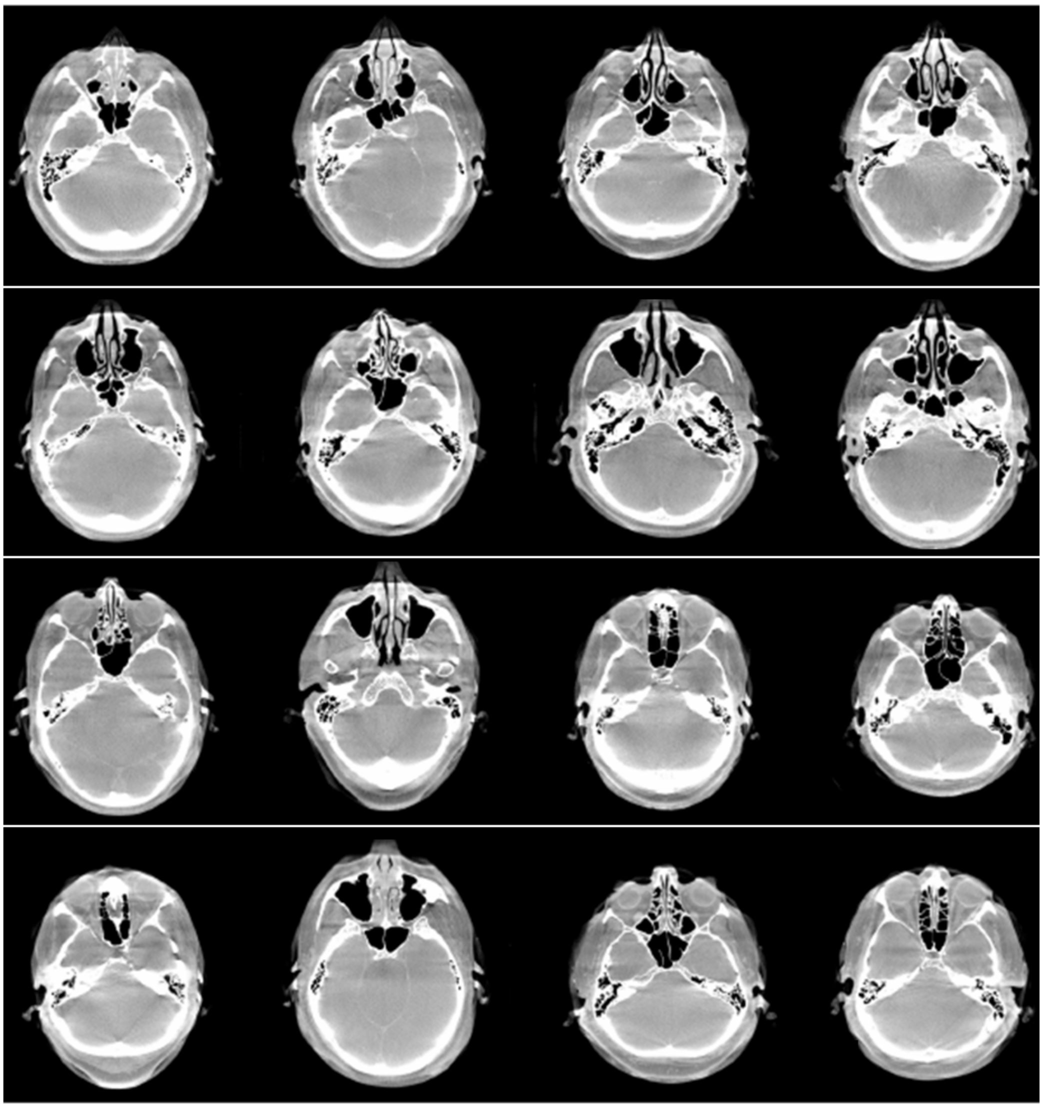

Figure 7.1: An overview of all 16 clinical datasets that were used for the comparative evaluation.

Forchheim, Germany). The detector dimension is $40 \times 30\,\mathrm{cm}^2$ with a full resolution of 2480×1920 pixels and thus is capable of acquiring the full patient head. All scans were routinely conducted using the typical configuration for head therapy control or complication management: 20-second short scan circular rotation over an angular range of 200°, containing 496 projection images in a 2×2 pixel binning mode (i.e., 1240×960 pixels with 0.308 mm / pixel). The source-isocenter and the source-detector distance of the imaging geometry are about 75 cm and 120 cm, respectively. In the following results, all clinical data sets were reconstructed onto a Cartesian grid ($512 \times 512 \times 350$) with a sampling spacing $\triangle x = \triangle y = \triangle z = 0.4$ mm.

The studied datasets are comprised of 16 different patients with intracranial aneurysms treated using either flow-diverter devices or stents. These acquisitions were acquired without contrast medium, immediately after stent or flow-diverter placement to examine parenchymal enhancement. Figure 7.1 gives an overview of transversal slice reconstructed from all acquired datasets. It can be seen that all pa-

Table 7.1: Definition of the four centered FOV sizes in the projection domain and the associated volume of interest size in the volume domain.

	Scan FOV [px^2]	Scan FOV [cm^2]	VOI [px^2]	VOI [cm^2]
ROI 1	580×580	17.8×17.8	d:280 × h:280	d:11.2 × h:11.2
ROI 2	480×480	14.7×14.7	d:230 × h:230	d:9.2 × h:9.2
ROI 3	380×380	11.6×11.6	d:180 × h:180	d:7.2 × h:7.2
ROI 4	280×280	8.62×8.62	d:130 × h:130	d:5.2 × h:5.2

tients were approximately aligned inside the FOV, which potentially reduces outlier occurrence when designing a uniform evaluation framework on the large datasets. Also, no actual truncation is observed on these datasets. This allows us to generate the associated reference images for quantitative image quality assessment.

7.1.2 Truncation Simulation

The strategy used to evaluate the proposed algorithms in Chapter 4 to Chapter 6 was to truncate clinical projection data virtually. We simulate the transaxial and axial data truncation by cutting off a specific number of detector columns and rows from the fully measured clinical data, depending on the ROI size and position. The benefit of using this virtual collimation is two-fold: First, this allows that corresponding non-truncated FDK reconstructions are always available for comparison; Second, this avoids introducing different levels of physical effects, such as X-ray scatter or polychromatic effects in the projection, which make a direct quantitative comparison impossible.

To quantify the impact of different truncation types on the proposed algorithms, we design two groups of the collimation involving overall eight different types of simulated truncation. The first group consists of several centered ROI cases, in which we virtually cropped the non-truncated projection data to four different degrees, as shown in Fig. 7.2. We denote these centered ROIs as ROI 1 ($17.8\,\mathrm{cm} \times 17.8\,\mathrm{cm}$), ROI 2 ($14.7\,\mathrm{cm} \times 14.7\,\mathrm{cm}$), ROI 3 ($11.6\,\mathrm{cm} \times 11.6\,\mathrm{cm}$) and ROI 4 ($8.62\,\mathrm{cm} \times 8.62\,\mathrm{cm}$), respectively. An overview of the configuration parameters in the centered ROI group is presented in Table 7.1.

In the second group, four off-centered ROIs with different positions are defined in the volume domain. Due to the fact that the size and shape of patient head may vary from one to another, we define these ROIs using a relative position with respect to each patient outline. Such outline information was created by a binary mask from the central slice of the reference reconstruction volume (non-truncated). As shown in Fig. 7.3, ROI 5, ROI 6 and 8 are defined inside the patient outline with a fixed diameter 52 mm (130 pixels), located at 32 mm (80 pixels), 50 mm (125 pixels) and 32 mm (80 pixels) away from the patient boundary, respectively. The position of ROI 7 is chosen intentionally closer to the patient boundary (24 mm) with a larger diameter (76 mm), such that it also partially contains the patient-air transition. The aim is to investigate how algorithms perform in such partially truncated data, in which either only the left portion or the right portion of the projection image is truncated.

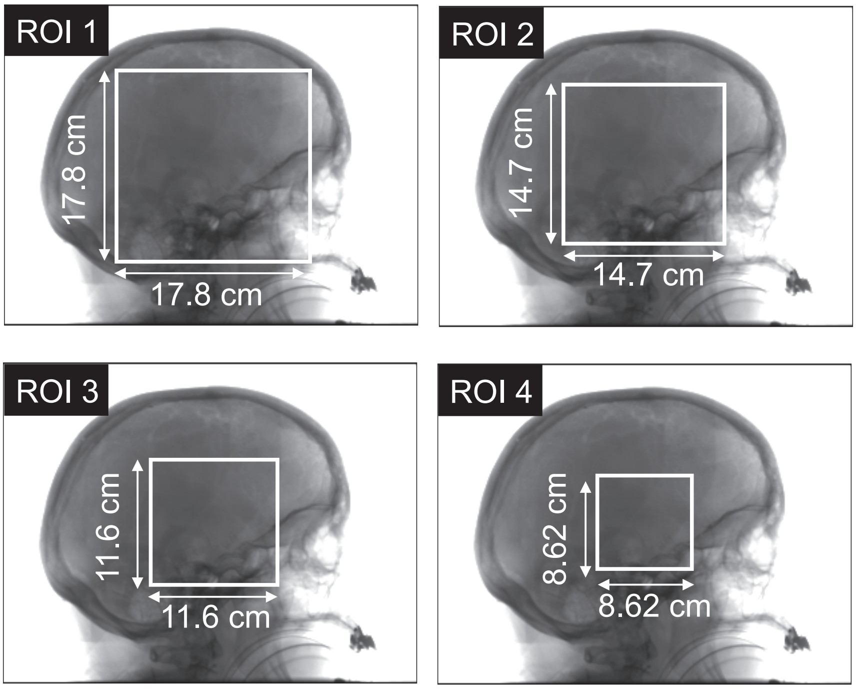
ROI 1
17.8 cm
17.8 cm
ROI 2
14.7 cm
14.7 cm
ROI 3
11.6 cm
11.6 cm
ROI 4
8.62 cm
8.62 cm

Figure 7.2: Illustration of the four centered ROI/FOVs used in the evaluation. The virtual collimation for these four centered ROIs was simulated by cutting off a specific number of detector columns and rows in the projection domain.

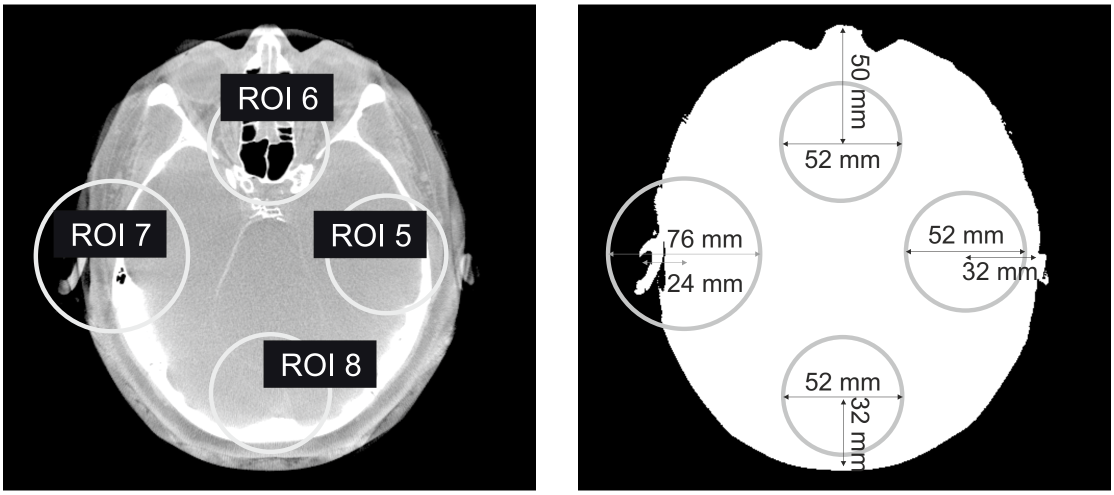
ROI 6
ROI 7
ROI 5
ROI 8
50 mm
52 mm
76 mm
24 mm
52 mm
32 mm
52 mm
32 mm

Figure 7.3: Illustration of the four off-centered ROIs used in the evaluation. These ROIs are defined in the volume domain and then the corresponding truncation windows are calculated using projection matrices.

Once the ROIs are defined in the volume domain, we re-project the ROI boundaries to obtain the associated FOV in the projection domain and perform virtual collimation as the centered case. Note that here we actually simulate asymmetric collimation. That means dependent on the location of the ROI, the position of truncation window may vary from one projection to the other. If the target ROI was repositioned through an isocentering procedure, then symmetric collimation can be applied.

7.1.3 Image Quality Metrics

To quantify reconstruction accuracy achieved by the proposed algorithms, two quantitative metrics were used in this thesis. The first image quality metric, the root mean squared error (RMSE), was measured within the entire 3D ROI as:

$$\mathrm{RMSE}(f(\mathbf{x}), f^{(\mathrm{Ref})}(\mathbf{x})) = \sqrt{\frac{1}{N}\sum_{\mathbf{x}\in\Omega}(f^{(\mathrm{Ref})}(\mathbf{x}) - f(\mathbf{x}))^2}, \tag{7.1}$$

where $f^{(\mathrm{Ref})}(\mathbf{x})$ represents the reference FDK volume reconstructed from non-truncated data, $f(\mathbf{x})$ represents the evaluated reconstructed volume from virtually truncated data, N indicates the number of voxels within the investigated ROI and Ω indicates the domain of the volume of interest.

As addressed in Section 1.1.3, a particular interest of C-arm based 3D ROI imaging is to identify low-profile micro-devices, such as flow-diverters or stents. Thus, accurate restoration of the structural information seems more relevant than attenuation coefficients or Hounsfield unit (HU) values. Besides, incorrect attenuation coefficients and HU values caused by a scaling/bias can also be compensated for in the volume domain by manual re-windowing. The second metric, correlation coefficient, would deliver the more useful quantitative information for this need. It is defined as the covariances of the two variables divided by the product of their individual standard deviations:

$$\mathrm{CC}(f(\mathbf{x}), f^{(\mathrm{Ref})}(\mathbf{x})) = \frac{\frac{1}{N}\sum_{\mathbf{x}\in\Omega}((f(\mathbf{x}) - \mu)(f^{(\mathrm{Ref})}(\mathbf{x}) - \mu_{\mathrm{Ref}})}{\sqrt{\frac{1}{N}\sum_{\mathbf{x}\in\Omega}(f(\mathbf{x}) - \mu)^2}\sqrt{\frac{1}{N}\sum_{\mathbf{x}\in\Omega}(f^{(\mathrm{Ref})}(\mathbf{x}) - \mu_{\mathrm{Ref}})^2}}, \tag{7.2}$$

where μ and μ_{Ref} denote the mean values of $f(\mathbf{x})$ and $f^{(\mathrm{Ref})}(\mathbf{x})$. The resulting value ranges from -1 to +1. Large positive values represent good agreement in terms of correlation.

7.1.4 Standard FDK Reconstruction

The standard FDK reconstruction [Feld 84] of non-truncated data is used as the reference for both the qualitative and quantitative evaluation in each clinical case. It is also interesting to see how the FDK algorithm performs on truncated data from the evaluated datasets. Figure 7.4 shows correlation coefficients of FDK reconstruction directly from truncated clinical data on the investigated ROIs. The results confirm that the direct application of FDK on truncated data will dramatically degrade image

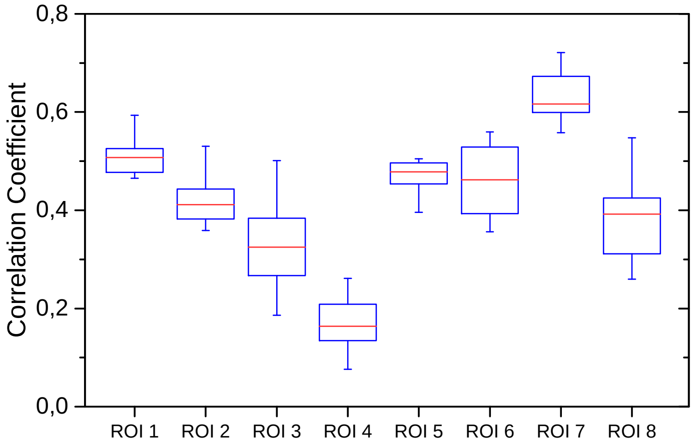

Figure 7.4: Summary of the quantitative evaluation of FDK from virtually truncated data through eight ROIs.

quality, which is reflected by fairly low average values of the correlation coefficient. Note that the image quality degradation increases with higher levels of data truncation. In addition, reconstructions from partially truncated data yield a relatively high accuracy due to less truncation in the transaxial direction.

7.2 ATRACT Specific Evaluation and Parametrization

The ATRACT algorithm that requires neither prior knowledge nor explicit extrapolation is suitable for any clinical workflow and thus can be considered as a baseline reconstruction. In this section, we present ATRACT specific evaluation and parametrization, in which the original 2D Radon-based ATRACT, 2D convolution based ATRACT (2D ATRACT) as well as 1D ATRACT are compared in terms of both runtime and reconstruction accuracy.

7.2.1 Implementation Details

This subsection describes the details of the implementation of the ATRACT algorithm. The Laplace operation was computed using the finite difference method with either a 3×1 kernel (1D Laplace) or a 3×3 kernel (2D Laplace) and thus filtering can be efficiently performed in the spatial domain. The convolution-based residual filtering was achieved using FFT in the Fourier domain. The kernel size was determined by the effective FOV size in the first projection: we chose the next power of 2 from the larger dimension of the FOV. Once the size was determined, the convolution kernel was created and applied to all projection images. To avoid singularities in the central values of the kernels, we estimated the central values by computing the mean value at $(u = \pm 0.1, v = \pm 0.1)$ in 2D ATRACT and $u = \pm 0.1$ in 1D ATRACT. Reconstruction resolution can be controlled for 2D/1D ATRACT by applying a Gaussian distribution function on the convolution kernel. For the evaluation, the resolution was matched by computing the modulation transfer functions (MTF) of the 2D/1D

ATRACT reconstructions and the FDK reconstruction with a Shepp-Logan filter using a simulated bead phantom (created by DRASIM, Siemens Healthcare GmbH, Forchheim, Germany). We applied the offset correction proposed in Eq. (4.25) and chose one of the investigated clinical datasets as the reference to calibrate the model coefficients. Note that for all evaluations the parameters were determined only once using this reference.

7.2.2 Computational Performance

An open-source reconstruction benchmark framework (RabbitCT [Rohk 09]) was employed to analyze the computational efficiency of the proposed methods. In this framework, the reconstruction performance is evaluated using a specific high-resolution dataset of a rabbit, which was acquired at the Department of Neuroradiology, University of Erlangen, Germany.

The execution time spent on processing all 496 projections with ATRACT algorithms was measured, and compared to that of a standard CPU based ramp filtering operation. Note that the Radon-based filtering in the original ATRACT used 1024 angular and 1024 of radial samples in Eqs. (4.10) and (4.11), so as to match the spatial resolution.

The runtimes of the filtering process for each of the algorithms are shown in Fig. 7.5 (top). A more comprehensive comparison is represented in Fig. 7.5 (bottom) by using speed-up factors with respect to the 2D Radon-based ATRACT.

As expected, the 2D Radon-based implementation of ATRACT filtering is very time-consuming (computation time is 25110 ± 116 s) due to the penalty of enormous interpolations in the non-local operation. The 2D ATRACT method, which uses an analytically derived 2D Cartesian kernel and FFT-based convolution, reduces runtime to 2.2% of the original version. 1D ATRACT delivers optimal computational performance, achieving an additional 5.5 times speed-up with respect to 2D ATRACT due to less computational complexity and avoidance of additional padding. We found that the 1D ATRACT filtering is only 10% slower than the ramp filtering, because it has only one additional pre-filtering step — the Laplace filtering, which is computationally inexpensive.

Further improvement in computational performance is gained by using a high-parallel graphic processing unit (GPU), the NVIDIA Quadro FX 5800. GPU versions (implemented using CUDA 4.0) of the three ATRACT methods generally reduce the runtimes to 5-6% of their CPU versions. It should be noted that the GPU version of the 2D Radon-based ATRACT is 60 times faster than its CPU version, due to the beneficial utilization of texture memory which is able to implicitly handle fast linear and bi-linear interpolations.

7.2.3 Image Quality Assessment

In this subsection we present evaluation results for both 1D ATRACT and 2D ATRACT that include visual inspection of image quality as well as quantitative analysis. The original 2D Radon-based ATRACT is mathematically identical to the 2D convolution-based ATRACT method, yielding the same robustness with respect

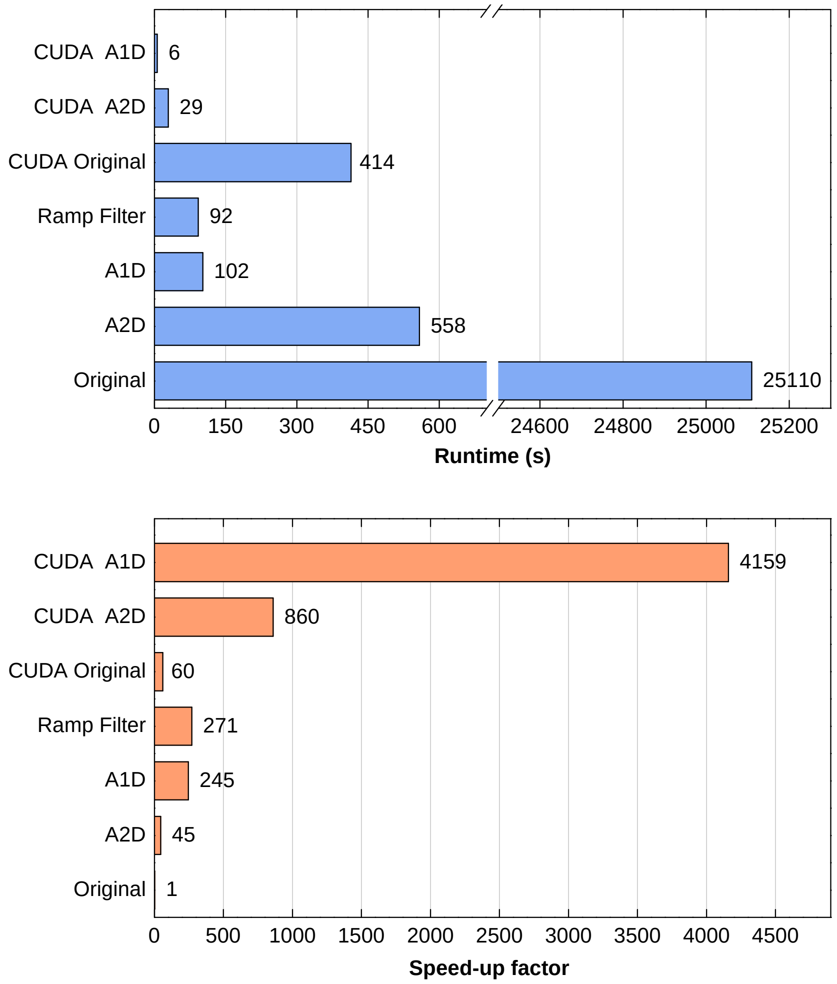

Figure 7.5: Runtime (top) and speed-up factor (bottom) of filtering 496 projections (1240 × 960) for each algorithm. "Original" indicates the direct implementation of the Radon-based filtering in the original ATRACT algorithm. "A1D" and "A2D" represent the CPU implementations of 1D ATRACT and 2D ATRACT, respectively. The results of corresponding GPU implementations of these algorithms are also presented. A NVIDIA Quadro FX 5800 was used for GPU implementations, CUDA version 4.0. CPU implementations were based on a single-threaded Intel® Xeon X5570.

to data truncation and hence will not be evaluated here. Note that even with the offset correction, accurate reconstruction of the attenuation coefficient is not always guaranteed (particularly in off-centered ROI cases). For a better quantitative interpretation, in this subsection we only present results evaluated using the correlation coefficient. For the associated RMSE results, we refer to the complete comparative evaluation in Section 7.5.2. In the following, we first start by analyzing the four centered ROI cases, followed by the off-centered truncation scenarios.

Centered ROI Case

We start with the visual assessment of image quality. First, the transversal, sagittal and coronal slices of a reconstructed volume from the medium truncated data (ROI 2) are depicted in Figs. 7.6 and 7.7, respectively. It can be seen that the straightforward application of FDK on truncated data suffers from the typical cupping artifacts manifesting as a radial gradient in the presented slices. The artifacts become increasingly stronger close to the truncation edge and mask the actual intensity of anatomical structures, as indicated by the gray arrows. In contrast, both ATRACT methods are able to effectively reduce truncation-induced cupping artifacts and yield visually identical image quality compared with that of the reference reconstruction from complete data. This indicates that the two-step filtering clearly outperforms the conventional one-step ramp filtering in the presence of data truncation.

Figure 7.8 depicts an example of the most severe truncation cases (ROI 4). For this visual inspection, we particularly chose a narrow grayscale window [-200HU, 400HU], which allows us to assess the capability of the proposed algorithms to restore the homogeneous soft tissue. Surprisingly, we found that even in this challenging case, both 1D ATRACT and 2D ATRACT still maintain reconstructions of high quality. No noticeable truncation artifacts are observed inside the ROI and the results are visually comparable to the FDK full data reconstruction in terms of the resolution and noise.

In addition to visually inspecting the reconstructed images, we also quantify reconstruction accuracy using the correlation coefficient. An overview of the quantitative comparison of the 1D ATRACT and 2D ATRACT algorithms using all 16 clinical datasets on the four centered ROI cases are presented in Fig. 7.9. Consistent with qualitative analysis, in general both methods are able to produce the ROI reconstructions of high accuracy, which is reflected in high correction coefficients of up to 0.98 for 1D and 0.97 for 2D ATRACT. This implies that the structural information within the ROI was nicely restored. As expected, the average values and the standard deviations of the correlation coefficient are clearly superior over the uncorrected FDK reconstructions (see Fig. 7.4).

It is also interesting to see that the 1D ATRACT and 2D ATRACT algorithms respond similarly to the four different centered ROIs, although 2D ATRACT is slightly better than its 1D counterpart in some cases. Moreover, from quantitative results, we found a phenomenon that with increasing degree of data truncation, image quality gradually degrades, accordingly. This particularly applies for ROI 2, 3 and 4. The phenomenon is also in good agreement with the observation from the investigation of explicit extrapolation schemes [Hsie 04, Hopp 08]. However, this observation does not apply to ROI 1, in which both 1D ATRACT and 2D ATRACT appear even slightly

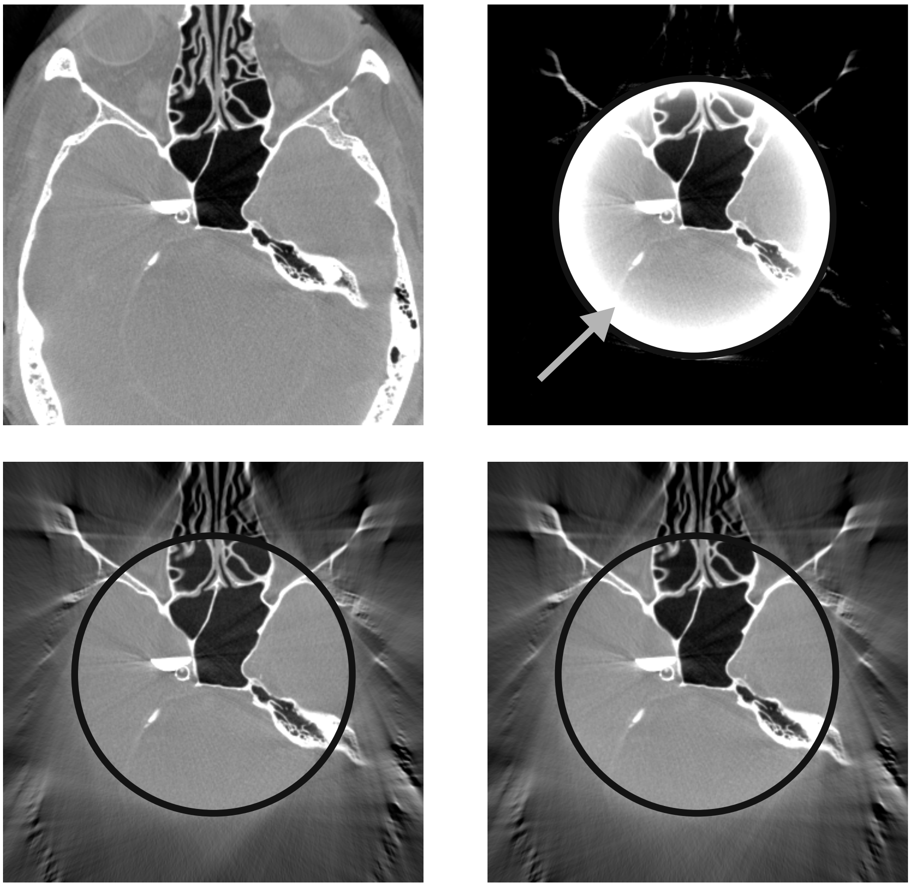

Figure 7.6: Transversal slice through the reconstruction results of different algorithms, in the grayscale window [-1000 HU,1000 HU]. Top left: FDK reference reconstruction from non-truncated data; Top right: FDK reconstruction from truncated data; Bottom left: 1D ATRACT reconstruction from truncated data; Bottom right: 2D ATRACT reconstruction from truncated data.

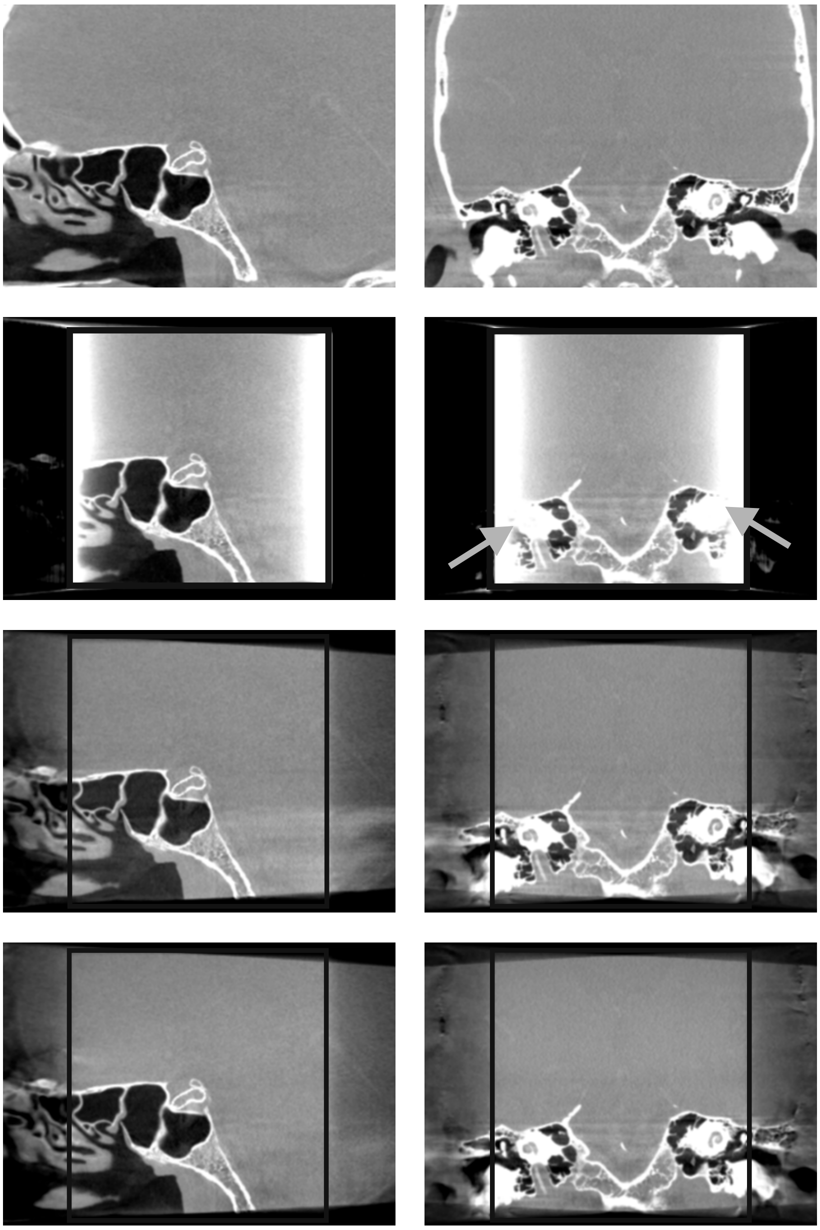

Figure 7.7: Sagittal and coronal slices through the reconstruction results of different algorithms, in the grayscale window [-1000 HU,1000 HU]. From top to bottom: FDK reference reconstruction from non-truncated data, FDK reconstruction from truncated data, 1D ATRACT and 2D ATRACT reconstruction from truncated data.

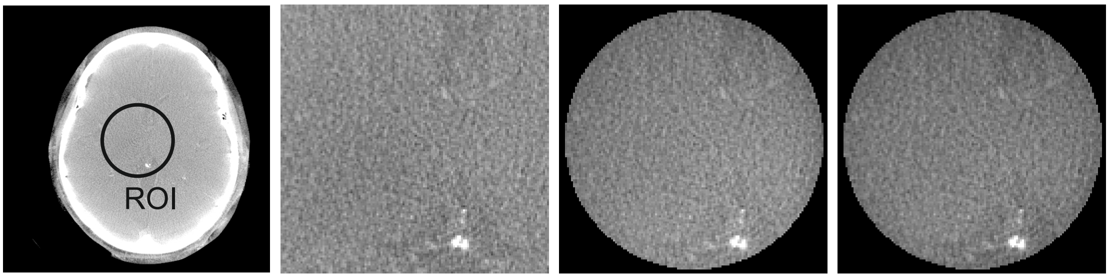

Figure 7.8: Transversal slices through the ATRACT results of a clinical dataset, in the grayscale window [-200 HU, 400 HU]. From left to right: FDK reference reconstruction from non-truncated data, zoom-in FDK reference reconstruction, 1D ATRACT based ROI reconstruction and 2D ATRACT based ROI reconstruction. The regions outside the FOV are indicated in black.

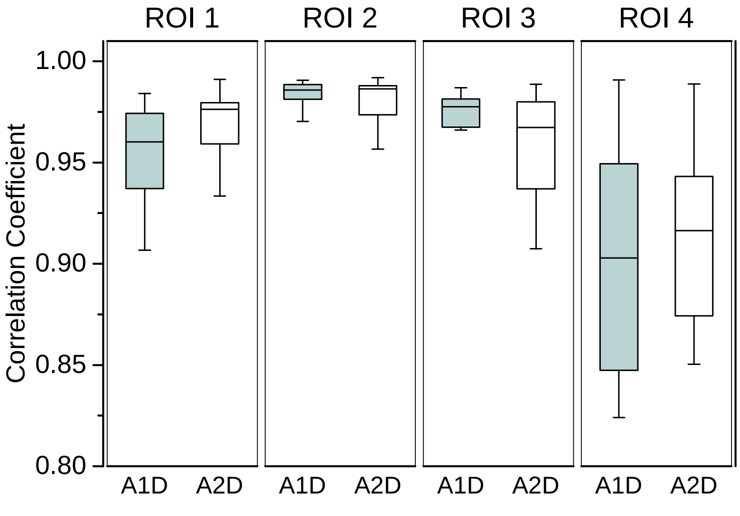

Figure 7.9: Summary of the quantitative evaluation of the 1D ATRACT and 2D ATRACT algorithms for the four centered ROI cases. Note that the given correlation coefficients are computed over all 16 clinical datasets.

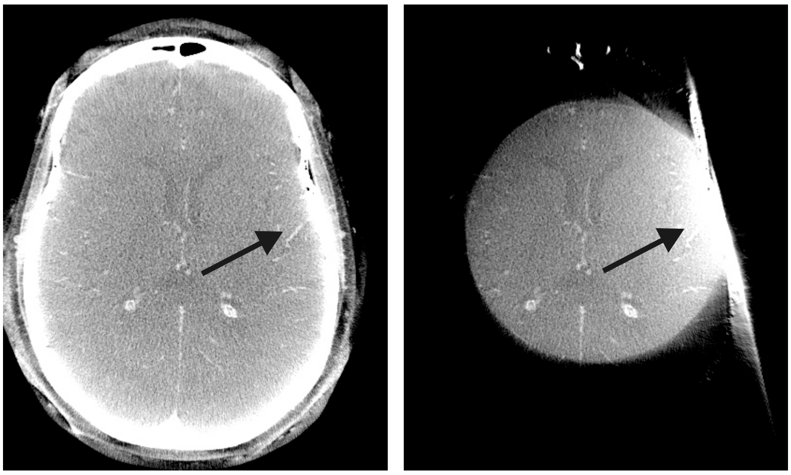

Figure 7.10: Illustration of the edge gradient artifact in ATRACT reconstruction. Left: FDK reference reconstruction from non-truncated data; Right: 2D ATRACT based ROI reconstruction.

inferior to the results from ROI 2. We observed that this degradation in ROI 1 occurs in the case when a significant dense object (e.g., skull in this case) is truncated in the transaxial direction. This is a typical behavior for data extrapolation schemes (we consider ATRACT as an implicit extrapolation scheme) since the continuation assumption which these methods reply on is violated because of confounding high dense objects at the truncation edge. Figure 7.10 illustrates such an edge gradient artifact that manifests as a noticeable intensity increase at the position where the skull bone is truncated.

Off-centered ROI Case

In off-centered ROI cases, we additionally investigated the performance of the corresponding ATRACT algorithms with the gradient compensation (denoted as ATRACT Plus below). Figure 7.11 visually demonstrates the effectiveness of the associated ATRACT Plus algorithms. The reconstructed coronal slices are selected from an example of clinical datasets on ROI 7. The slices are displayed using a narrow grayscale window to emphasize image gradient. As expected, due to asymmetric collimation a ramp/gradient is introduced in the ATRACT filtered projections and further propagates in the reconstructed volume, if no effective counter-measure is performed. Figure 7.11 (second row) and (third row) clearly indicates the gradient-like artifact that unbalances the intensity of the homogeneous region between left boundary (higher) and right boundary (lower). On the other hand, the corrected ATRACT Plus algorithms robustly reduce this gradient artifact and yield the improved results that are closer to the reference image; see Fig. 7.11 (fourth row) and (last row). Profiles through the presented slices are given in Fig. 7.12 for a quantitative comparison between these algorithms, which basically confirm our observation.

Quantitative results of the investigated algorithms are provided in Fig. 7.13. We found that the ATRACT Plus methods achieve higher accuracy in ROI 5 and ROI 7. Particularly for ROI 7, in which the partial data truncation is applied, the average

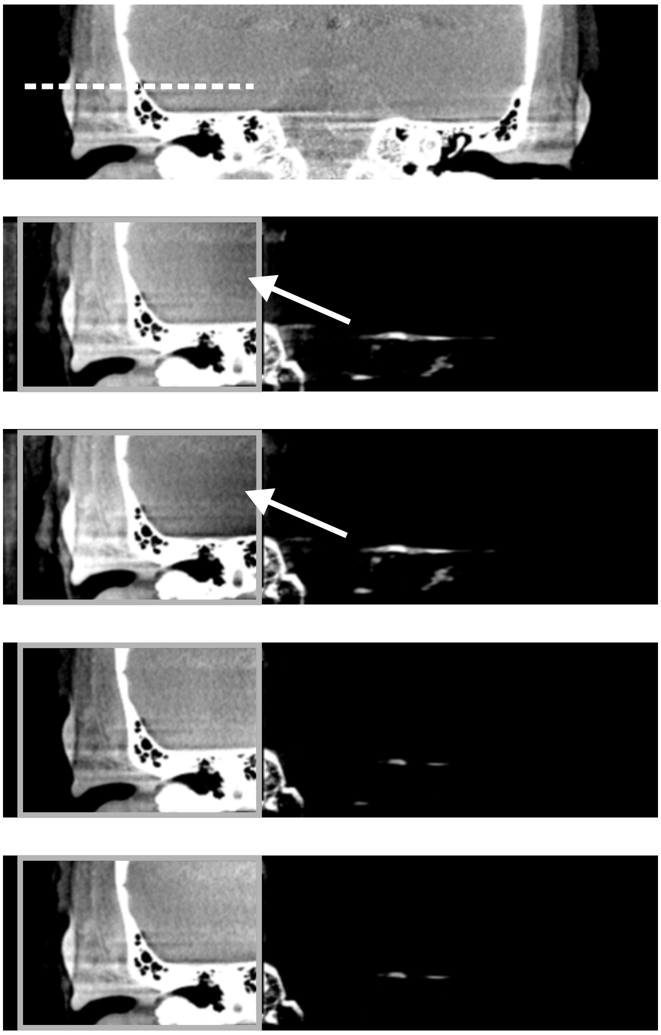

Figure 7.11: Coronal slices through the reconstruction results of different algorithms, in the grayscale window [-400 HU, 400 HU]. From top to bottom: FDK reference reconstruction from non-truncated data, 1D ATRACT, 2D ATRACT, 1D ATRACT Plus and 2D ATRACT Plus based ROI reconstructions. Reconstructed values along the central profiles indicated as a dashed-white line are given in Fig. 7.12.

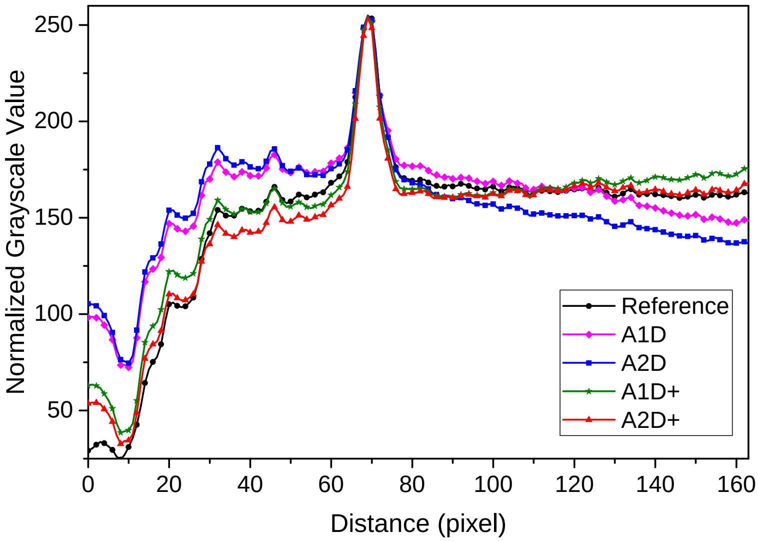

Figure 7.12: Comparison of the central profiles indicated as a dashed-white line in Fig. 7.11.

value and standard deviation of the correlation coefficient improve substantially, for instance for 2D ATRACT, from 0.93 ± 0.02 to 0.98 ± 0.01. These results suggest that the further improvement of reconstruction accuracy could be obtained, if the gradient appears large in the truncated projections.

For ROI 6 and 8, where the slope between two sides of the projection is less steep (since head's frontal length is typically smaller than its lateral width), an only subtle difference is observed between ATRACT with and without gradient correction. Furthermore, 2D ATRACT in general shows better reconstruction results than 1D ATRACT in off-centered cases. This can be explained by the benefit of its 2D filtering that is performed for all detector elements simultaneously. This reduces outliers that may be caused by individual 1D processing of detector lines.

7.3 SSR Specific Evaluation and Parametrization

While the shutter scan reconstruction (SSR) acquires information of both the ROI and PR, it requires a relatively low additional radiation dose to the patient. In this section, the three proposed reconstruction algorithms that are tailored for the shutter scan acquisition are comparatively evaluated on both the ROI and PR. For convenience, in the following we refer to these methods as the SSR-A, SSR-B and SSR-C method, corresponding to the joint weighted FDK/ATRACT method, the simple parallel volumetric combination and prior image driven detruncation method, respectively.

7.3.1 Implementation Details

The SSR-B and SSR-C methods involve an iterative wTV minimization [see Eq. (5.2)] to restore an initial image from a small number of non-truncated projections. This

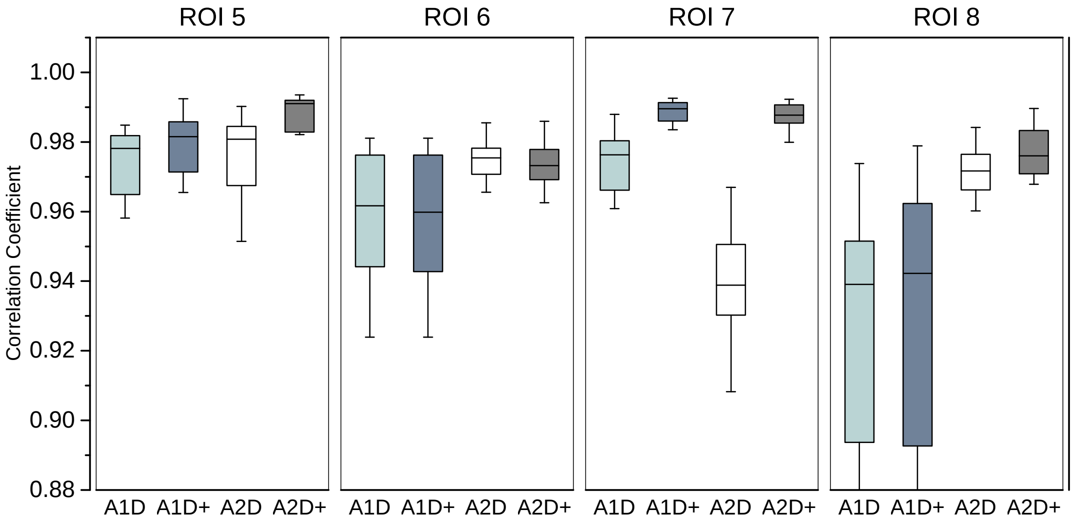

Figure 7.13: Summary of the quantitative evaluation of the 1D ATRACT/1D ATRACT Plus, 2D ATRACT/2D ATRACT Plus algorithms for the four off-centered ROI cases. Note that the given correlation coefficients are computed over all 16 clinical datasets.

wTV method follows the conventional iterative TV minimization framework, in which each iteration basically consists of a general iterative reconstruction (i.e., SART), followed by a steepest descent TV minimization. In order to accelerate the convergence speed, an ordered subset (OS) method [Huds 94] was applied in the SART method. The total 496 projections in one SART iteration are partitioned into ten subsets. The initial image was set to zero. After the SART update, a positivity constraint is applied to remove the negative pixel values, which corresponds to the projection over convex sets approach [Sidk 08]. Also, we found that a proper number of the TV iterations can get a balance between data fidelity and image smoothness. In this evaluation, eight iterations of TV gradient descent are performed in each inner iteration. At each TV gradient descent iteration, we first calculate the wTV gradient as follows

$$\begin{aligned}
&\frac{\partial \sum_{x,y,z=1}^{N_x,N_y,N_z} \omega_{x,y,z} \|\nabla f_{x,y,z}\|}{\partial f_{x,y,z}} \\
&\approx \omega_{x,y,z} \frac{3f_{x,y,z} - f_{x-1,y,z} - f_{x,y-1,z} - f_{x,y,z-1}}{\sqrt{\varepsilon + (f_{x,y,z} - f_{x-1,y,z})^2 + (f_{x,y,z} - f_{x,y-1,z})^2 + (f_{x,y,z} - f_{x,y,z-1})^2}} \\
&- \omega_{x+1,y,z} \frac{f_{x+1,y,z} - f_{x,y,z}}{\sqrt{\varepsilon + (f_{x+1,y,z} - f_{x,y,z})^2 + (f_{x+1,y,z} - f_{x+1,y-1,z})^2 + (f_{x+1,y,z} - f_{x,y,z-1})^2}} \\
&- \omega_{x,y+1,z} \frac{f_{x,y+1,z} - f_{x,y,z}}{\sqrt{\varepsilon + (f_{x,y+1,z} - f_{x-1,y+1,z})^2 + (f_{x,y+1,z} - f_{x,y,z})^2 + (f_{x,y+1,z} - f_{x,y+1,z-1})^2}} \\
&- \omega_{x,y,z+1} \frac{f_{x,y,z-1} - f_{x,y,z}}{\sqrt{\varepsilon + (f_{x,y,z+1} - f_{x-1,y,z+1})^2 + (f_{x,y,z+1} - f_{x,y-1,z+1})^2 + (f_{x,y,z+1} - f_{x,y,z})^2}},
\end{aligned} \tag{7.3}$$

where $f_{x,y,z}$ denotes the value in f assigned to the voxel with index (x, y, z) and $\varepsilon = 0.1$. After obtaining the wTV gradient, we normalize it by the maximal value. Next, we use a backtracking line search algorithm [Boyd 04] to find the proper step size to ensure the minimization. After all TV iterations, the weight matrix $\omega(\mathbf{x})$ is updated according to Eq. (5.3). More importantly, we observed that ϵ in Eq. (5.3) noticeably influences the reconstructed image quality. It typically lies in the range of $[0.0001, 0.1]$. In this evaluation, we empirically chose $\epsilon = 0.001$.

The wTV volume in the second method was reconstructed in a Cartesian grid of $512 \times 512 \times 350$ with a sampling spacing $\triangle x = \triangle y = \triangle z = 0.4$ mm. For the third method, wTV was used to generate an initial volume with a size of $256 \times 256 \times 256$ with a spacing $\triangle x = \triangle y = \triangle z = 1$ mm. To handle truncated data encountered in the SSR-A and SSR-B approaches, 1D ATRACT is used to generate the associated ROI volume.

To assess how image quality depends on the sparsity level of full projections, we define three full projection ratios, which contain 10, 50 and 100 non-truncated projections, respectively.

7.3.2 Image Quality Assessment

In this subsection, we present the evaluation results of the three shutter scan reconstruction algorithms in both qualitative and quantitative manner. We follow the same outline as before, by first visually assessing the reconstruction results, followed by quantitative analysis.

The visual inspection relates to the images shown in Figs. 7.14, 7.15 and 7.16. Figure 7.14 exemplarily depicts the reconstructions of all three approaches from one patient data. The projection data consists of 100 non-truncated projections and 396 truncated projections with a scan FOV of 8.62 cm × 8.62 cm (ROI 4). Together with a closer investigation of Region 1 and 2 shown in Fig. 7.15, we observe that the overall reconstruction results of all methods are visually close to the reference within the ROI but appear to be fairly different in the PR. The SSR-A and SSR-B methods adopt ATRACT to handle data truncation and thus effectively reduce the truncation-induced cupping artifact within the ROI. In the PR of the SSR-A method, although suffering from severe streaking artifacts (due to the straightforward application of analytic FDK on the sparse projection data), fine details of high contrast regions (e.g., bones) are well preserved; see Region 2. This is also partially because when backprojecting the two separate sets of projections into a single volume, the PR obtains additional information from the truncated projections. In contrast, the SSR-B approach yields less streaking artifacts in the PR. However, an overall smooth appearance is observed as a side effect of the TV regularization. This affects low contrast as well as high contrast objects in the PR.

The SSR-C method yields the most visually comparable result to the reference reconstruction within the ROI. Also, the transition between the ROI and PR is well handled, suggesting the projection-based transition smoothing seems more efficacious than the transition smoothing in the volume domain. Regarding the PR, it shows a compromised result between the other two approaches. However, due to the initial

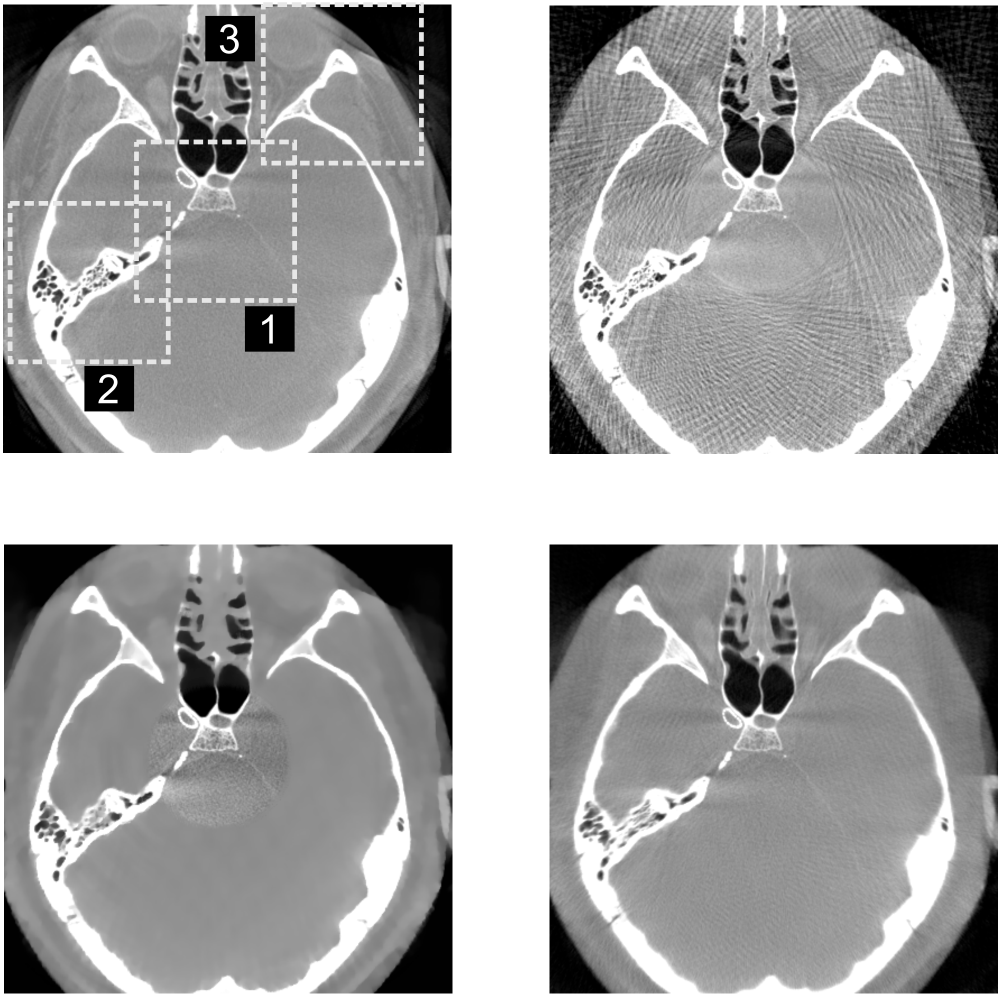

Figure 7.14: Reconstructions of all three SSR approaches from a simulated shutter scan data that consists of 100 non-truncated projections with a full FOV and 396 truncated projection with a scan FOV of 8.62 cm × 8.62 cm (ROI 4). (Top-left): reference reconstructed from non-truncated data, (top-right) the SSR-A approach, (bottom-left) the SSR-B approach and (bottom-right) the SSR-C approach.

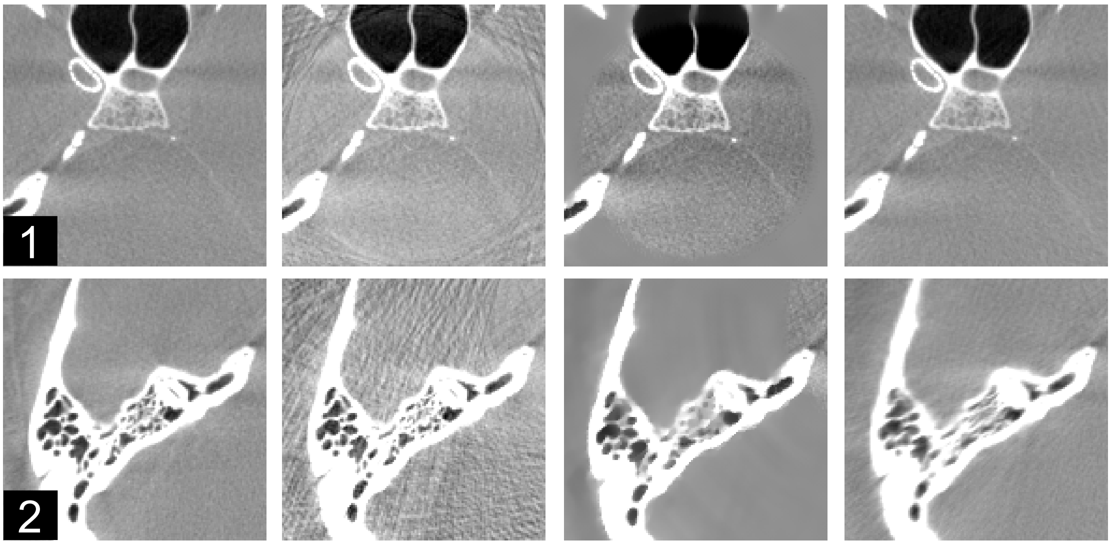

Figure 7.15: A close investigation of Region 1 (ROI) and 2 (PR) shown in Fig. 7.14. From left to right: the reference, the SSR-A, SSR-B and SSR-C approach.

wTV volume, the SSR-C method also yields a smooth appearance of the PR, with a structural information loss.

Figure 7.16 demonstrates how image quality of the PR degrades with decreasing full projection ratio. From top to bottom row, the non-truncated projection numbers are 100, 50 and 10, respectively. With 100 non-truncated projections, we can see that all methods are in line with the previous observation. However, when the non-truncated projection ratio decreases, e.g. to 50, the strength of streaking artifacts increases noticeably in the SSR-A approach but slightly in other two methods. In the case of only ten non-truncated projections, the SSR-A approach yields the worst image quality: almost no details of the soft tissue are preserved and visual inspection of image content seems difficult. The SSR-B approach, although yields less streaking than the SSR-A approach, suffers from a severe oversmooth effect and information loss. Contrary to these observations is the result from the SSR-C method, which appears in the robustness of image quality with respect to both the low and high contrast structure restoration in a low full projection ratio.

A quantitative assessment of all these algorithms with three full projection ratios (10, 50 and 100) is summarized in Fig. 7.17. The evaluation was conducted for the four centered ROI cases and image quality was analyzed in both the ROI and PR. The obtained metric values within the ROI quantitatively confirm our previous visual observations (the first two rows of Fig. 7.17). The SSR-C method achieved the best image quality in all ROI cases. The correlation coefficients remain stable even when the full projection ratio decreases. The value drops only marginally below 0.99 when the non-truncated projection number drops to 10. Since the SSR-B method is a simple volumetric combination between ATRACT and wTV, it yields a similar behavior to the ATRACT performance within the ROI. Also, note that it does not rely on the sparsity level since the truncated projections are handled independently. The performance of the SSR-A approach rapidly drops with decreasing number of full projections. It is interesting to see that at a low full projection ratio, the first

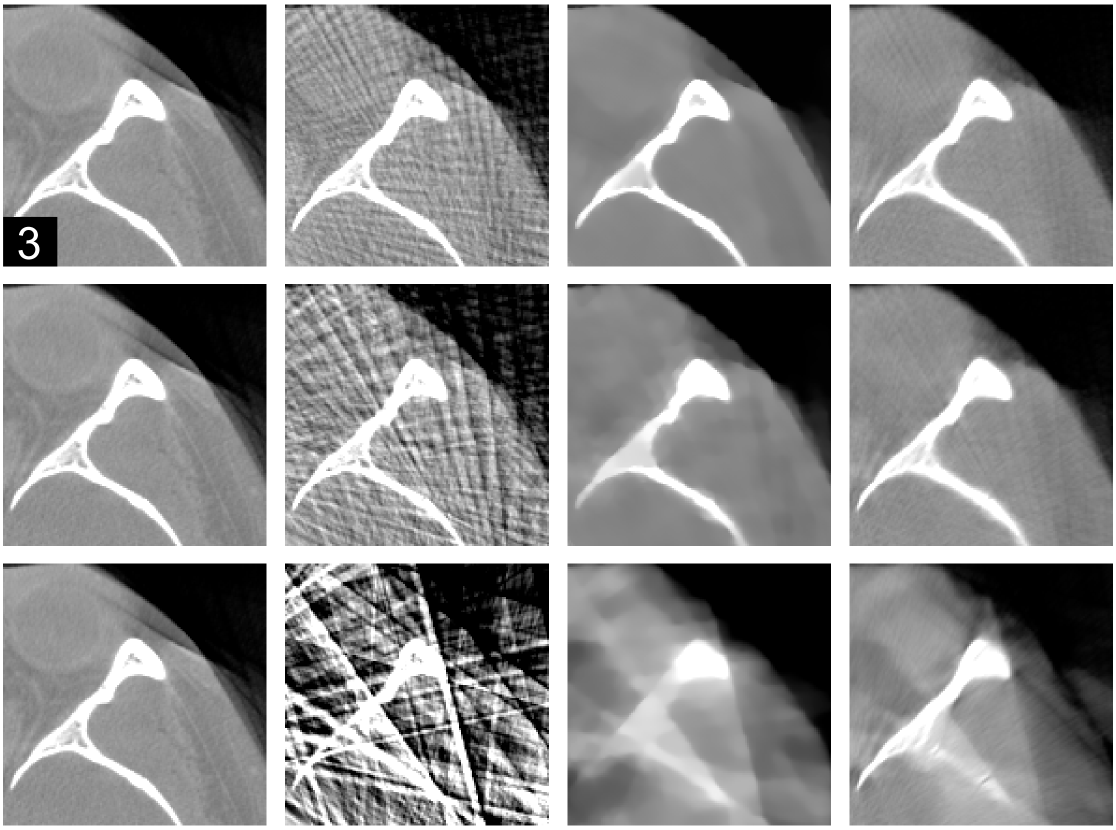

Figure 7.16: Illustration of the degradation of image quality in the PR for each of the considered methods with gradually decreasing of full projection ratio. The first row to the last row show the results of the three methods using 100, 50 and 10 non-truncated projections, respectively. From left column to right column: the reference, the SSR-A, SSR-B and SSR-C approach.

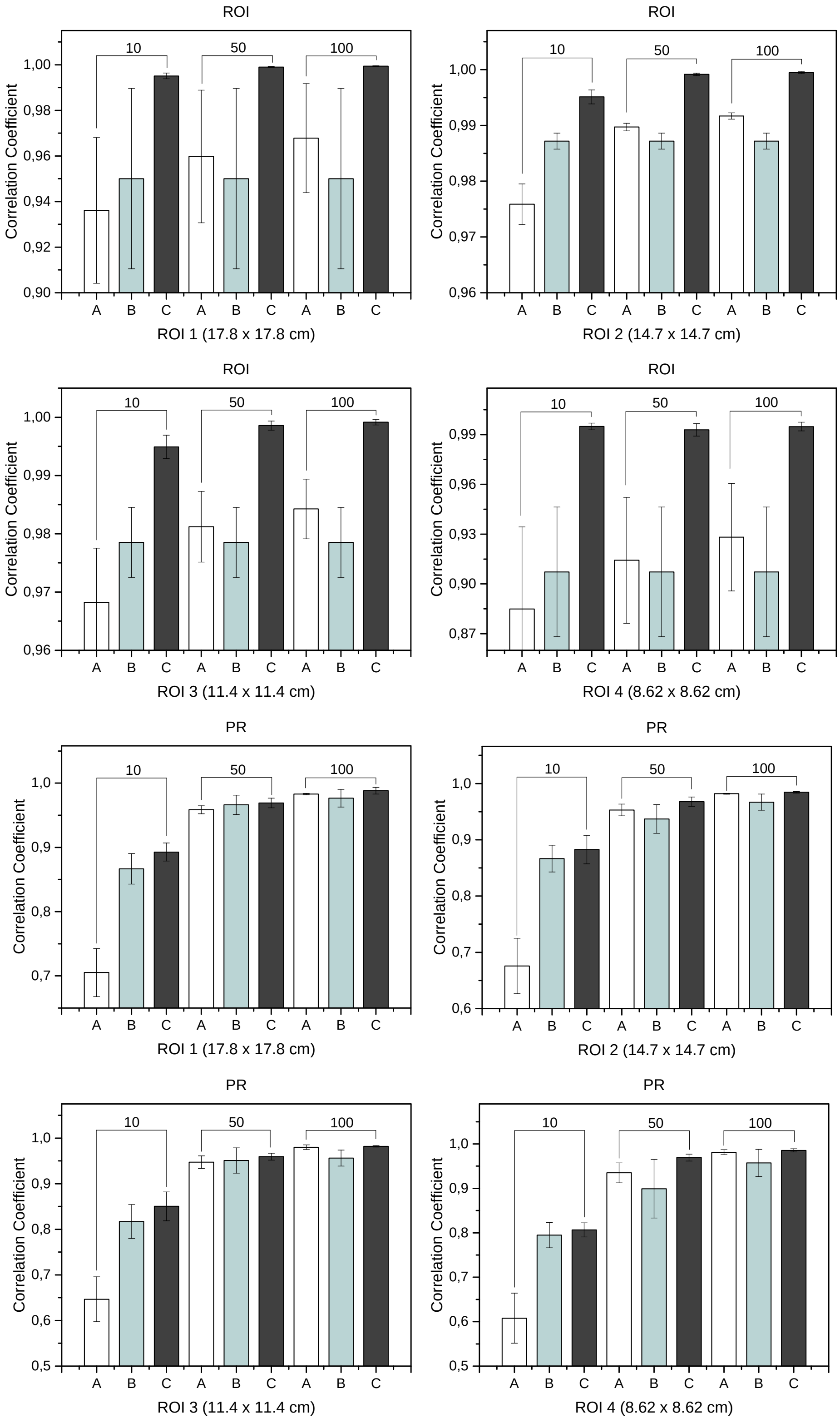

Figure 7.17: A summary of the quantitative assessment of three SSR algorithms with three full projection ratios (10, 50 and 100), for the four centered ROI cases (ROI 1-4). The image quality is evaluated in both the ROI and PR. Here, A, B and C denote the SSR-A, SSR-B and SSR-C method, respectively.

approach is even inferior to original ATRACT, although the same method is applied to reconstruct the ROI. This suggests that the projection-based scaling/offset correction appears to be nonlinear in the volume domain and may become cumbersome if the number of reference projections is far from enough.

Although all methods show a sparsity dependency in the quantitative evaluation of the PR, they still differ noticeably. As expected, the SSR-A approach highly depends on the number of full projections. It yields the lowest image quality (a correlation coefficient of about 0.65) in the PR when the number of full projections drops to 10. But it even shows comparable results to that of the SSR-C method, when the full projection number increases to 100. Again, the third method is always superior to the other proposed methods, regardless of the sparsity level and the ROI size. Its advantage is clearly visible at the lowest full projection ratio (a correlation coefficient of up to 0.98), which is consistent with the previous visual assessment. The SSR-B approach always yields an intermediate result and reflects the performance of wTV on sparse-view reconstruction.

7.4 PBE Specific Evaluation and Parametrization

In Chapter 6, a novel patient-bounded extrapolation (PBE) algorithm that improves conventional extrapolation schemes has been presented, based on the estimation of a 3D patient outline model. As input it requires two fluoroscopic images that could be obtained during the isocentering process prior to a 3D run. In this section, the feasibility of this method will be investigated.

7.4.1 Implementation Details

Even though a practical application would involve the extraction of the patient boundaries from low-dose fluoroscopic data, for proof of concept we here confined to extract the boundaries from two projections ($\lambda = -90°$ and $\lambda = 0°$) of a non-collimated 3D scan. The patient outline information was extracted in raw data. The pre-set air/tissue threshold was empirically determined. To enforce the smoothness of the transition region, the measured data and the extrapolation data are combined by a cosine-like smooth weighting function in a predefined transition interval. The length of transition region was set to 1/30 of the effective FOV width. In this evaluation we adapt two state-of-the-art extrapolation schemes, as described in Section 6.3. We denote these new methods as PWCE and PSRE, corresponding to the patient-bounded water cylinder extrapolation and patient-bounded square root extrapolation, respectively.

Suppose the patient outline is exactly known from all projections, instead of only two. This could be potentially realized by deploying an optical tracking system (e.g., 3D range imaging camera) to capture the patient outline and transform the outline into the C-arm coordinate system [Kold 11]. In this manner, the extrapolation scheme could be improved by incorporating a more accurate patient boundary information. We refer to this method as camera-based extrapolation (CBE). In the following evaluation, we simulate this camera-based extrapolation method by ending the extrapolation lines at the boundary position detected from all non-truncated

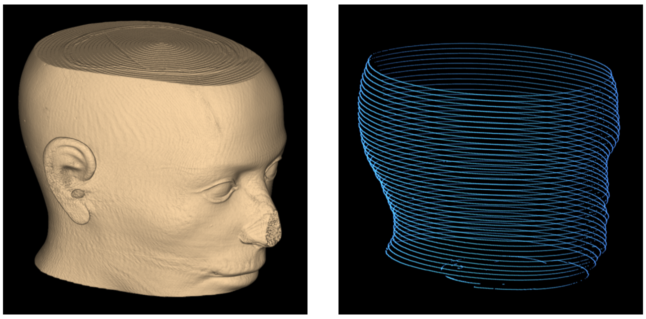

Figure 7.18: Visualization of a head phantom shape extracted from the non-collimated 3D reconstruction (left) and the 3D volumetric model estimated from two orthogonal projections with different ellipses in each slice (right).

projections. Note that this simulation is ideal in a sense that it does not account for some practical issues, e.g., inaccuracies caused by camera occlusions or potential errors that may be introduced by co-registration/calibration of the optical tracking system to the C-arm system.

Moreover, the heuristic water cylinder extrapolation (WCE) proposed by Hsieh *et al.* [Hsie 04] was investigated as a baseline and compared with our proposed algorithms.

7.4.2 Image Quality Assessment

In the following sections, we present evaluation results of both variants of the patient bounded extrapolation proposed in Section 6.3. Note that since reconstruction results of these two variants are almost visually identical, in the visual assessment part we only show the results of the PWCE method.

Patient Outline Estimation

The patient bounded extrapolation scheme simplifies the object shape as a 3D model consisting of a different ellipse in each slice. The estimation is carried out using two low-dose perpendicular prior images (e.g., fluoroscopic images). An example of the estimated ellipse model (only every tenth row is visualized) compared with the actual head phantom shape extracted from an FDK reconstruction on non-truncated data is shown in Fig. 7.18. Although fine shape details could not be preserved, the rough outline of the object is nicely described in the 3D ellipse model (see the similarity of the curvature of the back of the head).

Figure 7.19 shows a comparison of a non-truncated projection, a laterally truncated projection after applying the PWCE scheme and after the heuristic WCE scheme. The line profiles of the extrapolated projections over projection views of $\lambda = -40°$, $\lambda = 20°$ and $\lambda = 80°$ are presented in Fig. 7.20. We can see that since WCE solely relies on the local continuity at the truncation boundary, there is no guarantee that extrapolation lines describe the real outline of the patient. On the other hand, the PWCE method more accurately fits the data outside the measure FOV, even for projections that differ from the AP and ML views and in the case of severe truncation. Similar observations can also be obtained in the reconstruction

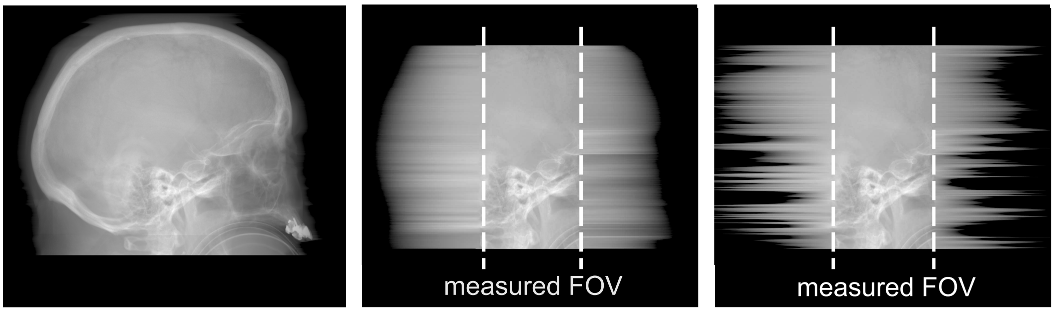

Figure 7.19: Comparison of a non-truncated projection (left), a laterally-truncated projection after applying the PWCE method (middle) and after the WCE method (right).

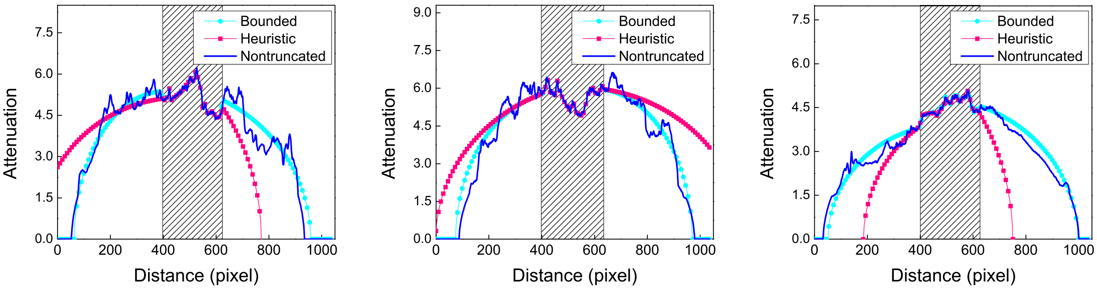

Figure 7.20: Comparison of the non-bounded traditional extrapolation (WCE) and patient-bounded extrapolation (PWCE) in a severe truncation case. Line profiles at projection views of $\lambda = -40°$ (left), $\lambda = 20°$ (middle) and $\lambda = 80°$ (right). Note that the bounded ellipse parameters are estimated using two single projections from $\lambda = -90°$ (ML) and $\lambda = 0°$ (AP). The shaded regions indicate the measured part of projections in ROI scan.

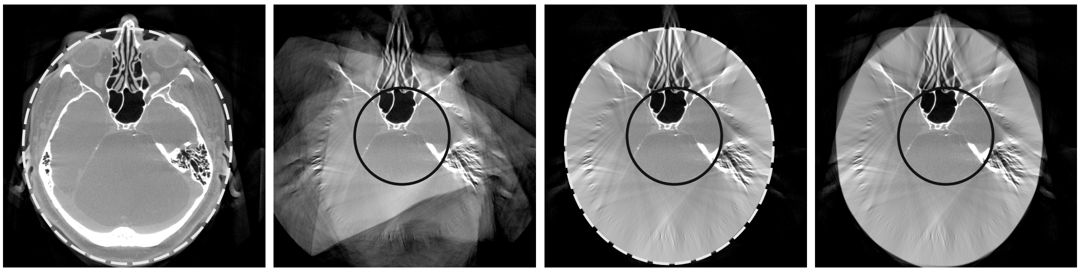

Figure 7.21: Comparison of (from left to right) the FDK reconstruction from non-truncated projection data, ROI reconstruction corrected by the conventional WCE method, ROI reconstruction from truncated data corrected by the PWCE method and ROI reconstruction from truncated data corrected by the CBE method. The dashed ellipses indicate the estimated outline of the patient and solid circles indicate the ROI.

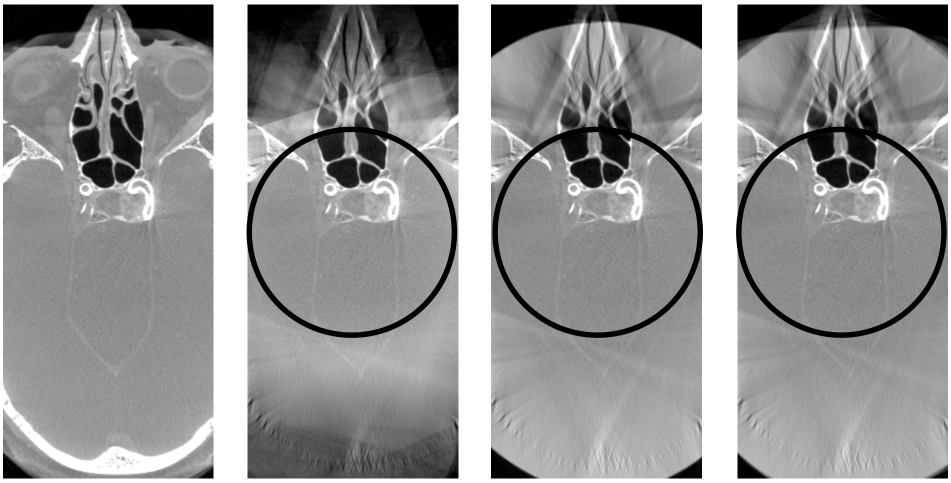

Figure 7.22: Transversal slices of the clinical data 1 (ROI 2) reconstructed by (from left to right): FDK on non-truncated data, the heuristic WCE method, the PWCE method and the CBE method from truncated data, in the grayscale window [-1000 HU, 1000 HU]. The black circles indicate the ROI.

slices. From Fig. 7.21 we can see that the fitted ellipse estimated by the PWCE method describes the actual object support (see the dashed ellipse) much better than the conventional WCE scheme, even though only ROI is of diagnostic interest.

Centered ROI Case

The reconstruction results using different truncation correction methods from the centered ROI cases are presented in Figs. 7.22-7.24, respectively. A comparison of the line profiles indicated as the dashed line in the slices is shown in Fig. 7.25. For visual inspection in the ROI 2 case, the WCE method as well as the patient-bounded methods (PWCE and CBE) are capable of avoiding the truncation-induced cupping-like artifact and produce acceptable reconstruction results. The portions of the patient inside the ROI are visually comparable to the reference FDK reconstruction; see Fig. 7.22. The line profiles shown in Fig. 7.25 (top) confirm this observation, although WCE exhibits a slight intensity increase close to the truncation boundary.

However, it becomes more challenging to correction algorithms when it comes to severe truncation cases. The WCE method cannot handle the truncation-induced cupping and also leads to a large offset on HU values; see Figs. 7.23 and 7.24 for a severe truncation case (ROI 4). These truncation artifacts can also be clearly observed from the line profile of the water cylinder extrapolation (see Fig. 7.25 (bottom)). This is because when encountering severe truncation, an accurate extrapolation estimation on unmeasured data is not possible for heuristic extrapolation schemes, due to less reliable data available and larger unpredictable unknown portion. In contrast, the PWCE method that incorporates patient boundary information is still robust with respect to these particular truncation cases. It is also interesting to see that PWCE always yields visually comparable results to that of the CBE scheme (see Figs. 7.23 and 7.24), even though the 3D shape model of the former method is only estimated from two projection views. This observation suggests that the estimated 3D shape

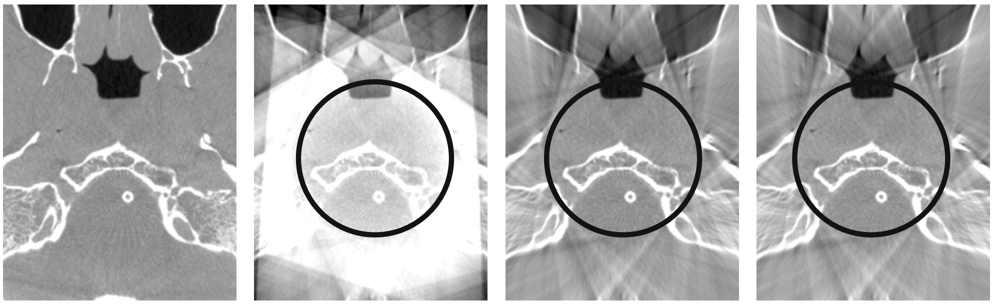

Figure 7.23: Transversal slices of the clinical data (ROI 4) reconstructed by (from left to right): FDK on non-truncated data, the WCE method, the PWCE method and the CBE method from truncated data, in the grayscale window [-1000 HU, 1000 HU]. The black circles indicate the ROI.

model nicely fits the patient head and exact patient boundary information in the projection domain seems not necessary.

The quantitative evaluations for symmetric truncation (ROI 1-4) are summarized in Fig. 7.26. In line with visual assessment, it is readily seen that in general quantitative accuracy is considerably improved by the proposed patient bounded methods compared with the heuristic approach. The average RMSE reached as little as 31.6 HU in the case of ROI 2, compared with 106.4 HU from the WCE method. In the severe truncation case (ROI 4) the WCE method yields substantially degraded quality image (RMSE of 312.8 ± 65.3 HU), due to the residual truncation artifacts, while the PWCE method still retains a reconstruction of high quality (RMSE of 33.8 ± 12.9 HU).

In terms of correlation coefficients, a very high value of above 0.995 was achieved by the PWCE method when reconstructing ROI 2. When it comes to a more severe truncation case, i.e., ROI 4, the differences between heuristic extrapolation and proposed extrapolation substantially enlarge, which is reflected by a difference of 0.28 for the correlation coefficient in Fig. 7.26. Consistent with the visual inspection, the CBE method is only slightly superior to the PWCE method (CC of 0.997 ± 0.001 vs. 0.995 ± 0.005 in ROI 2 and 0.976 ± 0.031 vs. 0.973 ± 0.035 in ROI 4). These results clearly demonstrate a good agreement of the reconstructed images with the reference image.

It is also interesting to see how two variants of patient bounded extrapolation, PWCE and PSRE, respond to different ROI cases. We note that in most of the studied cases PWCE yields better results than PSRE, although in the most severe truncation case (ROI 4) the differences between these two methods become subtle (e.g., 0.973 ± 0.035 vs. 0.974 ± 0.030).

Off-centered ROI Case

Figure 7.27 qualitatively compares the reconstruction results from all investigated methods for an off-centered ROI case. It was found that for WCE, truncation artifacts are most pronounced close to the truncation edge, manifesting as a noticeable intensity increase. This observation is not surprising since the argument still holds: truncation artifacts appear more severe to a side where the large unknown/unmeasured

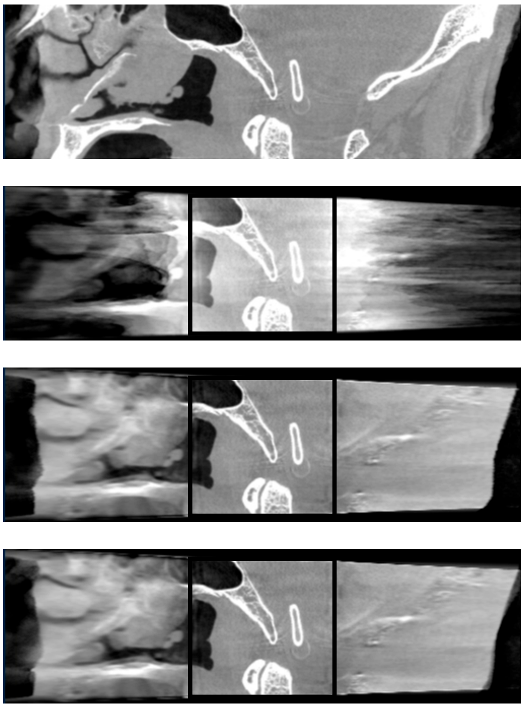

Figure 7.24: Sagittal slices of the clinical data (ROI 4) reconstructed by (from top to bottom): FDK on non-truncated data, the heuristic WCE method, the PWCE method and the CBE method from truncated data, in the grayscale window [-1000 HU, 1000 HU]. The black rectangles indicate the ROI.

projection data needs to be estimated. On the other hand, additional patient boundary information was demonstrated to be very beneficial to handle this difficulty, which is reflected by visually high image quality yielded by the PWCE method.

Quantitative evaluations for the off-centered cases (i.e., ROI 5-8) are depicted in Fig. 7.26. The results show that both proposed patient bounded approaches attain the mean values of the correlation coefficient higher than 0.99 in all ROI cases. Also, note that the average RMSE is somewhat inferior to the centered ROI cases (71.8 HU vs. 40.2 HU). Nonetheless, the error is still much lower than the one from the WCE method, whose average RMSE almost reaches 500 HU due to inaccurate estimations of the missing data.

It was found that in off-centered ROI cases, the evaluation results provide no definite answer when comparing PSRE and PWCE since in some cases one shows slightly superior over another whereas in other cases it is not.

7.5 Comparative Evaluation among ATRACT, SSR and PBE

An essential issue for optimizing X-ray imaging protocols involves searching a balance between image quality (e.g., image resolution, noise, image artifacts, etc.) and the patient dose. The methods we investigated above always come with a different trade-off between these two aspects. In this section, we present a detailed compara-

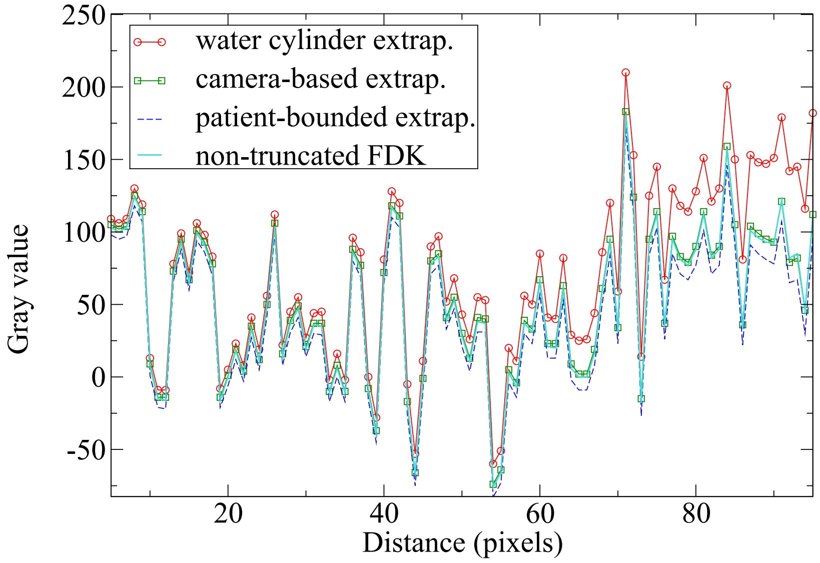

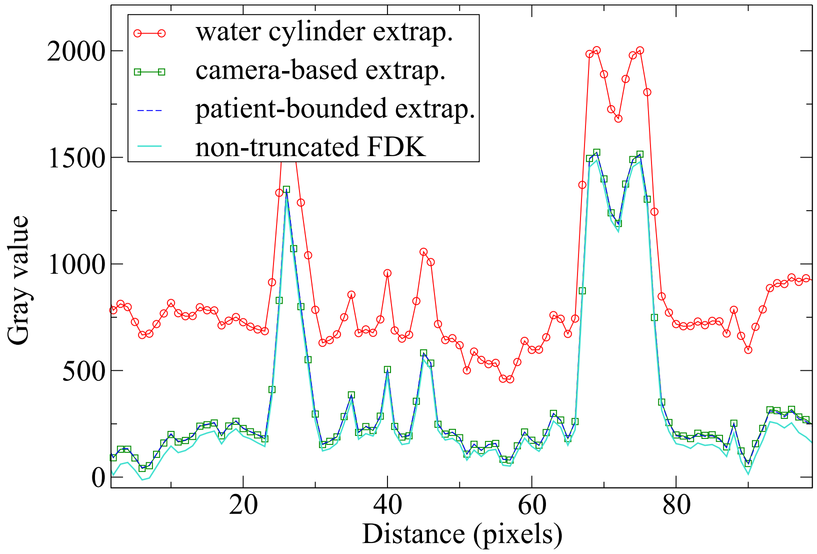

Figure 7.25: Plots of the line profile (indicated as the dashed line in the transversal slice) for each algorithm in the ROI 2 case (top) and in the ROI 4 case (bottom).

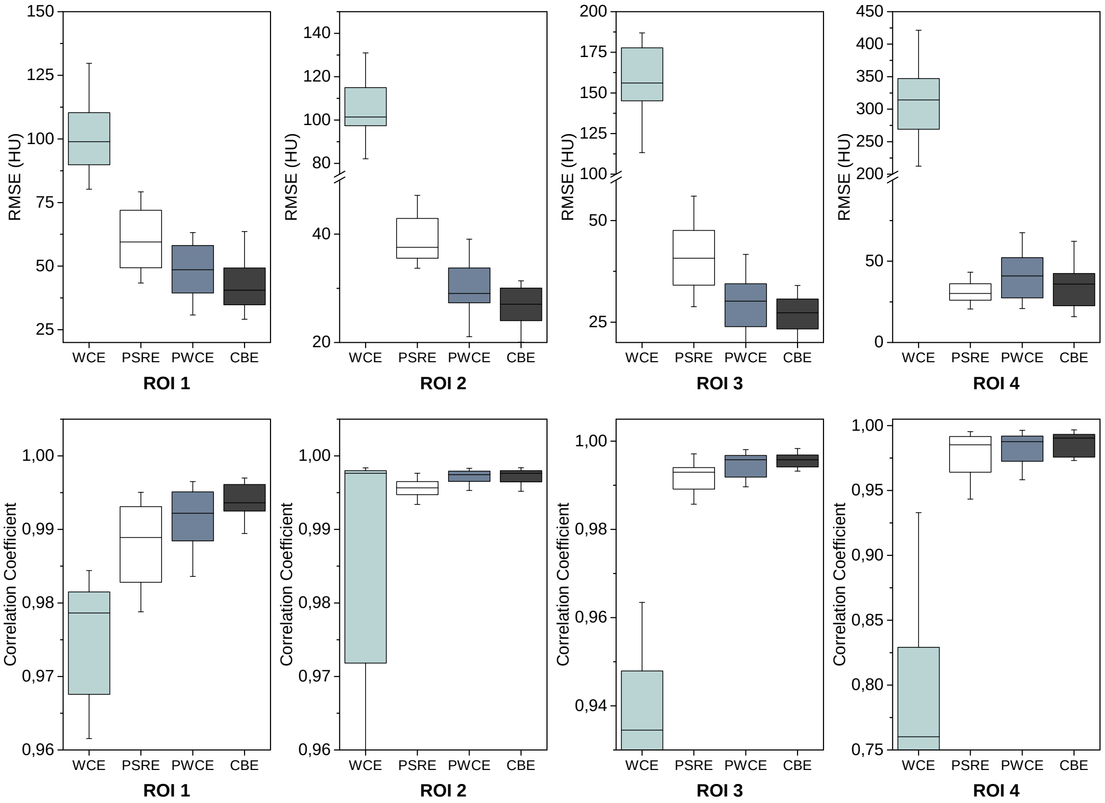

Figure 7.26: A summery of the quantitative assessment (RMSE and CC) in the centered ROI cases (ROI 1-4) for water cylinder extrapolation (WCE), patient bounded square root extrapolation (PSRE), patient-bounded water cylinder extrapolation (PWCE) and camera-based extrapolation (CBE).

tive evaluation of all investigated ROI reconstruction algorithms and quantify their trade-off between image quality and patient dose. Note that most of the algorithmic performances we investigate in the following are similar to those already evaluated in the Sections 7.2 to 7.4, while individually analyzing the robustness of these correction algorithms. The evaluation presented here, however, is more comprehensive. The involved algorithms include the 1D/2D ATRACT method, the patient bounded water cylinder extrapolation (denoted as PBE below) and the prior image based detruncation method using shutter scan (denoted as SSR below) with different full projection ratios. The refined water cylinder extrapolation [Zell 05] (denoted as WCE below) was also investigated as the baseline here and compared with the proposed algorithms above. This study is again evaluated on the large clinical datasets described in Section 7.1.1.

In the following evaluation, we focus on the quantitative assessment using the correlation coefficient that intuitively reflects the robustness of algorithms to restore structural information. A high root mean square error (RMSE) may also indicate a scaling/bias occurred in the reconstruction volumes, but such an artifact could be compensated for by adapting the visualization parameters.

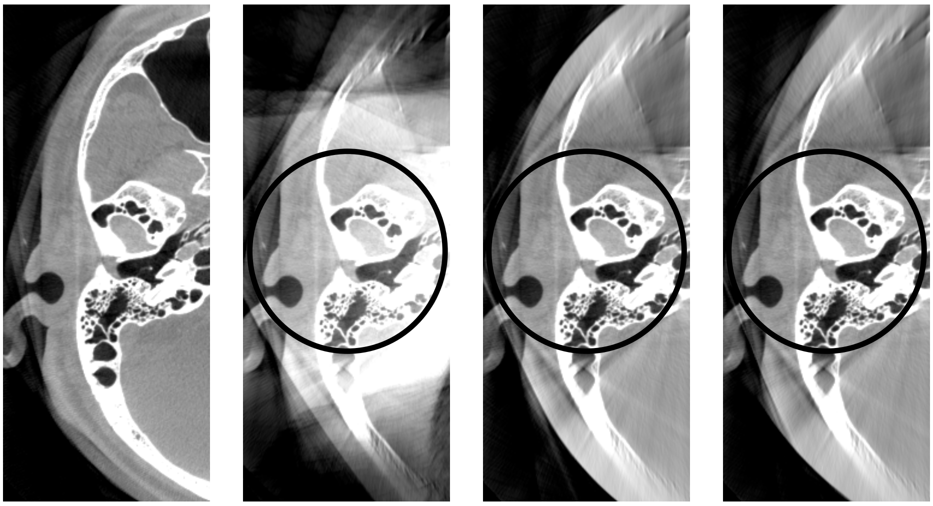

Figure 7.27: Transversal slices of the clinical data (ROI 7) reconstructed by (from left to right): FDK on non-truncated data, the heuristic WCE method, the PWCE method and the CBE method from truncated data, in the grayscale window [-1000 HU, 1000 HU]. The black circles indicate the ROI.

7.5.1 Image Quality Assessment

Centered ROI Case

Figure 7.29 shows the performance of all investigated algorithms on four decreased ROI sizes. It can be seen that the heuristic WCE scheme attains a fairly good result when the truncation is mild. This is mainly because in such cases the unmeasured data can be accurately estimated by a simple water cylinder model. However, when truncation becomes severe, the performance of WCE declines rapidly, yielding a correlation coefficient of only 0.69±0.20 with respect to the reference. Also considered as a heuristic extrapolation technique, ATRACT methods that come with a two-stage filtering, on the other hand, show less dependency on the truncation level. Thus, they could be the first choice for severe truncation cases, if no prior information is available.

Figure 7.29 also indicates how image quality is considerably improved with a little prior knowledge. The PBE method that incorporates patient boundary information is clearly superior over those of heuristic methods. It retains high accuracy (up to 0.99) to all centered truncation cases. With more prior information, it is found that decreasing the scan FOV has very little effect on the performance of the SSR method. It achieves the best results among these investigated methods, with a tenth of full projections (50 projections out of 496 in total). Note that it reaches not only a high mean value of the correlation coefficient, but also keeps a small standard deviation.

Although only four centered different ROI sizes are selected in this evaluation, we can fit the presented evaluation results to non-linear curves, to approximately estimate the behavior of the methods on unmeasured ROI sizes, as displayed in Fig. 7.30. The corresponding equations of each line fitting are presented in Table 7.2. All nonlinear curve fittings were carried out using Levenberg Marquardt iteration algorithm until the Chi-Sqr tolerance value of 1e-9 was reached.

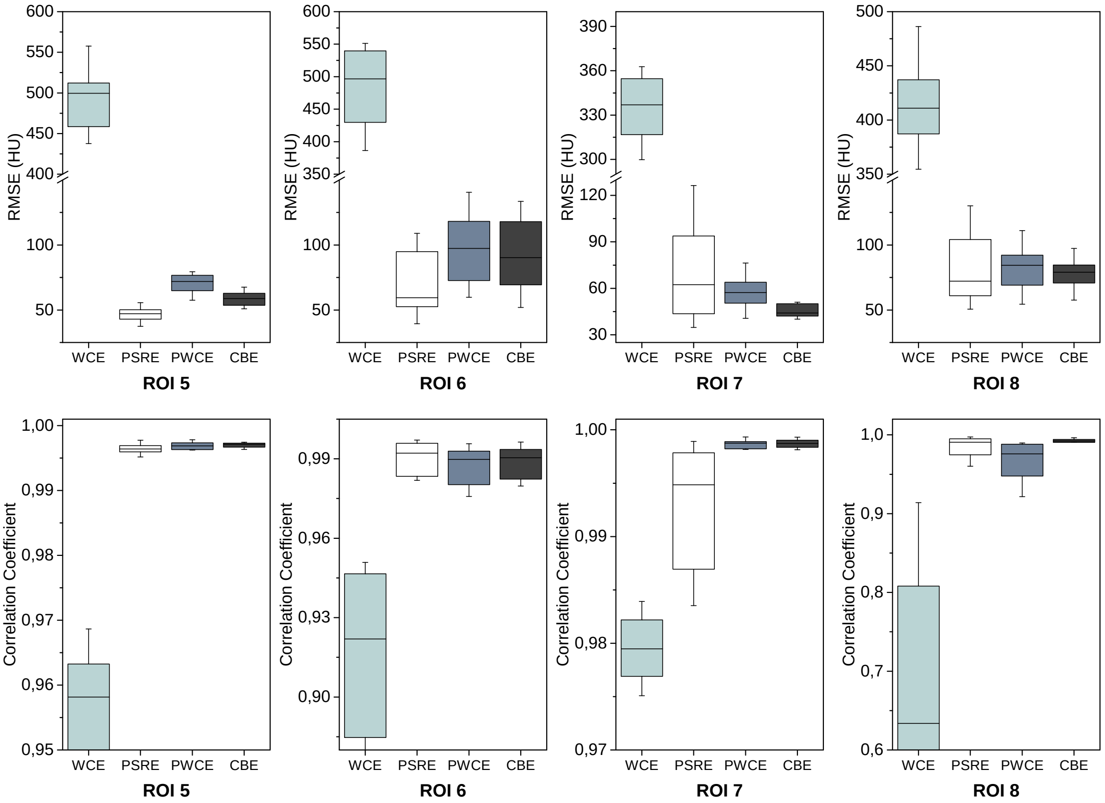

Figure 7.28: A summery of the quantitative assessment (RMSE and CC) in the off-centered ROI cases (ROI 5-8) for water cylinder extrapolation (WCE), patient bounded square root extrapolation (PSRE), patient-bounded water cylinder extrapolation (PWCE) and camera-based extrapolation (CBE).

Figures 7.31 and 7.32 depict the performance of various truncation reduction artifact methods versus results from the SSR algorithm coming with the different full projection ratios (grouped by the ROI size). Here, SSR1, 2, 3, 4 and 5 correspond to 5, 10, 25, 40 and 50 acquired full projections, respectively. In general, the results shown in Fig. 7.31 are consistent with the previous quantitative interpretation. It is found that the heuristic methods tend to have a relatively large deviation and several outliers. For instance, ATRACT is able to produce fairly good image quality in ROI 3: A correlation coefficient of up to 0.99 is achieved. At the same truncation level, it yields less accurate results in some studied cases (lower than 0.90). In contrast, with the help of the additional full projection information, the SSR algorithm shows very robust reconstruction results. It is found that with only ten full projections, the SSR method stably achieves a correlation coefficient of 0.99 in ROI 1 to 3. The lines corresponding to the range of Quartile 1, mean, median, and Quartile 3 almost overlap to each other, yielding the robustness of the method regardless of which patient data is selected. Figure 7.31 also suggests that acquiring more than 25 full projections seems unnecessary for SSR due to a bad trade-off between full projection ratio (related to patient dose) and image quality. Also, we found that the PBE scheme always achieves an intermediate result between the heuristic approaches and the SSR approach.

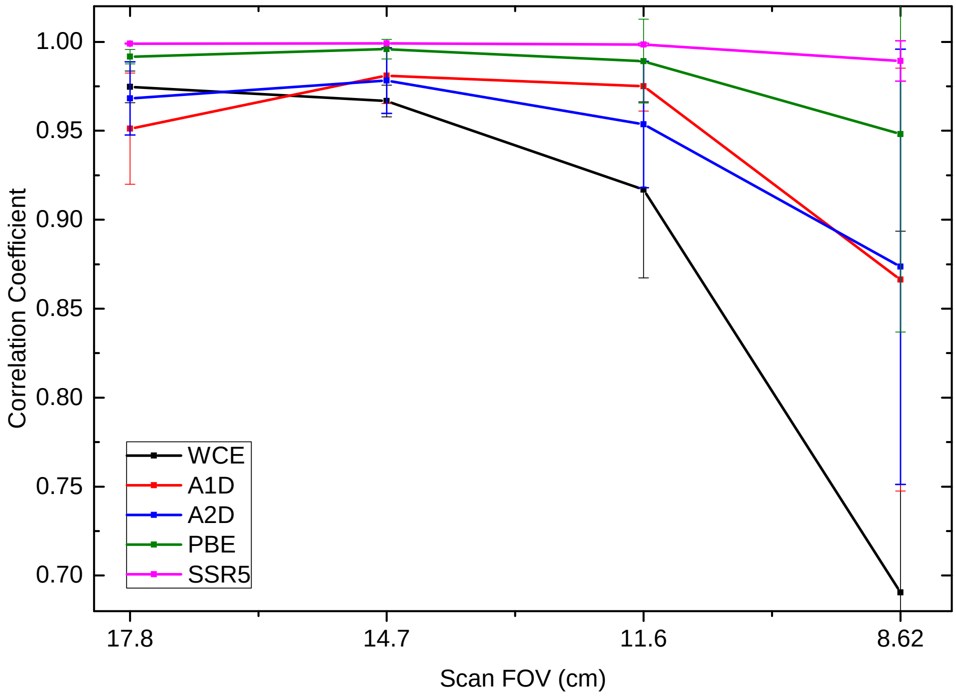

Figure 7.29: Algorithmic performance of the proposed methods on the four centered ROIs.

Furthermore, we particularly compare the performance of only PBE and SSR and show the results in Fig. 7.32. This allows us to study how image quality is improved with a steady increase in prior knowledge. To better estimate the increasing tendency, we fit the evaluated results (five measured full projection ratios) to an exponential function. Again, the fitting equations were computed in an iterative manner using Levenberg Marquardt algorithm until the Chi-Sqr tolerance value of 1e-9 was reached. The computed parameters for the nonlinear curve fitting are presented in Table 7.3.

Figure 7.32 delivers the information on which method could be used to achieve a better image quality with less full projections. For instance in ROI 2, in order to obtain the higher image quality than PBE (above its Quartile 3)[1], the SSR data acquisition, according to this figure, at least needs to acquire 16 full projections and 480 truncated ROI projections (496 projections in total). It is also found that the requirement of the full projection ratio varies depending on the ROI size. A general trend is: with reducing the size of the ROI, the number of required full projections increases accordingly so that the SSR method could outperform the PBE method. Thus, in the most severe truncation case (ROI 4) it may occur that even the SSR method with 50 full projections (as we can see that the improvement already reaches its saturation), within the ROI, is unable to yield better results than the PBE method.

---

[1] Suppose in this specific case we are only interested in the area inside the ROI.

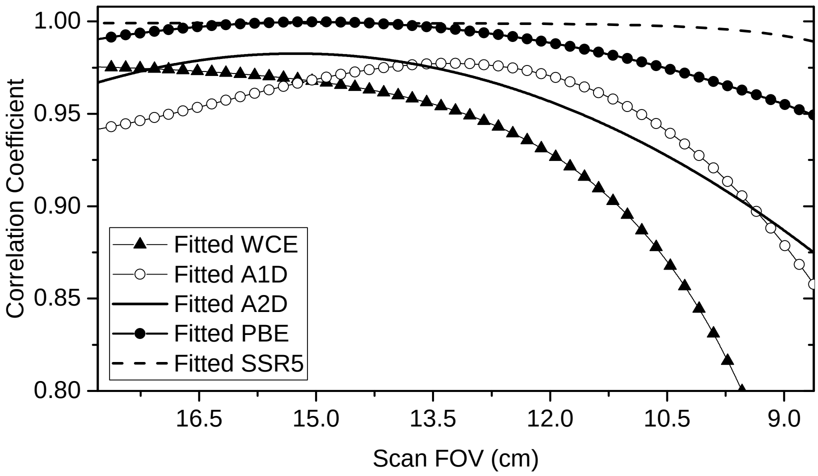

Figure 7.30: Nonlinear curve fitting of the four evaluated ROI sizes (Fig. 7.29) for predictably estimating the performance of unmeasured ROI sizes. The parameters of the fitted curves are presented in Table 7.2.

Model	Nr. Param.	Equation
Asymptotic	3	$y = a - b \cdot c^x$
Parabola	3	$y = a + b \cdot x + c \cdot x^2$
Cubic	4	$y = a + b \cdot x + c \cdot x^2 + b \cdot x^3$
Algorithm	Levenberg Marquardt	
Tolerance	1e-9	

Algorithm	WCE	A1D	A2D	PBE	SSR5
Model	Asymptotic	Cubic	Parabola	Parabola	Asymptotic
a	0.977	-0.617	0.414	0.723	0.999
b	25.85	0.312	0.074	0.036	46.54
c	0.593	-0.019	-0.002	-0.001	0.374
d	-	4.1e-4	-	-	-
Reduced Chi-sqr	5.25e-7	7.33e-8	3.10e-5	3.21e-6	1.61e-8
COD	0.981	0.957	0.995	0.978	0.999

Table 7.2: Nonlinear curve fitting of the presented evaluation results to various nonlinear curve models, for predictably estimating the behavior of methods on unmeasured ROI sizes. Here, COD denotes the correlation of determination that indicates how well data fit a statistical model.

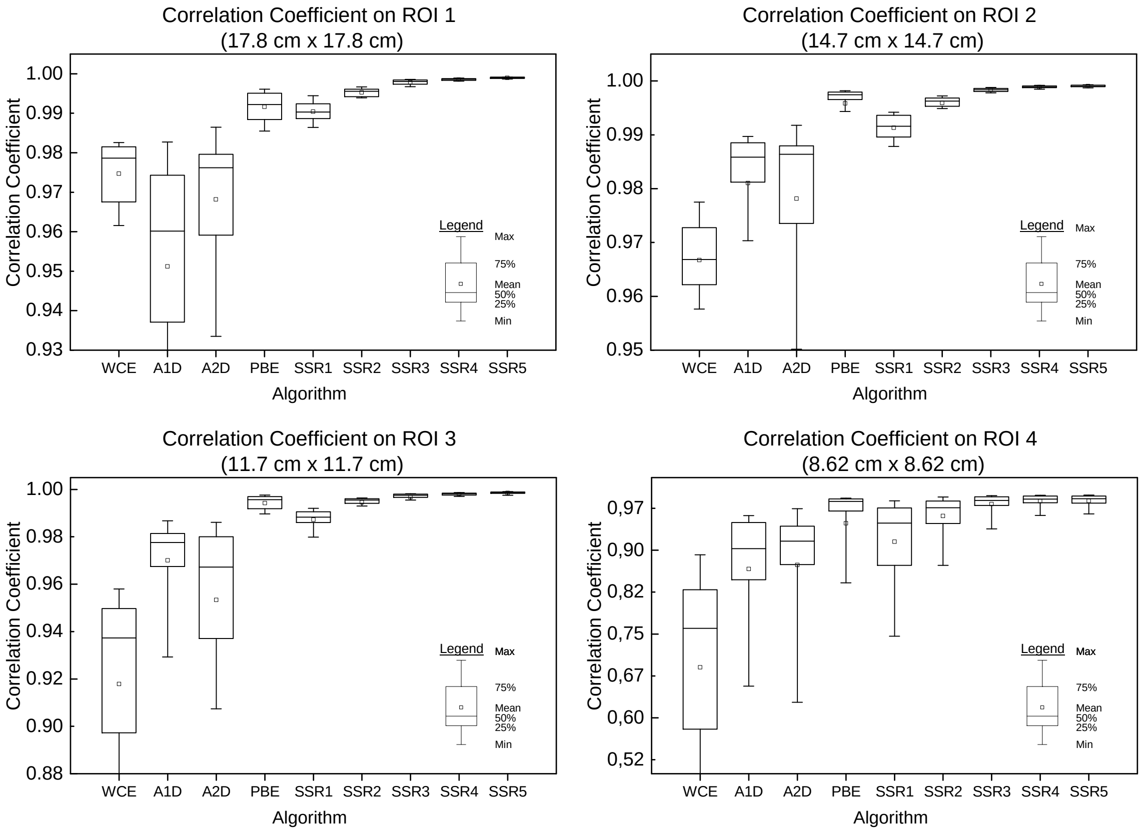

Figure 7.31: An overview of the quantitative assessment of various truncation artifact reduction methods on 16 clinical datasets for the four centered ROI cases. The results from the SSR algorithm come with different full projection ratios. Here, SSR1, 2, 3, 4 and 5 correspond to 5, 10, 25, 40 and 50 full projections that would be acquired during data acquisition, respectively. The plots are grouped by the ROI size.

Off-centered ROI Case

The algorithmic performance on each of the off-centered ROI cases was also compared and summarized in Fig. 7.33. In this study, we again investigated the variant of ATRACT with gradient compensation, namely ATRACT Plus, as they showed promising results in the off-centered ROI cases in Section 7.2.3.

In general, the performances of all ROI reconstruction algorithms are in good agreement with the observation in the centered ROI case. That is, for all off-centered ROI cases, best results are still obtained using the SSR method if a high full projection ratio is taken, followed by the PBE method and the ATRACT algorithm. The heuristic WCE method without prior information yields lowest image quality in ROI 5, 6 and 8. But in the case of ROI 7, it shows superior results over the uncorrected 1D and 2D ATRACT methods, both of which suffer from a severe gradient artifact caused by the off-centered ROI position.

It is found that the SSR method achieved a correlation coefficient as high as 0.998 for all ROI cases, if a tenth of full projections is acquired. Also, note that image quality of SSR degrades considerably with a reduction of full projection ratios. For instance, with only five full projections the mean values of the correlation coefficient

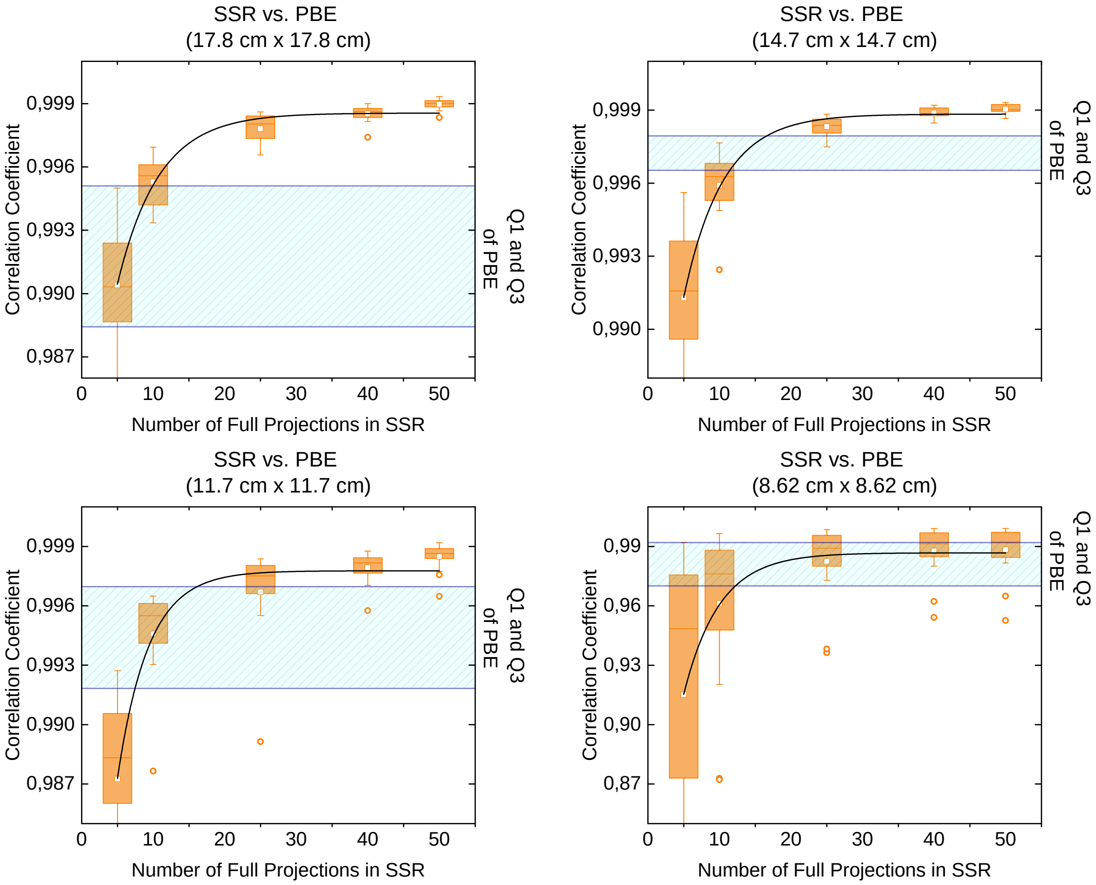

Figure 7.32: A direct comparison of the algorithmic performance between the patient bounded extrapolation (PBE) and shutter scan method (SSR).

are 0.986 for ROI 5, 0.975 for ROI 6 and 0.968 for ROI 8, respectively. On the other hand, the PBE method achieved overall higher correlation coefficients of 0.996 for ROI 5, 0.986 for ROI 6, and 0.993 for ROI 8, respectively. Interestingly, we also found that the performance of SSR declines relatively slowly in ROI 7, but still it is slightly inferior to PBE (0.993 vs. 0.998) with only five full projections.

It is clearly visible that with the developed gradient correction, both 1D ATRACT Plus and 2D ATRACT Plus, in off-centered ROI cases, produce satisfying reconstruction results, which are even close to those with prior information. The mean correlation coefficients for 1D ATRACT Plus and 2D ATRACT Plus are 0.979 and 0.985 for ROI 5, 0.957 and 0.973 for ROI 6, 0.988 and 0.987 for ROI 7 and 0.929 and 0.974 for ROI 8, respectively. These results confirm again that ATRACT could be the first selected approach for 3D ROI imaging, if no prior information is available. For a detailed comparison of 1D and 2D ATRACT or ATRACT with and without the gradient correction, we refer to Section 7.2.3 in this chapter.

7.5.2 Radiation Dose vs. Image Quality

Following the principle of ALARA, any imaging process based on ionizing radiation must be optimized towards dose reduction. The knowledge of the relationship

Description	Nonlinear Curve Fit for SSR
Model	Asymptotic
Nr. Parameters	3
Equation	$y = a - b \cdot c^x$
Iteration Algorithm	Levenberg Marquardt
Tolerance	1e-9

Parameters	ROI 1	ROI 2	ROI 3	ROI 4
a	0.998	0.998	0.997	0.986
b	0.019	0.018	0.033	0.019
c	0.841	0.832	0.793	0.817
Reduced Chi-sqr	2.21e-7	7.65e-8	7.39e-7	6.43e-6
COD	0.991	0.996	0.982	0.996

Table 7.3: Nonlinear curve fitting of the presented evaluation results (Fig. 7.32) for predictably estimating the behavior of the method on unmeasured full projection ratios. Here, COD denotes the correlation of determination that indicates how well data fit a statistical model.

that links image quality and radiation dose is of practical significance for such optimization. In this section, we study these two aspects for each of the investigated algorithms.

Theoretical integral dose reduction can be computed based on the dose area product (DAP) [Ardr 65], which can be further approximated to the first order as

$$D_{\text{int}} = D_{\text{x}} \cdot A, \tag{7.4}$$

where D_{int} is the integral dose to the patient, D_{x} is the dose due to the X-ray beam and A is the area of the scan FOV. In this study, we theoretically estimate the dose reduction according to Eq. (7.4). i.e., assuming the patient dose saving to be approximately proportional to the reduction of the area of the scan FOV. Note that here we also assume the patient encompasses the entire FOV. Let A_{Full}, A_{ROI} be the areas of the scan FOV for non-truncated data and truncated data, respectively. Then, to approximate the dose reduction in an ROI scan or shutter scan with respect to the full FOV scan, we define a dose percentage index (DPI) as follows:

$$\text{DPI} = \frac{k \cdot D_{\text{x}} \cdot A_{\text{Full}} + (1-k) \cdot D_{\text{x}} \cdot A_{\text{ROI}}}{D_{\text{x}} \cdot A_{\text{Full}}} = k + \frac{(1-k) \cdot A_{\text{ROI}}}{A_{\text{Full}}}, \tag{7.5}$$

where k indicates the full projection ratio, i.e., the number of full projections divided by the total projection number. For instance, consider a shutter scan acquisition that consists of 446 truncated projections with a scan FOV of 14.7 × 14.7 cm (ROI 2) and 50 full projections with the full FOV of 30 × 40 cm. The resulting DPI, according to Eq. (7.5), is 27.4 % with respect to a standard full FOV scan, yielding an additional dose of about 8% compared with a standard ROI scan (only truncation projections are acquired).

Figures 7.34 and 7.35 showed image quality against the computed DPI for all investigated methods in the four centered ROI cases. Image quality is evaluated

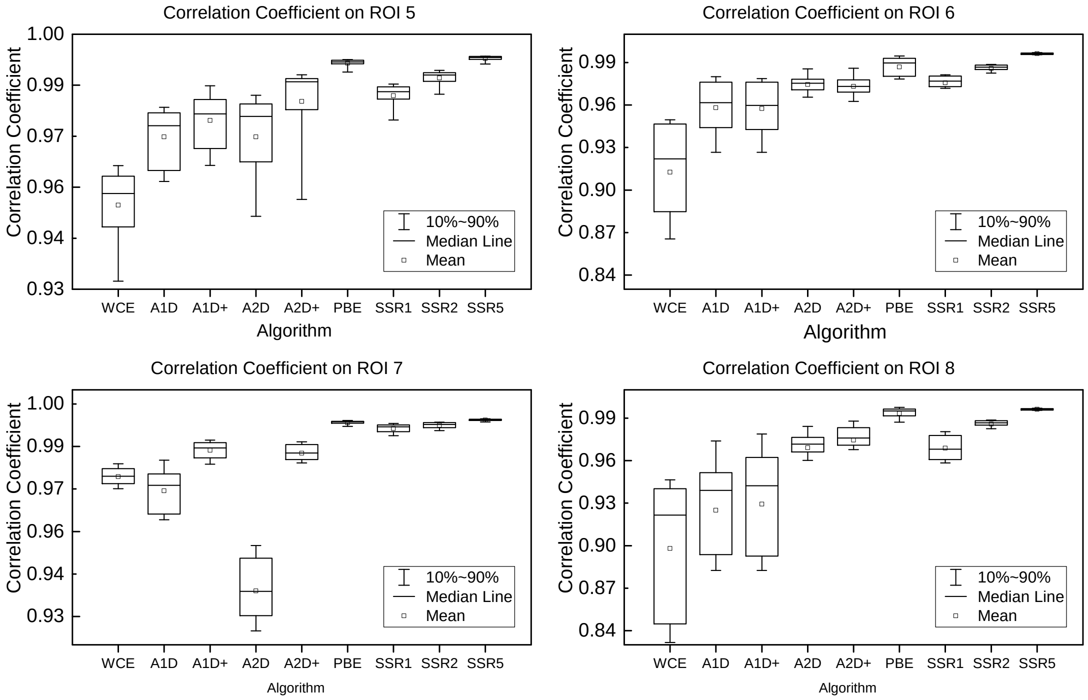

Figure 7.33: An overview of the quantitative assessment of various truncation artifact reduction methods on 16 clinical datasets for the four off-centered ROI cases. The results from the SSR algorithm come with different full projection ratios. Here, SSR1, SSR2 and SSR5 correspond to 5, 10 and 50 full projections that would be acquired during data acquisition, respectively. The plots are grouped by the ROI position.

using the correlation coefficient and RMSE, applied within the ROI and in the PR. Note that here we focus on the centered ROI cases (ROI 1-4) since they are more clinically applicable for current interventional settings.

All these figures show a similar observation on how image quality varies according to the DPI, although improvement ratios of the DPI may differ from one ROI to another. In the following, we provide two examples how to interpret these figures. The first example considers a data acquisition carried out using the scan FOV of 17.8× 17.8 cm (i.e., ROI 1). Figure 7.34 (top) suggests that in this specific case, WCE could be selected to generate a 3D ROI image of the highest quality (a correlation coefficient of 0.975 and an RMSE of 105.8 HU), if DPI has to be minimal. In order to further improve reconstruction accuracy, according to Fig. 7.34 (top), the PBE method could be a better choice than SSR1 in terms of both image quality (a correlation coefficient of 0.992 vs. 0.990) and DPI values (28.53% vs. 29.24%). In other words, with a 1% increase of the original dose of the standard ROI scan (i.e., 28.25%), PBE improves image quality from a correlation coefficient of 0.975 to 0.992. This seems to be an adequate trade-off when optimizing image quality versus patient dose in the current acquisition setting. So far, we only evaluated the image quality within the ROI. If the image quality of the PR is also taken into consideration, SSR1 is clearly superior over the PBE method in this aspect since the latter only extracts the patient boundary information instead of anatomical structures. As shown in Fig. 7.34 (top), SSR1

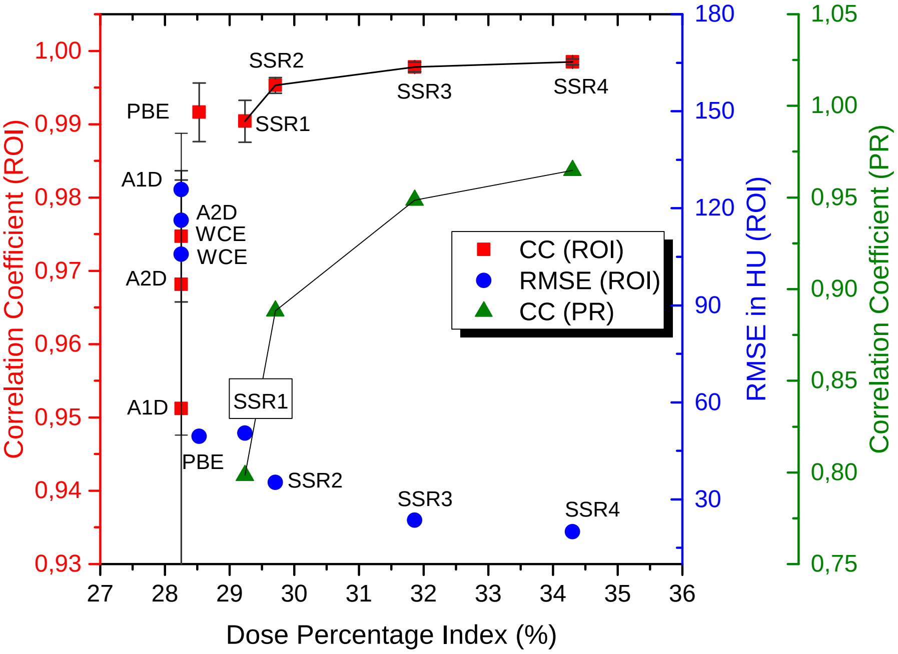

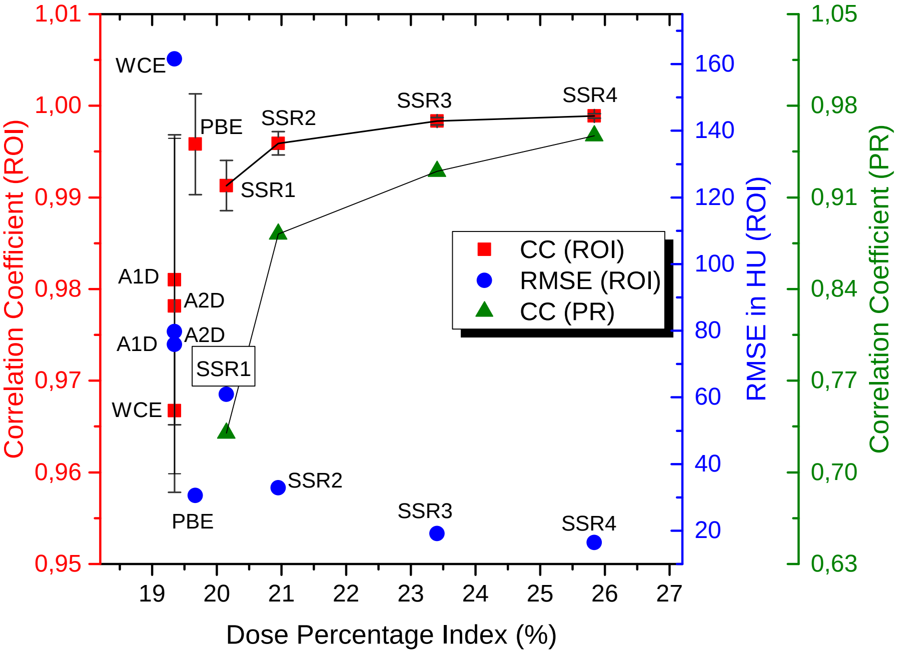

Figure 7.34: Investigation of the relationship that links image quality and radiation dose for all proposed algorithms in ROI 1 (top) and ROI 2 (bottom). Here, SSR1, SSR2, SSR3, and SSR4 denote the shutter scan reconstruction with 5, 10, 25, 40 acquired full projections, respectively.

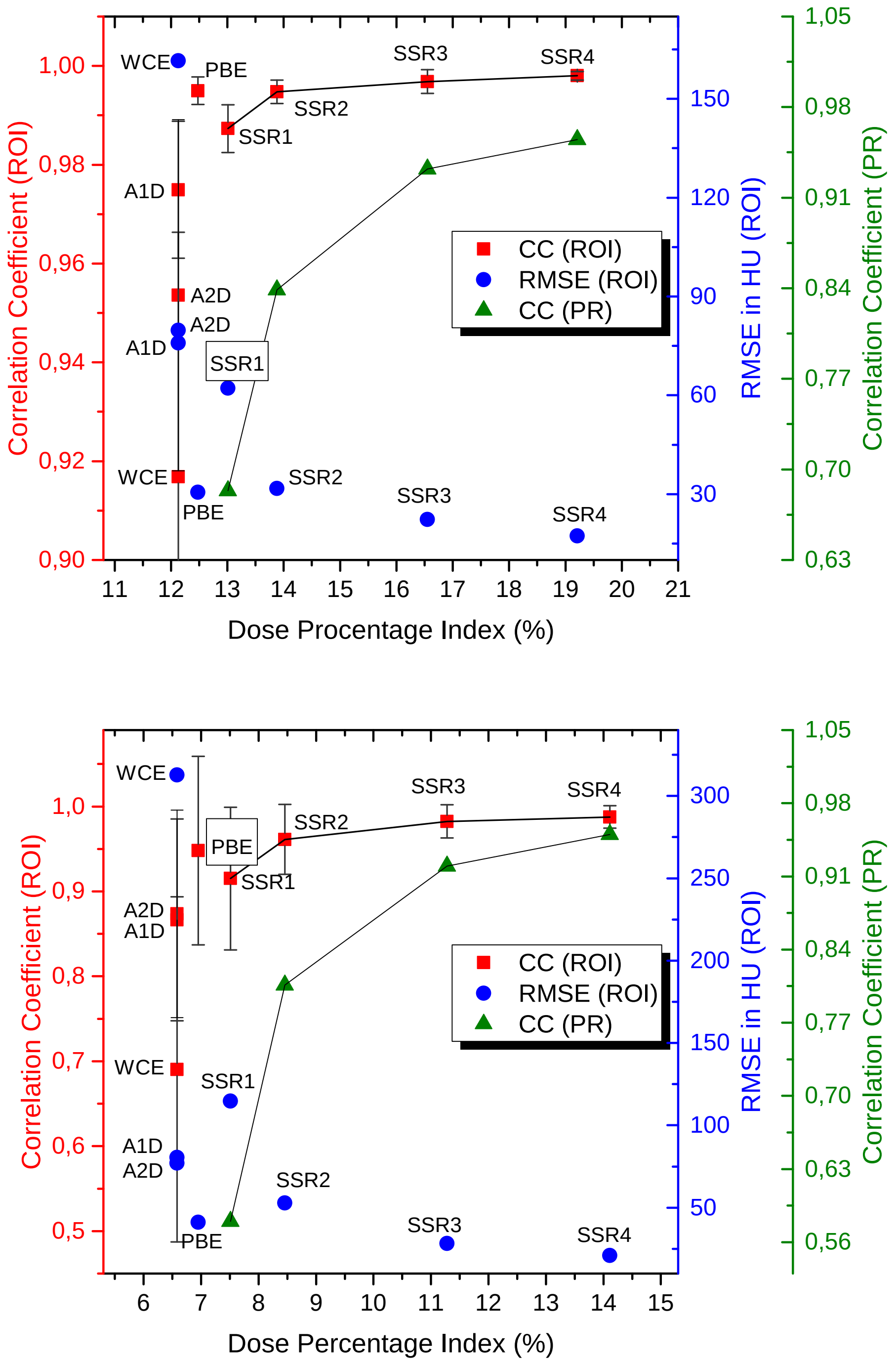

Figure 7.35: Investigation of the relationship that links image quality and radiation dose for all proposed algorithms in ROI 3 (top) and ROI 4 (bottom). Here, SSR1, SSR2, SSR3, and SSR4 denote the shutter scan reconstruction with 5, 10, 25, 40 acquired full projections, respectively.

reaches a correlation coefficient of 0.798 in the PR. Although not explicitly depicted in the figure, the correlation coefficient for PBE is only 0.231 in the PR. Moreover, Fig. 7.34 (top) also suggests that SSR2 could yield another interesting trade-off, since with an increase of 5.16% of the original dose, it is able to improve a correlation coefficient from 0.975 to 0.995 within the ROI and from 0.135 to 0.889 outside the ROI (i.e., in the PR). It is also noted that further increments of the patient dose only affect the PR since image quality within the ROI already attains a high level.

Let us consider another example concerning a data acquisition with a severe truncation with a scan FOV of $11.6 \times 11.6\,\mathrm{cm}$ – only 12.2% with respect to the standard full FOV scan. As shown in Fig. 7.35 (top), at this dose level the 1D ATRACT algorithm appears to be more superior over the other heuristic methods, yielding a correlation coefficient of 0.976 and an RMSE of 73.5 HU. With an increase of 2.88% of the original dose percentage, the correlation coefficient reaches as high as 0.994 when using the PBE method. It also can be seen in Fig. 7.35 (top) that further improvement on image quality within the ROI will cost much more additional dose and thus seems not adequate.

7.6 Summary and Discussion

This chapter presented a detailed comparative evaluation of all truncation artifact reduction methods proposed in Chapter 4 to 6. We applied these methods on 16 clinical datasets that were acquired in an interventional suite equipped with an angiographic system. Overall eight truncation scenarios with four centered ROIs defined by different sizes or off-centered ROIs defined by different positions are considered. Since each of the considered algorithms comes with several variants or parameter settings, we first conducted an algorithm-specific evaluation and parametrization, to quantify the impact of different truncation scenarios on image quality achievable with these variants.

In the comparison of 1D and 2D ATRACT, we observed that both methods come with a similar behavior in the presence of data truncation. In general, truncation-induced cupping artifacts are of considerably reduced strength, compared with that of the straightforward application of FDK on truncated data. This clearly demonstrates that the two-step filtering is superior to the conventional one-step ramp filtering in the presence of data truncation. However, both 1D and 2D ATRACT suffer from an edge gradient artifact attached to the edge where the high dense skull is truncated. This artifact somewhat affects their quantitative accuracy (see results in ROI 1). We assume this is a typical behavior for heuristic extrapolation methods since the continuation assumption that the methods reply on is violated because of confounding these high dense objects at the truncation edge. The evaluation results of off-centered ROI cases demonstrated the robustness of the empirical gradient correction method when the induced gradient is substantial (e.g., in ROI 5 and ROI 7).

The evaluation results of the SSR methods showed that the differences inside the ROI were quite small – all considered methods are able to obtain an ROI image of high quality, although the SSR-C method yields the most visually identical results to the reference. On the other hand, we observed that image quality and characteristics in PR region, which is also of particular interest for shutter scan applications, vary noticeably among the investigated methods. The SSR-A method, although suffering from severe streaking artifacts (due to the use of FDK), nicely preserves fine details of high contrast objects, such as bone structures. It was also found that image quality of the SSR-A method degrades dramatically with decreasing of the acquired full projection number. In contrast, the SSR-B approach yields less streaking artifacts but comes with an overall smooth appearance as a side effect of the wTV regularization. The SSR-C approach in general shows the best image quality also in the PR among these methods, particularly for the case in which only a low number of full projections are acquired. This observation is also quantitatively confirmed by its correlation coefficient, which drops marginally below 0.99 when the full projection number corresponds to 10.

We found that the PBE method leads to a major improvement in image quality, compared with the purely heuristic extrapolation method. The experimental results underlined that this particularly applies for severe truncation cases. Surprisingly, we found the 3D shape model estimated by only two perpendicular views is sufficient to describe the coarse patient outline for head cases. It is also shown that PBE is qualitatively and quantitatively comparable to the camera-based extrapolation (see [Kold 11]) in which the patient outline is known from all projections. Furthermore, the method robustly reduces the low-frequency bias in the reconstructed volume, which is reflected by the very low RMSEs. In the comparison of its two variants, the differences we observed were small, but overall the results of PWCE appeared to be slightly superior to those of the PSRE.

The final comparative evaluation presented in Section 7.5 clearly depicted the algorithmic performance of all investigated methods under the uniform evaluation framework. For the centered cases, the performance of the heuristic WCE method declines rapidly, when the truncation becomes severe. The ATRACT methods, on the other hand, showed less dependency on the truncation degree and thus appeared to be more robust in severe truncation case. However, a large deviation and several outliers arose in the results of all these heuristic methods. In contrast, benefiting from prior knowledge, the PBE and SSR methods were able to achieve ROI reconstructions in a more accurate and robust manner, which is reflected by the high correlation coefficients of about 0.99 in ROI 1 to 3 and about 0.96 in ROI 4 (the most severe truncation case). The performances of all considered algorithms for the off-centered ROI cases were in good agreement with the observations in the centered ROI case. That is, the best results were still obtained using the SSR method if 50 full projections are acquired, followed by the PBE method and the ATRACT algorithms. We note that the overall values of the correlation coefficient appeared to be lowest in ROI 8, in which the ROI volume contains the most soft tissue.

A particular interest of the evaluation is to quantify the relationship between image quality and radiation dose for all investigated algorithms. However, we emphasize that this is actually a multidimensional problem since in 3D ROI imaging, achieved image quality does not solely depend on the patient dose, but also varies with other factors, such as selected algorithms, truncation degrees or ROI positions, etc. The decision on which method should be used also depends on the specific clinical application, imaging scenario and availability of prior knowledge. For instance, the ATRACT methods could be selected in severe truncation cases, if no prior information is available; SSR has practical advantages to display useful information in the PR but at a cost of additional doses; The PBE method seems to find an adequate trade-off between image quality and patient dose but the prerequisite is the two non-truncated fluoroscopic images. Nevertheless, the conducted evaluation and presented results in this chapter, could be used as an indicator for the ease of such selection.

CHAPTER 8

Outlook

The work presented in this thesis focused on the technical development of various truncation artifact reduction techniques that are suitable for different 3D imaging scenarios. From the algorithmic perspective, the ATRACT algorithm has several practical advantages and thus could be potentially utilized in most interventional clinical routines. However, the evaluation in Section 7.2.3 showed the ATRACT results suffer from a noticeable artifact that is particularly pronounced at the edge where the high contrast object such as skull is truncated. One possibility to reduce such artifacts could be to perform a two-step algorithm: Firstly, we need to identify if high dense bones appear at the truncation edge by using a tissue-bone threshold; secondly, we could apply the metal artifact reduction techniques proposed in [Bal 06] and [Prel 10]. More specifically, we could produce a bone-only image by segmentation of an initial ATRACT reconstruction, followed by interpolating the bone structures that are transaxially truncated in the raw data using a bone mask sinogram. Finally, the bone structures are recovered in the second reconstruction by using the previous bone-only image.

The third approach of SSR (Section 5.3.3) appears to be more robust with respect to image quality in both the ROI and RP. However, the employment of the iterative method may prohibit its practical use in an interventional clinical setting. Alternatively, we could investigate other de-streaking strategies to produce streak-free initial images, such as the fast streak-removal methods studied in [Manh 14] or the edge-preserving nonlinear filters proposed in [Toma 98, Elad 02].

In this thesis, the sinogram completion method that makes use of the consistency conditions was investigated and validated in a 2D fan-beam imaging geometry. The next step is to extend the method and experiment to a 3D cone-beam geometry. To this purpose, we could follow the study from Patch [Patc 02] that investigated the consistency conditions for 3D tomography or the investigation of the 3D wedge in the Fourier domain [Brok 06].

Although in this thesis we use virtually truncated data to accomplish evaluation tasks, investigating the performance of the algorithms using patient data with physical collimation is also of practical importance. Note that the differences between an ROI scan and an associated full view scan lie in the level of physical effects, such as X-ray scatter, in the projections and also in the fact that patient is often repositioned between those scans. These differences may complicate the quantitative assessment when using the reconstruction of non-truncated data as a reference.

Furthermore, in Chapter 7 we theoretically calculated the patient dose based on its relation to the DAP in a first-order approximation [Ardr 65]. Another interesting field of future research is to measure the actual effective dose and dose distribution associated with different truncation levels, experimentally. One direction is to use the combination of thermoluminescence dosimeters (TLD) and anthropomorphic head phantoms that has been shown to be an efficacious method for the accurate, effective dose measurement [Zeli 12].

CHAPTER 9

Summary

In this thesis, we considered the problem of the improved restoration of an image from projection data that is laterally truncated, primarily aiming to reduce radiation doses to the patient. The contribution towards high-quality images from truncated data is several-fold, which is reflected in the subdivision of the thesis in two parts.

Part I introduces the clinical background and an overview of truncation artifact reduction methods. Chapter 1 starts with the motivation. That is, how to reduce patient dose while still retaining high image quality. In many clinical applications and workflows, such as follow-up examinations of deployed stents/flow-diverters during endovascular treatment, cochlear implants and needle biopsies, only a small portion of the patient may be of diagnostic interest. This enables the idea of 3D region of interest (ROI) imaging, utilizing an X-ray beam collimator to laterally and axially shield unnecessary radiation during image acquisition. In this manner, only the diagnostic ROI is being irradiated by X-rays, resulting in a substantial reduction of patient dose. However, 3D ROI imaging involves transaxially truncated projections from which conventional reconstruction algorithms generally yield a considerable degradation of image quality if no effective counter-measure against the truncation is performed. Thus, the primary focus of this work lies on the algorithmic development of various truncation artifact reduction techniques that are suitable for different imaging applications.

Chapter 2 provides a thorough literature overview of previously published work. It starts with a few examples to illustrate why the analytical FDK algorithm cannot tolerate any data truncation. Thereafter, it reviews the existing heuristic extrapolation methods as well as various data completion strategies. Chapter 2 also shows how the truncation problem can be partially solved using an alternative Radon inversion – the differentiated backprojection method (DBP). Then, its several variants and the associated data sufficiency conditions that these methods depend on are presented. Next, two ROI imaging-specific modifications, i.e., filtered ROI imaging and offset detector acquisition, are described, followed by the introduction of two alternative ROI reconstruction techniques, namely wavelet based localization and lambda tomography.

In Chapter 3, a new sinogram extrapolation method is proposed that uses sinogram consistency methods to estimate the missing sinogram data. We first derived the Fourier representation of Helgason-Ludwig consistency conditions that can be evaluated very efficiently via FFT. The derivation is of practical significance and leads to a new sinogram-based data completion scheme that incorporates these consistency conditions as a constrained optimization for an estimated model in the missing region. More specifically, the method extrapolates the truncated sinogram with forward-projected data from a uniform ellipse of which the parameters are determined by optimizing these consistency conditions of the extrapolated sinogram. The experimental results on the Shepp-Logan phantom suggest that this approach yields more accurate reconstructions than the standard water cylinder extrapolation (Hsieh *et al.* [Hsie 04]). The method also robustly reduces the low-frequency bias in the reconstructed volume, which is reflected by a good recovery of attenuation coefficients. The feature will potentially enable accurate segmentation and quantitative analysis of the reconstructed volume. Although the method is described for a 2D imaging geometry, it could be naturally extended to 3D reconstructions by repeating this sinogram completion processing slice-wise.

Part II focuses on the three truncation artifact reduction methods that can be readily applied in clinical practice. All these methods, which either follow the analytic FBP frame or are by construction in an iterative manner, are capable of generating a high-quality 3D image from transaxially truncated data. Chapter 4 presents a refinement of the truncation artifact reduction method – ATRACT, for 3D ROI imaging that is implicitly more robust with respect to severely truncated data. The advantage of this method is that it can be accomplished without explicit extrapolation or prior knowledge. In its original formulation, the non-local ramp filtering was decomposed into a 2D Laplace filtering and a 2D Radon-based residual filtering step. This algorithm, however, requires frequent interpolations and complicates the filtering procedure. For practical use, we present two variants of ATRACT. One is based on expressing the residual filter as an efficient 2D convolution with an analytically derived kernel. The second variant is to apply ATRACT in 1D to further reduce computational complexity. Furthermore, two empirical correction techniques to compensate remaining artifacts from the ATRACT results are suggested at the end of Chapter 4.

In some clinical applications, e.g., cancer or tumor treatments, reconstructing an image inside the ROI alone may be sub-optimal, since the outer region may also contain useful information, such as surrounding landmarks or so-called organs-at-risk. This motivates the study in Chapter 5, where the concept of a special interleaved acquisition strategy is proposed that would allow us to acquire both full FOV projection data and truncated data within a single scan. Even though this would involve acquiring a small number of non-truncated projections, the overall applied patient dose is still much below the amount of a conventional scan. However, acquired shutter scan data is in general not compatible with conventional reconstruction algorithms. Therefore, we suggest three reconstruction pipelines that are capable of dealing with such data. The first approach involves pre-processing two groups of projection data in a separate manner, followed by backprojecting filtered data in a single volume. The second approach is a direct volumetric combination of two individually reconstructed images with an additional transition smoothing in the radial direction. The last one yields a projection-based merge using forward-projected data from an initial TV minimization reconstruction. All methods are able to provide a particular ROI with high quality/resolution for diagnosis and the region outside the ROI with relatively low quality for orientation.

Chapter 6 again investigates the possibility of recovering accurate ROI images from pure truncated data alone. To this purpose, we exploit the patient-specific *a* *priori* shape knowledge for the extrapolation of truncated projections. The method is based on the fact that prior to a 3D scan, two fluoroscopic X-ray acquisitions are generally performed from two orthogonal views, to isocenter the patient with respect to the target to be scanned. First, we estimate the rough 3D patient shape based on two fluoroscopic projections, using per-slice ellipse fitting. Forward-projecting this 3D model for any projection angle acquired during the actual ROI scan gives the patient bounded information for the corresponding projection. Then, detruncated projection data could be obtained by adapting the extrapolated profile to fit the known profile boundary points. The method yields more practical advantages compared to most other data completion strategies (Ruchala *et al.* [Ruch 02], Wiegert *et al.* [Wieg 05] and Kolditz *et al.* [Kold 10]): 1) It involves no additional radiation when using fluoroscopic images that are routinely acquired during the patient isocentering process; 2) The model estimation can be readily integrated into the existing interventional workflow without additional hardware; 3) The method only involves small vector/matrix multiplications on boundary points and thus is computationally very efficient.

Chapter 7 presents a detailed comparative evaluation of all proposed 3D ROI reconstruction algorithms on 16 patient datasets that were acquired in an interventional clinical environment. First, we describe the experimental setup, followed by conducting the algorithm-specific evaluation and parametrization for each of three proposed methods. In the comparison of 1D and 2D ATRACT, we observed that in general both methods robustly reduce cupping artifacts and yield reconstruction of high accuracy. However, 1D and 2D ATRACT suffer from an edge gradient artifact in the particular cases where the high dense skull is truncated. This artifact somewhat affects their quantitative accuracy in the evaluation. Although the investigated three SSR methods yield small differences inside the ROI, we observed that image quality and characteristics in the PR, which is also of particular interest for shutter scan applications, vary noticeably among these methods. In general, the prior image driven detruncation method shows a better image quality in the ROI and PR than the other two SSR methods and appears to be less dependent on the sparsity of full projections. The results also show that the PBE method leads to a major improvement in image quality, compared to the purely heuristic extrapolation method. Its accuracy is comparable to the camera-based extrapolation, in which the patient outline would be known from all projections. This confirms the effectiveness of the 3D shape model that is estimated by only two orthogonal projection images. The final comparative evaluation clearly depicts the algorithmic performance of all investigated methods under a uniform evaluation framework. ATRACT methods have shown to be more robust than the water cylinder extrapolation in severe truncation case. Compared to these heuristic methods that come without prior knowledge, the PBE and SSR methods achieve ROI reconstructions in a more accurate and robust manner. But differences between the methods with and without prior knowledge become smaller in the presence of severe data truncation. At the end of Chapter 7, we studied the trade-off between image quality and radiation dose for each of the investigated algorithms. We pointed out that although this is a multidimensional problem, the presented work could be used as the first indicator for the selection of these studied algorithms.

Chapter 8 presents several possible investigations in the future. From the algorithmic perspective, the metal artifact reduction techniques proposed in [Bal 06] and [Prel 10] could be applied to reduce the residual edge gradient artifacts in ATRACT. To speed-up the SSR reconstruction, some fast streak-removal techniques such as the methods proposed in [Toma 98, Elad 02, Manh 14] could be further investigated. Moreover, the consistency condition-based sinogram completion could be extended to a more practical cone-beam algorithm by following [Patc 02, Brok 06]. From the experimental perspective, future work involves validating the algorithms using real collimated data that is also practically important. Furthermore, using TLDs and anthropomorphic head phantoms to experimentally measure the actual effective dose and dose distribution for different ROI scans seems another interesting field of future research.

Appendix

A.1 Prove that $T_n(s)\left(1-s^2\right)^{-1/2}\exp(jk\theta)$ Form Orthogonal Basis of $L_2(Z,(1-s^2)^{-1/2})$

$$\begin{aligned}
&\left\langle T_n(s)\left(1-s^2\right)^{-1/2}\exp(jk\theta),\, T_{n^*}(s)\left(1-s^2\right)^{-1/2}\exp(jk^*\theta)\right\rangle \\
&= \int_0^{2\pi}\int_{-1}^{1} T_n(s)\left(1-s^2\right)^{-1/2}\exp(jk\theta) \\
&\times T_{n^*}(s)\left(1-s^2\right)^{-1/2}\exp(jk^*\theta)\left(1-s^2\right)^{1/2} ds d\theta \\
&= \int_{-1}^{1} T_n(s)\, T_{n^*}\left(1-s^2\right)^{-1/2}\int_0^{2\pi}\exp(jk\theta)\exp(jk^*\theta) \\
&= \delta_{nn^*}\delta_{kk^*} \qquad (9.1)
\end{aligned}$$

A.2 Link Between Bessel Function and Chebyshev Polynomial

The Fourier transform of the Bessel function can be computed as

$$\int_{-\infty}^{\infty}\exp(-j\xi s)\, J_n(s)\, ds = \frac{2(-j)^n}{(1-\xi^2)^{1/2}} T_n(\xi), \qquad (9.2)$$

for $\xi^2 < 1$. We can swap the variables s and ξ and move the term $2(-j)^n$ to the left side:

$$\int_{-\infty}^{\infty}\exp(-j\xi s)\, J_n(\xi)\,\frac{1}{2(-j)^n} d\xi = \left(1-s^2\right)^{-1/2} T_n(s), \qquad (9.3)$$

where $s^2 < 1$.

Then, substituting ξ by $-\xi$ and computing the Fourier transform of both sides

$$\frac{J_n(-\xi)}{2(-j)^n} = \int_{-\infty}^{\infty}\left(1-s^2\right)^{-1/2} T_n(s)\exp(-j\xi s)\, ds. \qquad (9.4)$$

List of Symbols and Abbreviations

$\boldsymbol{\theta}$	Rotation angle vector	56
$\boldsymbol{\xi}$	Fourier coefficients of 2D function	33
Λ	Calderon operator	33
(u, v)	Detector coordinates	18
$\mathbf{a}(\lambda)$	X-ray source trajectory	18
$\mathbf{e}$	Direction unit vector	18
$\mathbf{J}$	Jacobian	56
$\mathbf{P}$	Projection matrix	80
$\mathbf{R}$	Rotation matrix	80
$\mathbf{t}$	Translation vector	80
$\mathbf{u}$	Detector coordinates	53
$\mathcal{R}$	Radon transform	54
μ	Mean value	67
$\nabla f_{x,y,z}$	Image gradient	70
ω	Weighting function	70
σ	Standard deviation	67
θ	Rotation angle	27
A	Area of the scan FOV	120
D	Source-detector distance	18
E	Effective dose	5
$e(u)$	Extrapolation function	22
$f(\mathbf{x})$	3D object density function	17
$f_{\text{2D}}(\mathbf{r})$	2D object function	24

G	2D Fourier transform of a function	53
g	2D cone-beam projection image	18
g_F	2D Filtered projection image	19
h_{2D}	2D analytic kernel of ATRACT	57
H_ϕ	Hilbert transform of 2D function at angle ϕ	27
$h_R(\cdot)$	Ramp filter kernel	20
J_n	First kind Bessel function of order n	39
P	1D Fourier transform of a function	54
$p(\theta, s)$	2D sinogram parameterized by angle θ and detector bin s	24
R	Source-isocenter distance	18
s	1D detector bin	27
T_n	First kind of Chebyshev polynomial of order n	38
AEC	Automatic exposure control	5
ALARA	As low as reasonably achievable	5
AP	Anterior-posterior view	77
ATRACT	Approximated truncation robust algorithm for computed tomography	51
CB	Cone-beam	17
CBE	Camera-based extrapolation method	106
CC	Correlation coefficient	89
CNR	Contrast noise ratio	65
CT	Computed tomography	3
DBP	Differentiated backprojection	27
DE	Differential evolution	44
DPI	Dose percentage index	120
DSA	Digital subtraction angiography	8
FBP	Filtered backprojection	10
FDK	Feldkamp-Davis-Kress method	10
FFT	Fast Fourier transform	11

FOV	Field of view	6
HLCC	Helgason-Ludwig consistency conditions	35
HOT	High order total variation	31
HU	Hounsfield unit	89
ML	Medio-lateral view	77
ML-EM	Maximum likelihood expectation maximization	31
MLC	Multileaf collimator	65
OS	Ordered subset	100
PBE	Patient bounded extrapolation	82
POCS	Projection onto convex sets	31
PR	Peripheral region	63
PSRE	Patient bounded square root extrapolation method	106
PWCE	Patient bounded water cylinder extrapolation method	106
RMSE	Root mean squared error	89
ROI	Region of interest	6
SART	Simultaneous algebraic reconstruction technique	100
SSR	Shutter scan reconstruction	65
SSR-A	Joint weighted FDK/ATRACT method	99
SSR-B	Simple parallel volumetric combination method	99
SSR-C	Prior image driven detruncation method	99
TLD	Thermoluminescence dosimeter	128
TV	Total variation	31
WCE	Water cylinder extrapolation method	107
wTV	Weighted total variation	69

List of Figures

1.1 Contribution of various X-ray imaging procedures in Germany (2012) 4
1.2 Four different clinical examples with the indicated ROI regions 7
1.3 Illustration of a truncated projection image 8
1.4 Illustration of a C-arm angiography system 9
1.5 2D fluoroscopic image vs. 3D C-arm CT volume 9
1.6 A graphical overview of the thesis structure 15

2.1 Geometry and associated notations 18
2.2 Illustration of non-local property of the FDK algorithm 20
2.3 Illustration of truncation artifact in the FDK algorithm 21
2.4 Illustration of the principle of the heuristic extrapolations 23
2.5 The principle of data completion method using a sine curve 24
2.6 Example of data completion using sine curve traces 25
2.7 Examples of reconstructions using the DBP method 29
2.8 Schematic illustration of the data sufficiency conditions 30

3.1 Illustration of the double-wedge region in the FT of a sinogram . . . 42
3.2 Flowchart of the sinogram completion using consistency conditions . 44
3.3 Results of Shepp-Logan phantom (Radius of ROI: 60 pixels) 46
3.4 Results of Shepp-Logan phantom (Radius of ROI: 30 pixels) 47
3.5 Line profile of sinogram-based consistency condition method 48
3.6 The cost function values w.r.t. two ellipse radii 49

4.1 Geometry and notations for 2D flat-panel detector 55
4.2 Illustration of the ATRACT convolution kernel 59
4.3 Illustration of the impact of truncation on different filters 60

5.1 Schematic illustration of the concept of the shutter scan 68
5.2 Flowchart of the first approach for SSR 70
5.3 Flowchart of the second approach for SSR 71
5.4 Illustration of the transition and inner region 72
5.5 Flowchart of the third approach for SSR 74
5.6 Illustration of how to compute two parameter masks 75

6.1 Illustration of fluoroscopic X-ray projections 81
6.2 Flowchart of the PBE method 81
6.3 Geometry and notations for PBE 82
6.4 Illustration of how to approximate the ellipse radii 84

7.1 An overview of all 16 clinical datasets 88
7.2 Illustration of the four centered ROIs 90

7.3 Illustration of four off-centered ROIs 90
7.4 Summary of quantitative evaluation on FDK 92
7.5 Runtime and speed-up factor for ATRACT 94
7.6 Transversal slices through the ATRACT results (ROI 2) 96
7.7 Sagittal and coronal slices through the ATRACT results (ROI 2) . . . 97
7.8 Transversal slices through the ATRACT results (ROI 4) 98
7.9 Quantitative evaluation of ATRACT (centered cases) 98
7.10 Illustration of the edge gradient artifact 99
7.11 Coronal slices through the ATRACT results (ROI 7) 100
7.12 Comparison of the central line profiles 101
7.13 Quantitative evaluation of ATRACT (off-centered cases) 102
7.14 Results of SSR with 100 full projections (ROI 4) 104
7.15 A closer investigation of Region 1 and 2 reconstructed by SSR 105
7.16 Illustration of sparsity dependency for SSR 106
7.17 Quantitative assessment of the three SSR methods 107
7.18 Visualization of a head phantom shape 109
7.19 Comparison of WCE and PBE in projection domain 110
7.20 Comparison of WCE and PBE by the line profiles 110
7.21 Comparison of WCE and PBE in the volume domain 110
7.22 Transversal slices through the PBE results (ROI 2) 111
7.23 Transversal slices through the PBE results (ROI 4) 112
7.24 Sagittal slices through the PBE results (ROI 2) 113
7.25 Plots of line profile for PBE and WCE 114
7.26 Quantitative assessment of PBE (centered cases) 115
7.27 Transversal slices through the PBE results (ROI 7) 116
7.28 Quantitative assessment of PBE (off-centered cases) 117
7.29 Algorithmic performance of all methods on the centered ROI cases . . 118
7.30 Nonlinear curve fitting of the results from the centered cases 119
7.31 Quantitative results of all investigated methods (centered cases) . . . 120
7.32 A direct comparsionof PBE vs. SSR 121
7.33 Quantitative results of all investigated methods (off-centered cases) . 123
7.34 DPI against CC for ROI 1 and ROI 2 124
7.35 DPI against CC for ROI 3 and ROI 4 125

List of Tables

1.1 Mean value of the Effective dose of X-ray relevant examinations . . . 4

7.1 Description of four centered ROI sizes 89
7.2 Nonlinear curve fitting of the results from the centered cases 119
7.3 Nonlinear curve fitting of SSR against the sparsity level 122

Bibliography

[Ahme 14] A. Ahmed, Z. Clark, B. Patel, B. Aagaard-Kienitz, D. Niemann, K. Royalty, S. Shafer, and C. Strother. “High-Quality Low-dose C-arm CT Imaging of flow diverting devices in the angiography suite”. In: , Ed., *Proceedings ASNR*, pp. O–305, 2014.

[Akpe 05] S. Akpek, T. Brunner, G. Benndorf, C. Strother, *et al.* “Three-dimensional imaging and cone beam volume CT in C-arm angiography with flat panel detector”. *Diagn Interv Radiol*, Vol. 11, No. 1, pp. 10–13, 2005.

[Ardr 65] G. Ardran and H. Crooks. “The measurement of patient dose”. *The British journal of radiology*, Vol. 38, No. 454, pp. 766–770, 1965.

[Azev 95] S. Azevedo, P. Rizo, and P. Grangeat. “Region-of-interest cone-beam computed tomography”. Tech. Rep., Lawrence Livermore National Lab., CA (United States), 1995.

[Bai 09] M. Bai, J. Chen, R. Raupach, C. Suess, Y. Tao, and M. Peng. “Effect of nonlinear three-dimensional optimized reconstruction algorithm filter on image quality and radiation dose: validation on phantoms”. *Medical physics*, Vol. 36, No. 1, pp. 95–97, 2009.

[Bai 13] T. Bai, X. Mou, Q. Xu, and Y. Zhang. “Noise Energy Estimation Based on the Sinogram and its Application to the Regularization Parameter Selection for Statistical Iterative Reconstruction”. In: *Proceedings of Fully3D 2013*, pp. 158–161, 2013.

[Bal 06] M. Bal and L. Spies. “Metal artifact reduction in CT using tissue-class modeling and adaptive prefiltering”. *Medical Physics*, Vol. 33, No. 8, pp. 2852–2859, 2006.

[Benn 05] G. Benndorf, C. M. Strother, B. Claus, R. Naeini, H. Morsi, R. Klucznik, and M. E. Mawad. “Angiographic CT in cerebrovascular stenting”. *American Journal of Neuroradiology*, Vol. 26, No. 7, pp. 1813–1818, 2005.

[Bere 93] C. A. Berenstein and D. Walnut. “Local inversion of the Radon transform in even dimensions using wavelets”. 1993.

[Berg 14] M. Berger, A. Maier, Y. Xia, J. Hornegger, and R. Fahrig. “Motion Compensated Fan-Beam CT by Enforcing Fourier Properties of the Sinogram”. In: *Proceedings of the third international conference on image formation in x-ray computed tomography*, pp. 329–332, 2014.

[Bier 13a] B. Bier, A. Maier, H. Hofmann, C. Schwemmer, Y. Xia, T. Struffert, and J. Hornegger. “Truncation correction for VOI C-arm CT using scattered radiation”. In: *Proceedings of SPIE*, p. 86682F9, 2013.

[Bier 13b] B. Bier, C. Schwemmer, A. Maier, H. Hofmann, Y. Xia, J. Hornegger, and T. Struffert. “Convolution-Based Truncation Correction for C-Arm CT Using Scattered Radiation”. In: H.-P. Meinzer, T. M. Deserno, H. Handels, and T. Tolxdorff, Eds., *Bildverarbeitung für die Medizin 2013*, pp. 338–343, Berlin Heidelberg, 2013.

[BMUB 13] BMUB. “Umweltradioaktivität und Strahlenbelastung im Jahr 2013”. Tech. Rep. , Bundesministerium für Umwelt, Naturschutz, Bau und Reaktorsicherheit (BMUB), 2013. Available at `http://www.bmub.bund.de/`.

[Boyd 04] S. Boyd and L. Vandenberghe. *Convex optimization*. Cambridge university press, 2004.

[Brok 06] J. Brokish and Y. Bresler. “Sampling requirements for circular cone beam tomography”. In: *Nuclear Science Symposium Conference Record, 2006. IEEE*, pp. 2882–2884, IEEE, 2006.

[Bron 06] A. V. Bronnikov. “Phase-contrast CT: Fundamental theorem and fast image reconstruction algorithms”. In: *Proceedings of SPIE*, p. 63180Q, 2006.

[Cand 08] E. J. Candes, M. B. Wakin, and S. P. Boyd. “Enhancing sparsity by reweighted L1 minimization”. *Journal of Fourier analysis and applications*, Vol. 14, No. 5-6, pp. 877–905, 2008.

[Chen 08a] L. Chen, C. C. Shaw, M. C. Altunbas, C. J. Lai, X. Liu, T. Han, T. Wang, W. T. Yang, and G. J. Whitman. “Feasibility of volume-of-interest (VOI) scanning technique in cone beam breast CT - A preliminary study”. *Medical Physics*, Vol. 35, No. 8, pp. 3482–3490, 2008.

[Chen 08b] L. Chen, C. C. Shaw, M. C. Altunbas, C.-J. Lai, X. Liu, T. Han, T. Wang, W. T. Yang, and G. J. Whitman. “Feasibility of volume-of-interest (VOI) scanning technique in cone beam breast CT - a preliminary study”. *Medical physics*, Vol. 35, No. 8, pp. 3482–3490, 2008.

[Chin 12] G. Chintalapani, P. Chinnadurai, A. Maier, H. Shaltoni, H. Morsi, and M. Mawad. “The Value of Volume of Interest (VOI) C-arm CT Imaging in the Endovascular Treatment of Intracranial Aneurysms-A Feasibility Study”. *Proceedings of ASNR*, 2012.

[Chin 15] G. Chintalapani, P. Chinnadurai, A. Maier, S. Bauer, Y. Xia, and M. Mawad. “The added value of volume-of-interest (VOI) C-arm CT imaging during endovascular treatment of intracranial aneurysms”. *AJNR*, 2015.

[Chit 04] R. Chityala, K. R. Hoffmann, D. R. Bednarek, and S. Rudin. “Region of Interest (ROI) Computed Tomography”. *Proceedings of Society Photo-Optical Instrumentation Engineers*, Vol. 5368, No. 2, pp. 534–541, 2004.

[Chit 05] R. Chityala, K. R. Hoffmann, S. Rudin, and D. R. Bednarek. “Artifact reduction in truncated CT using sinogram completion”. In: *Medical Imaging*, pp. 2110–2117, International Society for Optics and Photonics, 2005.

[Cho 07] S. Cho, J. Bian, C.-T. Pelizzari, C. A.and Chen, T.-C. He, and X. Pan. “Region-of-interest reconstruction in circular cone-beam microCT”. *Medical Physics*, Vol. 34, No. 12, pp. 4923–4933, 2007.

[Cho 96] P. S. Cho, A. D. Rudd, and R. H. Johnson. “Cone-beam CT from width-truncated projections”. *Computerized Medical Imaging and Graphics*, Vol. 20, No. 1, pp. 49–57, 1996.

[Clac 13] R. Clackdoyle. “Necessary and sufficient consistency conditions for fan-beam projections along a line”. *Nuclear Science, IEEE Transactions on*, Vol. 60, No. 3, pp. 1560–1569, 2013.

[Cons 09] E. Constantino and K. B. Ozanyan. “Tomographic imaging of surface deformation from scarce measurements via sinogram recovery”. *Sensors Journal, IEEE*, Vol. 9, No. 4, pp. 399–410, 2009.

[Cour 08] M. Courdurier, F. Noo, M. Defrise, and H. Kudo. “Solving the interior problem of computed tomography using a priori knowledge”. *Inverse problems*, Vol. 24, No. 6, p. 065001, 2008.

[Defr 06] M. Defrise, F. Noo, R. Clackdoyle, and H. Kudo. “Truncated Hilbert transform and image reconstruction from limited tomographic data”. *Inverse problems*, Vol. 22, No. 3, p. 1037, 2006.

[Dela 95] A. H. Delaney and Y. Bresler. “Multiresolution tomographic reconstruction using wavelets”. *Image Processing, IEEE Transactions on*, Vol. 4, No. 6, pp. 799–813, 1995.

[Denn 11] F. Dennerlein. “Cone-beam ROI reconstruction using the Laplace operator”. In: *Proceedings of Fully 3D 2011*, pp. 80–83, 2011.

[Denn 13] F. Dennerlein and A. Maier. “Approximate truncation robust computed tomography - ATRACT ”. *Physics in Medicine and Biology*, Vol. 58, pp. 6133–6148, 2013.

[Dobb 00] J. Dobbins. “Handbook of Medical Imaging: Physics and Psychophysics”. 2000.

[Doel 08] M. Doelken, T. Struffert, G. Richter, T. Engelhorn, C. Nimsky, O. Ganslandt, T. Hammen, and A. Doerfler. “Flat-panel detector volumetric CT for visualization of subarachnoid hemorrhage and ventricles: preliminary results compared to conventional CT”. *Neuroradiology*, Vol. 50, No. 6, pp. 517–523, 2008.

[Edho 86] P. R. Edholm, R. M. Lewitt, and B. Lindholm. “Novel properties of the Fourier decomposition of the sinogram”. In: *in Proceedings of the International Workshop on Physics and Engineering of Computerized Multidimensional Imaging and Processing*, pp. 8–18, 1986.

[Elad 02] M. Elad. “On the origin of the bilateral filter and ways to improve it”. *Image Processing, IEEE Transactions on*, Vol. 11, No. 10, pp. 1141–1151, 2002.

[Elba 02] I. Elbakri, J. Fessler, *et al.* “Statistical image reconstruction for polyenergetic X-ray computed tomography”. *Medical Imaging, IEEE Transactions on*, Vol. 21, No. 2, pp. 89–99, 2002.

[Fari 92] A. Faridani, E. L. Ritman, and K. T. Smith. “Local tomography”. *SIAM Journal on Applied Mathematics*, Vol. 52, No. 2, pp. 459–484, 1992.

[Feld 84] L. A. Feldkamp, L. C. Davis, and J. W. Kress. “Practical cone beam algorithm”. *Optical Society of America*, Vol. 1, pp. 612–619, 1984.

[Gies 99] M. Gies, W. A. Kalender, H. Wolf, C. Suess, and M. T. Madsen. “Dose reduction in CT by anatomically adapted tube current modulation. I. Simulation studies”. *Medical physics*, Vol. 26, No. 11, pp. 2235–2247, 1999.

[Gomp 06] G. V. Gompel, M. Defrise, and D. V. Dyck. "Elliptical extrapolation of truncated 2D CT projections using Helgason-Ludwig consistency conditions". In: *Proceedings of SPIE*, p. 61424B, 2006.

[Greg 03] J. Gregor, S. S. Gleason, and M. J. Paulus. "Conebeam x-ray computed tomography with an offset detector array". In: *Image Processing, 2003. ICIP 2003. Proceedings. 2003 International Conference on*, pp. II–803, IEEE, 2003.

[Helg 65] S. Helgason. "The radon transform on Euclidean spaces, compact two-point homogeneous spaces, and Grassmann manifolds". *Acta Math.*, Vol. 113, No. 1, pp. 153–180, 1965.

[Herb 15] M. Herbst, F. Schebesch, M. Berger, J.-H. Choi, R. Fahrig, J. Hornegger, and A. Maier. "Dynamic detector offsets for field of view extension in C-arm computed tomography with application to weight-bearing imaging". *Medical Physics*, Vol. 42, No. 5, pp. 2718–2729, 2015.

[Herm 81] G. T. Herman and R. M. Lewitt. "Evaluation of a preprocessing algorithm for truncated CT projections". *J. Comput. Assist. Tomogr.*, Vol. 5, pp. 127–135, 1981.

[Heus 11] D. Heuscher and F. Noo. "CT dose reduction using dynamic collimation". In: *IEEE Nuclear Science Symposium and Medical Imaging Conference*, pp. 3470–3473, 2011.

[Hoch 02] A. Hochmuth, U. Spetzger, and M. Schumacher. "Comparison of three-dimensional rotational angiography with digital subtraction angiography in the assessment of ruptured cerebral aneurysms". *American Journal of Neuroradiology*, Vol. 23, No. 7, pp. 1199–1205, 2002.

[Hopp 08] S. Hoppe, J. Hornegger, G. Lauritsch, and F. Dennerlein. "Truncation correction for oblique filtering lines". *Medical Physics*, Vol. 35, No. 12, pp. 5910–5920, 2008.

[Hsie 04] J. Hsieh, E. Chao, J. Thibault, B. Grekowicz, A. Horst, S. McOlash, and T. J. Myers. "A novel reconstruction algorithm to extend the CT scan field-of-view". *Medical Physics*, Vol. 31, No. 9, pp. 2385–2391, 2004.

[Hsie 09] J. Hsieh. "Computed tomography: principles, design, artifacts, and recent advances". SPIE Bellingham, WA, 2009.

[Huds 94] H. M. Hudson and R. S. Larkin. "Accelerated image reconstruction using ordered subsets of projection data". *Medical Imaging, IEEE Transactions on*, Vol. 13, No. 4, pp. 601–609, 1994.

[ICRP 07a] ICRP. "Radiological Protection in Medicine". Tech. Rep. 103, International Commission on Radiological Protection (ICRP), 2007. Available at `http://www.fda.gov/Radiation-EmittingProducts/`.

[ICRP 07b] ICRP. "The 2007 Recommendations of the International Commission on Radiological Protection". Tech. Rep. 105, International Commission on Radiological Protection (ICRP), 2007. Available at `http://www.fda.gov/Radiation-EmittingProducts/`.

[Kadr 95] D. J. Kadrmas, R. J. Jaszczak, J. W. McCormick, R. E. Coleman, and C. B. Lim. "Truncation artifact reduction in transmission CT for improved SPECT attenuation compensation". *Physics in medicine and biology*, Vol. 40, No. 6, p. 1085, 1995.

[Kaes 15] T. Kaestner, J. Hornegger, A. Maier, Y. Xia, and S. Bauer. "Truncation Robust C-Arm CT Reconstruction for Dynamic Collimation Acquisition Schemes". In: Springer, Ed., *Proceedings in Bildverarbeitung für die Medizin 2015*, pp. 516–521, 2015.

[Karp 88] J. S. Karp, G. Muehllehner, and R. M. Lewitt. "Constrained Fourier space method for compensation of missing data in emission computed tomography". *IEEE Trans Med Imaging*, Vol. 7, pp. 21–25, 1988.

[Kats 03] A. Katsevich. "A general scheme for constructing inversion algorithms for cone beam CT". *International Journal of Mathematics and Mathematical Sciences*, Vol. 2003, No. 21, pp. 1305–1321, 2003.

[Kats 06] A. Katsevich. "Improved cone beam local tomography". *Inverse Problems*, Vol. 22, No. 2, p. 627, 2006.

[Kats 12] E. Katsevich, A. Katsevich, and G. Wang. "Stability of the interior problem with polynomial attenuation in the region of interest". *Inverse problems*, Vol. 28, No. 6, p. 065022, 2012.

[Kats 97] A. I. Katsevich. "Local tomography for the generalized Radon transform". *SIAM Journal on Applied Mathematics*, Vol. 57, No. 4, pp. 1128–1162, 1997.

[Kold 10] D. Kolditz, Y. Kyriakou, and W. A. Kalender. "Volume-of-interest (VOI) imaging in C-arm flat-detector CT for high image quality at reduced dose". *Medical Physics*, Vol. 37, No. 6, pp. 2719–2730, 2010.

[Kold 11] D. Kolditz, M. Meyer, Y. Kyriakou, and W. A. Kalender. "Comparison of extended field-of-view reconstructions in C-arm flat-detector CT using patient size, shape or attenuation information". *Physics in Medicine and Biology*, Vol. 56, No. 1, pp. 39–56, 2011.

[Kold 12] D. Kolditz, T. Struffert, Y. Kyriakou, A. Bozzato, A. Dörfler, and W. Kalender. "Volume-of-interest imaging of the inner ear in a human temporal bone specimen using a robot-driven C-arm flat panel detector CT system". *American Journal of Neuroradiology*, Vol. 33, No. 10, pp. E124–E128, 2012.

[Kudo 08] H. Kudo, M. Courdurier, F. Noo, and M. Defrise. "Tiny a priori knowledge solves the interior problem in computed tomography". *Physics in Medicine and Biology*, Vol. 52, No. 9, p. 2207, 2008.

[Kudo 91] H. Kudo and T. Saito. "Sinogram recovery with the method of convex projections for limited-data reconstruction in computed tomography". *J. Opt. Soc. Am.*, Vol. 8, pp. 1148–1160, 1991.

[Lasi 07] G. M. Lasio, B. R. Whiting, and J. F. Williamson. "Statistical reconstruction for x-ray computed tomography using energy-integrating detectors". *Physics in medicine and biology*, Vol. 52, No. 8, p. 2247, 2007.

[Lear 14] D. Leary and J. L. Robar. "CBCT with specification of imaging dose and CNR by anatomical volume of interest". *Medical physics*, Vol. 41, No. 1, p. 011909, 2014.

[Loui 83] A. K. Louis and F. Natterer. "Mathematical problems of computerized tomography". In: *Proc. IEEE*, pp. 390–408, 1983.

[Lu 14] W. Lu, H. Yan, X. Gu, Z. Tian, O. Luo, L. Yang, L. Zhou, L. Cervino, J. Wang, S. Jiang, *et al.* "Reconstructing cone-beam CT with spatially varying qualities for adaptive radiotherapy: a proof-of-principle study". *Physics in medicine and biology*, Vol. 59, No. 20, p. 6251, 2014.

[Ludw 65] D. Ludwig. "The radon transform on Euclidean spaces". *Commun. Pure Appl. Math.*, Vol. 19, No. , pp. 49–81, 1965.

[Maie 12] A. Maier, B. Scholz, and F. Dennerlein. "Optimization-based Extrapolation for Truncation Correction". In: *2nd CT Meeting*, pp. 390–394, 2012.

[Maie 13] A. Maier. "New Approaches to Dose Reduction in Interventional CT Imaging". *International Hospital*, Vol. 38, No. 1, pp. 20–21, 2013.

[Malt 07] J. D. Maltz, S. Bose, H. P. Shukla, and A. R. Bani-Hashemi. "CT truncation artifact removal using water-equivalent thicknesses derived from truncated projection data". In: *IEEE Engineering in Medicine and Biology Society*, pp. 2905–2911, 2007.

[Manh 14] M. Manhart, A. Aichert, T. Struffert, Y. Deuerling-Zheng, M. Kowarschik, A. Maier, J. Hornegger, and A. Dörfler. "Denoising and artefact reduction in dynamic flat detector CT perfusion imaging using high speed acquisition: first experimental and clinical results". *Physics in Medicine and Biology*, Vol. 59, No. 16, pp. 4505–4524, 2014.

[Mazi 10] S. R. Mazin and N. J. Pelc. "Fourier properties of the fan-beam sinogram". *Med. Phys.*, Vol. 37, pp. 1674–80, 2010.

[McCo 09] C. H. McCollough, A. N. Primak, N. Braun, J. Kofler, L. Yu, and J. Christner. "Strategies for reducing radiation dose in CT". *Radiologic Clinics of North America*, Vol. 47, No. 1, pp. 27–40, 2009.

[Mikh 57] S. G. Mikhlin. *Integral Equations: And Their Applications to Certain Problems in Mechanics, Mathematical Physics and Technology*. Vol. , New York: Pergamon, 1957.

[Miss 00] U. Missler, C. Hundt, M. Wiesmann, T. Mayer, and H. Brueckmann. "Three-dimensional reconstructed rotational digital subtraction angiography in planning treatment of intracranial aneurysms". *European Radiology*, Vol. 10, No. 4, pp. 564–568, 2000.

[Mulk 05] T. H. Mulkens, P. Bellinck, M. Baeyaert, D. Ghysen, X. Van Dijck, E. Mussen, C. Venstermans, and J.-L. Termote. "Use of an Automatic Exposure Control Mechanism for Dose Optimization in Multi–Detector Row CT Examinations: Clinical Evaluation 1". *Radiology*, Vol. 237, No. 1, pp. 213–223, 2005.

[Natt 01] F. Natterer. *The Mathematics of Computerized Tomography*. Society for Industrial and Applied Mathematics, 2001.

[Noo 04] F. Noo, R. Clackdoyle, and J. D. Pack. "A Two-step Hilbert Transform Method for 2D Image Reconstruction". *Physics in Medicine and Biology*, Vol. 49, No. 17, pp. 3903–3923, 2004.

[Ohne 00] B. Ohnesorge, T. Flohr, K. Schwarz, J. P. Heiken, and J. P. Bae. "Efficient correction for CT image artifacts caused by objects extending outside the scan field of view". *Medical Physics*, Vol. 27, No. 1, pp. 39–46, 2000.

[Olso 94] T. Olson and J. DeStefano. "Wavelet localization of the Radon transform". *Signal Processing, IEEE Transactions on*, Vol. 42, No. 8, pp. 2055–2067, 1994.

[Park 82] D. L. Parker. "Optimal short scan convolution reconstruction for fan beam CT". *Medical physics*, Vol. 9, No. 2, pp. 254–257, 1982.

[Patc 02] S. K. Patch. "Consistency conditions upon 3D CT data and the wave equation". *Physics in medicine and biology*, Vol. 47, No. 15, p. 2637, 2002.

[Pohl 14] M. Pohlmann, M. Berger, A. Maier, J. Hornegger, and R. Fahrig. "Estimation of missing fan-beam projections using frequency consistency conditions". In: *Proceedings of the third international conference on image formation in x-ray computed tomography*, pp. 203–207, 2014.

[Prel 10] D. Prell, Y. Kyriakou, M. Kachelrie, and W. A. Kalender. "Reducing metal artifacts in computed tomography caused by hip endoprostheses using a physics-based approach". *Invest Radiol*, Vol. 45, No. 11, pp. 747–754, 2010.

[Prin 90] J. L. Prince and A. S. Willsky. "Constrained sinogram restoration for limited-angle tomography". *Opt. Eng.*, Vol. 29, pp. 535–544, 1990.

[Rash 97] F. Rashid-Farrokhi, K. Liu, C. A. Berenstein, and D. Walnut. "Wavelet-based multiresolution local tomography". *Image Processing, IEEE Transactions on*, Vol. 6, No. 10, pp. 1412–1430, 1997.

[Rits 13] L. Ritschl, M. Knaup, and M. Kachelriess. "Extending the dynamic range of flat detectors in CBCT using a compressed-sensing-based mulit-exposure technique". In: *The 12th International Meeting on Fully 3D Image Reconstruction in Radiology and Nuclear Medicine*, pp. 26–29, 2013.

[Roba 12] J. L. Robar, D. Parsons, A. Berman, and A. MacDonald. "Volume-of-interest cone-beam CT using a 2.35 MV beam generated with a carbon target". *Medical physics*, Vol. 39, No. 7, pp. 4209–4218, 2012.

[Rohk 09] C. Rohkohl, B. Keck, H. G. Hofmann, and J. Hornegger. "RabbitCT—an open platform for benchmarking 3D cone-beam reconstruction algorithms". *Medical Physics*, Vol. 36, No. 9, pp. 3940–3944, 2009.

[Ruch 02] K. J. Ruchala, G. H. Olivera, J. M. Kapatoes, R. J. Reckwerdt, and T. R. Mackie. "Methods for improving limited field-of-view radiotherapy reconstructions using imperfect a priori images". *Med. Phys.*, Vol. 29, pp. 2590–605, 2002.

[Rudi 92] S. Rudin and D. R. Bednarek. "Region of interest fluoroscopy". *Medical physics*, Vol. 19, No. 5, pp. 1183–1189, 1992.

[Scha 10] S. Schafer, P. B. Noel, A. Walczak, and K. Hoffmann. "Filtered region of interest cone-beam rotational angiography". *Medical Physics*, Vol. 37, No. 2, pp. 694–703, 2010.

[Scha 11] D. Schäfer, M. Grass, and P. van de Haar. “FBP and BPF reconstruction methods for circular X-ray tomography with off-center detector”. *Medical physics*, Vol. 38, No. S1, pp. S85–S94, 2011.

[Sen 13] K. Sen Sharma, C. Holzner, D. M. Vasilescu, X. Jin, S. Narayanan, M. Agah, E. A. Hoffman, H. Yu, and G. Wang. “Scout-view Assisted Interior Micro-CT”. *Physics in Medicine and Biology*, Vol. 58, pp. 4297–4314, 2013.

[Sidk 08] E. Y. Sidky and X. Pan. “Image reconstruction in circular cone-beam computed tomography by constrained, total-variation minimization”. *Physics in medicine and biology*, Vol. 53, No. 17, p. 4777, 2008.

[Sour 05] K. Sourbelle, M. Kachelriess, and W. A. Kalender. “Reconstruction from truncated projections in CT using adaptive detruncation”. *European Radiology*, Vol. 15, No. 5, pp. 1008–1014, 2005.

[Star 05] J. Starman, N. Pelc, B. Strobel, and R. Fahrig. “Estimating 0th and 1st moments in C-arm CT data for extrapolating truncated projections”. In: *Proceedings of SPIE*, pp. 378–787, 2005.

[Stor 97] R. Storn and K. Price. “Differential evolution - a simple and efficient heuristic for global optimization over continuous spaces”. *Journal of Global Optimization*, Vol. 11, pp. 341–359, 1997.

[Suga 02] T. Sugahara, Y. Korogi, K. Nakashima, S. Hamatake, S. Honda, and M. Takahashi. “Comparison of 2D and 3D digital subtraction angiography in evaluation of intracranial aneurysms”. *American Journal of Neuroradiology*, Vol. 23, No. 9, pp. 1545–1552, 2002.

[Toma 98] C. Tomasi and R. Manduchi. “Bilateral filtering for gray and color images”. In: *Computer Vision, 1998. Sixth International Conference on*, pp. 839–846, IEEE, 1998.

[UNSC 10] UNSCEAR. “Sources and Effects of Ionizing Radiation”. Tech. Rep. , United Nations Scientific Committee on the Effects of Atomic Radiation, 2010. Available at `http://www.unscear.org/unscear/en/publications/`.

[Van 04] G. Van Gompel, G. Tisson, D. Van Dyck, and J. Sijbers. “A new algorithm for 2D region of interest tomography”. In: *Proceedings of SPIE 5370*, pp. 2105–2113, 2004.

[Wang 02] G. Wang. “X-ray micro-CT with a displaced detector array”. *Medical physics*, Vol. 29, No. 7, pp. 1634–1636, 2002.

[Wang 06] J. Wang, T. Li, H. Lu, and Z. Liang. “Penalized weighted least-squares approach to sinogram noise reduction and image reconstruction for low-dose X-ray computed tomography”. *Medical Imaging, IEEE Transactions on*, Vol. 25, No. 10, pp. 1272–1283, 2006.

[Welc 97] A. Welch and R. Clark. “Toward accurate attenuation correction in SPECT without transmission measurements”. *IEEE Trans Med Imaging*, Vol. 16, pp. 532–541, 1997.

[Wieg 05] J. Wiegert, M. Bertram, T. Netsch, J. Wulff, J. Weese, and G. Rose. “Projection extension for region of interest imaging in cone-beam CT”. *Acad. Radiol.*, Vol. 12, No. , pp. 1010–23, 2005.

[Xia 12] Y. Xia, A. Maier, F. Dennerlein, H. Hofmann, and J. Hornegger. "Efficient 2D Filtering for Cone-beam VOI Reconstruction". In: IEEE, Ed., *2012 Proceedings of the IEEE Nuclear Science Symposium and Medical Imaging Conference*, pp. 2415–2420, 2012.

[Xia 13a] Y. Xia, A. Maier, F. Dennerlein, H. Hofmann, K. Müller, and J. Hornegger. "Reconstruction from Truncated Projections in Cone-beam CT using an Efficient 1D Filtering". In: SPIE, Ed., *Proceedings of SPIE, Medical Imaging 2013*, 2013.

[Xia 13b] Y. Xia, A. Maier, F. Dennerlein, and J. Hornegger. "Truncation Correction using a 3D Filter for Cone-beam CT". In: Fully3D, Ed., *Fully3D 2013*, pp. 118–121, 2013.

[Xia 14a] Y. Xia, S. Bauer, A. Maier, M. Berger, and J. Hornegger. "Patient-bounded Extrapolation for 3D Region of Interest Reconstruction in C-arm CT". In: U. of Utah Frederic Noo, Ed., *Proceedings of the third international conference on image formation in x-ray computed tomography*, pp. 414–417, 2014.

[Xia 14b] Y. Xia, F. Dennerlein, S. Bauer, H. Hofmann, J. Hornegger, and A. Maier. "Scaling calibration in region of interest reconstruction with the 1D and 2D ATRACT algorithm". *International Journal for Computer Assisted Radiology and Surgery (IJCARS)*, Vol. 9, No. 3, pp. 345–356, 2014.

[Xia 14c] Y. Xia, H. Hofmann, F. Dennerlein, K. Müller, C. Schwemmer, S. Bauer, G. Chintalapani, P. Chinnadurai, J. Hornegger, and A. Maier. "Towards Clinical Application of a Laplace Operator-based Region of Interest Reconstruction Algorithm in C-arm CT". *IEEE Trans Med Imaging*, Vol. 33/2014, No. 3, pp. 593–606, 2014.

[Xia 15a] Y. Xia, M. Berger, S. Bauer, S. Hu, A. Aichert, J. Hornegger, and A. Maier. "Data Extrapolation using 2D Fourier-based Helgason-Ludwig Consistency Conditions". *Physics in Medicine and Biology*, Vol. , No. , p. , 2015. Under review.

[Xia 15b] Y. Xia, S. Bauer, A. Maier, M. Berger, and J. Hornegger. "Patient-bounded extrapolation using low-dose priors for volume-of-interest imaging in C-arm CT". *Medical Physics*, Vol. 42, No. 4, pp. 1787–1796, 2015.

[Xia 95] W. Xia, R. M. Lewitt, and P. R. Edholm. "Fourier correction for spatially variant collimator blurring in SPECT". *IEEE Trans Med Imaging*, Vol. 14, pp. 100–115, 1995.

[Xu 10] J. Xu, K. Taguchi, and B. M. Tsui. "Statistical projection completion in X-ray CT using consistency conditions". *IEEE Trans Med Imaging*, Vol. 29, pp. 1528–1540, 2010.

[Yang 10] J. Yang, H. Yu, M. Jiang, and G. Wang. "High-order total variation minimization for interior tomography". *Inverse problems*, Vol. 26, No. 3, p. ID: 035013, 2010.

[Ye 07] Y. Ye, H. Yu, Y. Wei, and G. Wang. "A general local reconstruction approach based on a truncated Hilbert transform". *Journal of Biomedical Imaging*, Vol. 2007, No. 1, pp. 2–2, 2007.

[Yu 06a] H. Yu, Y. Wei, J. Hsieh, and G. Wang. "Data consistency based translational motion artifact reduction in fan-beam CT". *IEEE Trans Med Imaging*, Vol. 25, pp. 792–803, 2006.

[Yu 06b] H. Yu and G. Wang. "A general formula for fan-beam lambda tomography". *International journal of biomedical imaging*, Vol. 2006, 2006.

[Yu 06c] H. Yu, Y. Ye, and G. Wang. "Practical cone-beam lambda tomography". *Medical physics*, Vol. 33, No. 10, pp. 3640–3646, 2006.

[Yu 07] H. Yu and G. Wang. "Data Consistency Based Rigid Motion Artifact Reduction in Fan-Beam CT". *IEEE Trans Med Imaging*, Vol. 26, pp. 249–260, 2007.

[Yu 09a] H. Yu, G. Cao, L. Burk, Y. Lee, J. Lu, P. Santago, O. Zhou, and G. Wang. "Compressive Sampling Based Interior Reconstruction for Dynamic Carbon Nanotube Micro-CT". *J. Xray. Sci. Technol.*, Vol. 17, pp. 295–303, 2009.

[Yu 09b] H. Yu and G. Wang. "Compressed sensing based interior tomography". *Physics in medicine and biology*, Vol. 54, No. 9, p. 2791, 2009.

[Yu 09c] H. Yu, J. Yang, M. Jiang, and G. Wang. "Supplemental analysis on compressed sensing based interior tomography". *Physics in medicine and biology*, Vol. 54, No. 18, p. N425, 2009.

[Zamy 07] A. A. Zamyatin and S. Nakanishi. "Extension of the reconstruction field of view and truncation correction using sinogram decomposition". *Medical physics*, Vol. 34, No. 5, pp. 1593–1604, 2007.

[Zeli 12] M. I. Zelikman and S. A. Kruchinin. "Calibration of Thermoluminescent Dosimeters for Measuring Effective Dose in Computer Tomography". *Biomedical Engineering*, Vol. 46, No. 5, pp. 186–189, 2012.

[Zell 05] B. Zellerhoff, B. Scholz, E. P. Ruehrnschopf, and T. Brunner. "Low contrast 3D-reconstruction from C-arm data". In: *Proceedings of SPIE*, pp. 646–655, 2005.

[Zhan 07] B. Zhang and G. Zeng. "Two-dimensional iterative region-of-interest (ROI) reconstruction from truncated projection data". *Medical physics*, Vol. 34, No. 3, pp. 935–944, 2007.

[Zhao 00] S. Zhao and G. Wang. "Feldkamp-type cone-beam tomography in the wavelet framework". *Medical Imaging, IEEE Transactions on*, Vol. 19, No. 9, pp. 922–929, 2000.

[Zou 04] Y. Zou and X. Pan. "Exact image reconstruction on PI-lines from minimum data in helical cone-beam CT". *Physics in Medicine and Biology*, Vol. 49, No. 6, p. 941, 2004.